

UNCLASSIFIED

AD NUMBER

AD916290

LIMITATION CHANGES

TO:

Approved for public release; distribution is unlimited.

FROM:

Distribution authorized to U.S. Gov't. agencies only; Test and Evaluation; NOV 1973. Other requests shall be referred to Army Air Mobility Research and Development Lab., Fort Eustis, VA.

AUTHORITY

UDAAMRDL ltr 30 Mar 1976

THIS PAGE IS UNCLASSIFIED

THIS REPORT HAS BEEN DELIMITED
AND CLEARED FOR PUBLIC RELEASE
UNDER DOD DIRECTIVE 5200.20 AND
NO RESTRICTIONS ARE IMPOSED UPON
ITS USE AND DISCLOSURE.

DISTRIBUTION STATEMENT A

APPROVED FOR PUBLIC RELEASE;
DISTRIBUTION UNLIMITED.

AD

USAAMRDL TECHNICAL REPORT 73-78A

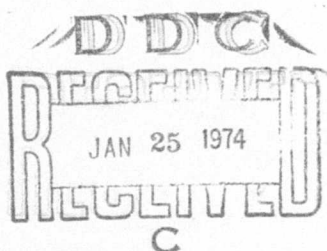
ARMORED STRUCTURAL HELICOPTER FUSELAGE STUDY

AD916290

By

Robert T. Welge
Walter E. Huebner

November 1973



EUSTIS DIRECTORATE
U. S. ARMY AIR MOBILITY RESEARCH AND DEVELOPMENT LABORATORY
FORT EUSTIS, VIRGINIA

CONTRACT DAAJ02-72-C-0018
SIKORSKY AIRCRAFT
DIVISION OF UNITED AIRCRAFT CORPORATION
STRATFORD, CONNECTICUT



Distribution limited to U.S. Government agencies only; test and evaluation; November 1973. Other requests for this document must be referred to the Eustis Directorate, U.S. Army Air Mobility Research and Development Laboratory, Fort Eustis, Virginia 23604.

DISCLAIMERS

The findings in this report are not to be construed as an official Department of the Army position unless so designated by other authorized documents.

When Government drawings, specifications, or other data are used for any purpose other than in connection with a definitely related Government procurement operation, the United States Government thereby incurs no responsibility nor any obligation whatsoever; and the fact that the Government may have formulated, furnished, or in any way supplied the said drawings, specifications, or other data is not to be regarded by implication or otherwise as in any manner licensing the holder or any other person or corporation, or conveying any rights or permission, to manufacture, use, or sell any patented invention that may in any way be related thereto.

Trade names cited in this report do not constitute an official endorsement or approval of the use of such commercial hardware or software.

DISPOSITION INSTRUCTIONS

Destroy this report when no longer needed. Do not return it to the originator.



DEPARTMENT OF THE ARMY
U. S. ARMY AIR MOBILITY RESEARCH & DEVELOPMENT LABORATORY
EUSTIS DIRECTORATE
FORT EUSTIS, VIRGINIA 23604

This study was performed under Contract DAAJ02-72-C-0018 with Sikorsky Aircraft Division of United Aircraft Corporation. Results of the study show the feasibility of fabricating a helicopter fuselage that will be invulnerable to small-arms fire.

This report has been reviewed by the Eustis Directorate, U.S. Army Air Mobility Research and Development Laboratory, and is considered to be technically sound. It is published for the exchange of information and the stimulation of future research.

This program was conducted under the technical management of Mr. James L. Perkinson, Jr., Technology Applications Division.

A confidential appendix to this report, entitled "Ballistic Test Data", has been published separately.

Project 1F163211D157
Contract DAAJ02-72-C-0018
USAAMRDL Technical Report 73-78A
November 1973

ARMORED STRUCTURAL HELICOPTER FUSELAGE STUDY

Final Report

Sikorsky Engineering Report 50834

By

Robert T. Welge
Walter E. Huebner

Prepared by

Sikorsky Aircraft
Division of United Aircraft Corporation
Stratford, Connecticut

for

EUSTIS DIRECTORATE

U. S. ARMY AIR MOBILITY RESEARCH AND DEVELOPMENT LABORATORY
FORT EUSTIS, VIRGINIA

Distribution limited to U.S. Government agencies only;
test and evaluation; November 1973. Other requests for
this document must be referred to the Eustis Directorate,
U.S. Army Air Mobility Research and Development
Laboratory, Fort Eustis, Virginia 23804.

ABSTRACT

This program was initiated to evaluate the feasibility of using dual hardness steel armor as primary structure for a helicopter fuselage to enhance survivability in a hostile environment involving small-arms fire.

This report is the result of the work conducted under a two-phase program. The Phase I effort involved the preliminary design of an aerial armored reconnaissance system (AARS) aircraft for the aerial scout mission, with a defined threat as provided by U.S. Army. An extensive materials study was also conducted to determine the characteristics of the armor under severe environmental conditions. The armor thickness required to defeat the defined threat was established by ballistic testing, which was followed by static and fatigue testing on damaged and undamaged armor specimens. Fatigue crack initiation and propagation were also measured, and residual life after ballistic damage was identified. Ballistic tests were conducted at high and low temperatures to determine the effects of temperature on the ballistic capability of the armor.

During Phase II, a special test facility was constructed, and a full-scale center section of the helicopter was fabricated and tested under loads determined in Phase I. Ballistic tests were also conducted on the center section test specimen while subjected to simulated flight loads. A second center section was also fabricated for subsequent testing by the U.S. Army.

Design, analysis and test results indicate that dual hardness steel armor provides a structural material which is suitable for both primary structure and ballistic protection for an integrally armored helicopter fuselage.

FOREWORD

This report was prepared by Sikorsky Aircraft Division of United Aircraft Corporation, under USAAMRDL Contract DAAJ02-72-C-0018, Project 1F163211D157, and concerns the work performed during the period of November 1971 through May 1973 on both phases of a two-phase program.

The ballistic testing is documented in a separate appendix, which is classified confidential.

The contract was administered by the Eustis Directorate, U.S. Army Air Mobility Research and Development Laboratory, with Mr. J. Perkinson serving as technical supervisor.

Sikorsky Aircraft personnel who made technical contributions to the program and their areas of activity are as follows:

G. R. Stack	Program Manager
R. T. Welge/W. E. Huebner	Program Engineering Managers
N. F. K. Kefford	Preliminary Design
T. A. Reilley	Design
T. M. Murphy	Materials
M. H. Horowitz	Materials
P. M. Menkes	Crashworthiness
J. B. Sainsbury-Carter	Structures
J. H. Conaway	Structures
B. P. W. Stocker	Test
H. L. Kearney	Test
J. J. Corso	Test
J. J. Barto	Manufacturing Engineering
J. J. Nette	Manufacturing
A. J. Milton	Loads/Criteria

The cooperation of D. J. Papetti of U.S. Army Mechanics and Material Research Center in conducting the ballistic tests is gratefully acknowledged.

TABLE OF CONTENTS

	<u>Page</u>
ABSTRACT	iii
FOREWORD	v
LIST OF ILLUSTRATIONS	xi
LIST OF TABLES	xx
LIST OF SYMBOLS AND ABBREVIATIONS	xxiii
INTRODUCTION	1
PRELIMINARY DESIGN CONFIGURATION	3
Objective	3
Approach	3
Aircraft Description	3
Aircraft Performance	18
Mass Properties	25
Mathematical Design Model	31
MIDSECTION DESIGN	32
Objective	32
Approach	32
Discussion	32
BALLISTIC-PROTECTED JOINTS	39
Objective	39
Approach	39
Discussion	39
CRASHWORTHINESS DESIGN/ANALYSIS	40
Objective	40
Approach	40
Discussion	44
Vertical Crash	44
Longitudinal Crash	46
Side Crash	49
Structural Support Crash Loads	49

	<u>Page</u>
LOADS AND CRITERIA	52
Objective	52
Approach	52
Discussion	52
Design Flight Loads and Criteria	52
Design Ground Loads and Criteria	52
Center Section Applied Static Loads	59
Fatigue Criteria and Design Loads	59
RELIABILITY/MAINTAINABILITY	68
Objective	68
Approach	68
Discussion	68
AIRCRAFT DESIGN AT ALTERNATE GROSS WEIGHTS	74
Objective	74
Approach	74
Discussion	74
DETAILED STRUCTURAL ANALYSIS	79
Objective	79
Approach	79
Discussion	86
Finite Element Analysis	86
Fatigue and Fracture Analysis	98
Fuselage Fitting Analysis	111
MATERIALS CHARACTERISTICS	119
Objectives	119
Approach, Procedures and Results	119
Material	119
Welding Procedure	120
Tensile Properties	120
Fatigue Testing	126
Crack Propagation	135
Fracture Toughness	145
Stress Corrosion Susceptibility	149
Residual Stress Measurement	153
Residual Static Strength	161
Residual Fatigue Properties	167
Crack Propagation from Ballistic Damage	177
Discussion	182

	<u>Page</u>
TEST SPECIMEN FABRICATION	188
Summary	188
Fabrication Procedures	188
Armor	188
Fittings	188
Assembly Procedures	190
Welding	190
Subassembly	190
Final Assembly	192
Manufacturing Problems	192
Residual Stress Cracking	192
Fusion Line Cracking	197
Heat-Affected Zone Cracking	197
Corrective Action	197
Laser Welding	201
ARMORED FUSELAGE TEST FACILITY	213
General	213
Configuration Definition	213
Load Type Selection	213
Load Simulation	213
Mission Spectrum	213
Load Application Scheme	215
Support Frame	215
Dummy Gearbox	217
Dummy Landing Gear	217
Control System	220
Feedback System	220
Error Detection	220
Programmer	220
Instrumentation System	224
TESTING OF THE STRUCTURAL ARMOR FUSELAGE SPECIMENS	225
Introduction	225
Testing the First Specimen	225
Testing the Second Specimen	233
Static Tests	233
3600-Hour Fatigue Test	233
Ballistic Test	252
600-Hour Fatigue Test	252
Residual Strength Test	263
Final Inspection	263
CONCLUSIONS	265

	<u>Page</u>
RECOMMENDATIONS	266
LITERATURE CITED	269
APPENDIX. Armored Structural Helicopter Fuselage Study ballistic test data(confidential - under separate cover)	
DISTRIBUTION	271

LIST OF ILLUSTRATIONS

<u>Figure</u>		<u>Page</u>
1	AARS Baseline Aircraft.	5
2	Relative Vulnerability in Band 20 Degrees Above to 40 Degrees Below Horizontal.	10
3	Alighting Gear Isometric.	13
4	Structural Armor Fuselage Gross Weight Versus Disc Loading and C_T/σ	16
5	Transmission Mounting Isometric	19
6	AARS Power Required Versus Speed	22
7	AARS Hover Performance	23
8	AARS Equivalent Parasite Drag Area	24
9	Net Vertical Drag	26
10	Helicopter Design Model Flow Chart.	33
11	Midsection Isometric	35
12	Lower Midsection Door Design	37
13	Upper Midsection Door Design	38
14	Weld Protection Concepts.	41
15	Fitting Bolt Protection Concept	42
16	Barrel Nut Bolt Retention Concept	43
17	Landing Gear Vertical Displacement Versus Vertical Impact Velocity	45
18	Airframe and Pilot Motions for 42-FPS Vertical Crash. . . .	47
19	Longitudinal Load Factor Versus Ground Roll-Out Distance for 50-FPS Initial Velocity.	48
20	Longitudinal Load Factor Versus Crushing Distance for 20-FPS Centroidal Nose Impact	50

<u>Figure</u>		<u>Page</u>
21	Lateral Velocity for Aircraft Roll-Over to Begin Versus Initial Roll Angle	51
22	Center Section Applied Loads and Geometry	60
23	AARS V-N Diagram for Limit and Fatigue Design	64
24	Maneuver Load Spectrum.	65
25	Impact Landing Load Distribution - Cumulative Frequency of Occurrences for Aircraft Life = 3600 Hours	66
26	Skid Gear Load Versus Sink Speed.	67
27	Torque Versus Cumulative Frequency of Occurrence for Aircraft Life = 3600 Hours	69
28	Load Factor Cumulative Frequency of Occurrences in Vertical Takeoff Maneuvers for Aircraft Life = 3600 Hours	70
29	Useful Load Versus Gross Weight	75
30	AARS Alternate Configuration - No Passengers	77
31	AARS Alternate Configuration - Four Passengers	81
32	Gross Weight Versus Payload and Endurance	83
33	Alternate Armament Configuration at Increased Gross Weight.	84
34	Gross Weight Versus Armor Thickness	85
35	AARS Center Section Test Specimen	87
36	NASTRAN Finite Elements in AARS Model	88
37	Detail of Beam Elements in AARS Finite Element Model	89
38	Plate Gridwork in AARS Aft Support Tab Design	91
39	Structural Model of AARS Roof Plate	92

<u>Figure</u>		<u>Page</u>
40	Structural Model of Aft Support Tab and Engine Air Intake.	93
41	AARS (NASTRAN) Structural Displacements for Symmetrical Dive and Pullout - 216 Knots	95
42	Maximum Principal Stresses (KSI) in Plate Elements in Symmetric Dive and Pullout (216 Knots)	96
43	Bending Stresses (KSI) in Bar Elements in Symmetric Dive and Pullout (216 Knots)	97
44	Critical Stress Areas - AARS Center Section	99
45	Base Material Constant Life Diagram.	102
46	Welded Material Constant Life Diagram.	103
47	Configuration for Crack Propagation Analysis	109
48	Base Material Crack Propagation Rate, R = 0.1	110
49	Transmission Support Structure - Strut Designation	111
50	Landing Gear Support Struts.	112
51	Fatigue Test Load Spectrum	114
52	Left-Hand Forward Transmission Support Structure Attachment Fitting	117
53	Upper Forward Landing Gear Attachment Fitting.	118
54	Macrostructural Appearance of DHS Used in All Phases of Material Characterization Testing, ~10X.	121
55	Microstructural Appearance of DHS Used in All Phases of Material Characterization Testing, 500X.	122
56	Hardness Profile of Typical Welded Specimen.	123
57	Macrostructural Appearance of Typical Weld, ~2.3X.	124
58	Undamaged Base Fatigue Test Specimen	127
59	Undamaged Welded Fatigue Test Specimen	128

<u>Figure</u>	<u>Page</u>
60 Base Undamaged Fatigue Specimen	129
61 Welded Undamaged Fatigue Specimen	129
62 Vibratory Stress Versus Cycles to Fracture, Base Undamaged Material, R = 0.1	130
63 Vibratory Stress Versus Cycles to Fracture, Welded Undamaged Material, R = 0.1	132
64 Typical Fracture Surface, Base Undamaged Fatigue Specimen 6.5X	134
65 Typical Fracture Surface, Welded Undamaged Fatigue Specimen, 4X	134
66 Crack Propagation Test Specimen	136
67 Base Undamaged Crack Propagation Specimen	137
68 Welded Undamaged Crack Propagation Specimen	137
69 Crack Length Versus Cycles, Base Undamaged Specimen S/N BP-1, Second Stress Level	139
70 Crack Length Versus Cycles, Base Undamaged Specimen S/N BP-1, First Stress Level	140
71 Crack Length Versus Cycles, Base Undamaged Specimen S/N BP-3	141
72 Crack Length Versus Cycles, Welded Undamaged Specimen S/N WC-1	142
73 Crack Length Versus Cycles, Welded Undamaged Specimen S/N WC-2	143
74 Crack Length Versus Cycles, Welded Undamaged Specimen S/N WC-3	144
75 Typical Fracture Surface, Base Undamaged Crack Propagation Specimen, 1X	145
76 Typical Fracture Surface, Welded Undamaged Crack Propagation Specimen, 1X	146
77 Three-Point Bend Fracture Toughness Specimen	147
78 Cantilever Beam Fracture Toughness Precrack Setup	148

<u>Figure</u>		<u>Page</u>
79	Ambient Fracture Toughness Test Setup	148
80	Cantilever Beam Fixture for Environmental Cracking Susceptibility Test	151
81	Deflection Calibration for Cantilever Beam Loaded Stress Corrosion Specimens	152
82	Typical Specimen Appearance After 500-Hour Exposure . . .	154
83	Weight Gain After 500-Hour Exposure to 5% NaCl, 95° F	155
84	Weight Loss After Removal of Corrosion Product.	155
85	Specimen Appearance After Removal of Corrosion Product	156
86	Remnant Tensile Strength After 500-Hour Exposure to 5% NaCl at 95° F	159
87	Residual Stress Distribution	162
88	Ballistic Penetration, Ambient Temperature.	163
89	Impact Cratering, Ambient Temperature	163
90	Impact Cratering, -65° F.	164
91	Ballistic Penetration, +250° F.	164
92	Ballistically Damaged Base Fatigue Test Specimen.	168
93	Ballistically Damaged Welded Fatigue Test Specimen.	169
94	Base Damaged Fatigue Specimen With Hard Side Surface Damage.	170
95	Base Damaged Fatigue Specimen With Through Hole	170
96	Welded Damaged Fatigue Specimen	171
97	Vibratory Stress Versus Cycles to Fracture, Base Damaged Material, R = 0.1	173
98	Vibratory Stress Versus Cycles to Fracture, Welded Damaged Material, R = 0.1	175
99	Vibratory Stress Versus Cycles to Fracture, Mean Curve Comparison, R = 0.1	176

<u>Figure</u>	<u>Page</u>
100 Typical Base Damaged Microstructural Appearance Showing White Streaks and Associated Cracks, 500X	178
101 Typical Fracture Surfaces of Base Damaged Fatigue Specimens 1.7X	179
102 Typical Fracture Surface, Welded Damaged Fatigue Specimen, 2.2X	180
103 Base Damaged Crack Propagation Specimen	181
104 Welded Damaged Crack Propagation Specimen	181
105 Crack Length Versus Cycles, Base Damaged Specimen S/N BDA-8	184
106 Crack Length Versus Cycles, Welded Damaged Specimen S/N WDA-7	185
107 Fracture Surface, Welded Damaged Crack Propagation Specimen, 1X	187
108 Typical Center Section Subassembly	189
109 Welded Attachment Fittings	189
110 Exploded View of Center Section Showing Major Structural Subassemblies	191
111 Aft Bulkhead Assembly Fixture	193
112 Welding of Aft Bulkhead Assembly	193
113 Lower Center Section Assembly Fixture	194
114 Completed Lower Center Section	194
115 Completed Center Section	195
116 Typical Residual Stress Crack After Stop-Drilling	196
117 Crack Removed and Ready for Weld Repair	196
118 Secondary Residual Stress Crack	198
119 Secondary Crack During Weld Repair	198
120 Typical Fusion Line Cracking	199

<u>Figure</u>		<u>Page</u>
121	Fusion Line Cracking Around Repair Plug Weld	199
122	Typical Corner Heat-Affected Zone Crack	200
123	Typical Edge Heat-Affected Zone Crack	200
124	Crack Size Distribution	204
125	Crack Locations, Specimen 1	205
126	Crack Locations, Specimen 2	207
127	Laser Weld Cross Section, 9X	210
128	Typical Laser Weld Hardness Profile, Thickness 0.305 Inch, Speed 50 Inches per Minute	211
129	Weld Hardness Profile Comparison	212
130	Fatigue Test Load Spectrum	216
131	Support Frame	218
132	Dummy Gearbox	218
133	Test Article Installed in Test Facility	219
134	Control Console	221
135	Control System Block Diagram	222
136	Loading System	223
137	Programmer Schematic	224
138	Structural Armor Fuselage Test Setup, Specimen S/N-1	226
139	Structural Armor Fuselage Test Setup, Specimen S/N-1	227
140	Structural Armor Fuselage Test Setup, Specimen S/N-1	227
141	Structural Armor Fuselage Test Setup, Specimen S/N-2	228

<u>Figure</u>		<u>Page</u>
142	Structural Armor Fuselage Test Setup, Specimen S/N-2	228
143	Structural Armor Fuselage, Strain Gage Locations	229
144	Structural Armor Fuselage, Static Stress Correlation, Specimen S/N-2, Area 1	234
145	Structural Armor Fuselage, Static Stress Correlation, Specimen S/N-2, Area 3	235
146	Structural Armor Fuselage, Static Stress Correlation, Specimen S/N-2, Area 4	236
147	Structural Armor Fuselage, Typical Strain Gage Installation, Specimen S/N-2, Areas 3 and 4 . .	237
148	Typical Stress Concentration Calculation, Area 4 . .	237
149	Structural Armor Fuselage, Load Factor Distribution - Cumulative Frequency of Occurrences in Vertical Takeoff Maneuvers for Aircraft Life of 3600 Hours . .	238
150	Structural Armor Fuselage, Impact Landing Load Distribution - Cumulative Frequency of Occurrence for Aircraft Life of 3600 Hours	239
151	Structural Armor Fuselage, Maneuver Load Factor Distribution - Cumulative Frequency of Occurrence for Aircraft Life of 3600 Hours	240
152	Structural Armor Fuselage, Hover Turn Torque Distribution - Cumulative Frequency of Occurrence for Aircraft Life of 3600 Hours	241
153	Structural Armor Fuselage, Dual Hardness Steel Material S-N Curve	243
154	Structural Armor Fuselage, Ballistic Test Target Areas, Armor-Piercing Projectiles	253
155	Structural Armor Fuselage, Ballistic Test Target Areas, Ball Projectiles	253
156	Structural Armor Fuselage, Ballistic Test Setup, Showing Typical Spall Containment Arrangements . . .	254

<u>Figure</u>		<u>Page</u>
157	Structural Armor Fuselage, Ballistic Test Setup Showing Weapon and Chronograph	254
158	Structural Armor Fuselage, Ballistic Test Setup Showing Typical Spall Containment Arrangements	255
159	Structural Armor Fuselage, Ballistic Test Setup Showing Weapon and Chronograph	255
160	Ballistic Impact Zones, Rounds 1 and 2, Armor- Piercing Projectiles	256
161	View of Fuselage Inside Surface Behind Impact Zones of Rounds 1 and 2	256
162	Ballistic Impact Zone, Round 3, Armor-Piercing Projectile	257
163	Ballistic Impact Zone, Round 4, Armor-Piercing Projectile	257
164	Ballistic Impact Zone, Round 5, Armor-Piercing Projectile	258
165	View of Fuselage Inside Surfaces Behind Impact Zones of Rounds 4 and 5	258
166	Ballistic Impact Zone, Round 6, Armor-Piercing Projectile	259
167	Ballistic Impact Zone, Round 7, Armor-Piercing Projectile	259
168	Ballistic Impact Zone, Round 8, Ball Projectile . . .	260
169	Ballistic Impact Zone, Round 9, Ball Projectile . . .	260
170	Ballistic Impact Zone, Round 10, Ball Projectile . . .	261
171	Ballistic Impact Zone, Round 11, Ball Projectile . . .	261
172	Ballistic Impact Zone, Round 12, Ball Projectile . . .	262
173	Ballistic Impact Zone, Round 13, Ball Projectile . . .	262
174	Residual Strength Test, Measured Stress Versus Percent of Design Limit Load - Pullout	264

LIST OF TABLES

<u>Table</u>		<u>Page</u>
I	Summary of Baseline Aircraft Attributes.	7
II	AARS Point Design - Summary Weight Statement	8
III	AARS Point Design - Mission Analysis	9
IV	AARS Mission Equipment	21
V	Results Summary of Panel Point Analysis.	28
VI	Basic Aircraft Parameters for Loads and Criteria	53
VII	Flight Loads and Criteria.	54
VIII	Summary of Limit Flight Loads, Load Factors, and Angular Accelerations.	55
IX	Summary of Limit Ground Loads, Load Factors, and Angular Accelerations.	58
X	Forward and Aft Fuselage Loads Applied to Center Section.	61
XI	Rotor Head and Gun Inertia Loads	62
XII	AARS - Operational Usage Spectrum, 3600 Hours	63
XIII	Summary of Fatigue Data (Limit Loads).	71
XIV	AARS Alternate Design With No Passenger Capacity	76
XV	AARS Alternate Design With Capacity for Four Passengers .	80
XVI	Stresses at Critical Points in AARS Center Section (KSI)	101
XVII	Nominal Mean and Vibratory Stresses.	104
XVIII	Theoretical Stress Concentration K_t and Modified Vibratory Stress σ_v^*	107
XIX	Fatigue Life in Flight Hours	108
XX	Transmission Support Strut Loads	113

<u>Table</u>		<u>Page</u>
XXI	Landing Gear Support Strut Loads.	113
XXII	Number of Cycles per Load Block	114
XXIII	Repeated Load Amplitudes and Cycles - Transmission Struts	115
XXIV	Repeated Load Amplitudes and Cycles - Landing Gear Struts	116
XXV	Tensile Test Results.	125
XXVI	Fatigue Test Results - Base Undamaged Material.	131
XXVII	Fatigue Test Results - Welded Undamaged Material.	133
XXVIII	Crack Propagation Results - Base Undamaged Material.	138
XXIX	Crack Propagation Results - Welded Undamaged Material.	138
XXX	Fracture Toughness Test Results	150
XXXI	Stress Corrosion Susceptibility Results	160
XXXII	Residual Strength, Ballistically Impacted Base Specimens	165
XXXIII	Residual Static Strength, Ballistically Impacted Welded Specimens	166
XXXIV	Fatigue Test Results - Base Damaged Material.	172
XXXV	Fatigue Test Results - Welded Damaged Material.	174
XXXVI	Crack Propagation Results - Base Damaged Material	183
XXXVII	Crack Propagation Results - Welded Damaged Material.	183
XXXVIII	Crack Documentation, Specimen #1	202
XXXIX	Crack Documentation, Specimen #2	203
XL	Operational Usage Spectrum	214

<u>Table</u>		<u>Page</u>
XLI	Applied Loads	215
XLII	Loading System Ranges	217
XLIII	AARS Structural Armor Fuselage Static Stress Survey Results	231
XLIV	In-Flight Damage Calculations, Specimen 2, Area 1 (Gages 1 and 2)	244
XLV	In-Flight Damage Calculations, Specimen 2, Area 3 (Gages 4 and 5)	246
XLVI	In-Flight Damage Calculations, Specimen 2, Area 4 (Gages 6 and 7)	248
XLVII	Static Test Damage Calculations, Specimen S/N-2, Area 1 (Gages 1 and 2)	250
XLVIII	Static Test Damage Calculations, Specimen S/N-2, Area 3 (Gages 4 and 5)	250
XLIX	Static Test Damage Calculations, Specimen S/N-2, Area 4 (Gages 6 and 7)	251

LIST OF SYMBOLS AND ABBREVIATIONS

a, 2a	Half and total crack length (in.)
A	constant
A/C	aircraft
alt.	altitude
AR_{VT} , AR_{HT}	tail vertical and horizontal aspect ratios
b	width (in.)
BDGW	basic design gross weight
BL	buttock line, lateral fuselage coordinate (in.)
C	constant
C_L	centerline
$C_{T/O}$	blade loading (unit less)
CG_x , CG_y , CG_z	location of center of gravity with reference to a specified coordinate system (in.)
cpm	cycles per minute
D	deceleration (feet per second per second)
DES. U.L.	design useful load
DL	disc loading (psf)
$d \frac{2a}{dN}$	crack propagation rate (in./cycle)
E	Young's Modulus (psi)
F_r	reliability factor (data scatter)
F_s	size effect factor
F_x , F_y , F_z	loads, referenced by subscript to coordinate directions (lb). Additional subscripts designate component: AF - aft fuselage, FF - forward fuselage, i - inertia, G - gun, MR - main rotor, RH - rotor head, as F_{xMRi}
GW	gross weight (lb)

H.S.	hard side (refers to dual-hardness steel)
I_{xx} , I_{yy} , I_{zz} , I_{xy}	moments of inertia, referenced by subscript to coordinate direction (in. ⁴)
J	total number of flight conditions
K	constant
ΔK	stress intensity range (ksi - $\sqrt{\text{in.}}$)
K_c	critical stress intensity (ksi - $\sqrt{\text{in.}}$)
K_f	fatigue stress concentration factor
K_{Ic}	fracture toughness (ksi - $\sqrt{\text{in.}}$)
K_s	surface finish stress concentration factor
K_t	theoretical stress concentration factor
L	length (in.)
LH	left hand
L_R	rotor lift (lb)
L_S , \bar{L}_S	skid load, average skid load
M_x , M_y , M_z	moments, referenced by subscript to coordinate directions (in.-lb)
N_x , N_y , N_z	longitudinal, lateral, and vertical load factors (g)
n	exponential constant
n_i	number of cycles at i th flight condition per hour
N_i	fatigue life for the i th flight condition (hr)
T_h	fatigue life under variable load conditions (hr)
T/N	test number
U_v	vertical drop energy (ft-lb)
U.L.	useful load
V	velocity (fps)

v_d	limit dive speed (kn)
v_h	design maximum level-flight speed (kn)
v_o	velocity at which the projectile has zero probability of penetration (fps)
v_v	oleo sink speed (fps)
v_y	lateral velocity (fps)
w	height (in.)
W	weight (lb), subscripted by component
WL	waterline, vertical fuselage coordinate (in.)
X	magnification
x_o	lift offset ratio
XMSN	transmission
$\ddot{\alpha}_x, \ddot{\alpha}_y, \ddot{\alpha}_z$	radial acceleration (rad/sec^2)
β	flapping angle (deg)
δ	deflection (in.)
ϵ_{LG}	landing gear deflection (in.)
η_s	oleo efficiency
θ_L	angle (deg)
σ	stress (psi or ksi)
σ_s, σ_v	steady, vibratory stress (psi or ksi)
σ_v^*	modified vibratory stress (psi or ksi)
$2\theta, 2\theta_\sigma, 2\theta_\psi$	diffraction angle, subscripted to denote angle incidence
Ω_R	blade tip speed (fps)

INTRODUCTION

During the recent years of the Southeast Asian conflict, the high loss rate among light observation helicopters (LOH) has indicated the vulnerability of this type of aircraft to small-arms ground fire. By the nature of its mission, an LOH must spend a large proportion of its operating life at low speed and low altitude. Conventional airframes are easily penetrated, allowing critical component damage to flight controls, powerplant, and hydraulics and electrical systems, and resulting in a high pilot mortality rate. Methods for reducing this vulnerability must be pursued.

The approach that has been investigated by Sikorsky is a complete armor capsule that could yield a more cost effective, but heavier aircraft than one with discrete armor sections over critical components. At the same time, it is envisioned that a production armor airframe would not be of one thickness, but that the thickness of each section would be determined by analysis of the threat and the degree of component masking at that locality. Thus, the conventional airframe is replaced by armor sheets which serve the dual purposes of protecting the aircraft, and carrying all flight and ground loads. In the latter regard, the armor airframe is now many times stronger than a conventional structure and can therefore withstand crash loads and prevent penetration of the living space by tor blades and ground obstacles. Moreover, dense components such as the transmission can be mounted directly onto the skin of the airframe and will not tear loose on crash impact.

Since 1965, Sikorsky has been developing the Advancing Blade Concept (ABC) rotor. This system has two rigid coaxial counterrotating rotors. The absence of flapping and lead-lag hinges produces mechanical simplicity, ruggedness, and low maintenance. The elimination of the tail rotor yields a compact aircraft.

The marriage of the ABC rotor system and the structural armor airframe formed the basis of Sikorsky's Aerial Armored Reconnaissance System (AARS). To support the development of the concept, Sikorsky completed two initial studies under contract with U.S. Army Mechanics and Materials Research center. Under Contract DAAG46-71-C-0042, the effects of steady stress on ballistic impact resistance of dual hardness steel (DHS) armor were examined, as well as the mechanical properties of ballistically damaged specimens. Fatigue and crack propagation characteristics were also studied. Results indicated suitability of DHS as a primary airframe structure. Under Contract DAAG46-69-C-0159, the feasibility of design, fabrication, and manufacture of such an airframe was established. Manufacturing techniques for cutting, joining, and finishing were evaluated. Welded joints were found to be practical, with a need to protect the heat-affected zone at the weld with external strips of DHS along the joint. Also, the optimum airframe shape was established from considerations of threat density from a given direction. The prismatic shape proved to be the least vulnerable, and is clearly superior to any curved shape when it is considered that DHS is most readily available in flat pieces.

During this same time period, the ABC was being further developed through

testing of a 40-foot-diameter rotor in the Ames wind tunnel, partially funded under Army Contract DAAJ02-67-C-0102. Subsequent to the successful completion of the program, the Army awarded contract DAAJ02-72-C-0020 to design, build and test the ABC Technology Demonstrator Flight Research Aircraft.

The other logical step was to fabricate and to mechanically and ballistically test a specimen airframe. Accordingly, under this contract (DAAJ02-72-C-0018), Sikorsky has designed an AARS aircraft, with particular emphasis on crash survivability, reliability/maintainability, and availability, while conforming to the mission requirements. This preliminary design configuration was then used as a basis for detailed design of the airframe midsection.

Concurrently, the required armor thickness was established from a series of ballistic tests on dual hardness steel specimens. Means of providing equivalent protection to the ballistically degraded areas surrounding welds were developed and tested. The effects of elevated and reduced temperature on the ballistic properties of the material were also evaluated.

An extensive series of tests was performed on material of the required thickness, and on welds, to determine static and fatigue properties, fracture toughness, residual stress distribution and the effect of environmental exposure. Similar tests were performed on material after ballistic impact to determine residual static and fatigue properties.

Flight loads and criteria were established, so that detailed structural analysis of the armor shell and fittings for transmission and landing gear mounts could be performed. A model of the aircraft center section was established using the NASA Structural Analysis Program (NASTRAN) which, coupled with the established mechanical properties, predicted static structural integrity and fatigue life in excess of design requirements. A crash survivability analysis was also successfully completed.

Finally, a facility was constructed to allow testing of actual center sections to determine mechanical properties before and after ballistic damage, to demonstrate ballistic capability under flight load conditions, and to confirm the NASTRAN analysis. Two center sections were fabricated and successfully tested to establish the suitability of integrally armored airframe construction.

PRELIMINARY DESIGN CONFIGURATION

OBJECTIVE

The objective of the AARS preliminary design study was to establish a practical aircraft configuration using dual hardness steel armor as primary structure. The design constraints and equipment required in an actual aircraft were to meet the specifications of a reconnaissance mission. In addition to the establishment of the configuration, the study was intended to determine group weights, performance, and flight and ground loads.

APPROACH

The design of the aircraft incorporated the latest technology in dynamic components and used information obtained in previous studies on crashworthy design concepts and optimum aircraft shapes (Reference 1).

A compact and functional design was obtained using dual hardness steel armor as primary structure and incorporating the Advancing Blade Concept (ABC) rotor system, gearbox, and control system. Also incorporated was a crash-resistant seat design developed under an Army/Sikorsky contract. The prismatic shape of the fuselage was established in a previous company-funded program as optimal for ballistic protection.

The preliminary design effort took the form of a series of design iterations with information from the various disciplines that are involved in the design and production of an aircraft. Aircraft weights, performance, mission fuel, and design features such as gearbox rating and engine size were evaluated using Sikorsky's Helicopter Design Model (HDM) computer program, which is described later in this section.

AIRCRAFT DESCRIPTION

The fuselage shell is fabricated of dual hardness steel armor. A three-view general arrangement drawing of the AARS aircraft is shown in Figure 1. The basic information on size, installed power, rotor geometry, etc., is given in Table I. A summary weight statement is given in Table II, and the mission analysis is documented in Table III.

Design philosophy dictated a rigid armored capsule containing crew living space, transmission, powerplant, electronics bay, and flight controls, with sufficient energy-absorbing devices within the skid landing gear to meet crash survivability criteria.

Fuselage

Armor effectiveness depends not only on areal density, but also on projectile velocity and obliquity. Hence, shape analyses have been made to establish the optimal fuselage shape on the basis of ballistic protection and operational usage with due consideration for manufacturing techniques.

Five fuselage shapes were analyzed in 1969 under a Sikorsky IR&D program (Reference 1). Care was taken to provide the same internal space and comfort levels in all shapes, because the aircraft weight and relative vulnerability characteristics depend heavily on surface area. A sphere, modified sphere, cylinder, ovoid, and prism were studied. Relative vulnerability analyses were based on the assumption of a homogeneous threat emanating from the inner surface of a surrounding sphere. Integrating the probability of penetrating the hull over the desired azimuth and elevation angles yielded the relative capability of each shape to defeat a given threat. The relative vulnerability of a surface is a function of the presented area, impact obliquity, material properties, and projectile penetration capability.

Figure 2 shows the relative azimuthal vulnerability versus elevation angle for elevation angles ranging from 40 degrees below horizontal to 20 degrees above horizontal. This is a reasonable definition of the threat direction, based on the threat analysis, although the majority of fire would probably come from the horizontal to 30 degrees below. Note that the vulnerability value for the spherical shape is not a constant 1.0. Although the threat density is constant over the area of the threat surface, the circumference of the threat circle decreases as the elevation angle increases. Therefore, the relative azimuthal vulnerability values are multiplied by the cosine of the elevation angle to be consistent with this assumption. Integration of the areas under these curves shows the prism to be 6% better (less vulnerable) than the reference spherical shape, while the modified sphere is 20% worse, the cylindrical shape is 14% worse, and the ovoid is 2% worse. If the threat is assumed to be from the horizontal to a -30 degree elevation, the prism is calculated to be 16% less vulnerable than the sphere. The prism is clearly the superior shape. On this basis, a prismatic shape was chosen for the general fuselage configuration.

The prismatic shape of the armored section is formed from flat welded sections. The heat-affected zones at each welded joint are protected by strips of dual hardness steel (DHS) bonded externally over the vulnerable area. The means of attachment of these strips is discussed on page 39. For a production aircraft, many of these welded joints will be avoided by forming the fuselage in larger sections prior to heat-treating.

Crash survivability of the AARS is increased by use of DHS. The dual hardness steel airframe surrounding the crew and heavy components is many times stronger than conventional aluminum alloy construction. The rugged airframe shell preserves living space for the crew in the event of a severe crash. In addition, it virtually eliminates the possibility of rotor blade penetration of the cabin. The strength of the DHS airframe structure also lends itself to support of heavy components in such manner that they will not tear loose during crash impact. Crew seat and landing gear energy absorption concepts were employed to meet the 95th percentile crew survivability limits set forth in USAAVLABS TR 70-22. No deformation of the fuselage was assumed in the crashworthiness analysis, which is documented on pages 40 through 51.

The armored section extends from the forward nose bulkhead, canted to prevent plowing in longitudinal ground impact, to station 237 aft of the powerplant installation. The nose consists of a frangible birdcage structure

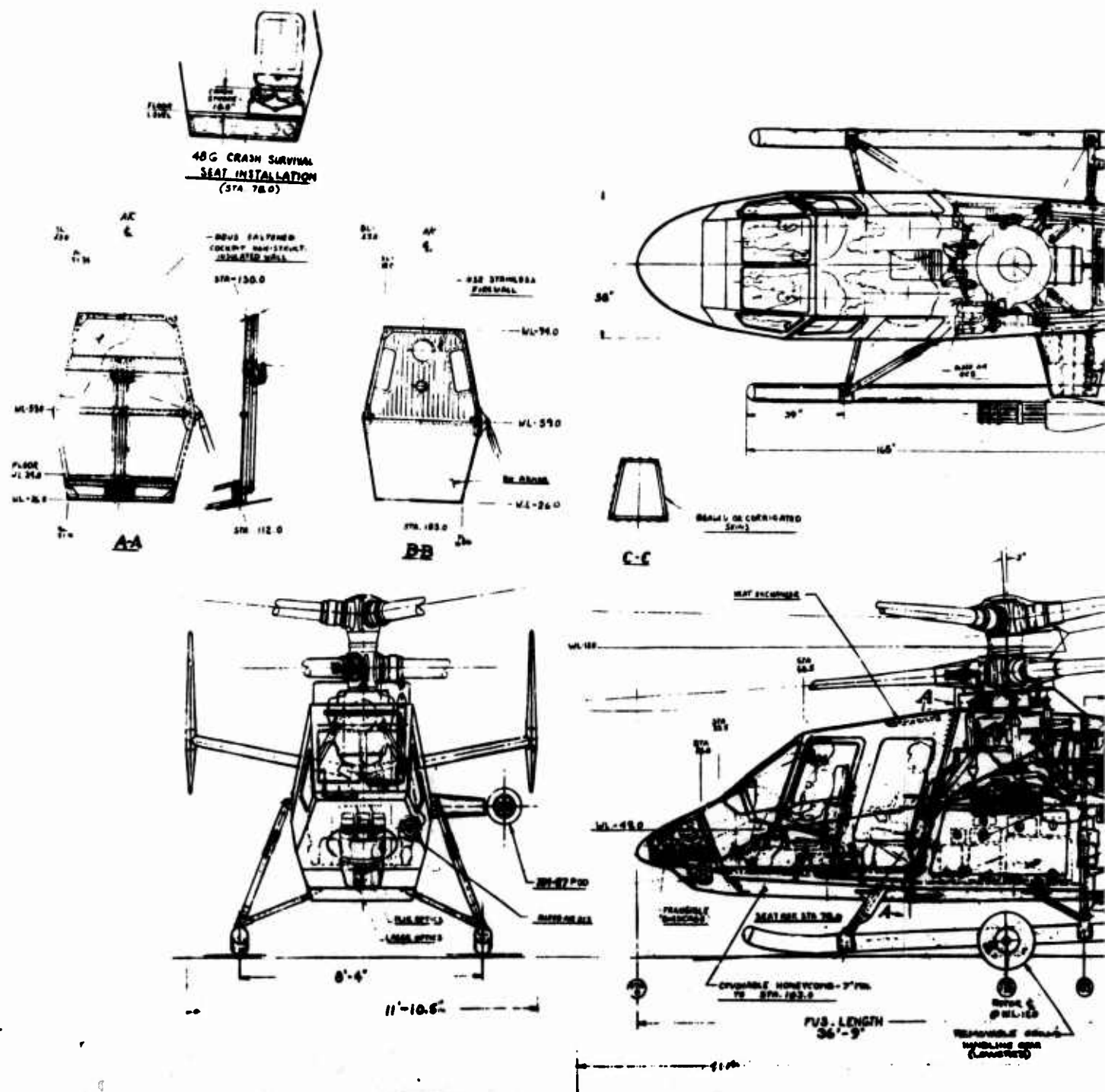
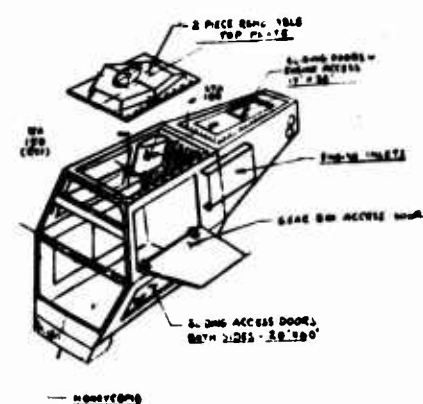
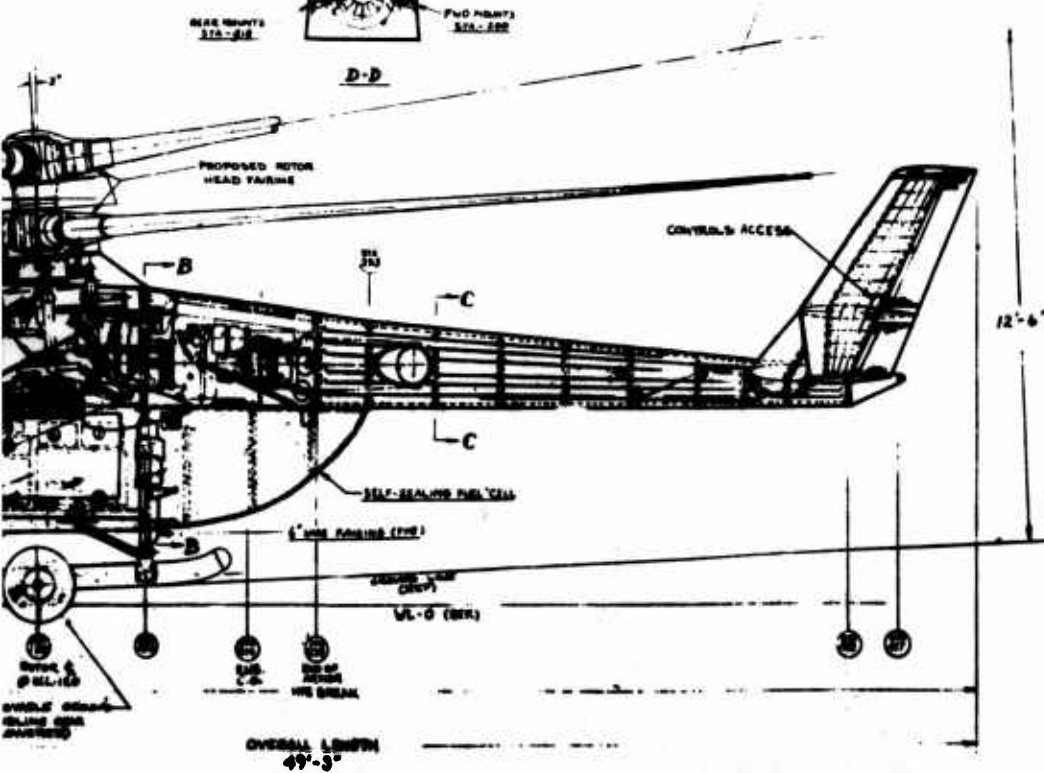
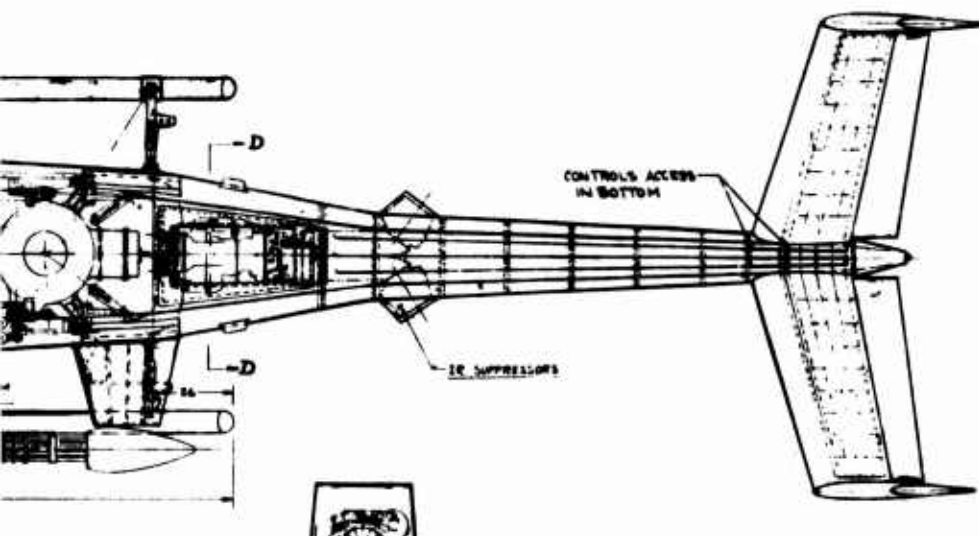


Figure 1. AARS Baseline Aircraft.



2

TABLE I. SUMMARY OF BASELINE AIRCRAFT ATTRIBUTES

Design Gross Weight, lb	12,295
Weight Empty, lb	9,402
Usable Fuel, lb	1,466
Disc Loading, psf	9.78
Vertical Drag, % GW	2.6
Equivalent Flat Plate Area, ft ²	12.8
Overall Mechanical Efficiency	0.95
 <u>Main Rotor (ABC)</u>	
Radius, ft	20
Chord (80% radius), ft	1.117
Taper Ratio	2:1
Solidity	0.1064
Tip Speed, (QR), fpm	700
C _T /σ (4000 ft, 95°F)	0.1
Twist, deg	-10
Blades per Head	3
Aspect Ratio	17.9
 <u>Engine Sizing and Design Powers</u>	
Number of Engines (Rubberized T700-GE-700)	1
Engine Scale Factor	1.5327
Intermediate Rated Power (SIS), hp	2400
Hover OGE (4000 ft, 95°F) Power, hp	1662
Cruise Power @ 170 Kt (4000 ft, 95°F), hp	1292
MGB Design Power, hp	1763
Engine RPM	14840
 <u>Tail Surfaces ("H" Configuration)</u>	
Horizontal: Area, ft ²	43.0
Span, ft	11.875
Aspect Ratio	3.08
Vertical: Area (total), ft ²	36.0
Span (each), ft	5.2
Aspect Ratio	2.0
 <u>Body</u>	
Armor Thickness, in.	0.305
Total Wetted Area, ft ²	388.52
Total Area, Glass, ft ²	19.34
Total Area, Armor, ft ²	263.14
 <u>Dimensions</u>	
Overall Length, ft	49.25
Fuselage Length, ft	36.75
Overall Height, ft	12.5
Tread, ft	8.25
Fuselage Width, ft	4.83
 <u>Armament</u>	
XM-27 7.62 mm Minigun (1)	+10/-20
Trainable Elevation, deg	

TABLE II. AARS POINT DESIGN - SUMMARY WEIGHT STATEMENT

Group	Weight (lb)
Main Rotor Group	1131.
Wing Group	0.
Tail Group	219.
Tail Rotor/Fan	0.
Tail Surfaces	219.
Body Group	4329.
Alighting Gear	471.
Flight Controls	543.
Engine Section	64.
Propulsion Group	1851.
Engines	533.
Air Induction	10.
Exhaust System	10.
Lubricating System	0.
Fuel System	271.
Engine Controls	49.
Starting System	42.
Auxiliary Propulsion Propellers	0.
Drive System	936.
Auxiliary Power Unit	0.
Instruments	111.
Hydraulics	36.
Electrical Group	275.
Avionics	258.
Furnishings	237.
Air Conditioning and Anti-Ice	45.
Auxiliary Gear	10.
Vibration Suppression	0.
Technology Savings	-176
Contingency	0.
Weight Empty	<u>9402.</u>
Fixed Useful Load	427.
Pilot	200.
Copilot	200.
Oil-Engine	4.
-Trapped	3.
Fuel-Trapped	20.
Payload	1000.
Rescuees	400.
Armament	245.
Mission Equipment	355.
Fuel-Usable	1466.
Gross Weight	12296.

TABLE III. AARS POINT DESIGN - MISSION ANALYSIS

Mode	GW (1b)	Speed (kn)	Distance (nm)	Time (min)	Power (shp)	Fuel (1b)	Specific Fuel Consumption
Hover	12275	-	-	3.0	1658.2	39.8	.4796
Cruise	12143	120.0	60.0	30.0	695.5	222.8	.6408
Loiter	11842	90.0	90.0	60.0	479.2	378.3	.7894
Hover	11623	-	-	5.0	1510.2	61.4	.4882
Loiter	11499	90.0	45.0	30.0	467.7	187.4	.8014
Hover	11375	-	-	5.0	1457.0	59.8	.4928
Dash	11268	170.0	42.5	15.0	1175.9	154.7	.5262
Cruise	11083	120.0	60.0	30.0	651.9	215.5	.6611
Hover	10964	-	-	2.0	1372.3	22.9	.5016
Reserve - Loiter	10891	90.0	30.0	20.0	447.3	122.9	.8241

Total Mission Fuel: 1465.5 lb
 Gross Weight at Takeoff: 12294.8 lb
 Altitude = 4000 ft., Temperature = 95°F for all cases.
 Total Mission Time: 180 min
 Rotor Radius: 20.0 ft. Parasite Drag: 12.8 ft²

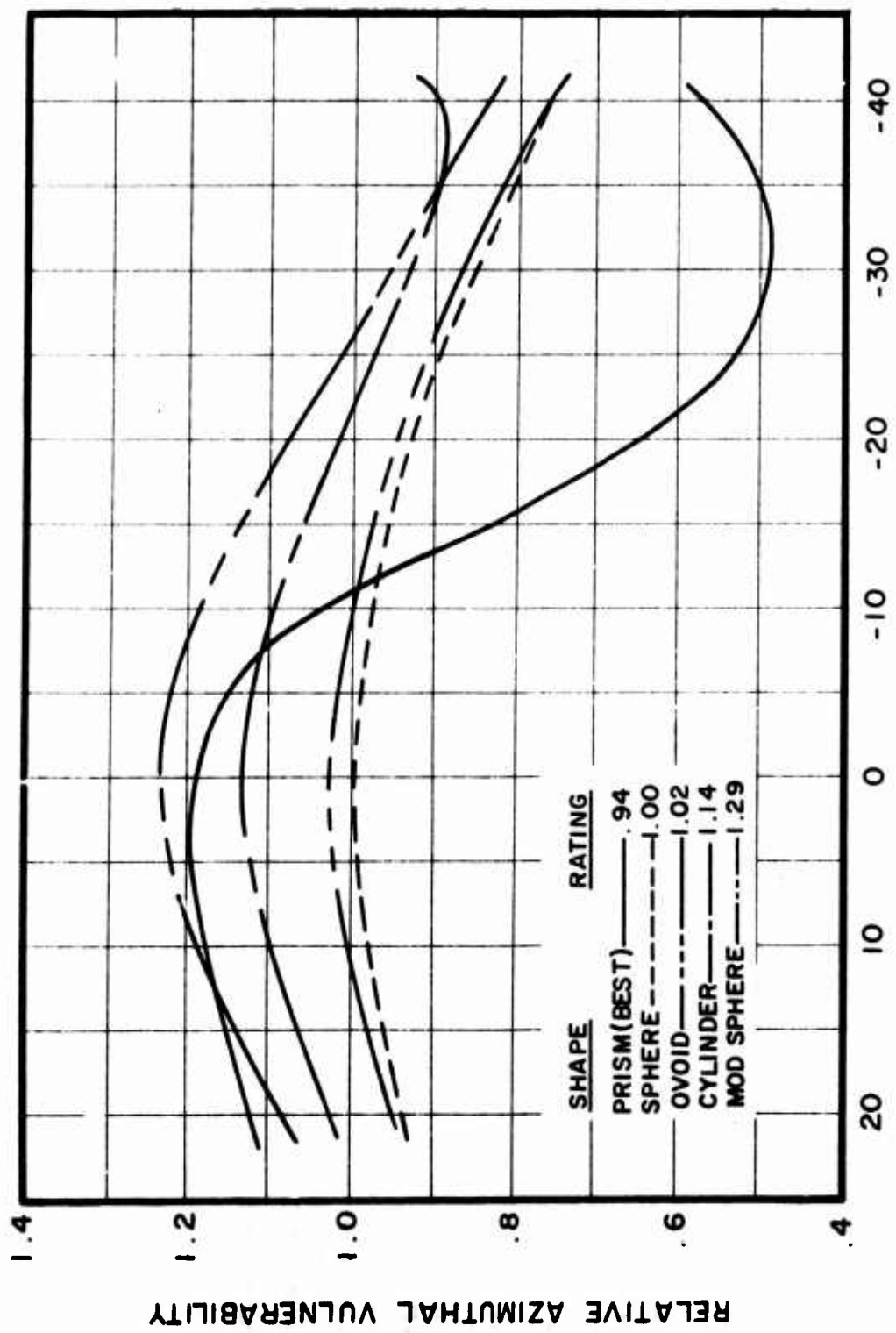


Figure 2. Relative Vulnerability in Band 20 Degrees Above to 40 Degrees Below Horizontal.

with aluminum skin. This structure contains low-light-level TV (LLLTV) and night sensing equipment to meet the mission requirements set forth in a reconnaissance mission. The whole assembly hinges about station line 26 at water line 57, for inspection and maintenance, and is designed to crush on longitudinal nose impact to limit deceleration to 10g, for a 20 fps impact velocity, as discussed on pages 44 to 46. The underside of the cabin and midsection is covered with a 7-inch layer of crushable honeycomb and a non-spark outer skin, for crashworthiness. Crew space and passenger space are accessible through armored doors on either side. It is anticipated that a means will be needed to fire the doors open by a compressed air bottle arrangement in the event that the aircraft may be lying on one side after a crash. (Each door weighs 100 pounds.) The forward doors have windows of armor glass. The windshield is of similar material. Crew seats are of the crash-survivable type discussed on pages 44-46. Passenger seats are of simple foldaway type. Flight control rods run beneath the cabin floor between the crew-seat support structures, accessible through removable floor panels, and are not attached to the fuselage outer skins. The forward midsection bulkhead (AA in Figure 1) consists of peripheral framing, a structural tube as a cross-brace, and a nonstructural acoustic/thermal shield. This shield is removable in two equal parts on either side of the centerline, for access to the midsection.

Midsection armor forms a hexagonal cross-section volume containing the main gearbox and support structure, flight control servos and linkages, lower swashplate assembly, electronics, air-conditioning/heater unit, battery, and ammunition canister. This section was designed in detail to enable fabrication and testing of mechanical and ballistic properties, as described on pages 225ff. The tail section consists of the tail cone of light semi-monocoque structure, extending from aft of the powerplant installation, and the horizontal and vertical stabilizers. A manufacturing break exists at station 237, to enable complete removal of the tail section and replacement of the jet-pipe infrared suppression assembly. This break will also facilitate removal of the powerplant itself.

The H-style empennage configuration increases horizontal tail effectiveness and locates vertical surfaces in a region of clean air outboard of the tumbling flow behind the rotor head. The vertical area provides adequate directional stability similar to that attained in the S-67 and S61F aircraft. Rudders provide directional control in cruise flight, becoming effective with increasing flight speed as the differential collective low speed yaw control system is phased out. Rudder controls run beneath the armored deck supporting the powerplant and then through the tail boom to a bellcrank. An access panel is provided at the bellcrank.

Fuel System

The fuel tank is situated aft of bulkhead B-B of Figure 1 and is not contained within the armored shell. The tank is of crashworthy and self-sealing construction and is encased in a fiberglass cover that disperses the fuel loads. The tank increases the armor protection of the midsection aft end by removing energy from impacting rounds before they meet the armor itself. The tank assembly will hinge about a horizontal line along the left

side of the fuselage at waterline 59, to permit cleansing of the tank and inspection of the monitoring points of the powerplant installed above. A flexible fuel line makes it unnecessary to disconnect fuel lines when rotating the tank.

Powerplant

The powerplant is a single rubberized advanced technology turboshaft engine based on the T700-GE-700. The engine is sized by the design hover requirement. It is mounted within the armored section aft of Bulkhead B-B, in the manner shown in Figure 1. The top of this fuselage section contains a sliding door for inspection and maintenance. The complete panel can be unbolted and removed to enable engine removal after decoupling from the transmission and detachment of the fuselage section aft of station 237. Access points for maintenance are indicated in Figure 1. Because of degradation in ballistic properties of armor at high temperatures, it may be necessary to cool the region between the engine and the armored sides. This would be achieved by reflector surfaces and air induction.

Alighting Gear

The skid alighting gear is designed to withstand crash loading conditions up to a vertical impact speed of 20 fps. A diagram of the complete alighting gear assembly is shown in Figure 3. The skids are steel tubes with attached fittings to accommodate the struts, which extend to fittings exterior to the fuselage midsection.

The four primary members contain oleos and auxiliary energy absorbing devices. Drag links and secondary struts mounted to the fuselage complete a structurally stable system. Flexing of the complete assembly is achieved through pin joints or spherical bearings at the fittings in the manner shown in Figure 3, thus eliminating bending loads. The spherical bearings are necessary, because rotation of the forward members during a complete oleo stroke does not take place about a single axis.

Ground-handling equipment is also illustrated in Figure 3. The assembly to be attached to each skid consists of two wheels connected by a bridging structure. The aircraft is jacked onto the wheels through hydraulic pressure generated from a hand-pump arrangement. The aircraft can carry its own ground-handling equipment in flight.

Rotor

Sikorsky was recently awarded a contract (DAAJ02-72-C-0020) by the U. S. Army to design, fabricate and flight test two ABC (Advancing Blade Concept) Technology Demonstrator Research Aircraft. These aircraft will be used to explore the capabilities of the ABC rotor system in the pure helicopter configuration as well as in the auxiliary propulsion mode at speeds of up to 300 knots.

The AARS design incorporates the ABC rotor system with the corresponding flight control and drive system details and weights taken from the ABC

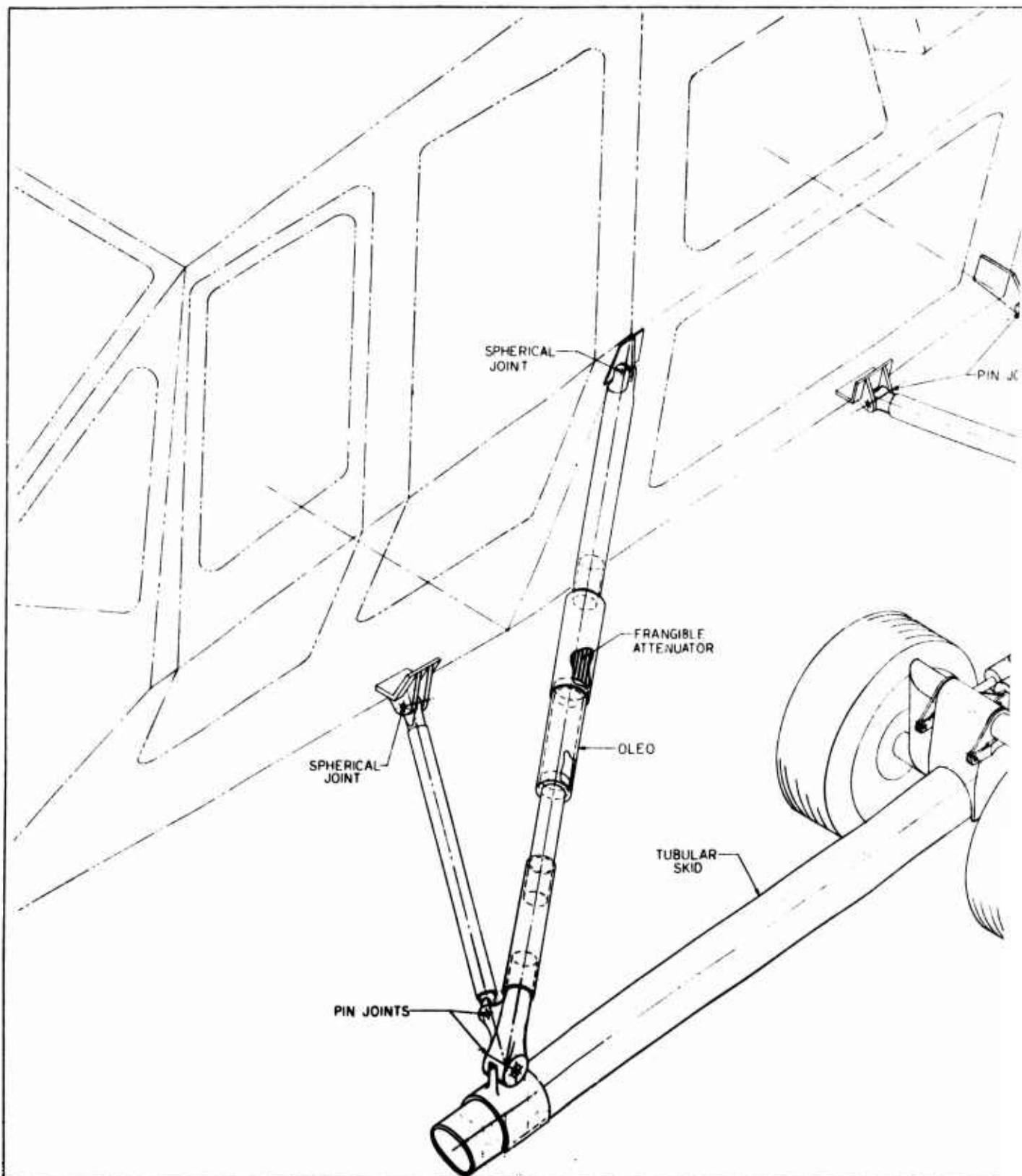
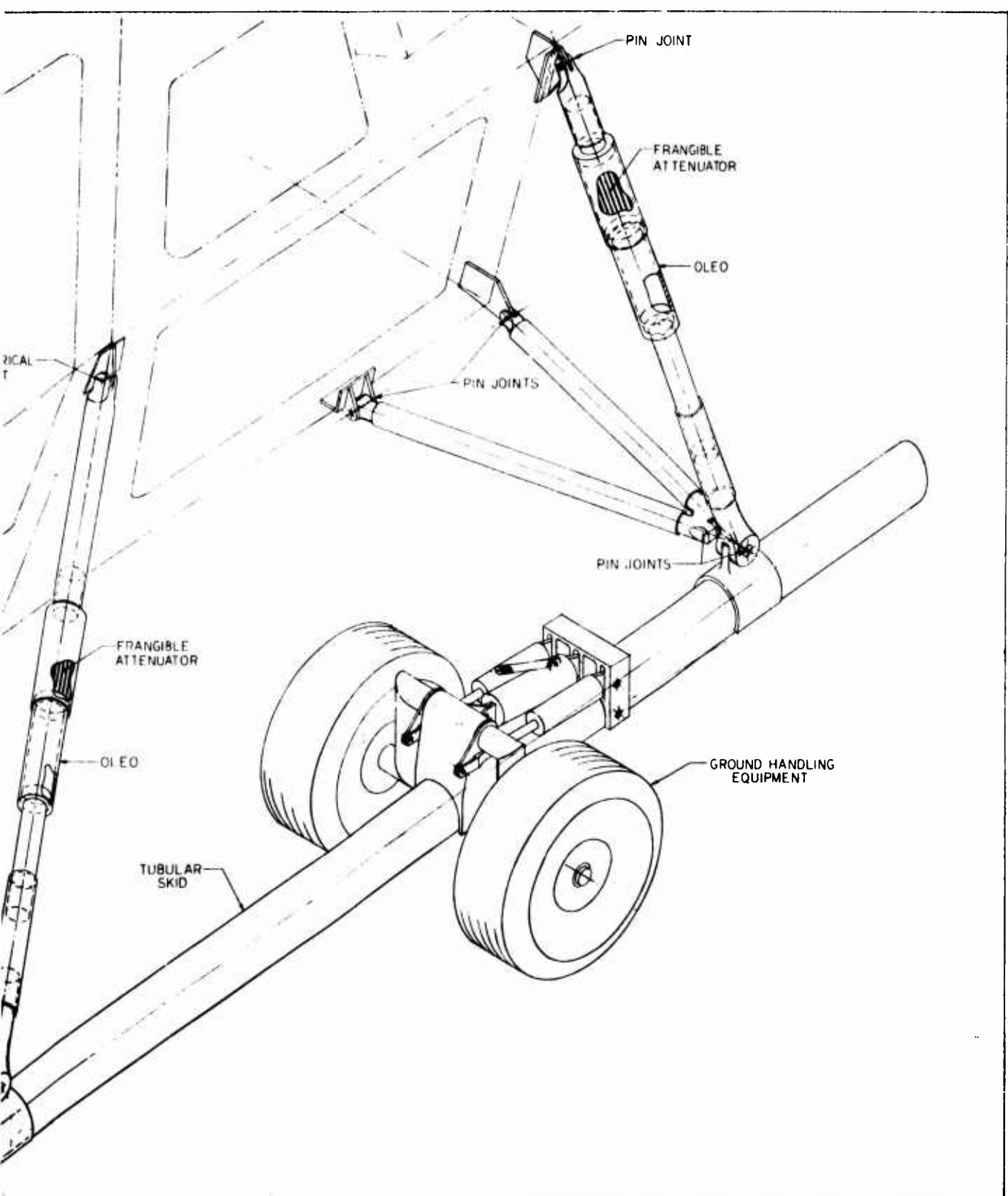


Figure 3. Alighting Gear Isometric.



isometric.

2

demonstrator program, as they existed at the inception of this program.

AARS mission effectiveness will be enhanced by the ruggedness, invulnerability, high reliability, and maintainability of this mechanically simple rotor system.

The powerplant is sized by the design hover condition. This enables the aircraft to perform over the desired speed range, as defined in a reconnaissance mission, with no auxiliary propulsion.

Aircraft compactness is a result of the coaxial rotor arrangement, which eliminates the tail rotor and improves the efficiency of the rotor in hover. This results in a small diameter rotor and powerplant size for a given hover requirement. Due to the rigidity of the blades and the absence of a flapping hinge, vertical compactness is achieved to an extent never realized in flapping coaxial rotors, which require separation for blade clearance. Vertical hub separation is minimal, and upper rotor controls are internal, thereby reducing rotor drag and controls vulnerability when compared with articulated rotor systems.

The mechanical drive system of the ABC is simpler than that of conventional helicopters, since the tail rotor has been eliminated. Rotor counterrotation is achieved in the main gearbox by planetary gearing, which is inherently counterrotating.

Rotor compactness and simplicity also provide a rugged lift system relatively invulnerable to ground fire when compared with a conventional articulated system.

Figure 4 shows the rationale behind the selection of the rotor radius and chord size for the AARS design. Aircraft gross weight is plotted as a function of blade loading, C_T/σ , and disc loading, DL. A high C_T/σ value is indicative of a small blade area and hence less blade weight, but it decreases rotor efficiency and so demands higher installed power. The selected C_T/σ at 0.1 yields minimum aircraft gross weight. High disc loadings produce more compact and generally lighter rotor systems, but reduced rotor efficiency. The disc loading to produce minimum aircraft gross weight was rejected on the grounds that the large radius would defeat one of the objectives of the AARS rotor compactness. Storage space, aircraft vulnerability, and aesthetics were also considered. A rotor radius of 20 feet was selected, giving a disc loading at design gross weight of 9.79 pounds per square foot.

Control System

Conventional helicopter cockpit controls are provided for the pilot and co-pilot. Control throughout the flight envelope is achieved by the pilot in exactly the same manner as in conventional helicopters, but the controls are linked and mixed differently because of the phasing requirements of the rigid rotor system.

The major control subsystems are:

Payload = 1000 Lb
Endurance = 90 Min (on Station)

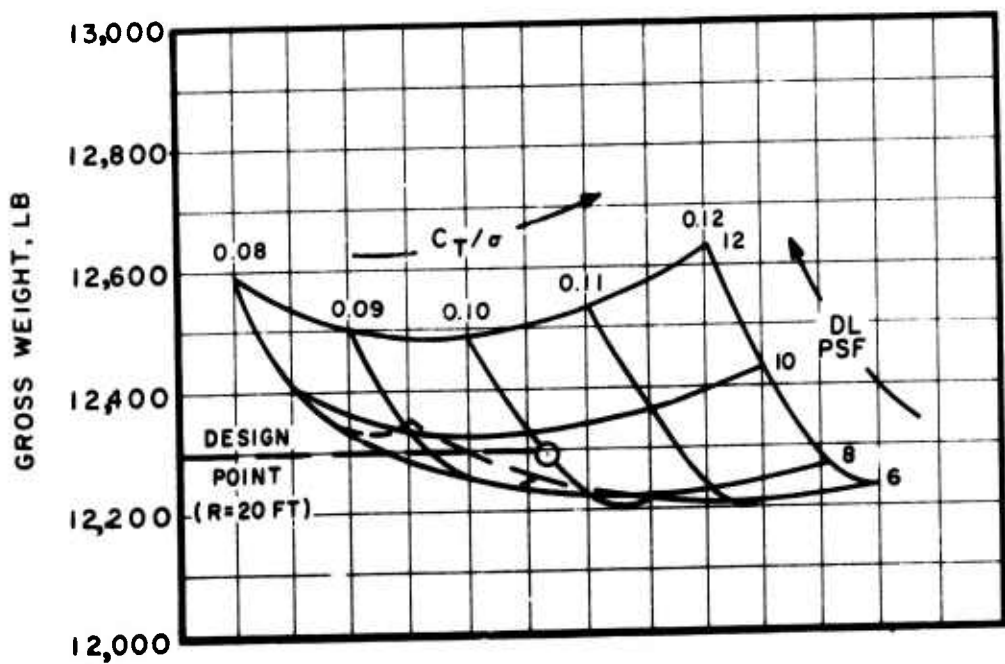


**Figure 4. AARS: Structural Armor Fuselage Gross Weight
Vs. Disc Loading and C_T/σ .**

- (1) Dual cockpit collective, cyclic, and directional controls.
- (2) A mechanical mixer providing properly phased inputs to the primary servos. The mixer includes an adjustable resolver to compensate mechanically for precession angle changes in each rotor.
- (3) Three two-stage primary servos for each rotor system, each stage capable of reacting flight loads.
- (4) Trim actuators with a mechanical override to control:
 - (a) Differential longitudinal trim
 - (b) Differential lateral trim
 - (c) Differential collective trim
 - (d) Rudder trim
 - (e) Cyclic spring centering.

Directional control is achieved with differential collective in the low speed regime. This is phased out with increasing flight speed and rudder effectiveness.

Transmission

The entire gearbox, rotor shaft, and rotor assembly is supported on a framework of steel structural members in the manner shown in Figure 5. The truss mount for the gearbox, coupled with access doors on both sides of the fuselage, provides excellent maintenance characteristics. Loads are carried to the four corners of the fuselage midsection at waterline 59 and are transmitted directly into the landing gear on vertical ground impact. The gearbox supporting structure is mounted to the interior of the armor skin by way of the welded steel fittings.

The ABC transmission provides equal torque distribution to each rotor. The main gearbox consists of an input shaft, bevel-gear reduction stage, compound spur-gear planetary, accessory section, and two counterrotating coaxial output shafts. The main gearbox is located in the fuselage center section forward of the powerplant installation. The accessory section, located aft on the main gearbox, drives the tachometer generator for the main rotor and the hydraulic pumps.

A freewheeling unit permits rotor disengagement from the engine during autorotation and permits reengagement in flight.

Armament

The installation of the XM-27 system is shown in Figure 1. Two thousand rounds of 7.62 mm ammunition are stored in a rectangular canister arranged

longitudinally along the left side of the lower midsection. Access to the canister is through the sliding doors on the side of the fuselage. Details of the gun-pod mount fittings are discussed under Midsection Design.

It is anticipated that a superior piece of equipment for a production aircraft would be a weapon mounted flush with the aircraft belly in the stowed position but capable of deployment in flight to permit a field of fire up to -70° in elevation and $\pm 180^{\circ}$ in train.

Equipment

The AARS equipment listed in Table IV consists of essential fixed navigation and communication units and removable mission-oriented items. The weight of the fixed items totals 192.7 pounds. With a 34% allowance for installation, 258 pounds is accounted within weight empty. The gun with ammunition and night sensing equipment is accounted within the 1000 pounds of removable payload (see Table II).

AIRCRAFT PERFORMANCE

Cruise performance of the AARS aircraft was determined using a Sikorsky developed computer program incorporating yawed blade element theory with a coaxial rotor configuration. This method has been correlated with the ABC Ames Wind Tunnel Test results, as described in Reference 2. The AARS power required versus aircraft speed curve is shown in Figure 6. It is seen that the hover design point determines the installed engine power required.

Hovering performance was calculated using the Sikorsky figure of merit ratio method corrected for coaxial rotor systems. This method is based on empirical flight and whirl stand test data. Figure 7 summarizes this analysis and shows the gross weight capability of the AARS aircraft at 4000 feet, 95°F, as a function of engine power available. The power required for this aircraft at these conditions and at the aircraft design gross weight of 12,296 lb is 1730 hp.

Total aircraft parasite drag was calculated from an assessment of each component whose drag coefficient depends on shape and Reynolds number, as in Reference 3. Aerodynamic interference and surface finish effects are also accounted for. The equivalent flat plate area is calculated from the drag coefficient and reference area. The total aircraft equivalent area is the sum of the component parts, including the interference and surface finish corrections, leakage, and momentum drags.

The resulting total aircraft equivalent area is 12.8 ft^2 . Figure 8 shows the total wetted area versus equivalent flat plate area for the AARS and for other Sikorsky models.

Vertical drag was estimated using the Sikorsky polar moment of inertia method. The method assumes a parabolic spanwise blade loading, which results in a triangular spanwise velocity distribution where the velocity is zero at the rotor hub and maximum at the blade tip. Weighting the area in

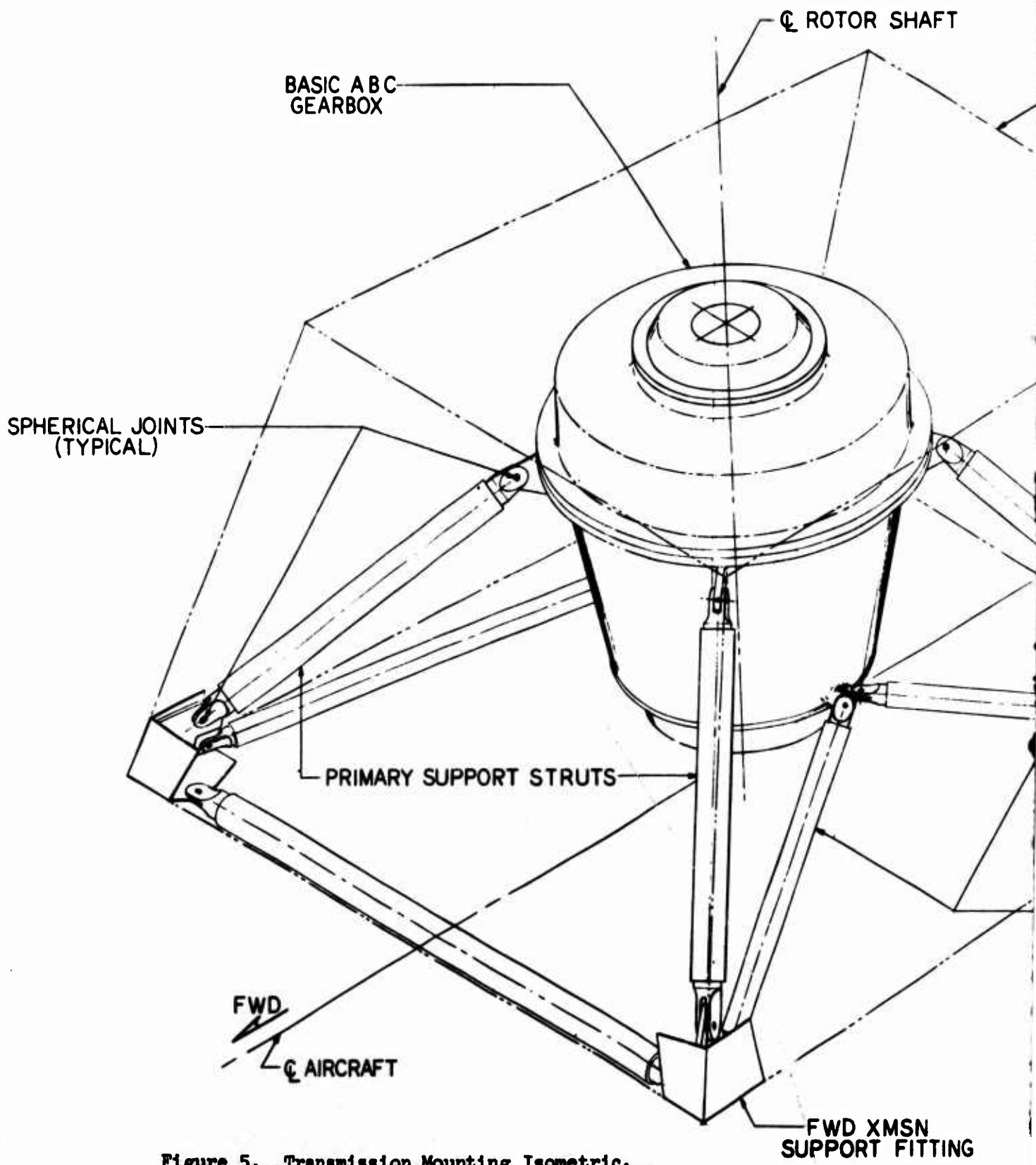
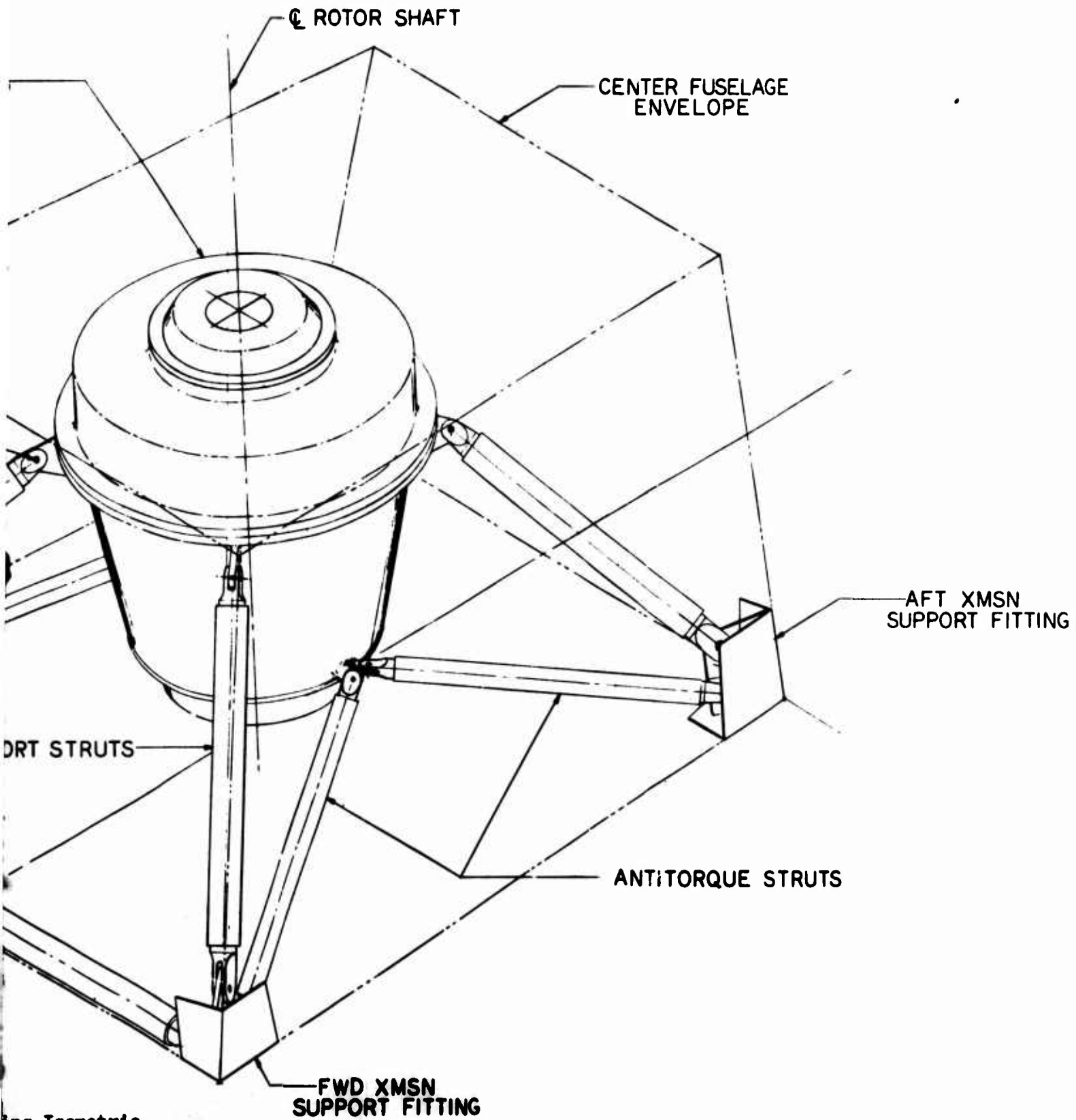


Figure 5. Transmission Mounting Isometric.



ing Isometric.

2

TABLE IV. AARS MISSION EQUIPMENT

Item	Nomenclature	Weight (lb)	Fixed/ Removable	Location
UHF/AM Radio	AN/ARC 116	7.5	F	Cockpit Console
VHF/AM Radio	AN/ARC 115	7.2	F	Cockpit Console
VHF/FM Radio	AN/ARC 114	7.0	F	Cockpit Console
Secure Voice	KY 28 Coder	15.0	F	Electronics Bay, Midsection
Intercom - 4 Sta.	Control	1.0	F	Cockpit
IFF Test Set	CFE	3.0	F	Cockpit Console
IFF R/T	-	3.0	F	Electronics Bay
IFF Encoder	AN/APX 72	17.2	F	Electronics Bay
IFF Control	AN/APX 72	13.5	F	Electronics Bay
VHF/FM Homing	-	3.0	F	Electronics Bay
LF/ADF 52	ARC 114	7.0	F	Electronics Bay
VOR/LC	AN/ARN 89	18.2	F	Electronics Bay
Loran D Display	AN/ARN 82	8.6	F	Instrument Panel
Electronic	AN/ARN 85	19.5	F	Electronics Bay
Night Vision Monitor	AN/ARN 85	62.0	F	Electronics Instrument Panel
Night Vision Sensor	-	20.0	R	Nose
Night Vision Sens.Elec.	-	125.0	R	Electronics Bay
Laser Designator Range Finder	-	105.0	R	Electronics Bay
Laser Des. Ram. Elec.	-	20.0	R	Nose
XM-27	-	15.0	R	Left Side
+ 2000 rounds	-	245.0	R	

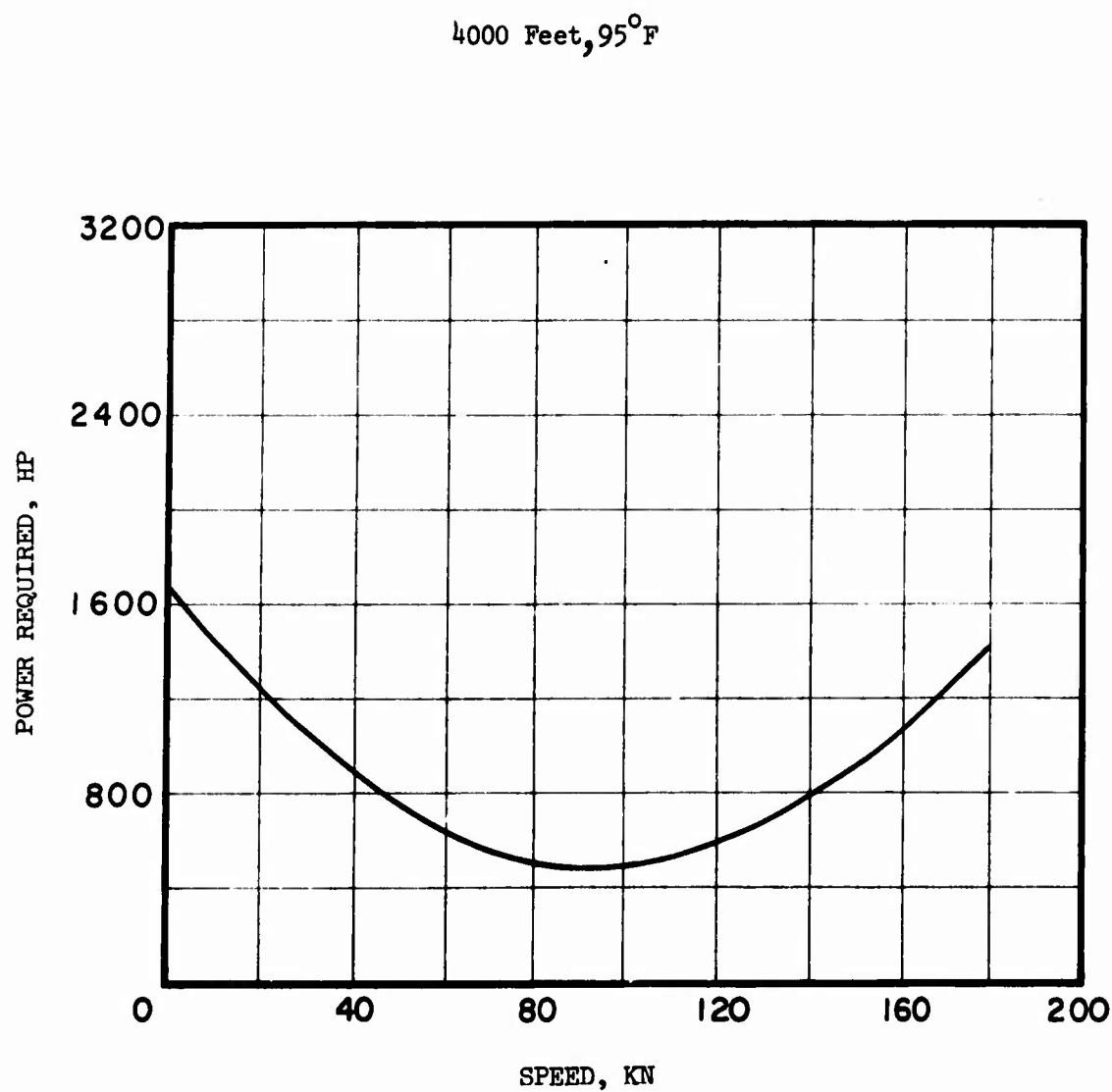


Figure 6. AARS Power Required Vs Speed.

Engine Power Vs Gross Weight

Radius = 20 feet Vertical Drag = 2.6% GW 4000 feet, 95°F
Chord = 1.117 feet Tip Speed = 700 fps
Number of blades = 6 Twist = -10°

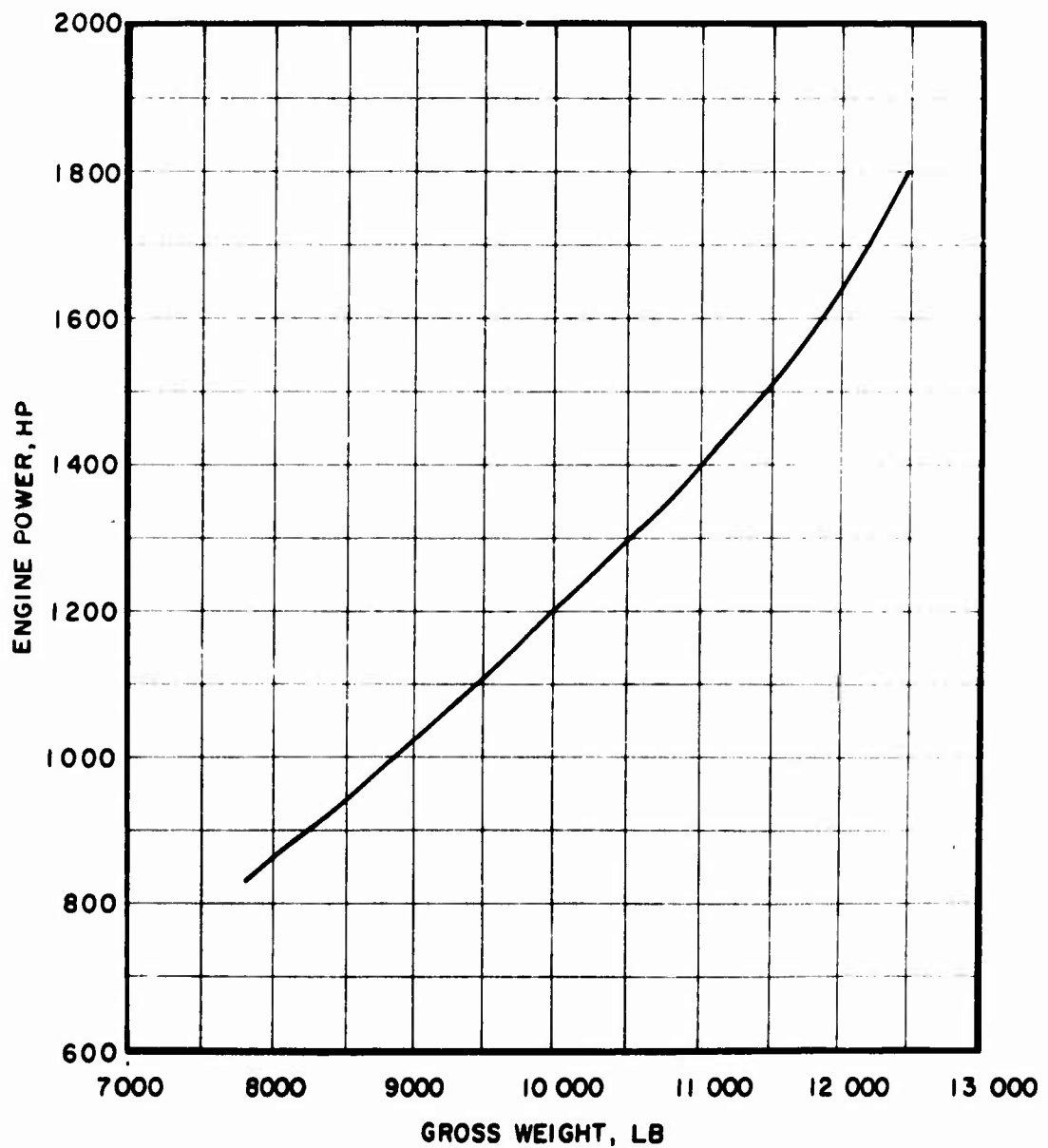


Figure 7. AARS Hover Performance.

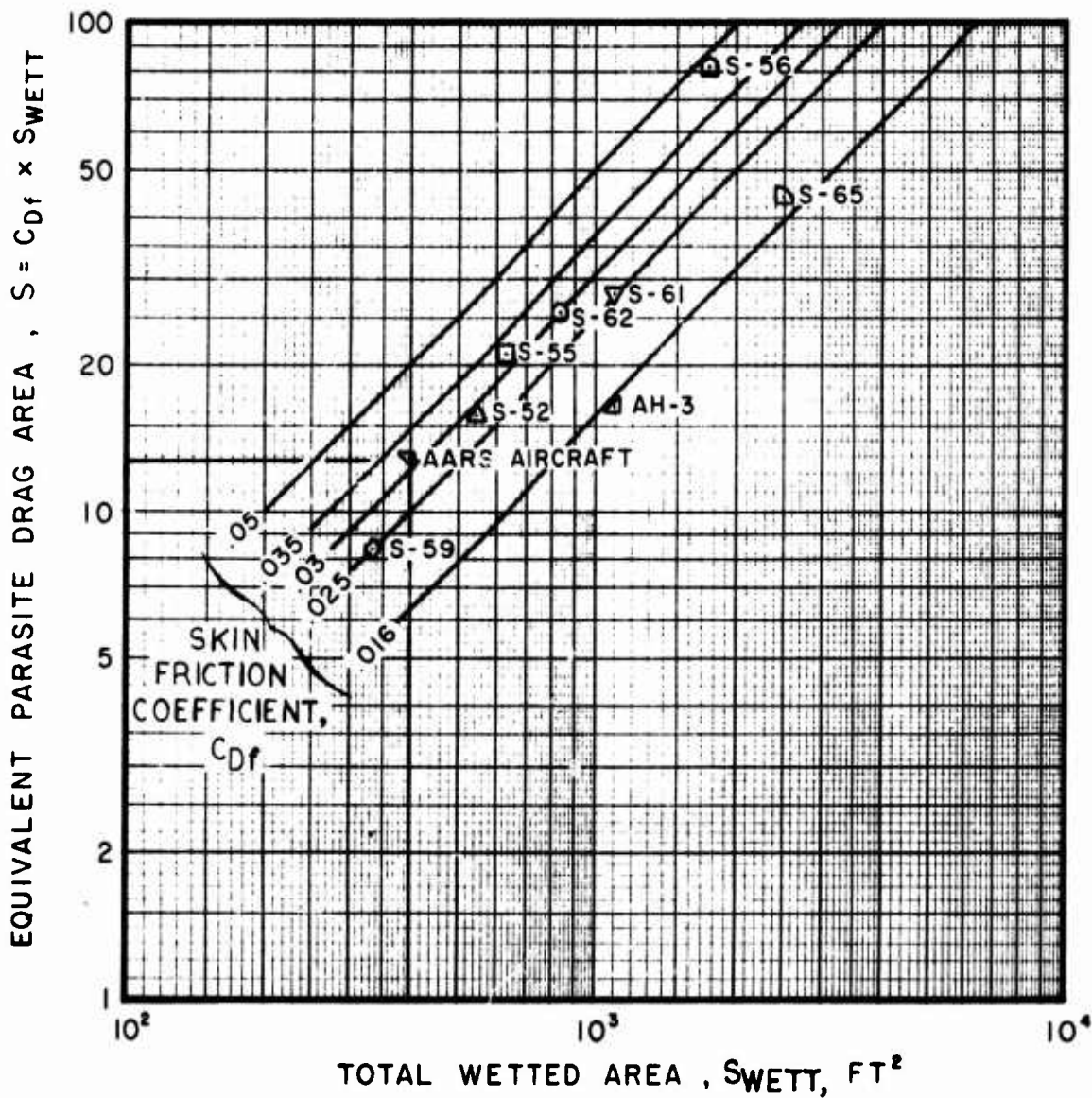


Figure 8. AARS Equivalent Parasite Drag Area.

the rotor slipstream by the slipstream dynamic pressure at the particular area provides the basis for this method. Section drag coefficients, thrust recovery, and flow peculiarities are not calculated directly. They are accounted for by using flight test results for the variation of the net vertical drag with the polar area moment ratio.

Figure 9 shows the polar moment of inertia ratio to be 0.02. The line used for predicting the AARS vertical drag was selected from the test data as the line parallel to the flat plate experimental line, passing through the S-64A point, which has the body shape most similar to the AARS. The net vertical drag is 2.6%.

MASS PROPERTIES

The weights of the various structural components were obtained by means of trending and fixed weight equations. The resulting weights were used in a Sikorsky developed computerized design analysis program and in the generation of panel point weights. A nine-point mass and inertia distribution formed the basis for the development of applied loads. The panel point weights and their locations are shown in Table V.

Rotor - The AARS main rotor is a coaxial ABC design with composite blades and a titanium head. The blade weight estimate is based on two design points, which were used to derive an equation using blade radius and chord as parameters. These are generally accepted as the major driving parameters for rotor blade weight. The hinge and hub equation is basically the articulated rotor equation, using the same exponent but modifying the coefficient to account for titanium.

$$\text{Blades: } W_{bl} = 7.25 (RC)^{0.79} \quad (1)$$

where R = radius in feet

C = mean geometric chord in feet

$$\text{Unit Hinge Assembly: } W_{hi} = 37.17 \left[\left(\frac{GW}{2000} \right) \left(\frac{R}{10} \right)^{0.725} X_o \right]^{0.725} \quad (2)$$

where X_o = lift offset ratio = 0.15

$$\text{Unit Hub: } W_{hub} = 57.7 \left[\left(\frac{GW}{1000} \right) \left(\frac{R}{10} \right)^{0.725} X_o \right]^{0.725} \quad (3)$$

$$\text{Fairings: } W_f = 0 \text{ (Assumed integral with hub)}$$

$$\text{Rotor Group: } W_{rg} = 2 (bW_{bl} + bW_{hi} + W_{hub}) \quad (4)$$

where b = number of blades per rotor

Comparison with Sikorsky Test Data.
AARS Most Like S-64A Shape. Line through S-64A with
the Flat Plate Slope Used for AARS.

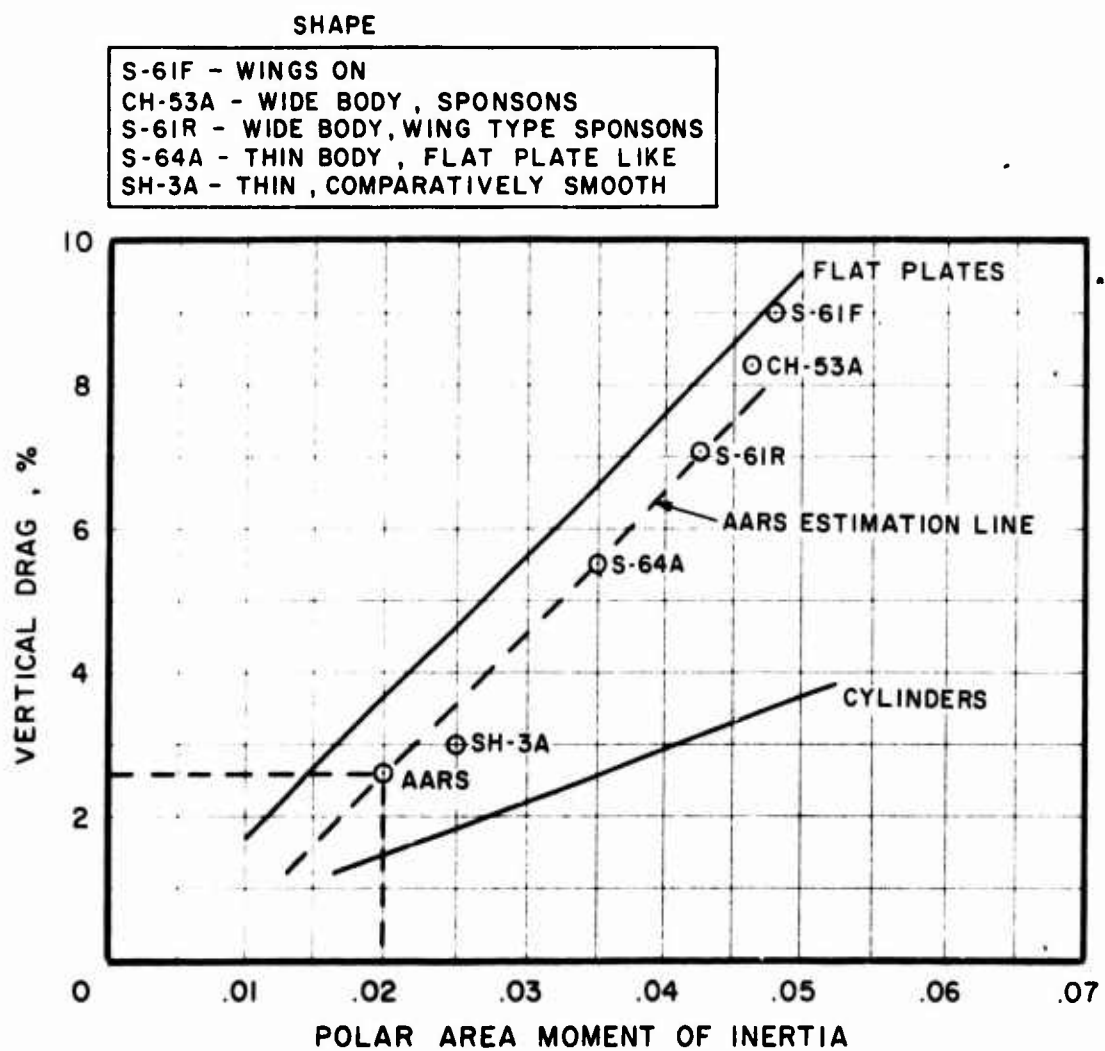


Figure 9. AARS Aircraft - Net Vertical Drag.

Tail Surfaces - The tail surface equation is derived from statistical data for existing horizontal and vertical surfaces whose areas are S_{ht} and S_{vt} .

$$W_h = (16.59) \left(\frac{S_{ht}}{10} \right)^{1.25} \quad (5)$$

$$W_v = (16.59) \left(\frac{S_{vt}}{10} \right)^{1.25} \quad (6)$$

Body Group - Wetted area has been found to be the major parameter for predicting fuselage weight. This has been used with appropriate factors applied to the various fuselage components to determine body weight. In addition, calculations were made of many of the detailed parts.

- (1) $BD1 = \text{glass areal density} - \text{psf}$
 $BD2 = \text{DHS areal density} - \text{psf}$
 Total glass area = 19.34 ft^2
 Total DHS area (planform) = 263.14 ft^2
 - (2) Tail cone weight = $4.9 \times (\text{TCS})^{2/3}$
 where TCS is tail cone wetted area
 - (3) Secondary structure = 29 lb
 - (4) Framing = 65 lb
 - (5) Protective strips = $0.066 \times (\text{glass weight}) + 0.0475 \times (\text{DHS weight})$
 - (6) Fittings = 76 lb
 - (7) Fairings = 20 lb
- By summing items (1) to (7): $W_{\text{Body}} = [19.34 \times BD1 + 263.14 \times BD2 + 4.9 \times (\text{TCS})^{2/3} + 65 + 0.066 \times (\text{glass weight}) + 0.0475 \times (\text{DHS weight}) + 76 + 20]^{1.02}$ (7)

Alighting Gear -(Skids). A simplified statistically based equation is used for the skid-type alighting gear using gross weight as the parameter, with a separate equation for the oleos, based additionally on stroke and sink speed.

$$\text{Weight of basic skid gear} = 4.2 \left(\frac{GW}{1000} \right)^{0.8} + 5 \text{ lb} \quad (8)$$

$$\text{Weight of oleos} = 9.5 \left[\frac{GW}{1000} \right] \left(\text{Stroke} + \frac{V_v^2}{128.7} \right)^{1.02} \text{ lb}$$

$$\text{where } V_v = \text{sink speed (fps)} \quad (9)$$

TABLE V. RESULTS SUMMARY OF PANEL POINTS ANALYSIS

Item	Weight (lb)	STA (in.)	BL (in.)	WL (in.)	I_{xx}	I_{yy}	I_{zz}	I_{xz}
1	88	0.0	0	43.0	0	-	-	-
2	405	29.0	0	58.1	595	-	-	-
3	2075	59.0	0	56.0	2928	-	-	-
4	2483	119.5	0	50.2	3505	-	-	-
5	3475	181.0		53.2	4905	-	-	-
6	1209	252.0	0	56.4	1706	-	-	-
7	10	292.0	0	72.4	--	-	-	-
8	181	352.0	0	87.5	--	-	-	-
9	57	416.0	0	84.6	--	-	-	-
10	245	154.0	54	39.0	--	-	-	-
Rotor	1131	150.0	0	120.0	--	-	-	-
Shaft	290	150.0	0	150.0	--	-	-	-
Gearbox	646	150.0	0	80.0	--	-	-	-
Dynamic System	2067	150.0	0	102.79	1889	1889	-	-
TOTAL A/C	12295	146.646	1.102	67.702	29200	152028	140094	5465

Flight Controls - The flight control equation is an articulated rotor equation using gross weight and load factor as parameters. To account for the added components of a coaxial rotor, we have increased the weight by 14%.

$$W = (1.14) (138) \left(\frac{GW \times N_z}{10,000} \right)^{0.81} \text{lb} \quad (10)$$

where N_z = limit load factor = 3.5

Engine Section - The engine section weight is a function of the engine weight and number of engines.

$$W = 0.12 (N_{eng}) (W_{unit eng}) \text{ lb for mounts, firewalls} \quad (11)$$

where N_{eng} = number of engines (assuming cowl is of steel and included with body weight).

Engine and Engine Related Items - In order to rubberize the engine, a scaling factor is used. The resulting engine weight is then used in the equations for engine section and engine-related items.

$$\text{Engine: } W = 348 \times (\text{Engine Scale Factor}) \text{ lb} \quad (12)$$

$$\text{Engine Related Items: } W_{ERI} = 32.1 \left(\frac{W_{Total eng}}{100} \right)^{0.875} \text{ lb} \quad (13)$$

$$\text{Air Induction} = 0.07 W_{ERI}$$

$$\text{Exhaust} = 0.07 W_{ERI}$$

$$\text{Engine Controls} = 0.35 W_{ERI}$$

(Lube included in engine weight)

$$\text{Starting} = 0.30 W_{ERI}$$

Fuel System - The fuel system weight is estimated in two parts, the system weight and the tank weight.

$$W = 48.3 \left(\frac{W_{Fuel}}{1000} \right)^{0.875} + 139 \left(\frac{W_{Fuel}}{1000} \right) \text{ lb} \quad (14)$$

Auxiliary Propulsion - None

Drive System - The drive system weight is estimated in two parts, the main gearbox and the rotor shaft. The main gearbox weight is considered a function of torque and reduction ratio. The shaft weight is a function of gross weight and rotor radius.

$$\text{Main Gearbox: } W = 103.36 \left(\frac{\text{HP}}{\text{RPM}} \right)^{0.75} \left(\frac{\text{RPM}_{\text{in}}}{\text{RPM}_{\text{out}}} \right)^{0.15} \text{ lb} \quad (15)$$

$$\text{Main Rotor Shaft: } W = 2.406 \left[\left(\frac{\text{GW}}{2000} \right) \left(\frac{R}{10} \right) X_o \right]^{0.5} \times (L) \quad (16)$$

where L = length of main rotor shaft = $(4.5 \times R)$ in.

R = main rotor radius in feet

X_o = lift offset ratio = 0.15

Fixed Equipment - Instrument, hydraulic, electrical, auxiliary gear and air-conditioning weights are based on ABC demonstrator weight. Electronics and armament weights are dictated by the requirements of a reconnaissance mission. The furnishings weight is taken from the ABC demonstration with crash survivable seats added.

Instruments: $W = 86 + 25 \text{ lb } x (\text{Number of Engines})$
ABC Demonstrator

Hydraulics: $W = 36 \text{ lb}$ (ABC Demonstrator)

Electrical: $W = 275 \text{ lb}$ (ABC Demonstrator)

Electronics: $W = 258 \text{ lb}$ (ABC Demonstrator + AARS special equipment)

Armament: $W = 245 \text{ lb}$ (XM-27 system + 2000 rounds) (included in payload)

Furnishings: $W = 237 \text{ lb}$ (ABC Demonstrator + crash survivable seats + collapsible seats for rescuees)

Air Conditioning and Anti-Ice: $W = 45 \text{ lb}$ (ABC Demonstrator)

Auxiliary Gear: $W = 10 \text{ lb}$ (ABC Demonstrator)

Advanced Technology Saving - A technology saving of 176 pounds is taken as representative of the proposed time frame for development.

12.77% of main gearbox weight

23% of main rotor shaft weight

15% of tail weight

Fixed Useful Load

	<u>Weight (lb)</u>
Pilot	200
Copilot	200
Oil- Usable and Trapped	7
Trapped Fuel	0.0025 (W_{fuel})

Payload - 1000 pounds required, of which 245 pounds has been already classified as armament and 355 pounds as mission equipment, of which 285 pounds is removable avionics. This leaves 400 pounds to account for two rescuees.

MATHEMATICAL DESIGN MODEL

Sikorsky has developed a helicopter design model (HDM) which has been used in every recent aircraft preliminary design contract and proposal. HDM provides reliable mission and design constraint trade-off capabilities. This model was used in the design phase of this study and in the subsequent task of determining aircraft sensitivity to size effects.

The computerized model includes the following major features:

- A weights subroutine accounts for each aircraft subsystem, allowing sufficient component breakdown to reflect each subsystem weight.
- A semiempirical power required analysis correlates to within 2 percent of power required for existing aircraft in the Sikorsky inventory while taking proper account of rotor aerodynamic limits.
- An engine subroutine loads sea level engine data and ratings and computes altitude performance. This subroutine has been consistently within 2 percent accuracy.
- A mission analysis routine provides enough flexibility to divide any arbitrary mission into discrete elements at the required altitude, temperature, speed, etc., while reducing aircraft weight for burned-off fuel.
- A design routine sets up constraints on the preliminary design and sizes the aircraft subsystems to meet design constraints and requirements. The routine also checks gearbox ratings, engine ratings, and rotor aerodynamic limits throughout the design mission and either does not allow them to be exceeded or prints out the limit exceeded, as per user preference.
- An aircraft balance routine locates subsystem weights and assures center of gravity location for satisfactory aircraft balance.
- An antitorque subroutine sizes the tail rotor or tail fan to

satisfy MIL-H-8501A control power and damping requirements (not used for this study.)

- . An outer-loop capability provides flexibility to trend on most major aircraft design parameters and effectiveness parameters.

HDM has been used accurately to predict new configurations for the S-58T helicopter and the S67 gun ship. It has been used as the primary preliminary design sizing tool on the following contracts and proposals:

- . U.S. Army Advanced Anti-Torque Study
- . U.S. Army HLH Proposal
- . U.S. Army UTTAS Proposal
- . NASA/Army Rotor System Research Aircraft Study
- . U.S. Navy VTOL Escort Study
- . U.S. Navy LAMPS Proposal.

A flow chart of HDM is shown in Figure 10.

MIDSECTION DESIGN

OBJECTIVE

The objective of the AARS midsection design effort was to define the geometry in sufficient detail for structural analysis and fabrication of the test specimens.

APPROACH

Initial specifications of the midsection were taken from the general configuration resulting from the preliminary design effort. Detailed geometry of the flat armor sections was derived. The results of the flight and ground loads analysis indicated the required strengths of the welded fittings at the transmission and landing gear mounts. Upper and lower access doors were designed with a view to easy manipulation, while retaining protection of the interior from the defined threat. The fuselage sides were extended beyond the bulkheads defining the midsection, to enable attachment of the loading test rig. Protective armor strips exterior to the welded joints were designed to cover the heat-affected zones.

The effort was continually monitored by structural analysts, to ascertain the capability of the components to withstand the design loads, and by manufacturing personnel to provide feasibility of fabrication.

DISCUSSION

Figure 11 shows the test specimen midsection isometrically. For a production aircraft, weight can be saved by bringing the armor line up the bulkhead A-A of Figure 1 to waterline 59, and then rearward to the bulkhead B-B, thus forming an armored deck between the transmission and electronics bay.

Access to electronics, ammunition can, and air-conditioning unit is through the lower sliding doors on either side. Figure 12 shows details of these doors. The rear door slides in the plane of the airframe. The forward door

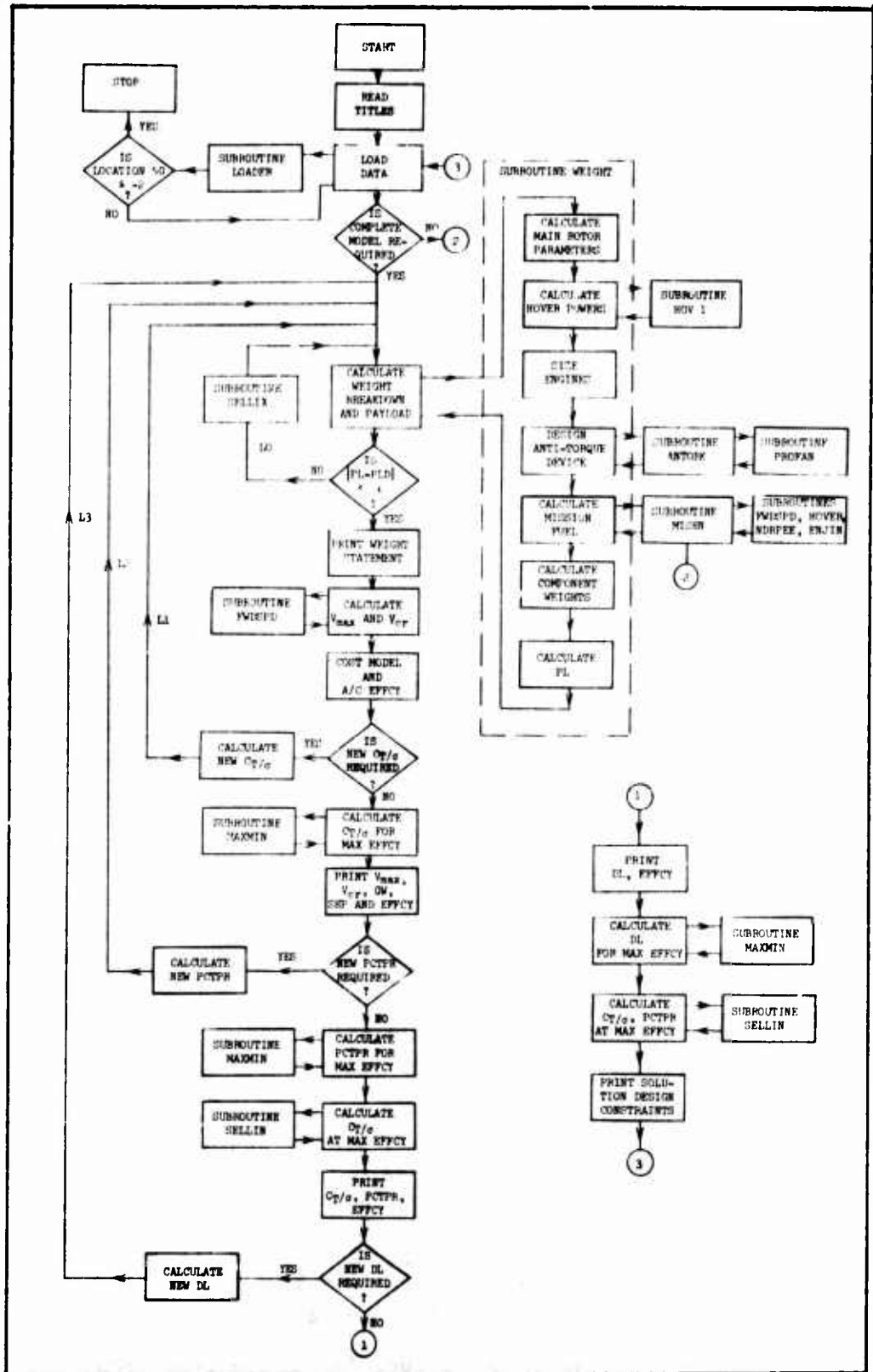


Figure 10. Helicopter Design Model Flow Chart.

slides outside it. Door guides are protected by armored rails bolted around the door area periphery. Doors are latched at the forward and aft ends by single clips released from the inside. In a production aircraft, these clips would be released and engaged collectively by a mechanism running up into the cabin. For the test specimen, attachment tabs for the loading rig are provided by extending lower midsection walls forward and upper aft, within the planes of the midsection walls.

The lower midsection contains electronics, battery, air-conditioner, and ammunition can, as shown in Figure 1. This equipment is mounted on trays resting on longitudinal beams attached in turn to the frames at bulkheads A-A and B-B of Figure 1. Thus, no equipment mounts attach to the armored skin directly, which would have required bolts through the skin and associated bolt protection.

The upper midsection contains the main gearbox, accessory power output, flight control servos and linkages, and the engine inlet. A nonstructural absorbent barrier separates upper and lower midsections, acting as a transmission drip-pan. The upper midsection is accessible through hinged doors on either side.

Figure 13 shows greater detail of the doors. The exterior hinges at the lower horizontal door line permit the door to hang vertically when open, for maximum accessibility to the transmission and flight control servos. The doors close into the plane of the fuselage skin, with overlapping bonded strips around the door periphery to protect the surrounding space. Pit-pins through the hinges can be removed after unlatching a door from within. Exterior and interior handles mounted with the same bolts enable the door to be completely removed. Alternately, the pins can be removed after opening the door.

The midsection top consists of two removable pieces joined along a station line through the midpoint of the rotor shaft. These fuselage sections are of DHS and are bolted to angled brackets welded to the sides to render them structural. The raised center of this assembly would thus protect the oil cooler, lower swashplate, and flight controls from the threat from above.

Figure 11 also shows details of the steel fittings at gearbox and landing gear mounts. Care has been taken to focus the loads along the mounts for these components, at the four corners of the midsection at waterline 59. Because of the multiplicity of load path angles at the transmission fittings, machining would be impractical. These fittings are, therefore, welded together from four components, three faces attaching to skin elements, and the central member attaching to the support struts. These fittings are bolted to the armored skin, with the external bolt heads protected with pieces of DHS, as discussed on pages 39-40. Only the left-hand forward fitting assembly of the test specimens will be protected in this way, simply to demonstrate the integrity of the concept.

The protective strips exterior to the welded joints are bent around the angle of the fuselage sides. The strips are made of two adjoining parts for the sharper corners, where the bend radius of the material prohibits

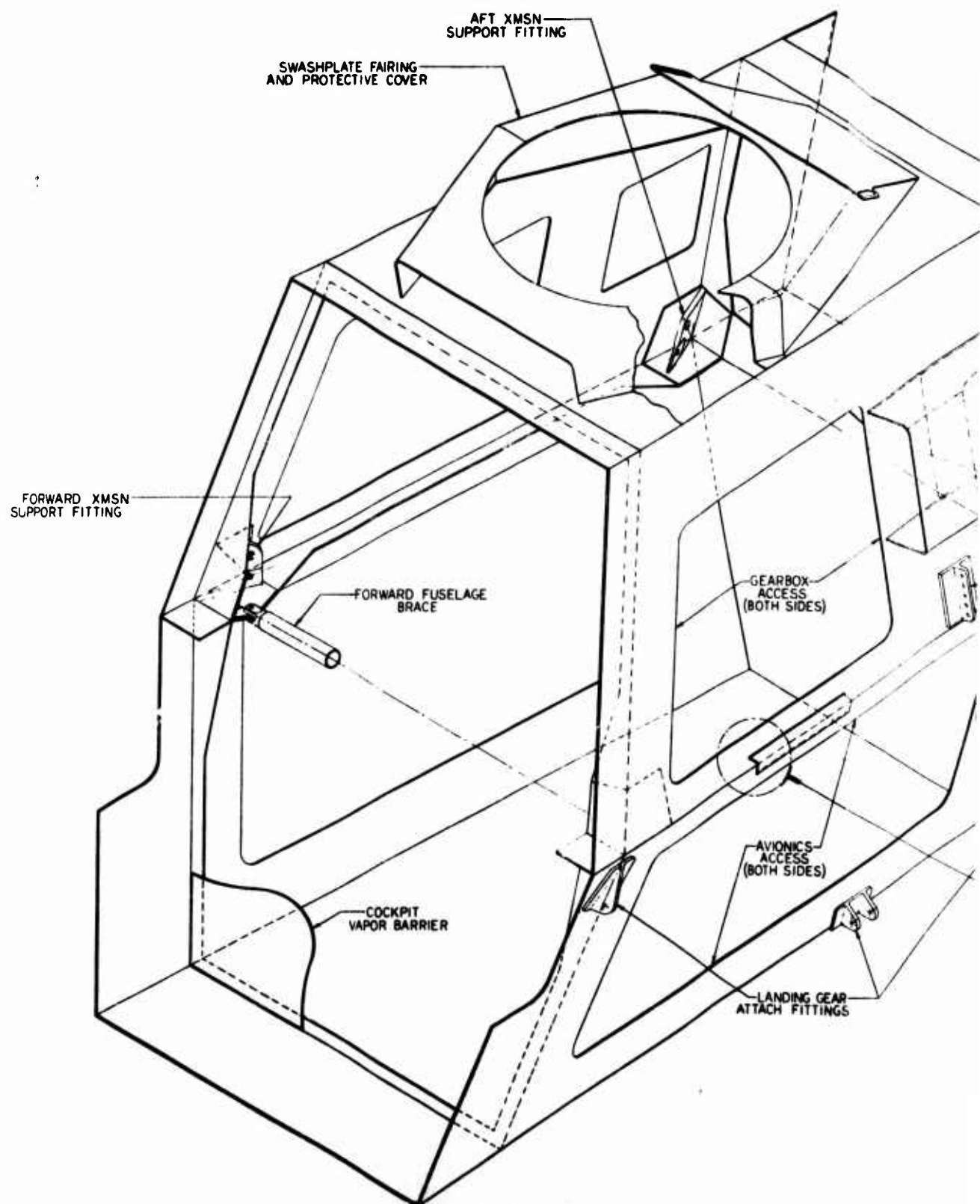
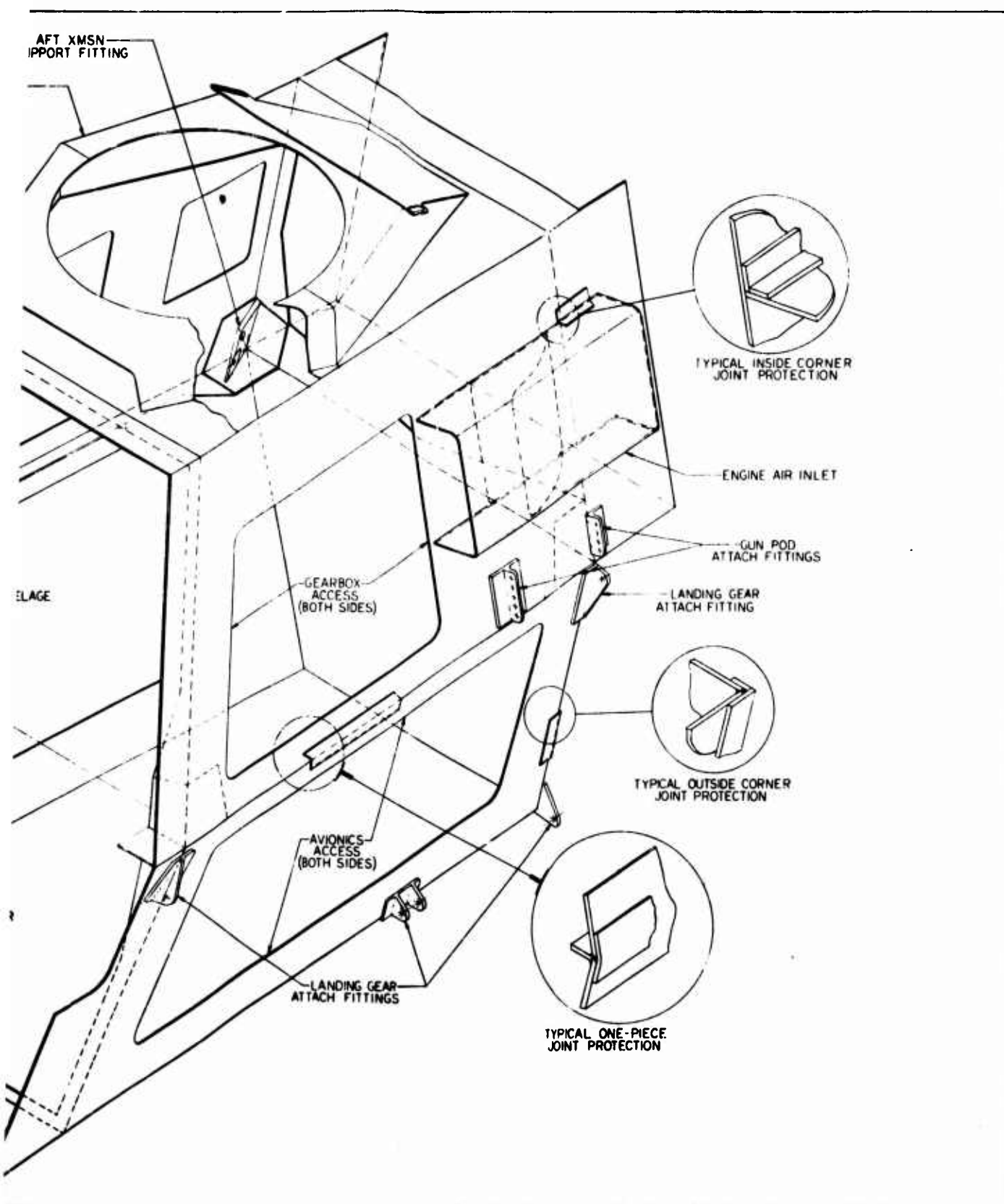


Figure 11. Midsection Isometric.



sometric.

2

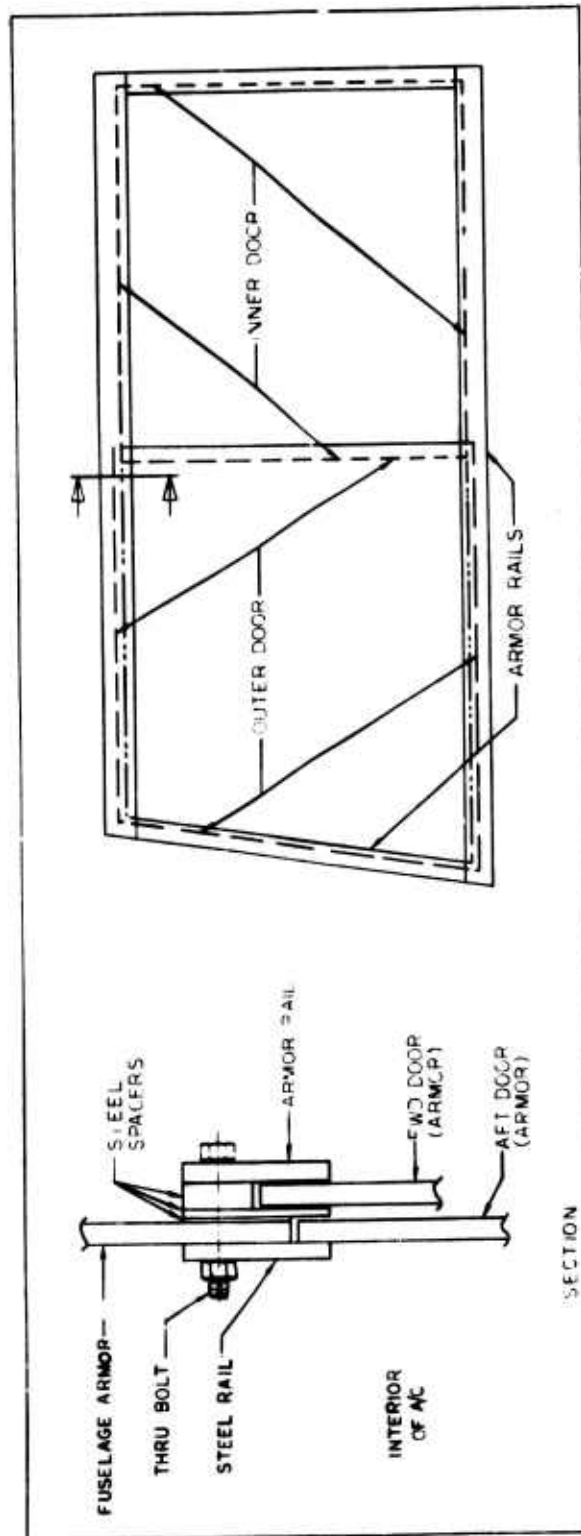


Figure 12. Lower Midsection Door Design.

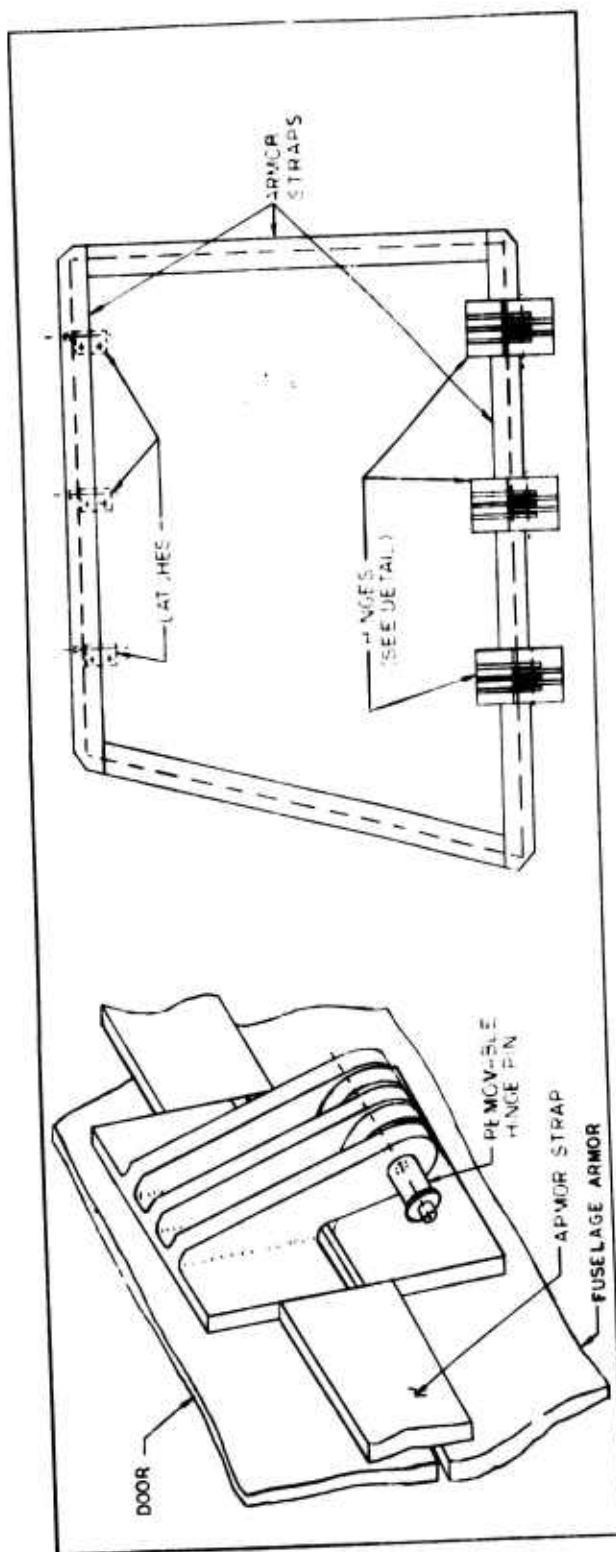


Figure 13. Upper Midsection Door Design.

single component fabrication. These two parts of each protective strip are laid so as to orient the joint between them in the direction of least expected threat, as shown in Figure 11. These ballistically tolerant joints and the bolt protection concept are discussed in the following section.

BALLISTIC-PROTECTED JOINTS

OBJECTIVE

The objective of the AARS ballistic-protected joints study was to design and test concepts to protect (a) heat-affected zones around a welded joint in the armor structure and (b) bolts attaching transmission and landing gear fittings to the armor.

APPROACH

The threat to heat-affected zones at the welds must be defeated before contact with primary fuselage structure. This philosophy eliminates concepts that give protection on the inside of the aircraft. Outside protection prevents damage to the basic structure and increases ease of fabrication, inspection, maintainability, and repairability.

Two methods of attaching protective strips over the heat-affected zones at welded joints were designed and then tested for ballistic properties. One method was chosen for implementation on the midsection test specimen. The strips were of DHS, wide enough to cover the entire heat-affected zone even though the material ballistic characteristics are relatively unaffected at the fringes of the defined zone. In a production version, this will enable the edges of the strips to be chamfered, thereby reducing aircraft weight and providing aerodynamic cleanliness as well as a deflecting surface for impacting projectiles.

A method was devised for protecting bolt heads at fitting attachments. This arrangement was specified at one-fitting group (left, forward) for the test specimens, in order to demonstrate the concept.

DISCUSSION

The midsection test specimens are made up of flat sections welded together to form the hexagonal cross section. The heat-affected zones at welded corners extend for approximately 1 inch on either side of the weld. Within this region, the material is less able to withstand the threat. Exterior protective strips of DHS, 2-1/2 inches wide, are required, therefore, and are attached along each weld. Because the minimum bend radius of DHS material is 1 inch, the strip has to be made of two halves at corners more acute than 150 degrees of included angle. Thus, the only corner within the test specimen at which the strip can consist of a single component is along waterline 59, the junction between upper and lower sections. Where two components are required, the joint between them is exposed to the direction of least threat. Figure 11 shows the arrangement of all the strips. Two means of attachment were tested, and these are illustrated in Figure 14:

- a. stud concept
- b. bonded concept

Both concepts were tested for ballistic properties, using DHS strips of the same thickness as those for the fuselage primary structure. Both provided the required protection to the heat-affected zone. As the bonded approach is simpler and less expensive, it was selected for the study. As noted in the two preceding sections, many of these welded corners may be avoided on a production aircraft by forming the corners prior to heat-treating the material. Also, a reduced strip thickness will suffice, with savings in aircraft weight.

The fittings at transmission and landing gear mounts are bolted directly to the fuselage armor skin. Bolt heads thus are exposed to the threat on the outside of the aircraft and therefore must be protected. Figure 15 shows the concept to be used to demonstrate a bolt protection method. A section of DHS covers a cluster of bolt heads, bonded to an aluminum spacer that has holes to accommodate the bolt heads. On a production aircraft, this outer bonding might be replaced with a stud attachment to facilitate inspection and tightening of the bolts.

An altogether different concept, likely to be employed on a production aircraft, is the barrel nut method of bolt attachment. This is illustrated in Figure 16. A group of bolts fasten into corresponding barrel nuts within an aluminum block inside the aircraft. It has been demonstrated that a bolt head can receive a hit at design impact velocity with no appreciable rupturing of the barrel nut block and no secondary projectiles. The entire barrel nut assembly can be replaced after repeated hits at the same fitting.

The results of the ballistic tests on the above concepts are documented in the separate confidential appendix to this report.

CRASHWORTHINESS DESIGN/ANALYSIS

OBJECTIVE

The objective of the AARS crashworthiness study was to establish personnel and structure survivability in conditions representing the 95th percentile accidents of Reference 5.

APPROACH

The design includes provisions for controlled deformations at force levels consistent with human tolerance and prevents penetration of living space by the impacting medium. An energy absorption analysis of the landing gear was performed to establish 20 fps vertical impact capability of the gear, and a similar analysis was performed for the 95th percentile accidents of Reference 5. The feasibility of limiting the pilot's vertical deceleration forces to 18g within his living space was established, and critical crash loads were determined for design of structural supports. No deformation of the structure was assumed in the crashworthiness analysis.

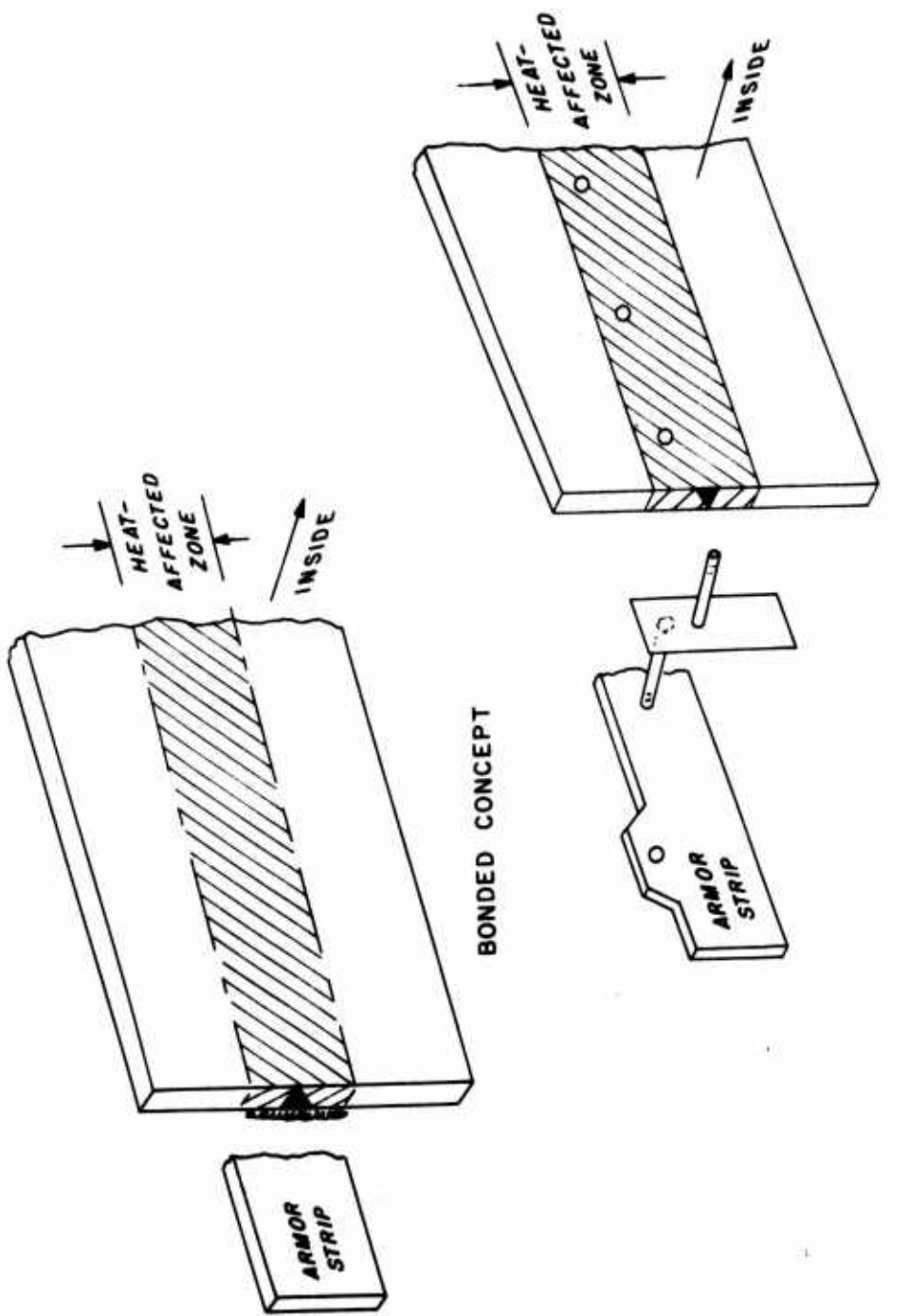
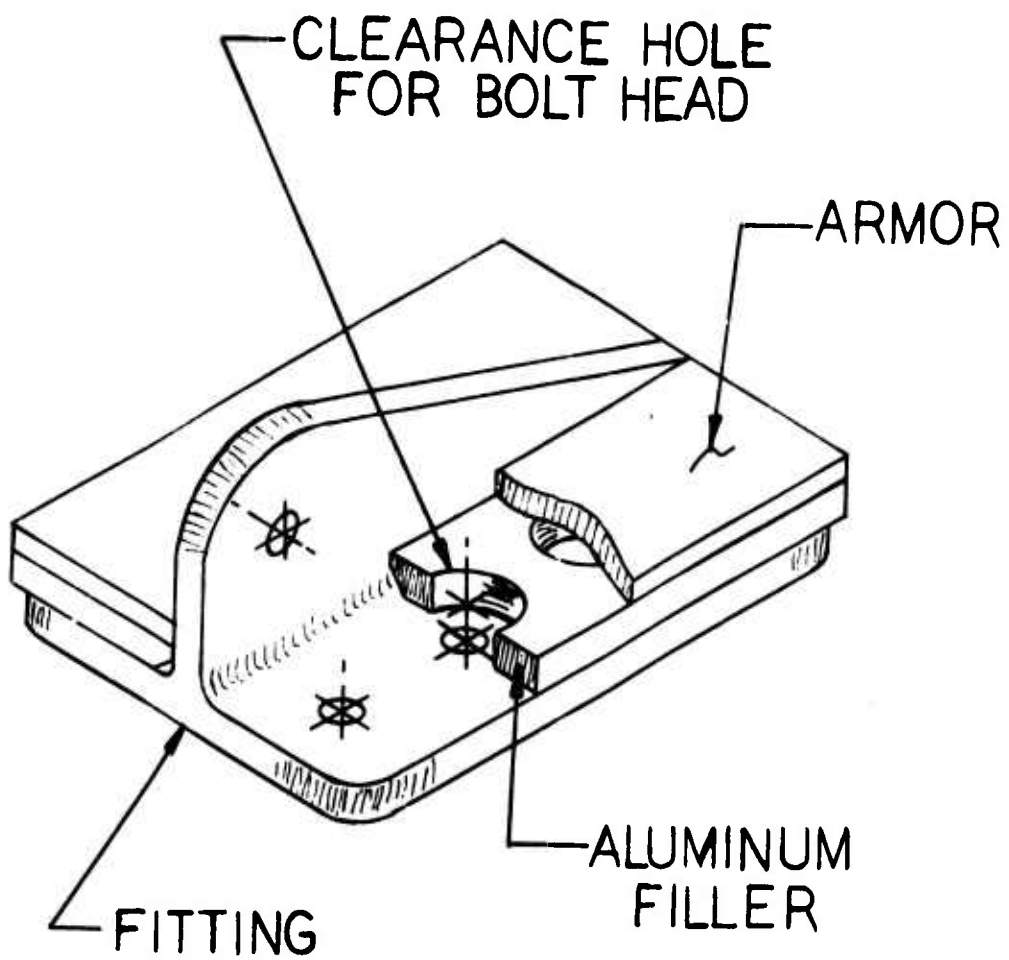


Figure 14. Weld Protection Concepts.



TYPICAL FITTING PROTECTION

Figure 15. Fitting Bolt Protection Concept.

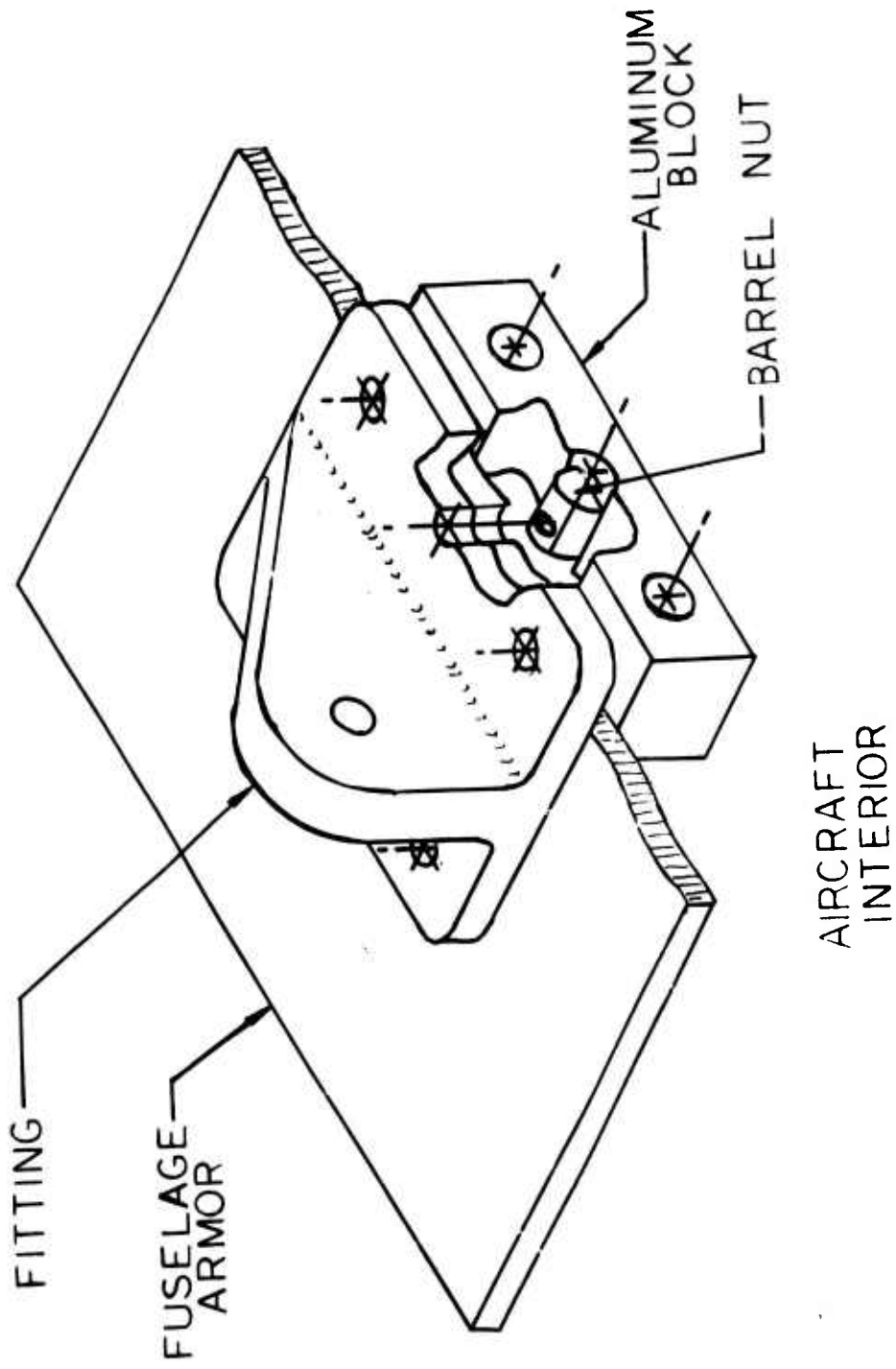


Figure 16. Barrel Nut Retention Concept.

The displacement, δ , through which to accomplish a constant deceleration, D , from an initial speed V_1 to a final V_2 is given by:

$$\delta = \frac{V_1^2 - V_2^2}{2D} \quad (17)$$

In the subsequent discussion, all accelerations are assumed to be constant over the time interval of application, except where stated otherwise.

DISCUSSION

Vertical Crash

The landing gear is designed to a limit sink speed of 8 fps, which is equivalent to 9.8 fps ultimate sink speed (50% increase in system kinetic energy). The oleo vertical stroke required to maintain a landing load factor at the aircraft cg equivalent to that of the basic flight load factor of 3g is 6 inches. Minimum distance from the fuselage bottom to the ground is 14 inches (Figure 17), which leaves 8 inches displacement available to attenuate the specified 20 fps impact to a maximum load of 10g without permanent deformation of the body. Aircraft kinetic energy above 9.8 fps is absorbed either by a honeycomb or a rolling wire torus energy absorber, incorporated in the landing gear oleos, both of which have been demonstrated for this type of application.

To withstand 20 fps vertical impact and attenuate the load to 10g, the energy absorber vertical stroke required is 5.6 inches (Figure 17). The total stroke required is 11.6 inches, which is within the 14-inch clearance available between the aircraft lower surface and the ground. Figure 17 shows that 23 fps vertical sink speed can be absorbed before the fuselage impacts the ground. In order to prevent the landing gear ancillary energy absorber from bottoming out, the fuselage ground clearance and landing vertical displacement will have to be tuned to provide that the fuselage impacts the ground before the landing gear runs out of stroke. This will help prevent the landing gear from being wiped off in vertical crash. The results of the landing gear analysis to provide 20 fps vertical impact speed capability and attenuate the loads to 10g are shown in Figure 17.

Above 20 fps vertical impact, the aircraft kinetic energy is absorbed by the sacrificial honeycomb attached to the bottom of the fuselage (Figure 1). The honeycomb is covered by a nonsparking exterior shell and is internally braced to withstand the drag loading imposed on it due to forward speeds.

At the 95th percentile accident of 42 fps vertical impact, 22.7 percent of the initial kinetic energy is absorbed by the landing gear, and the remainder is absorbed in crushing the fuselage bottom surface honeycomb. (Note that the honeycomb is precrushed to eliminate transient peak loads.) Limiting the maximum vertical deceleration to 48g to permit use of an energy absorption seat similar to that developed under Army Contract DA 23-204-AMC-03369T for the CH-54 aircraft, the maximum fuselage crushing (during

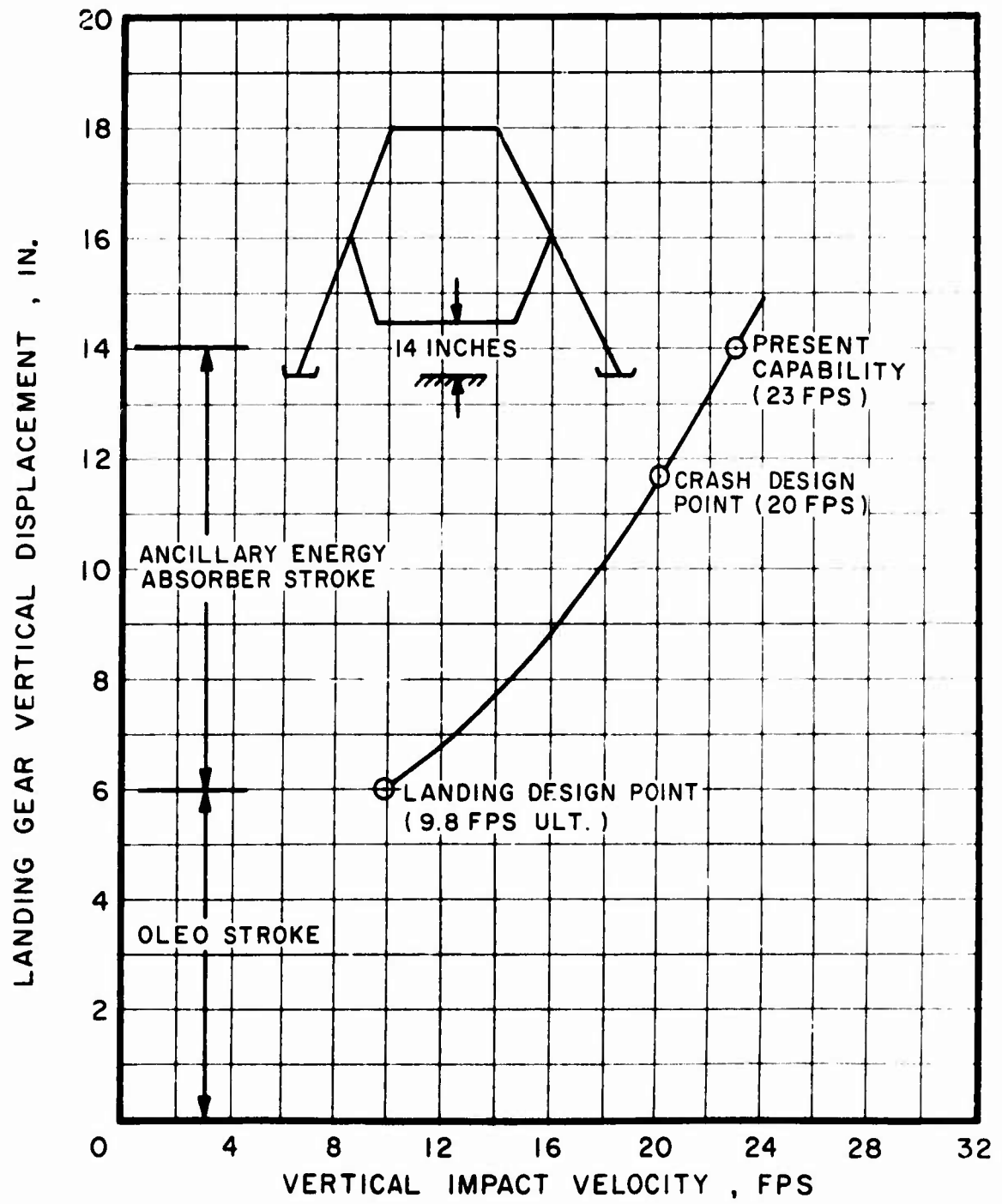


Figure 17. Landing Gear Vertical Displacement
Vs Vertical Impact Velocity.

centroidal impact) is 5.28 inches. Using 80% honeycomb efficiency, the material depth required is 6.6 inches, which is less than the 7-inch minimum precrushed depth available on the fuselage lower surface. The 7-inch depth limits the aircraft vertical deceleration to 45g for the 95th percentile accident.

To limit the crew's load to 18g as required by Reference 5, the seat is designed to activate at 18g by use of a load limiting device similar to the rolling wire torus system used by Sikorsky in response to Army Contract DA 23-204-AMC-03369T. The details of the seat design are beyond the scope of this analysis. However, the feasibility of limiting the crew's load to 18g is established by considering the vertical speed of the seat at the instant that the fuselage underside makes contact with the ground during a 95th percentile accident. This speed is 36.9 fps, yielding a displacement requirement of 14.2 inches. This displacement through crushing the honeycomb on the fuselage underside is 0.8 inch. The nominal space available between the bottom of the seat and the top of the floor is 10 inches, which is greater than the 8.6-inch stroke required to limit the crew loading to 18g. Time histories of seat and airframe motions during a 95th percentile accident are shown in Figure 18.

Longitudinal Crash

The kinetic energy due to the 95th percentile accident of 50 fps longitudinal velocity change is absorbed primarily in ground friction and soil deformation. The impulsive deceleration due to scooped-up earth mass is minimized by the canted armor bulkhead at fuselage station 26. The parameter required to calculate this impulsive deceleration (time required for the momentum exchange between the aircraft and accelerated earth mass) is unknown. However, using the data from Figure 2-4 of Reference 5, and extrapolating to 50 fps initial horizontal impact velocity, the impulsive deceleration is below 10g. This is well within human tolerance and crash structural design criteria discussed subsequently. If ground friction were the dominant decelerating force, the average horizontal load factor would be below 10g for a sliding distance over 4 feet (Figure 19). There is no apparent difficulty in meeting the 95th percentile longitudinal crash when aircraft kinetic energy is absorbed totally either in soil deformation or ground friction. The critical mode for horizontal crash is centroidal impact (impact on the aircraft nose).

Considering that the aircraft slides and impacts on its nose, the living space is protected and the deceleration forces are attenuated by absorbing the kinetic energy of impact on the sacrificial tubular structure forward of the cockpit area (see Figure 1). A recent revision of Reference 5 states a design crash criterion of 20 fps for nose impact that represents 16% of the energy of a 50 fps longitudinal velocity crash. If 84 percent of the initial kinetic energy is absorbed in ground friction and soil deformation, the longitudinal velocity (equivalent to residual kinetic energy) is 20 fps. The nose structure is designed to collapse at 25g peak load in order to (a) limit aircraft deceleration so as not to exceed human tolerance limit and (b) limit loads not to exceed the cockpit armor plate instability level, thus protecting crew living space. Figure 20 shows that 4.7 inches of

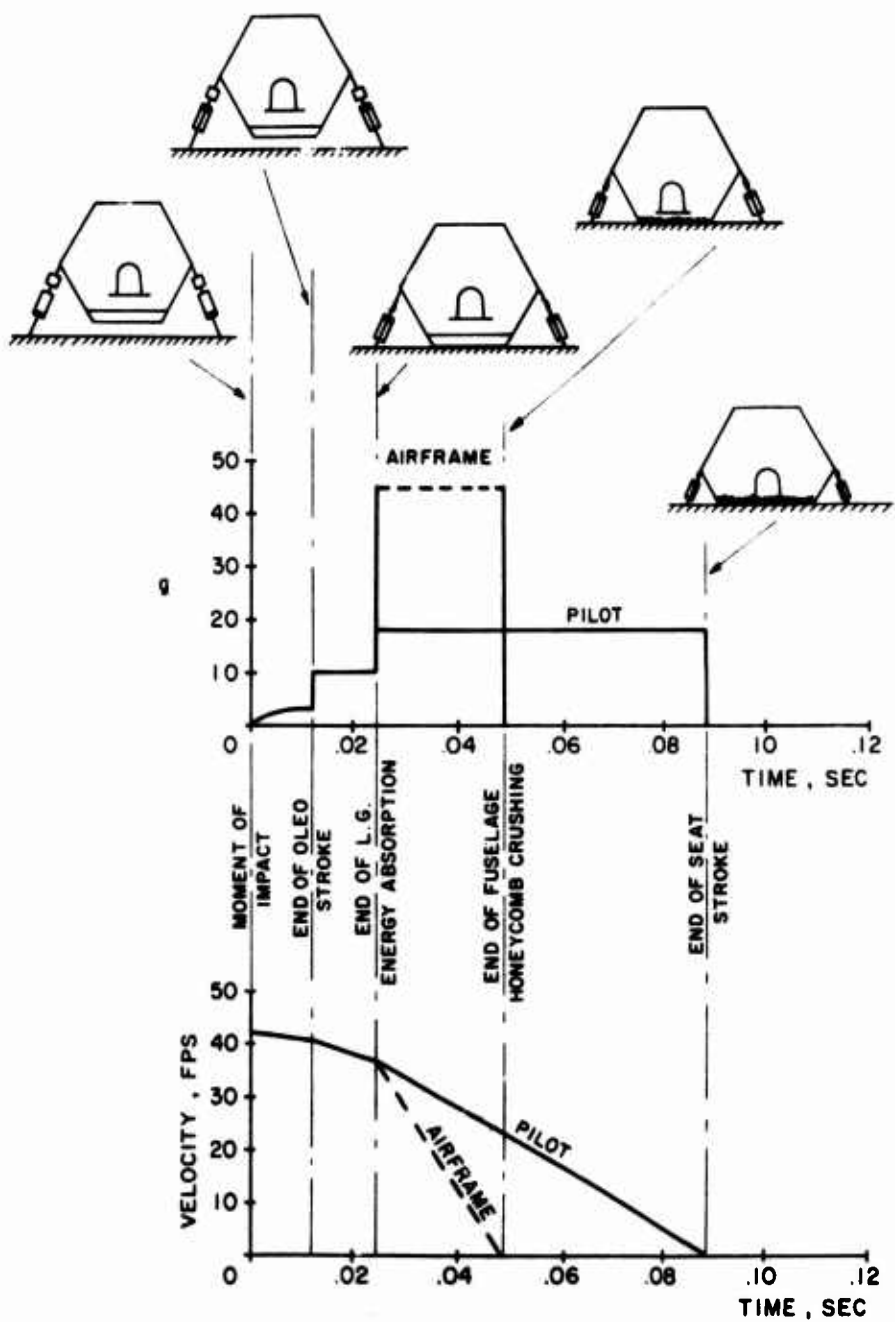


Figure 18. Airframe and Pilot Motions for 42 FPS Vertical Crash.

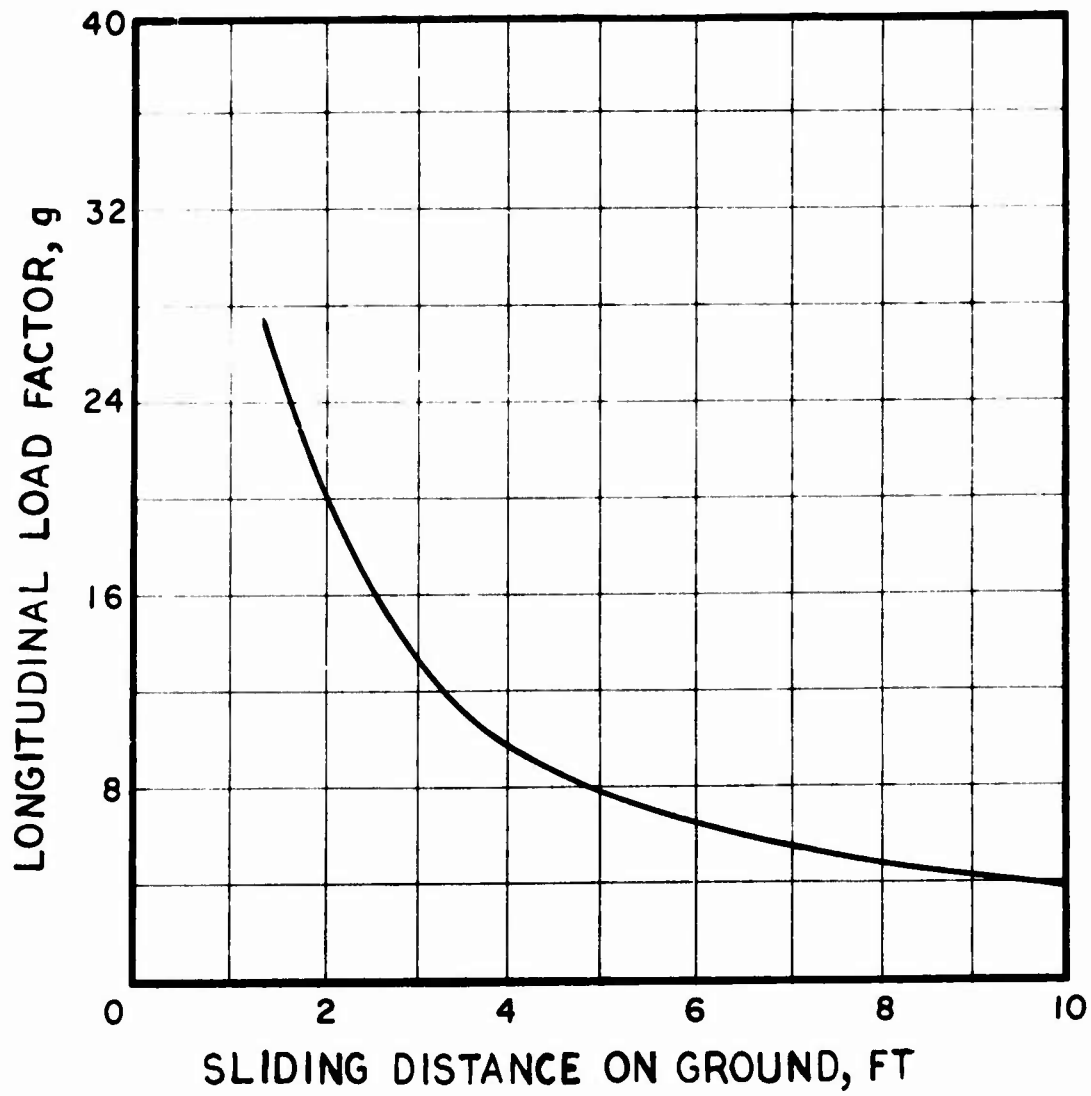


Figure 19. Longitudinal Load Factor Vs Ground Roll-Out Distance for 50 FPS Initial Velocity.

crushing is required to absorb the kinetic energy of a 20 fps impact at a 25g peak sinusoidal pulse. The equipment in the nose is assumed to be crushable and will permit the required displacement within the average length of 25 inches available for the sacrificial nose structure.

Side Crash

The 95th percentile side crash accident is 25 fps lateral velocity change (Reference 5). Part of this kinetic energy is absorbed in rolling the aircraft over and in deforming the rigid ABC blades. Figure 21 shows the aircraft roll-over characteristics. For zero initial roll angle, a lateral velocity of 10.2 fps is required for aircraft roll-over to occur, which is equivalent to 16.7% of the initial kinetic energy of the aircraft. The kinetic energy absorbed in deforming the rotor blades and tail surface is not known. Again, assuming that 84% of the initial kinetic energy is absorbed in initiating aircraft roll-over, deforming the rotor blades, crushing the horizontal tail, deforming the ground, and sliding on the ground, the velocity of impact is 10 fps, equivalent to the residual kinetic energy that has to be absorbed by fuselage centroidal impact. The fuselage collapse strength in side crash is unknown. In order to limit the peak load to the 20g human tolerance limit specified by Reference 5, the fuselage displacement required for a sinusoidal impulse is $1\frac{1}{2}$ inches, which is nominally within the space available between the pilot's torso and the side of the cockpit.

Structural Support Crash Loads

Peak decelerations for the 95th percentile accident are 45g vertical and 25g longitudinal. The lateral load of 20g, based on human tolerance data supplied in Reference 5, is generally not a critical failure mode except for design of seats, cockpit equipment, and fuel tank supports.

Transmission support and engine mount crash load factors are $N_x = 25$, $N_z = 45$. The lateral crash is not a critical mode for crew survival. The transmission support is designed with a greater strength in the forward mount than in the aft mount. As a result, the mode of failure causes the transmission and rotor head to fall away from the cabin area in vertical impact.

The cockpit equipment and fuel tank support crash load factors are $N_x = 25$, $N_y = 20$, and $N_z = 45$. The equipment located behind the crew area presents a potential hazard to the crew and is designed for a forward crash load factor of $N_x = 25$.

The landing gear crash load factor is $N_z = 10$. The landing gear mode of failure will be at the gear lower structural members in order to prevent failure at the transmission mounting structure, which is at the same location as the oleo upper mount.

The crew seat and support is designed to the human tolerance limits of $N_x = 45$ longitudinal and $N_y = 20$ lateral, as specified by Reference 5. In the vertical direction, N_z is 18 for the seat movable segment, and N_z is 45 for the seat fixed structure and seat support.

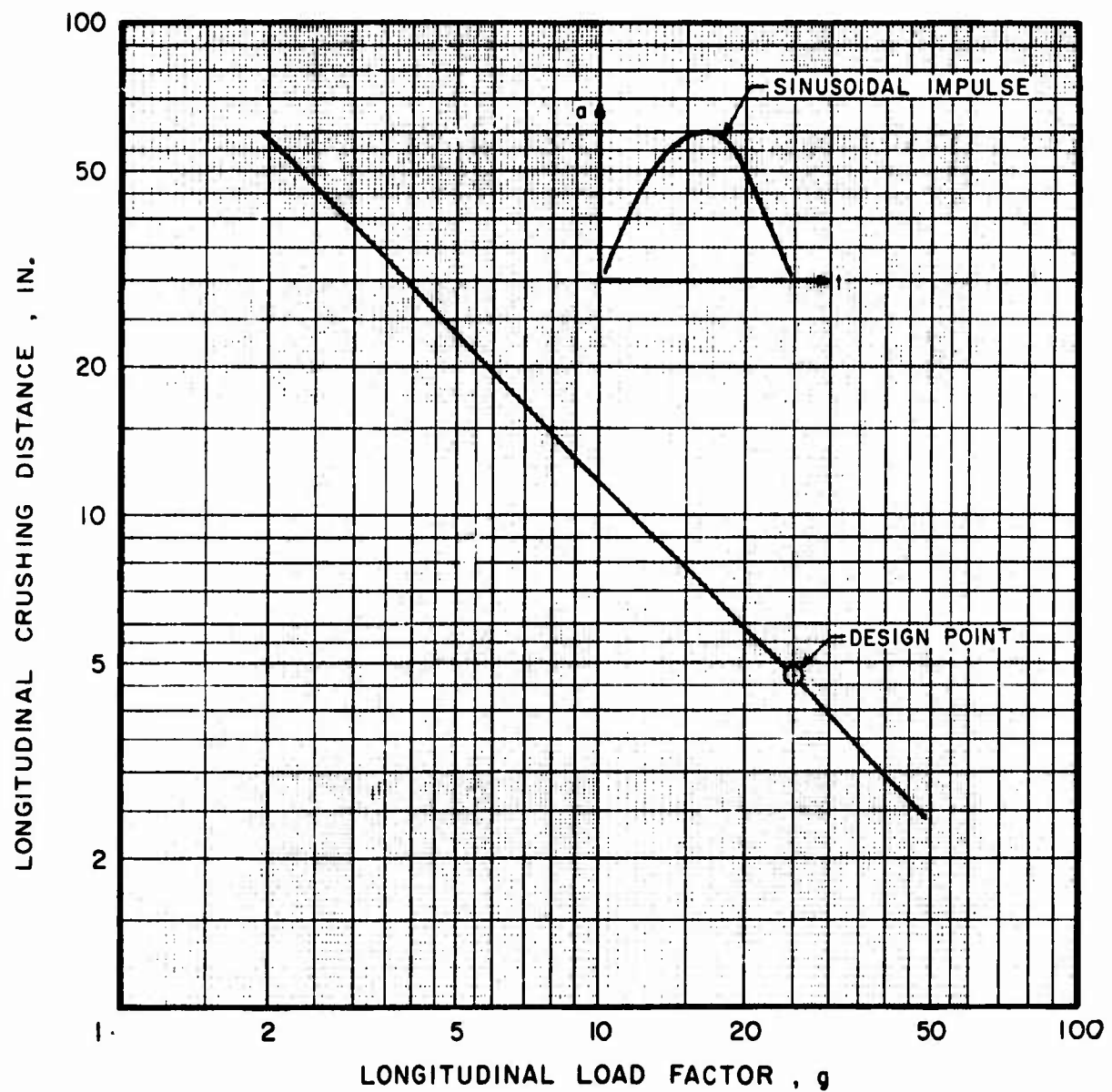


Figure 20. Longitudinal Load Factor Vs
Crushing Distance for 20-fps
Centroidal Nose Impact.

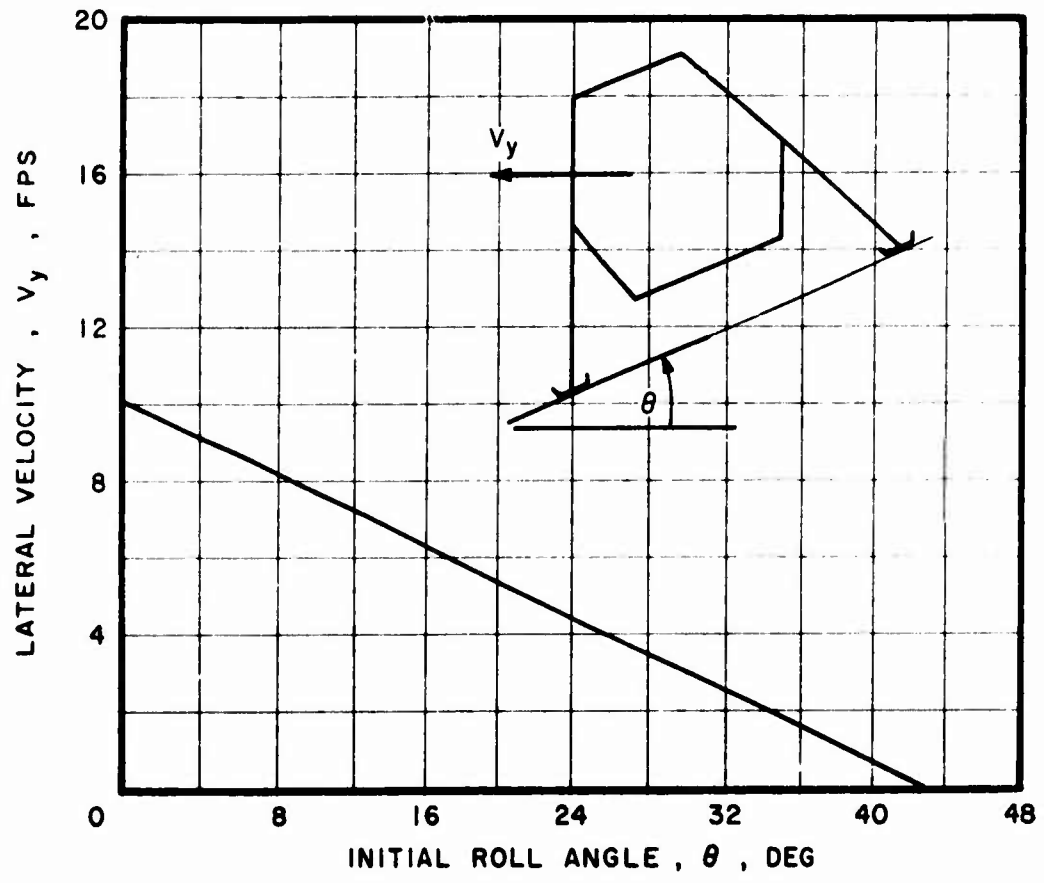


Figure 21. Lateral Velocity for Aircraft Roll-Over to Begin Vs Initial Roll Angle.

LOADS AND CRITERIA

OBJECTIVE

The objective of the AARS loads and criteria study is to establish repeated design loads.

APPROACH

Criteria for flight loading were generated in accordance with requirements of Reference 6. Basic aircraft parameters for this analysis are listed in Table VI. Design flight loads were established by a general computerized procedure normally used for airframe design. In this program, the rotor system is simply regarded as a force and moment producer. Rotor forces and moments are those required to satisfy a particular maneuver specification. Airloads are computed based on the dynamic equilibrium of the rotor and all the component forces representing the aircraft. Aircraft geometry and mass properties were taken from the results of the preliminary design studies.

Design ground loads were developed from energy considerations during oleo stroking, from criteria specified in Reference 7.

Center section applied static loads were developed from flight and landing conditions already determined.

Fatigue criteria were developed from an operational usage spectrum defined by the mission profile of Reference 8.

The resulting complete definition of ground and flight static and repeated loads was used to design the facility to test the AARS midsection specimen.

DISCUSSION

Design Flight Loads and Criteria

The flight loads design criteria are summarized in Table VII. Computerized analysis of these flight conditions yielded the results summarized in Table VIII.

Design Ground Loads and Criteria

To calculate the loads applied to the skid gear, the following assumptions were made:

- (1) Rotor lift and skid loads act through the aircraft cg.
- (2) No rotor drag or head moments exist.
- (3) The aircraft will settle vertically on the skid gear.

TABLE VI. BASIC AIRCRAFT PARAMETERS FOR LOADS AND CRITERIA

Basic Design Gross Weight = 12295 lb

Main Rotor RPM Ranges:

power on	design minimum = 630
	design maximum = 700
	limit = 770*

power off	design minimum = 630
	design maximum = 700
	limit = 770*

*This is a deviation from Reference 6 which specified limit =
1.25 x design maximum rather than 1.1 x design maximum

Flight Speeds

design maximum level flight, V_h = 180 kn
limit dive, V_d = 1.2 V_h = 216 kn

Available Engine Horsepower (Sea Level Standard Day)

intermediate rated power (30 min) = 2400 hp

Center of Gravity

cg_x = 146.64 in.
cg_z = 62.7 in.

Limit Maneuver Load Factors

Maximum N_z = 3.5g
Minimum N_z = -0.5g

Surface Areas and Center of Pressures:

	Horizontal Stabilizer	Vertical Fin	Fuselage	Main Rotor
Area, ft ²	43	36	-	-
STA, in.	390	410	150	150
BL, in.	0	0	0	0
WL, in.	77	95	53	120

Sink Speed:

Sink Speed, V_v = 8 fps

TABLE VII. AARS FLIGHT LOADS AND CRITERIA

Cond. No.	Condition (Reference)	Velocity (kn)	Tip Speed (Dps)	N_Z (g)	α_x (rad/sec ²)	α_y (rad/sec ²)	α_z (rad/sec ²)
1	Level Flight (3.2.2.1)	180	770	1.0	0	0	0
2	Symmetrical Dive & Pullout (3.2.2.3)	216	770	3.5	0	1.0 (b)	0
3	Vertical Takeoff (3.2.2.4)	0	770	3.5	0	0	0
4	Rolling Pullout (3.2.3.1)	216	770	2.8	4.0 (c)	1.0 (b)	-
5	High Speed Rudder Kick (3.2.3.2)(d)	216	770	1.0	(f)	0	(f)
6	Steady State Side Slip (3.2.3.2)(d)	216	770	1.0	0	0	0
7	Recovery from Side Slip (3.2.3.2)(d)	216	770	1.0	(f)	0	(f)
8	Hovering Turn (e)	0	630	1.0	(f)	0	(f)

- (a) All conditions are at basic design gross weight and maximum horsepower.
- (b) Based on ABC control capability (limited). Could change if aircraft moments of inertia are appreciably different.
- (c) α_x limited to 4.0 based upon ABC control capability study and are subject to change as a function of aircraft inertia.
- (d) Investigate conditions with V_x close to 0.
- (e) Accomplish turn by adding maximum differential torque at 90% rotor rpm.
- (f) Calculated

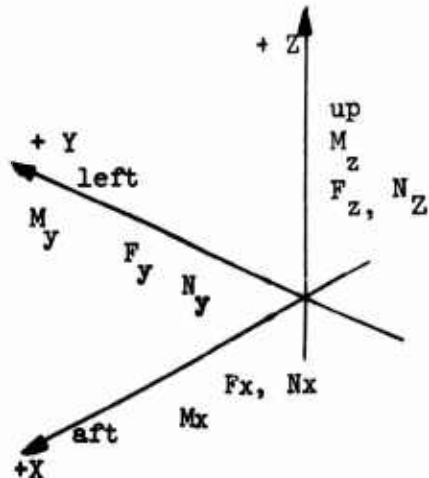
TABLE VIII. SUMMARY OF LIMIT FLIGHT LOADS, LOAD FACTORS
ANGULAR ACCELERATIONS - AARS

Cond. No.	Description	Velocity (kn)	Tip Speed (fps)	β (deg)	N_x (g)	N_y (g)	N_z (g)	$\ddot{\alpha}_x$ (rad/ sec ²)	$\ddot{\alpha}_y$ (rad/ sec ²)	(r s)
1	Level Flight	180	770	-7	0	0	1.0	0	0	0
2	Symmetrical Dive & Pullout	216	770	7	.10	0	3.5	0	1.0	0
3	Vertical Takeoff	0	770	-	0	0	3.5	0	1.489	0
4	Rolling Pullout - 1st Solution	216	770	-2.5	0	-.042	2.8	3.932	1.0	0
5	Rolling Pullout - 2nd Solution	216	770	18	.10	-.029	2.8	3.93	1.0	0
6	High Speed Rudder Kick	216	770	-8	-.02	-.141	1.0	0	-.058	-3
7	Steady Side Slip - 15°	216	770	-8	-.12	-.52	1.0	0	-.058	0
8	Recovery From Side Slip - 15°	216	770	-8	-.12	-.62	1.0	1.322	-.058	-
9	Hover Trim - Max. Differential Torque	0	630	-	0	0	1.0	0	.425	0

Cond. No.	Horizontal Stabilizer		Vertical Stabilizer		
	F_x	F_z	F_x	F_y	F_z
1	-170	-1703	0	0	0
2	34	505	0	0	0
3	0	0	0	0	0
4	-110	-1769	0	0	0
5	-552	3242	0	0	0
6	-274	-2632	-243	-1774	0
7	-274	-2632	-98	-1194	0
8	-274	-2632	-98	-2388	0
9	0	0	0	0	0

Note:

All units are in lb, in., sec
unless otherwise specified.



Positive Sign Convention, Left
Rule for Moments and Accelerations

FLIGHT LOADS, LOAD FACTORS AND
TIONS - AARS

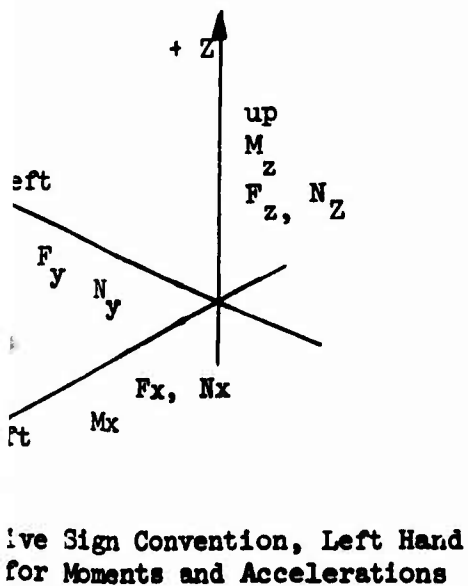
	N _z (g)	$\ddot{\alpha}_x$ (rad/ sec ²)	$\ddot{\alpha}_y$ (rad/ sec ²)	$\ddot{\alpha}_z$ (rad/ sec ²)	Rotor Loads						Fuselage Loads					
					F _x	F _y	F _z	M _x	M _y	M _z	F _x	F _y	F _z	M _y (Pitch)	M _z	
	1.0	0	0	0	-1079	0	15364	0	-210299	0	1248	0	-1060	-81914	0	
	3.5	0	1.0	0	-756	0	39786	0	375418	0	1922	0	708	84057	0	
	3.5	0	1.489	0	0	0	42000	0	342880	0	0	0	0	0	0	
42	2.8	3.932	1.0	.208	-1874	-502	36545	125609	9832	8116	1984	0	-176	-57812	0	
29	2.8	3.93	1.0	.215	444	-355	26143	124042	76356	8015	1308	0	-214	258125	0	
41	1.0	0	-.058	-3.906	-1475	77	17274	-40653	-355513	-2627	1751	0	-2642	-130450	0	
2	1.0	0	-.058	0	-1475	77	17274	-40653	-355513	-2626	667	-4060	-2642	-130450	325000	
2	1.0	1.322	-.058	-.262	-1475	77	17274	-40653	-355513	-2626	667	-4060	-2642	-130450	325000	
	1.0	0	.425	.95	0	0	12000	0	98000	114000	0	0	0	0	0	

Aircraft Mass Data

GW = 12295	I _{xx} = 29200
CG _x = 140.64	I _{yy} = 135500
CG _y = 0	I _{zz} = 120000
CG _z = 62.7	I _{xz} = 5465

Load Geometry

	STA	BL	WL
Fuselage	150	0	53
Horizontal Stabilizer	390	0	77
Vertical Stabilizers	410	0	95
Main Rotor	150	0	120



2

Five Sign Convention, Left Hand
for Moments and Accelerations

The vertical drop energy of the aircraft (U_v) may be expressed as

$$U_v = \left(\frac{v^2}{2g} \right) + \delta_{LG} (GW) \quad \text{where} \quad v_v = \text{sink speed of } 8 \text{ fps} \quad (18)$$

δ_{LG} = deflection of the landing gear

GW = basic design gross weight =
12295 lb

The energy absorbed by the landing gear and rotor for pure vertical deflection of the aircraft cg on the skids is

$$U_s = (\bar{L}_s + L_R) \delta_{LG} \quad \text{where} \quad \bar{L}_s = \text{the average skid load} \quad (19)$$

L_R = rotor lift

Equating the two energies and recognizing that

$$\bar{L}_s = \eta_s L_s \quad \text{where} \quad \eta_s = \text{efficiency of the oleo} \quad (20)$$

$= .8 \text{ (assumed)}$

L_s = skid peak load,

and that $L_R = \frac{2 GW}{3}$, (21)

we obtain

$$L_s = \left(\frac{GW}{\eta_s} \right) \times \left(\frac{v^2}{2g \delta_{LG}} \right) + .333 \quad (22)$$

The stroke of the oleo was determined such that the landing load factor at the aircraft cg would be equal to the basic flight load factor, $N_z = 3.5$. The stroke that yields this load factor is 6 inches. The conditions analyzed are those specified by Reference 7, namely:

- (1) Level Landing - Para. 6.261 - (F_x, F_z)
- (2) Level Landing with Side Load - Para. 6.262 - ($F_x, \pm F_y, F_z$)
- (3) Nose Down Landing - Para. 6.263 - (F_x, F_z)

In addition to the above conditions, a 20 fps landing attenuated to 10g was investigated. This condition is an ultimate design condition for the skid gear. The results of the ground loads analyses are summarized in Table IX.

TABLE IX. SUMMARY OF LIMIT GROUND LOADS, LOAD FACTORS, AND ANGULAR ACCELERATIONS

Cond. No.	Description	Load Factors			Angular Accelerations			
		Sink Speed (fps)	N_x (g)	N_y (g)	N_z (g)	α_x (rad/sec ²)	α_y (rad/sec ²)	α_z (rad/sec ²)
10	Level Landing F_x , F_z	8	1.34	0	3.594	0	-3.7	0
11	Level Landing F_x , F_y , F_z	8	.67	.721	2.128	17.088	-1.938	-.025
12	Level Landing F_x , - F_y , F_z	8	.67	-.721	2.128	-17.088	-1.938	-.025
13	Nose Down Landing F_x , F_z	8	2.311	0	3.056	0	9.265	0
14	Crashworthiness F_z ,	20	-.273	0	10.1	0	9.068	0

Skid Loads				Rotor Loads			Cond. No.	
Left Skid		Right Skid		F_x	F_y	F_z		
F_x	F_y	F_z	F_x	F_y	F_z	F_x	F_y	F_z
8040	0	17550	8040	0	17550	0	8000	10
4020	4325	8780	4020	4325	8780	0	8000	11
4020	-4325	8790	4020	-4325	8780	0	8000	12
12830	0	14470	12830	0	14470	2070	7726	13
-1500	0	56000	-1500	0	56000	-280	8000	14

Note:

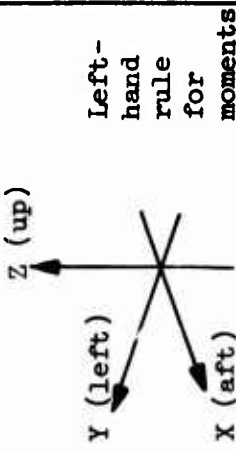
- (1) All units are lb, in., sec unless otherwise specified.
- (2) All loads and geometry are in the aircraft axis.
- (3) Condition 14 is an ultimate design condition for the skid support structure and a limit design condition for fuselage structure.

Skid Applied
Load Geometry

Cond.	STA	BL	WL
10	135.5	±49.5	5
11	135.5	±49.5	5
12	135.5	±49.5	5
13	50	±49.5	5
14	135.5	±49.5	5

Aircraft Mass Data

$GW = 12295$	$I_{xx} = 29200$
$CG_x = 146.646$	$I_{yy} = 152028$
$CG_y = 0$	
$CG_z = 62.7$	$I_{zz} = 120000$
$I_{xz} = 5465$	



Center Section Applied Static Loads

Figure 22 is a schematic of the center section applied loading. The loads applied to the center section by the forward and aft fuselage sections were calculated for the flight and landing conditions previously specified. The results are summarized in Table X. A summary of the rotor head and gun inertia loads is presented in Table XI.

Fatigue Criteria and Design Loads

- (a) The mission profile for the UH type helicopter, as specified in Reference 8, was used to generate the operational usage spectrum given in Table XII.
- (b) The operational $V - N_z$ diagram for use in repeated loads is given in Figure 23. The maximum load factor capability in hover was calculated using a conservative rotor figure of merit of 1.0 and all engine power available at sea level standard. This gave a maximum rotor thrust of 17,000 pounds.
- (c) This value of T would give $N_z = 1.414$, but a conservative value of $N_{z_{max}}$ equal to 2.0 in hover was assumed. The cut-offs at the corners of the limit design $V - N_z$ diagram to arrive at the fatigue design $V - N_z$ diagram are conservative estimates that are based on ABC rotor trends.
- (d) The flight maneuver spectrum is given in Figure 24 and is based on that for the CH-53A. The frequency of occurrence of different levels of load factor over the expected life of the aircraft is shown.
- (e) The ground load spectrum is given in Figure 25. This is based on the frequency distribution of sink speeds used in Reference 9. A plot of gear load versus sink speed is given in Figure 26.
- (f) The fuselage spectrum generated for the AARS is based on the following assumptions:
 - (1) Turns are comparable to pullouts.
 - (2) Damage will occur only in the following maneuvers:
 - symmetrical dive and pullouts (including turn)
 - vertical takeoffs
 - hovering turns
 - impact landing
 - (3) High frequency, low amplitude rotor head excitations are not included in the fatigue loading.

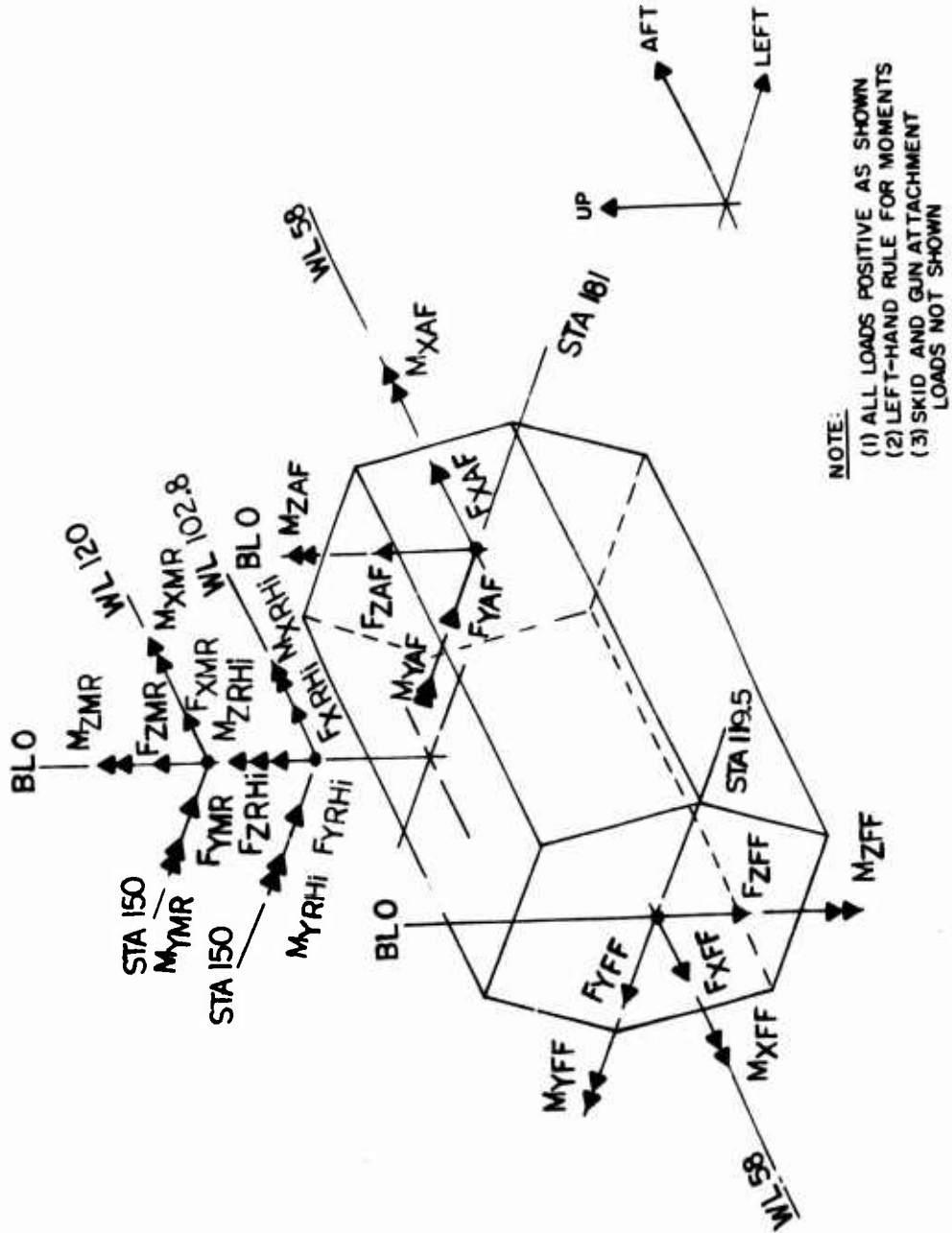


Figure 22. Center Section Applied Loads (Fuselage, Rotor Head Aerodynamic and Inertia) and Geometry.

TABLE X. FORWARD AND AFT FUSELAGE LOADS APPLIED TO CENTER SECTION

Cond.	Forward Fuselage Loads					Aft Fuselage Loads				
	F _{XFF}	F _{YFF}	F _{ZFF}	M _{XFF}	M _{YFF}	F _{XAF}	F _{YAF}	F _{ZAF}	M _{XAF}	M _{YAF}
1	0	0	6152	0	259495	0	-169	0	-6743	0
2	366	0	16485	0	532745	0	-354	0	-15037	0
3	-180	0	18190	0	651032	0	128	0	-15480	0
4	-121	115	15313	28939	577701	3695	-24	-300	-14507	729
5	366	168	10938	29261	231166	1959	-940	-363	-3650	-453413
6	-90	2343	6871	7185	312120	-142222	-430	1833	-7892	-198276
7	-577	1347	6871	6907	314103	-232071	190	427	-7892	46700
8	-577	3058	6871	21895	314103	-330804	190	1561	-7892	726195
9	0	-737	4867	-2569	167624	40349	0	-715	-4743	-402360
10	6970	0	14602	0	409788	0	-6674	0	-19812	-46227
11	3498	5598	8852	150048	256823	-174218	-3345	-4871	-11553	656775
12	3496	-5598	8852	-150048	256823	174218	-3345	4871	-11553	-375407
13	10125	0	22061	0	857314	0	-10163	0	-7523	135558
14	-2430	0	55704	0	2074664	0	2078	0	-40607	0
										826116

Note:

- 1) All loads are limit.
- 2) All loads are positive as shown in Figure 22.
- 3) Units are lb, in., sec.

TABLE XI. ROTOR HEAD AND GUN INERTIA LOADS

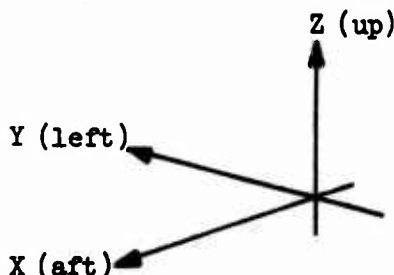
Cond.	Gun			Rotor Head *				
	F_{XGi}	F_{YGi}	F_{ZGi}	F_{XRHi}	F_{YRHi}	F_{ZRHi}	M_{XRHi}	M_{YRHi}
1	0	0	-90	0	0	-2143	0	0
2	-1	0	-313	-436	0	-7482	0	-1889
3	12	0	-312	-331	0	-7473	0	-2812
4	10	-28	-299	-221	960	-6006	-7427	-1889
5	1	-29	-299	-435	931	-6006	-7427	-1889
6	-47	19	-90	32	374	-2144	0	109
7	10	47	-90	270	1114	-2144	0	109
8	-22	50	-106	254	1671	-2152	-2479	109
9	15	-1	-89	-88	-18	-2135	0	-802
10	-149	0	-330	-2049	0	-7770	0	6989
11	-76	-199	-405	-1005	2253	-4700	-32279	3661
12	-75	199	16	-1005	-2253	-4491	32279	3661
13	-135	0	-259	-7011	0	-6376	0	-17502
14	96	0	-885	-1430	0	-21261	0	-17129

* Items supported by main gearbox support structure (rotor, shaft, gearbox, blades).

Note:

- (1) Units are lb, in., sec.
- (2) All loads are limit except as specified in Note 3.
- (3) Loads for condition 14 are ultimate for the gun and rotor head support structure and limit for fuselage structure.

<u>Rotor Head Data</u>	
$W = 2143$	$I_{xx} = 1889$
$CG_x = 150$	$I_{yy} = 1889$
$CG_y = 0$	
$CG_z = 102.8$	<u>Gun Data</u>
$W = 90 \text{ lbs}$	
$CG_x = 154$	
$CG_y = 54$	
$CG_z = 39$	



Load Positive Sign Convention

TABLE XII. AARS - OPERATIONAL USAGE SPECTRUM, 3600 HOURS

TABLE XII. AARS - OPERATIONAL USAGE SPECTRUM, 3600 HOURS						
Item	Occur- rence in 100 Hrs	Occur- rence in A/C Life A/C Life ver	Sec per Maneu- ver	Time in Maneu- ver (hr)	% of Aircraft Life	Mission Profile in Percent of Aircraft Life
1) Steady Hovering	9.32					
2) Sideward Flight	.932					
3) Reward Flight	.466					
4) Forward Level Flight						
Speed = 20% VH						
40% VH						
50% VH						
60% VH						
70% VH						
80% VH						
90% VH						
VH 115% VH						
5) Takeoff Power Climb						
6) Full Power Climb						
7) Power Dives						
8) Right Turns						
9) Left Turns						
10) Autorotation						
11) Takeoff (Equal No. of Landings)	400					
12) Hovering Turns	14400	6				
13) Control Reversals - Hovering	36000	12				
14) Landing Approach	36000	1				
15) Partial Power Descent	180000	4				
16) Control Reversals	18000	16				
17) Pull-ups	28800	1.5				
18) Power To Autorotaton	250	3				
19) Autorotaton To Power	40	1440	2			
20) Autorotaton Pull-ups	40	1440	4			
Ground-Air-Ground Cycles	100	1440	4			

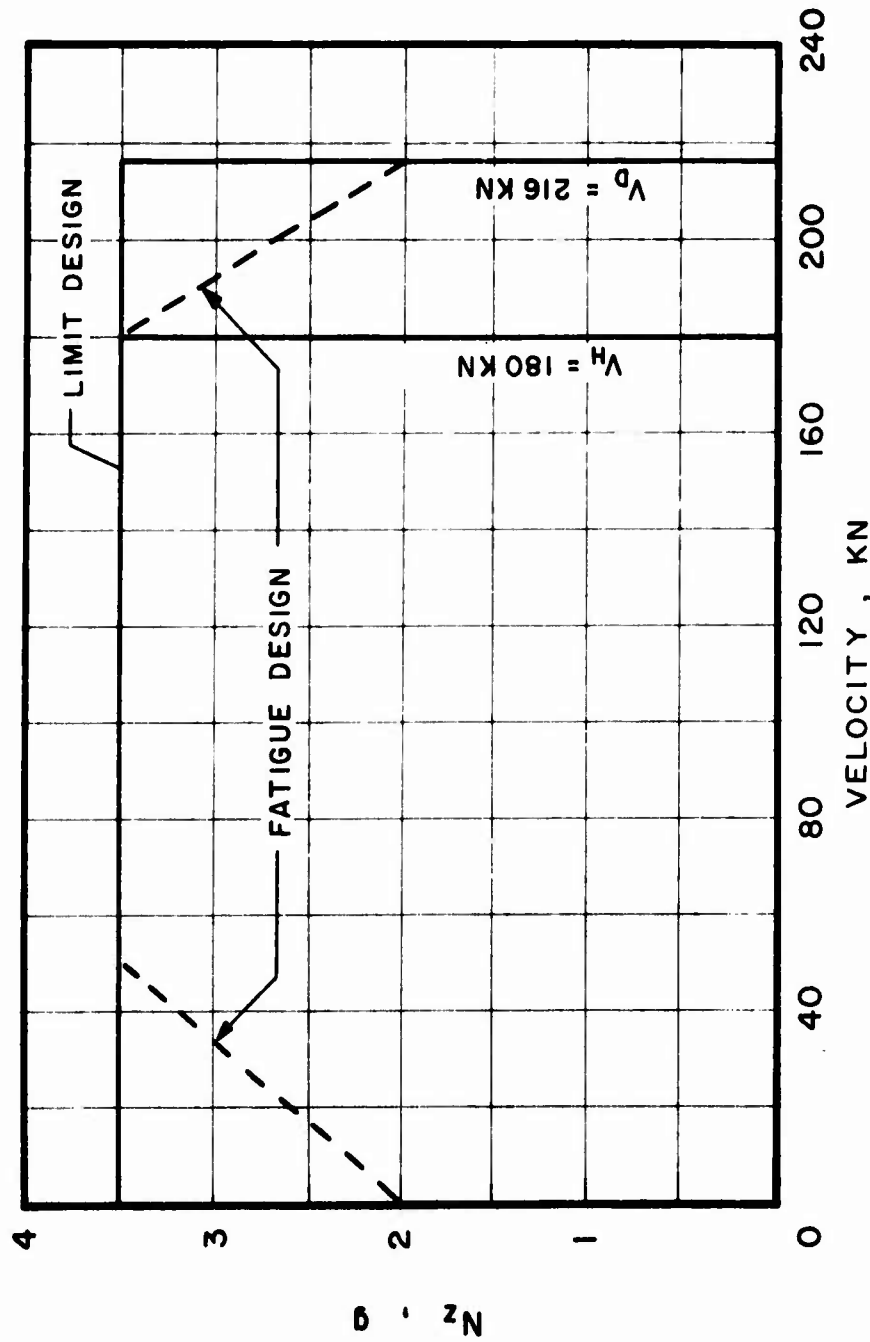


Figure 23. AARS V-N Diagram for Limit and Fatigue Design.

Aircraft Life of 3600 Hours

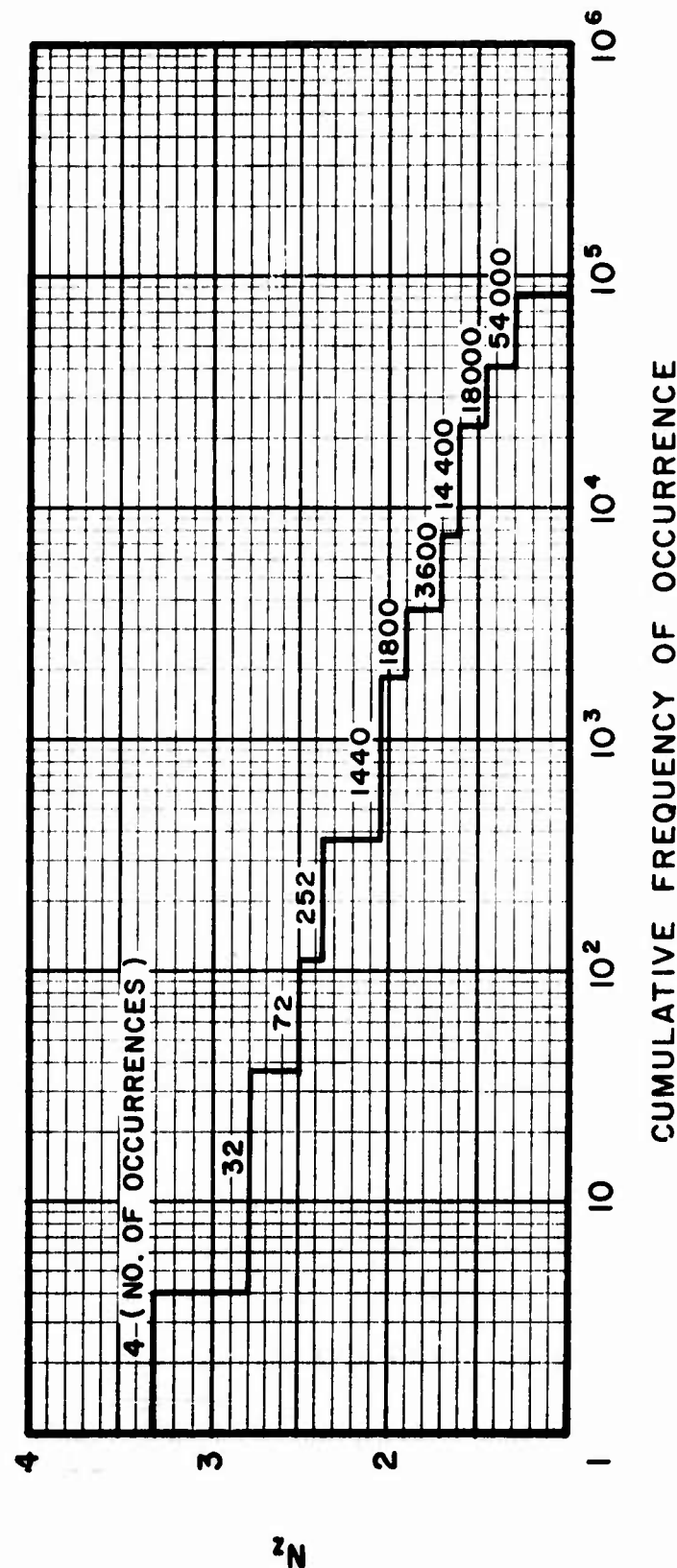


Figure 24. Maneuver Load Spectrum.

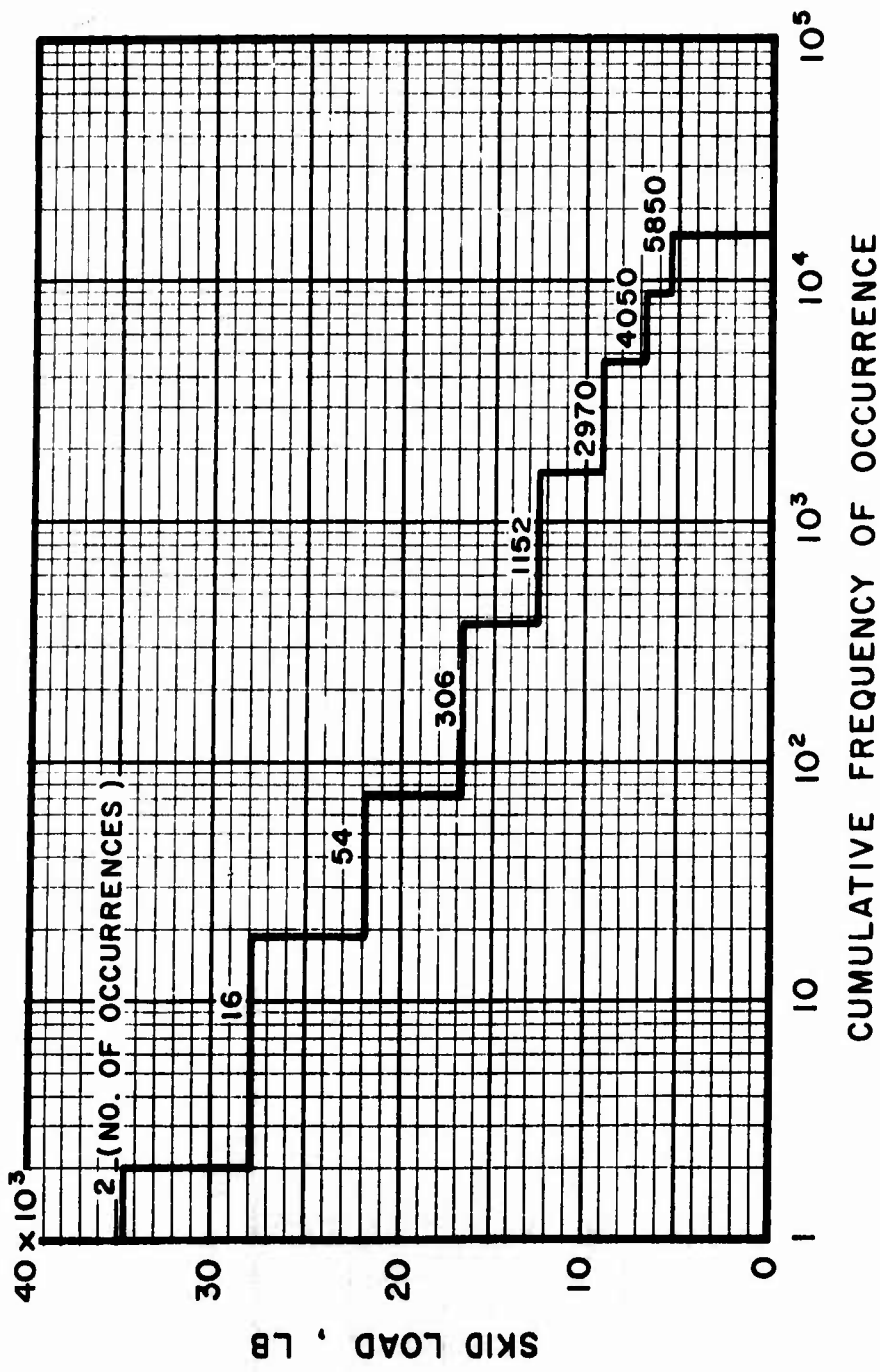


Figure 25. Impact Landing Load Distribution - Cumulative Frequency of Occurrence for Aircraft Life = 3600 Hrs.

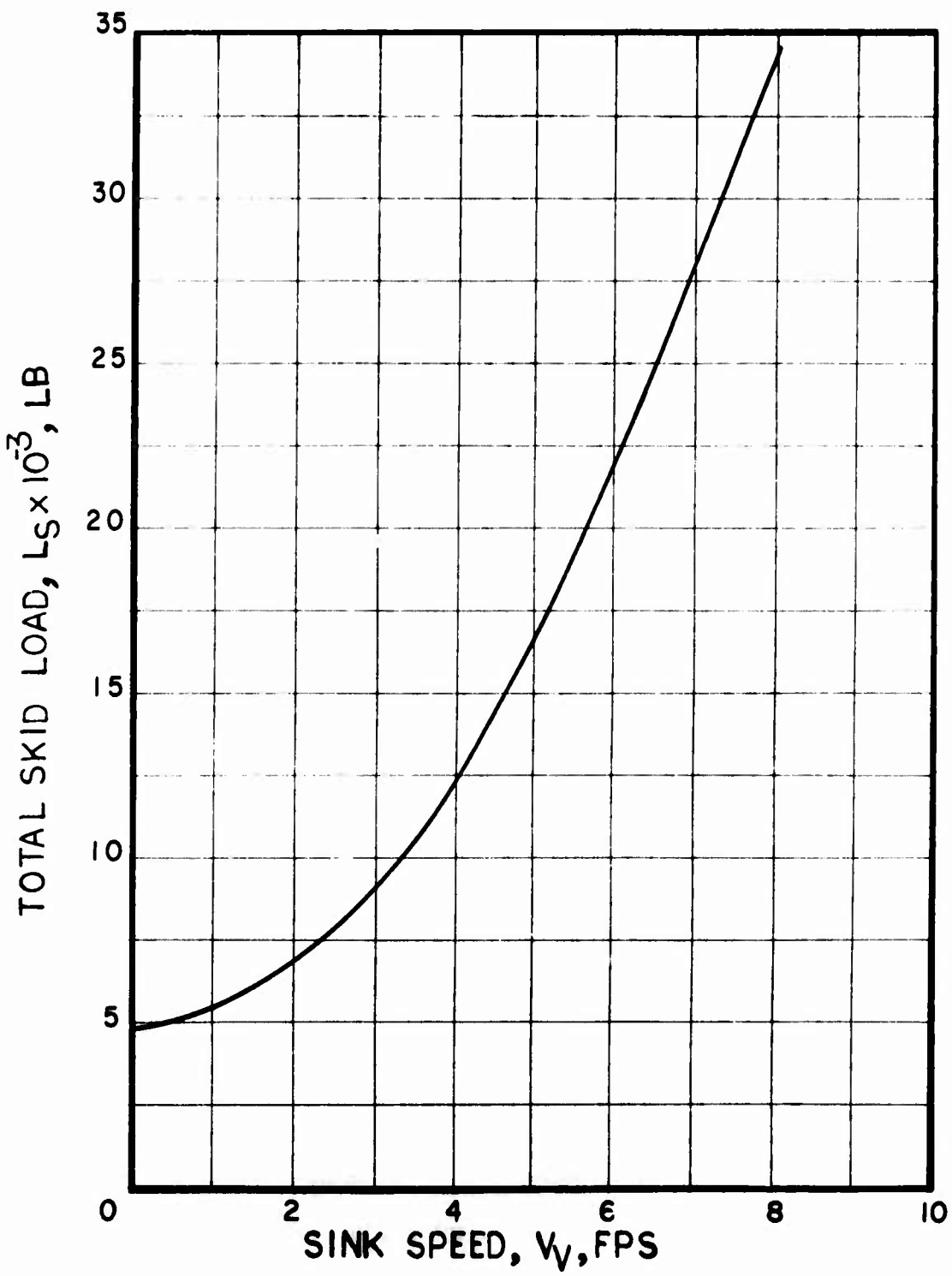


Figure 26. Skid Gear Load Vs Sink Speed.

- (4) Torque for hovering turn conditions is distributed as shown in Figure 27.
- (5) The frequency distribution of vertical load factor for jump takeoff condition is as shown in Figure 28.

The steps in the accumulative frequency distributions, given in Figures 25 through 28, have been reduced to facilitate fatigue testing. A summary of the fatigue data is given in Table XIII.

RELIABILITY/MAINTAINABILITY

OBJECTIVE

The objective of the AARS reliability/maintainability study was an aerial vehicle that requires no maintenance except for 500-hour periodic inspection. Refueling and minimal servicing of hydraulic system, engine, transmission, and rotor constituted the basic requirements to maintain self-supportability.

APPROACH

A preliminary design review and analysis was performed. The criteria used to evaluate the current design were those defined in a reconnaissance mission. Comparative analyses, realizing current aircraft reliability/maintainability limitations and next-generation requirements, were made to establish currently acceptable criteria and the goals of the production model.

Three basic and specific concerns with the design of the AARS were analyzed:

Design (component and system reliability)
Accessibility
Installation, location, servicing (component and system)

DISCUSSION

The design of the aircraft was influenced extensively in order to attain optimum reliability/maintainability characteristics and sufficient opportunity for including changes in production aircraft. The various systems and components are designed to meet the requirements of a reconnaissance mission, including reliability of 94% for a 3-hour mission. The following breakdown shows where the effects of reliability in design have produced improvements in the design:

- 1) Main transmission is designed for on-condition overhaul
- 2) Rotor blades are designed for on-condition replacement
- 3) Standard hydraulic systems - reduced number of connections and use of swaged fittings to reduce leakage

Hovering Turn Torque Distribution - 36000 Occurrences

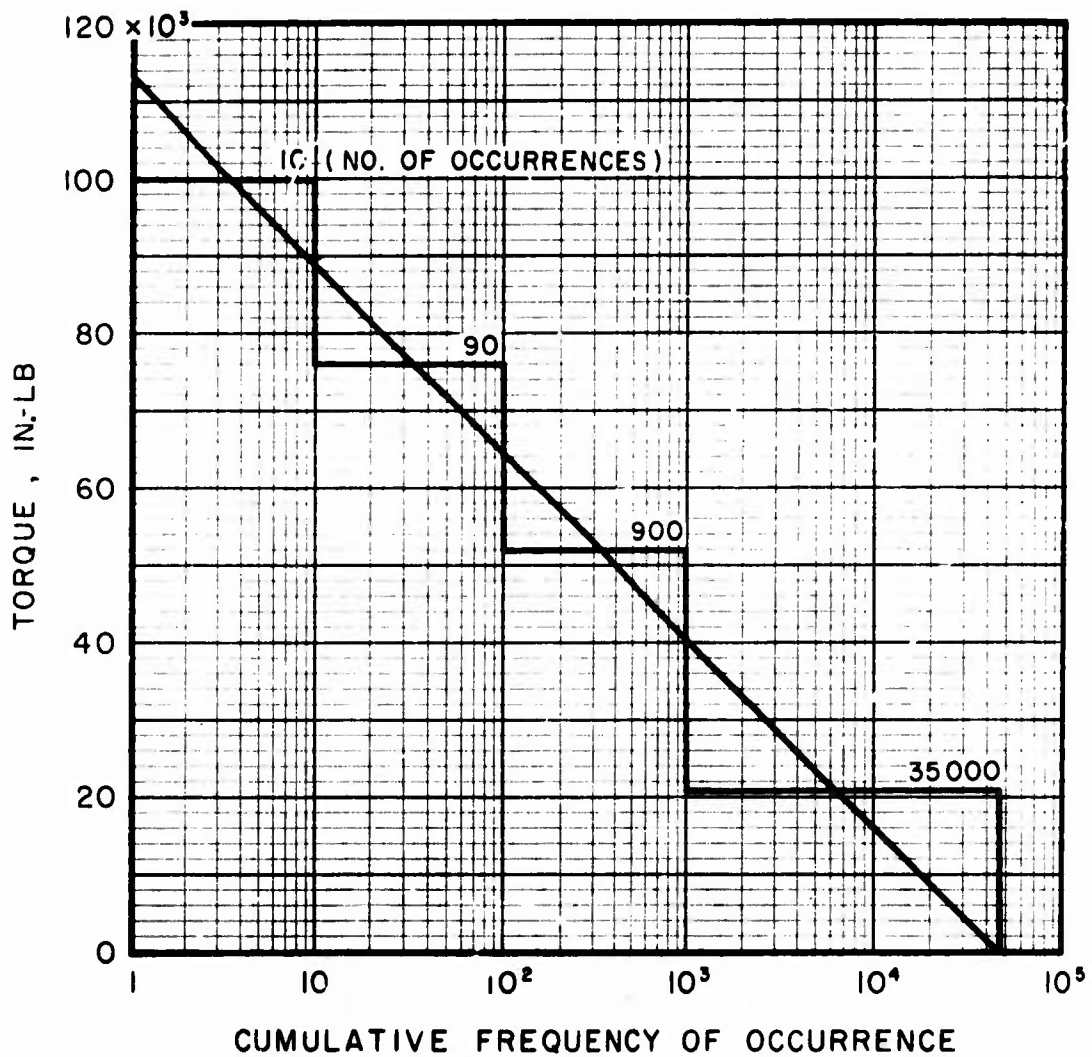


**Figure 27. Torque Vs Cumulative Frequency of Occurrence
for Aircraft Life = 3600 Hrs.**

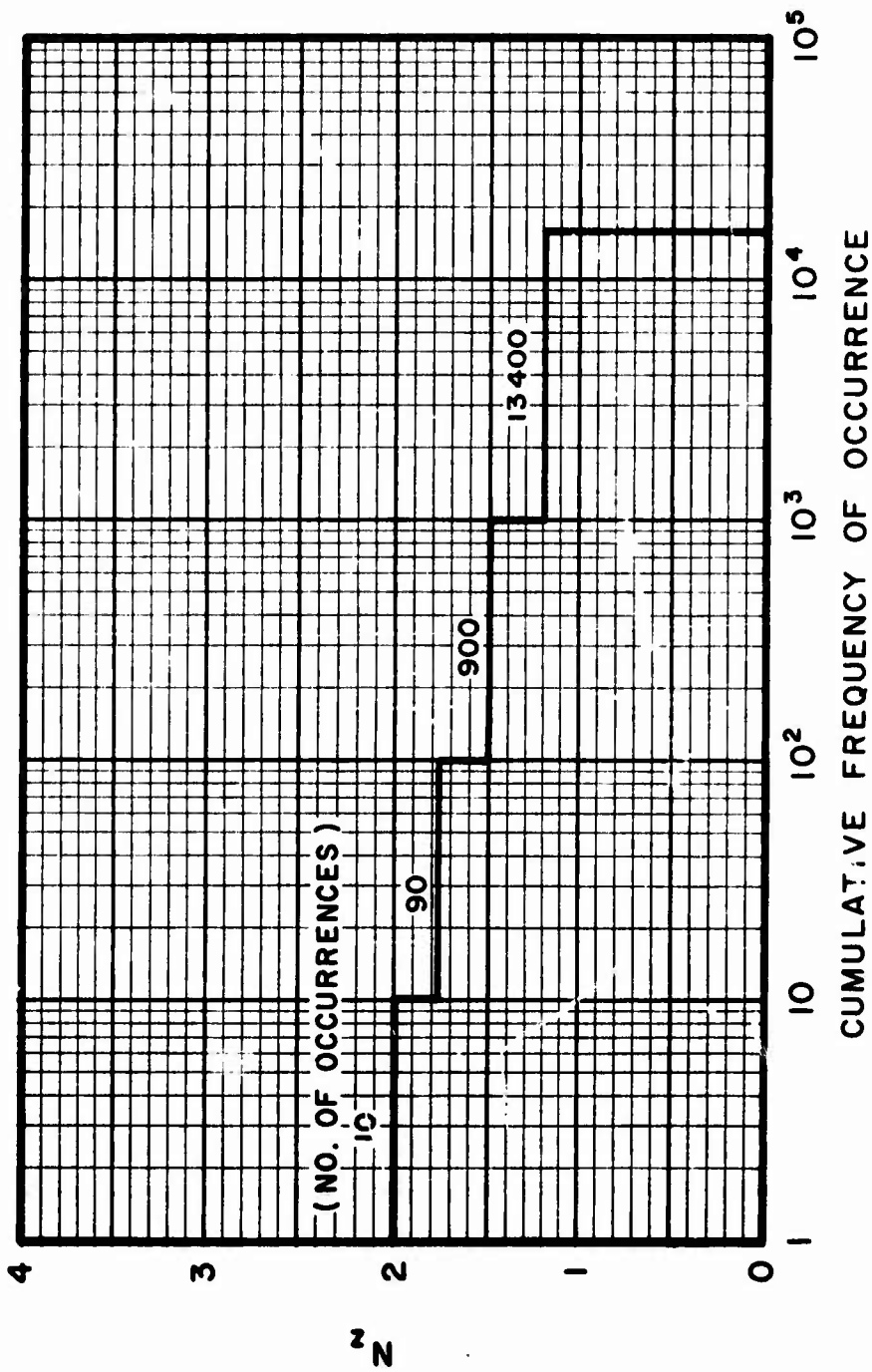


Figure 28. Load Factor Cumulative Frequency of Occurrences in Vertical Takeoff Maneuvers for Aircraft Life = 3600 Hrs.

TABLE XIII. SUMMARY OF

Type of Condition	Cond. No.	No. of Cycles	Velocity (kn)	Load Factors			$\frac{\alpha_x}{\text{sec}^2}$
				N_x (g)	N_y (g)	N_z (g)	
<u>Flight</u>							
Symmetrical Dive + Pullout	1	4	184	.05	0	3.31	0
Symmetrical Dive + Pullout	2	32	197	.05	0	2.8	0
Symmetrical Dive + Pullout	3	324	207	.10	0	2.4	0
Symmetrical Dive + Pullout	4	1440	216	.10	0	1.97	0
Symmetrical Dive + Pullout	5	81800	216	.10	0	1.66	0
Vertical Takeoff	6	10	0	0	0	2.00	0
Vertical Takeoff	7	90	0	0	0	1.77	0
Vertical Takeoff	8	900	0	0	0	1.5	0
Vertical Takeoff	9	13400	0	0	0	1.2	0
Hovering Turns	10	10	0	0	0	1.0	0
Hovering Turns	11	90	0	0	0	1.0	0
Hovering Turns	12	900	0	0	0	1.0	0
Hovering Turns	13	35000	0	0	0	1.0	0
<u>Landing</u>							
Level Landing F_x, F_z	14	18	0	1.107	0	3.082	0
Level Landing F_x, F_z	15	353	0	.675	0	2.142	0
Level Landing F_x, F_z	16	4039	0	.392	0	1.517	0
Level Landing F_x, F_z	17	9702	0	.235	0	1.133	0
Level Landing F_x, F_z	18	8	0	.338	$\pm .364$	1.401	± 8.61
Level Landing F_x, F_y, F_z	19	82	0	.192	$\pm .211$	1.091	± 5.00
Level Landing F_x, F_y, F_z	20	198	0	.117	$\pm .126$.918	± 2.98
Total No. of Cycles:							
Symmetrical Dive + Pullout					= 83600		
Vertical Takeoff					= 14400		
Hovering Turn					= 36000		
Landing					= 14400		

SUMMARY OF FATIGUE DATA (LIMIT LOADS)

Angular Accelerations			Rotor Loads (Aerodynamic)						Skid Loads		
$\frac{\alpha_x}{\text{sec}^2}$	$\frac{\alpha_y}{\text{sec}^2}$	$\frac{\alpha_z}{\text{sec}^2}$	F_x	F_y	F_z	M_{XH}	M_{YH}	M_{ZH}	Left and Right Skids (Landing Only)		
									F_x	F_y	F_z
0	1.0	0	- 753	0	37752	0	339039	0			
0	1.0	0	-1108	0	33258	0	221057	0			
0	1.0	0	- 651	0	27385	0	305458	0			
0	1.0	0	- 867	0	23622	0	186904	0			
0	1.0	0	- 851	0	20855	0	113069	0			
0	1.935	0	0	0	24000	0	342880	0			
0	2.003	0	0	0	21250	0	342880	0			
0	2.084	0	0	0	18000	0	342880	0			
0	2.173	0	0	0	14400	0	342880	0			
0	.834	0	0	0	12000	0	36000	100000			
0	.653	0	0	0	12000	0	36000	76000			
0	.417	0	0	0	12000	0	36000	50000			
0	.175	0	0	0	12000	0	36000	21000			
0	-3.06	0	0	0	8000	0	0	0	7130	0	14270
0	-1.86	0	0	0	8000	0	0	0	4360	0	8720
0	-1.08	0	0	0	8000	0	0	0	2525	0	5050
0	-.645	0	0	0	8000	0	0	0	1505	0	3015
±8.61	-.932	± .013	0	0	8000	0	0	0	2180	±2180	4360
±5.00	-.54	± .007	0	0	8000	0	0	0	1265	±1265	2530
±2.98	-.323	± .004	0	0	8000	0	0	0	755	± 755	1510

2

- 4) Six interchangeable servo assemblies
- 5) Highly reliable structural airframe and support fittings
- 6) Tail cone designed for quick removal and/or repair
- 7) Frangible birdcage nose cone to absorb crash loads

Directly related to the ability to maintain the aircraft with minimum personnel in the least amount of time under all environmental operating conditions is the attention given to design in providing adequate accessibility to components and systems. Many accessibility features have been designed into the airframe. The following high density maintenance areas have been made fully accessible by the use of doors, removable panels, or hinged covers.

- 1) Forward optics compartment nose-cone door hinges about upper horizontal hinge line, providing full access of optics systems.
- 2) Service doors on both sides of the airframe at the transmission level open to reveal the transmission and accessories, flight controls, tandem servos, and hydraulic systems packages.
- 3) Two-piece removable rotor/transmission mast cover plate for rotor/transmission removal.
- 4) Sliding doors on lower fuselage sides open to avionics components mounted with quick release mounts and plug-in connectors.
- 5) Quick replacement of all instruments by front access.
- 6) Interchangeable landing skids and forward shock strut.
- 7) Replaceable main rotor blades without need for special tools.
- 8) Engine access for normal servicing and inspection through top sliding door. Removable panel and tail cone for quick engine replacement.
- 9) Protected control rods under crew cabin floor accessible through floor panel.
- 10) Inspection panels for control bell cranks in tail cone and stabilizers.
- 11) Rotor tie and brake to prevent rotation when performing maintenance tasks on engine power train or blades.
- 12) Ground handling mobility by hydraulically actuated quick-attaching dolly wheels.

Specific allocations of reliability goals and maintainability demands for the dynamic systems have not been attempted at this point in the design stage. The simplicity of the design and the small number of power train, hydraulic, electronic, landing gear, and flight control components greatly reduce the maintenance burden and increase reliability. The airframe structure is expected to require no repair or maintenance other than repair of combat damage.

AIRCRAFT DESIGN AT ALTERNATE GROSS WEIGHTS

OBJECTIVE

The objective of the AARS alternate gross weights study was to establish the sensitivity of the design to changes in required useful load.

APPROACH

Useful load is defined as the sum of payload, usable fuel, and crew. Alternate AARS design points were evaluated at the established design useful load, $\pm 20\%$. This enabled generation of a useful load versus gross weight line.

The sensitivity of the AARS design to changes in useful load depends on the constraints on body interior volume. For example, additional passenger carrying capability implies expansion of the body envelope, whereas externally-mounted items such as armament or ordinance do not affect body size. Because the armored body weight forms a large proportion of the AARS gross weight, the sensitivity was analyzed for a number of ways of varying useful loads, including those producing smallest and largest sensitivities.

DISCUSSION

From Table II, the design useful load is 2893 pounds. Alternate design points were required therefore at useful loads of 3,439 and 2,293 pounds. The mathematical model used to generate the design aircraft parameters was rerun at different payload requirements. From this, useful load was plotted against gross weight, as shown in Figure 29. The three lines on Figure 29 represent three interpretations of the change in useful load:

- (1) Variable body size incurred by changing number of passengers
- (2) Variable body size incurred by changing payload
- (3) Constant body size

The design rotor disc loading of 9.79 psf was preserved for this study. For line (a), it was estimated that 15 inches of body length can be removed when the requirement to accommodate two passengers is removed. This corresponded to 24 square feet of armor. Some space behind the crew seats would still be available for equipment and for easy access to the midsection. A weight statement for an aircraft with no passengers and a useful load of 2,293 pounds is given in Table XIV. Figure 30 shows a drawing of this aircraft. Table XV gives a weight statement at a useful load of 3,439 pounds with 4

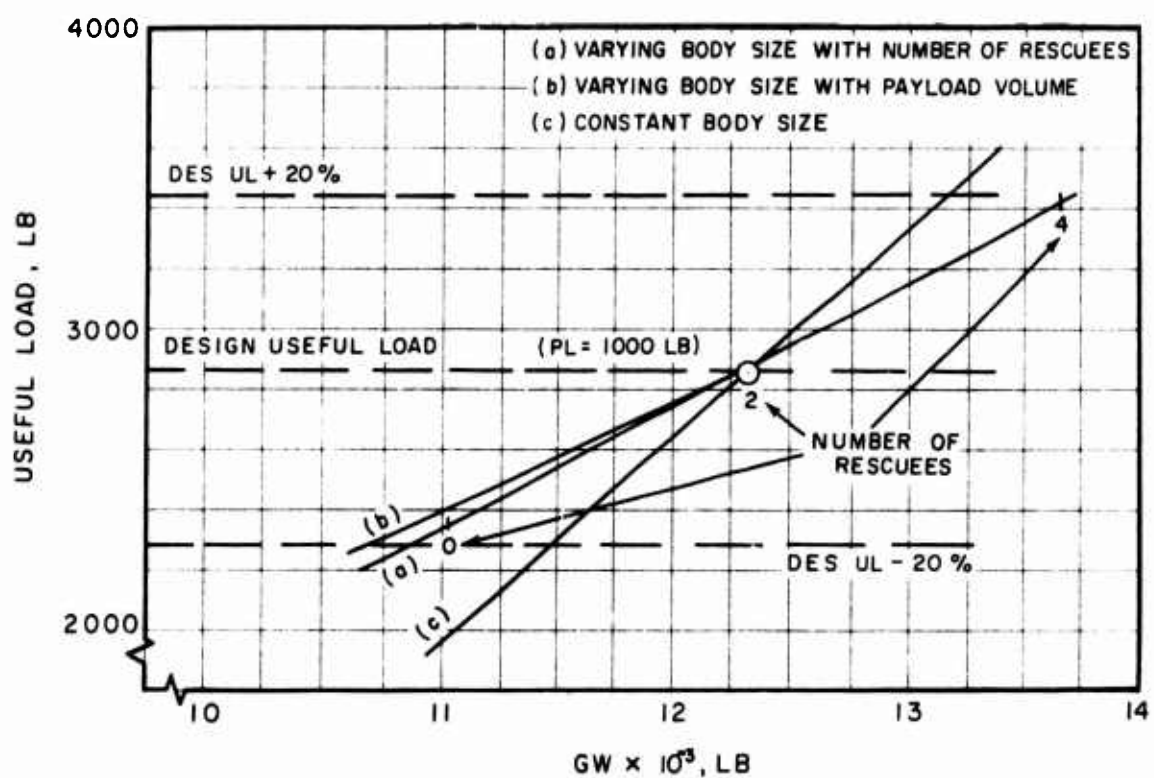
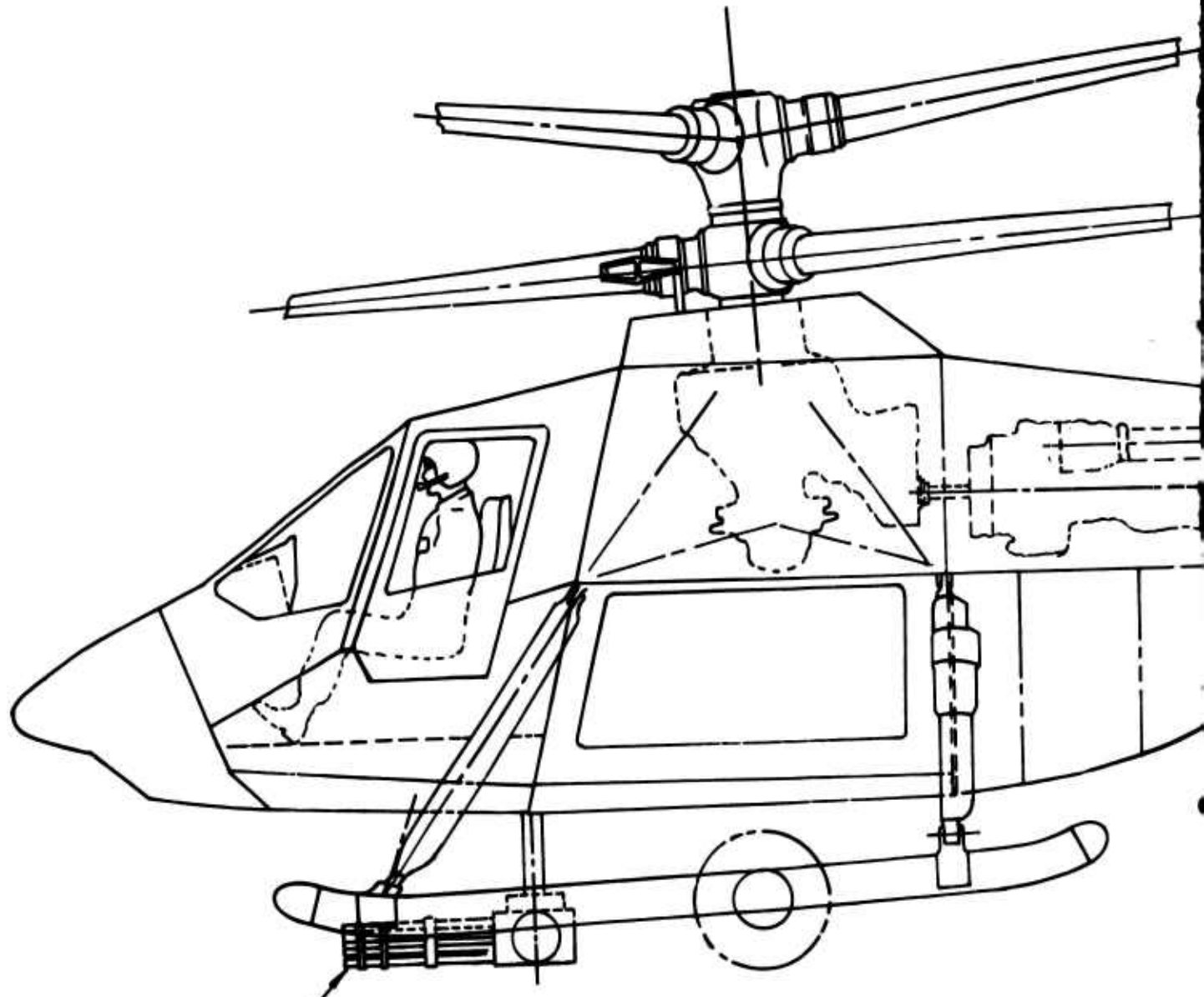


Figure 29. Useful Load Vs Gross Weight.

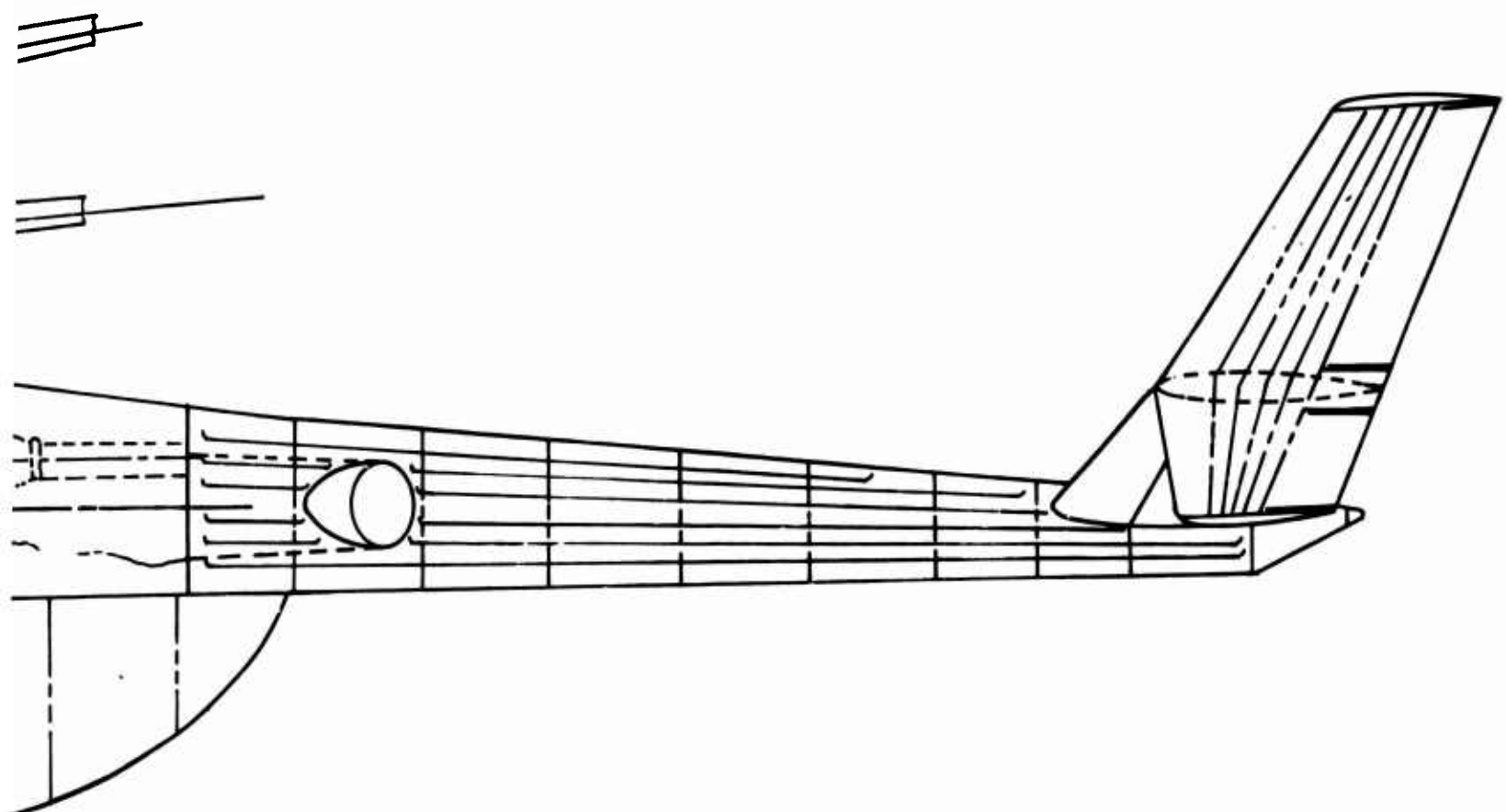
TABLE XIV. AARS ALTERNATE DESIGN WITH NO PASSENGER CAPABILITY

Group	Weight (lb)
Main Rotor Group	1012.
Wing Group	0.
Tail Group	203.
Tail Rotor/Fan	0.
Tail Surfaces	203.
Body Group	3992.
Alighting Gear	425.
Flight Controls	492.
Engine Section	57.
Propulsion Group	1636.
Engines	475.
Air Induction	9.
Exhaust System	9.
Lubricating System	0.
Fuel System	245.
Engine Controls	44.
Starting System	38.
Auxiliary Propulsion Propellers	0.
Drive System	816.
Auxiliary Power Unit	0.
Instruments	111.
Hydraulics	36.
Electrical Group	275.
Avionics	258.
Furnishings	222.
Air Conditioning and Anti-Ice	45.
Auxiliary Gear	10.
Vibration Suppression	0.
Technology Savings	-155.
Contingency	0.
Weight Empty	<u>3618.</u>
Fixed Useful Load	427.
Pilot	200.
Copilot	200.
Oil-Engine	4.
-Trapped	3.
Fuel-Trapped	20.
Payload	573.
Rescuees	0.
Armament	245.
Mission Equipment	328.
Fuel-Usable	1320.
Gross Weight	10939.



BELLY-MOUNTED MINI-GUN
(SHOWN DEPLOYED)

Figure 30. AARS Alternate Configuration, No Passengers,
GW = 10900 lb , Rotor Radius = 18.85 ft.



)

2

passengers. It was estimated that a 15-inch extension to the passenger compartment would permit outward-facing seating in the manner shown in Figure 31. The slope of this line is 0.41 pound of useful load per pound of gross weight. For line (b) of Figure 29, the two-passenger requirement was retained, but the payload container volume (the lower fuselage midsection) was made a function of payload weight, assuming a uniform constant payload density. The change in armor area was evaluated from the assumption that surface area varies as the 2/3 power of volume or weight.

For line (c) of Figure 29, body size was assumed constant; that is, useful load could be increased within the confines of the design configuration. This yielded a slope of 0.68 pound of useful load per pound of gross weight.

Trending of all weight parameters was properly accounted for, as defined in the mass properties section. Also, transmission and engine housing volumes were always adjusted to account for their size, trended from the design configuration as functions of horsepower ratings.

As useful load includes fuel, increased useful load can be achieved by extending the mission endurance time, here defined as the total spent loitering on station. Figure 32 shows a plot of gross weight versus payload and endurance with lines of constant useful load. Constant body size was assumed. It is shown that 20% increase in useful load, at constant payload, enables an increase of 65 minutes in endurance over a nominal 90 minutes.

A 20% increase in useful load can also be achieved with additional external ordnance. A suggested configuration of armament is shown in Figure 33, and consists of two XM-157 rocket pods, holding 7 rockets apiece and weighing 210 pounds total, with a belly-mounted gun replacing the XM-27 used in the initial design configuration.

Figure 34 shows the relationship between gross weight and armor thickness, assumed constant over the same body size as the aircraft shown in Figure 1.

DETAILED STRUCTURAL ANALYSIS

OBJECTIVE

The objective of the AARS detailed structural analysis study was to determine the internal load and stress distributions within the center section of the fuselage for all critical load cases. In addition, fatigue crack propagation analysis was to be performed for critical regions in and away from the heat-affected zones of the dual hardness steel and for evaluation of structural integrity of the various fittings.

APPROACH

The two large access doors and the engine air intake opening in each side plus the transmission opening on the top make for complex internal load paths. In order to provide satisfactory structural integrity for this design, NASTRAN (NASA Structural Analysis), a large general-purpose finite element computer program, was used for the analysis.

TABLE XV. AARS ALTERNATE DESIGN WITH CAPACITY FOR FOUR PASSENGERS

Group	Weight (lb)
Main Rotor Group	1253.
Wing Group	0.
Tail Group	234.
Tail Rotor/Fan	0.
Tail Surfaces	234.
Body Group	4665.
Alighting Gear	518.
Flight Controls	593.
Engine Section	72.
Propulsion Group	2114.
Engines	598.
Air Induction	11.
Exhaust System	11.
Lubricating System	0.
Fuel System	299.
Engine Controls	54.
Starting System	46.
Auxiliary Propulsion Propellers	0.
Drive System	1095.
Auxiliary Power Unit	0.
Instruments	111.
Hydraulics	36.
Electrical Group	275.
Avionics	258.
Furnishings	252.
Air Conditioning and Anti-Ice	45.
Auxiliary Gear	10.
Vibration Suppression	0.
Technology Savings	-202.
Contingency	0.
Weight Empty	<u>10233.</u>
Fixed Useful Load	427.
Pilot	200.
Copilot	200.
Oil-Engine	4.
-Trapped	3.
Fuel-Trapped	20.
Payload	1439.
Rescuees	800.
Armament	245.
Mission Equipment	394.
Fuel-Usable	1621.
Gross Weight	13720.

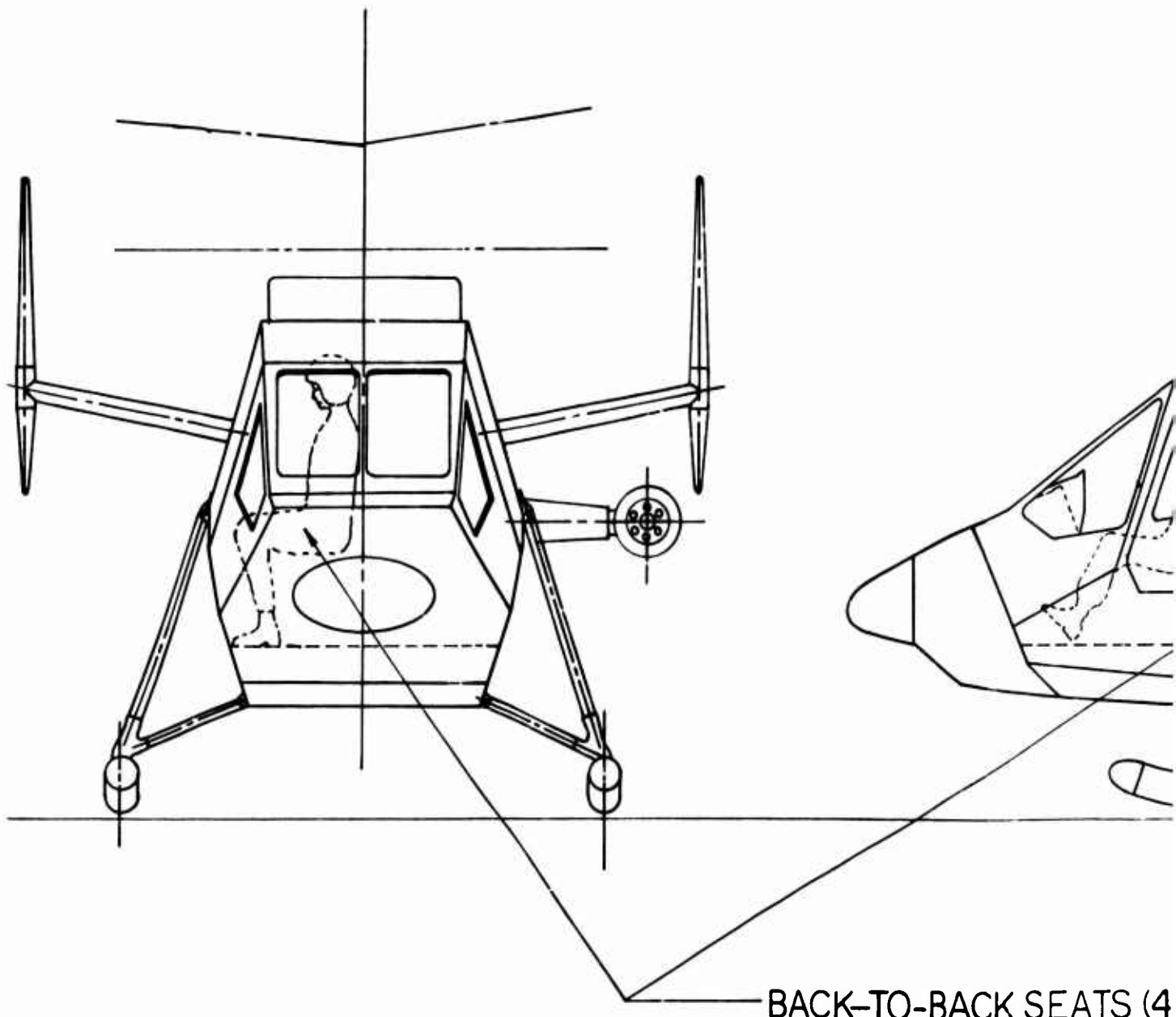
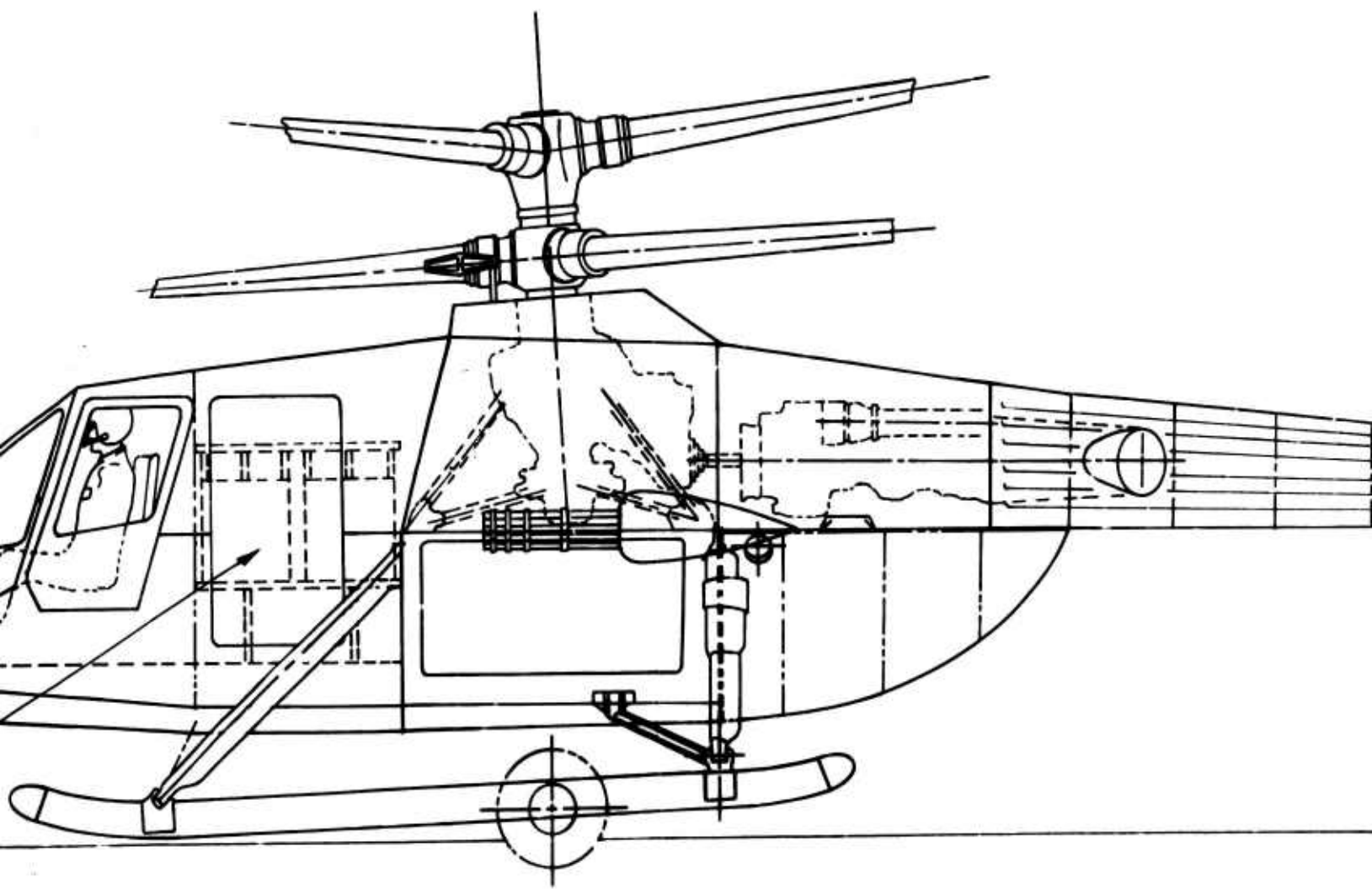
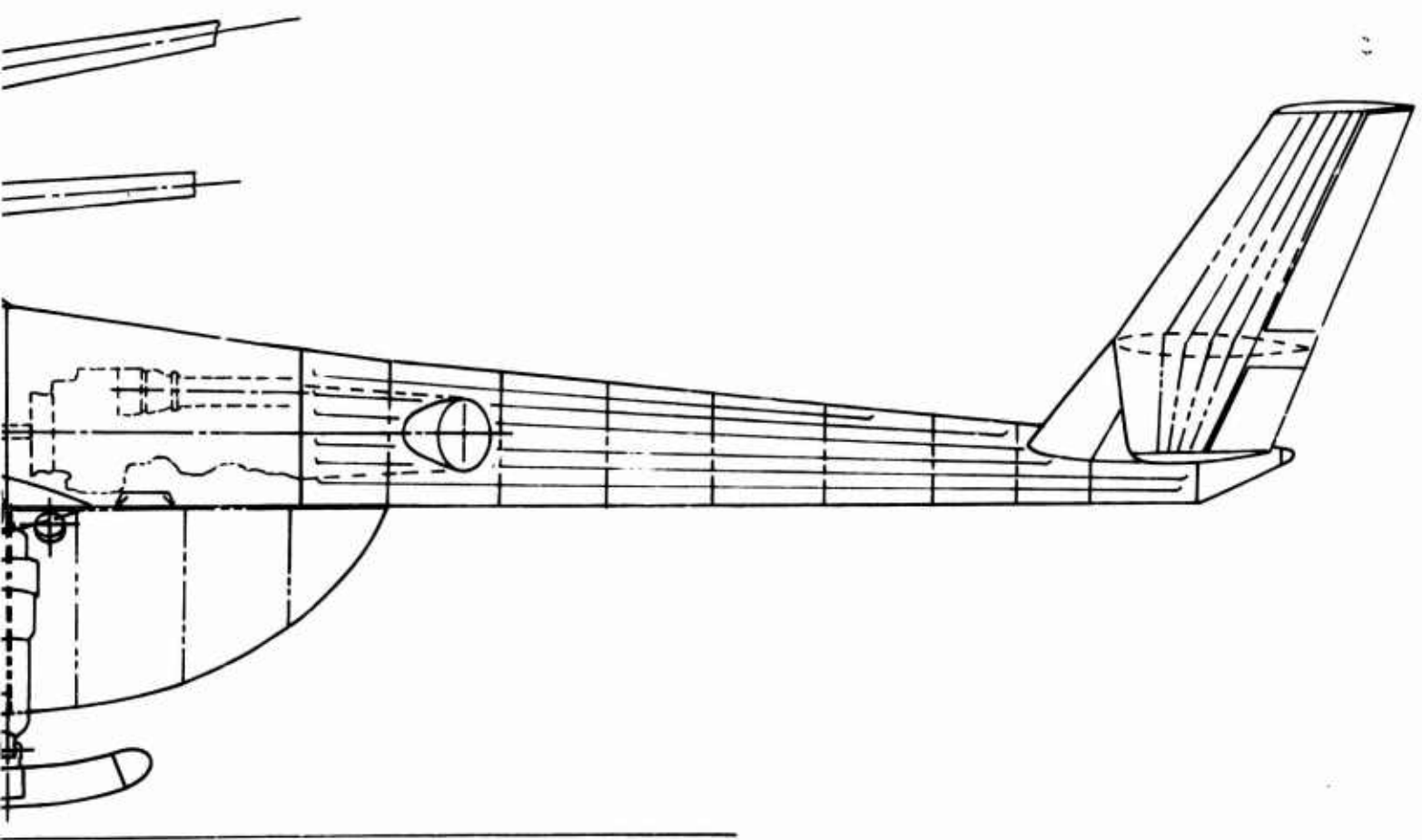


Figure 31. AARS Alternate Configuration, Four Passengers,
GW = 13720 lb , Rotor Radius = 21.15 ft.



TS (4)



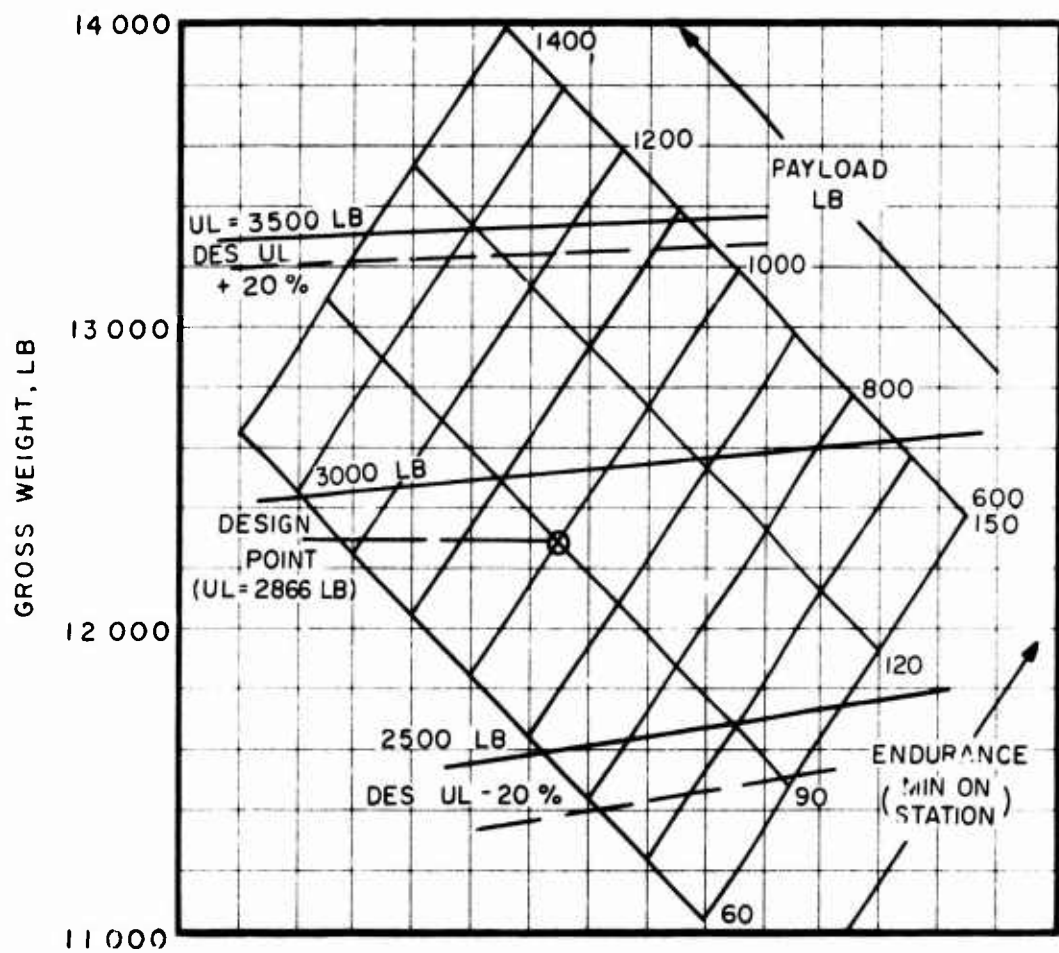


Figure 32. Gross Weight Vs Payload and Endurance.

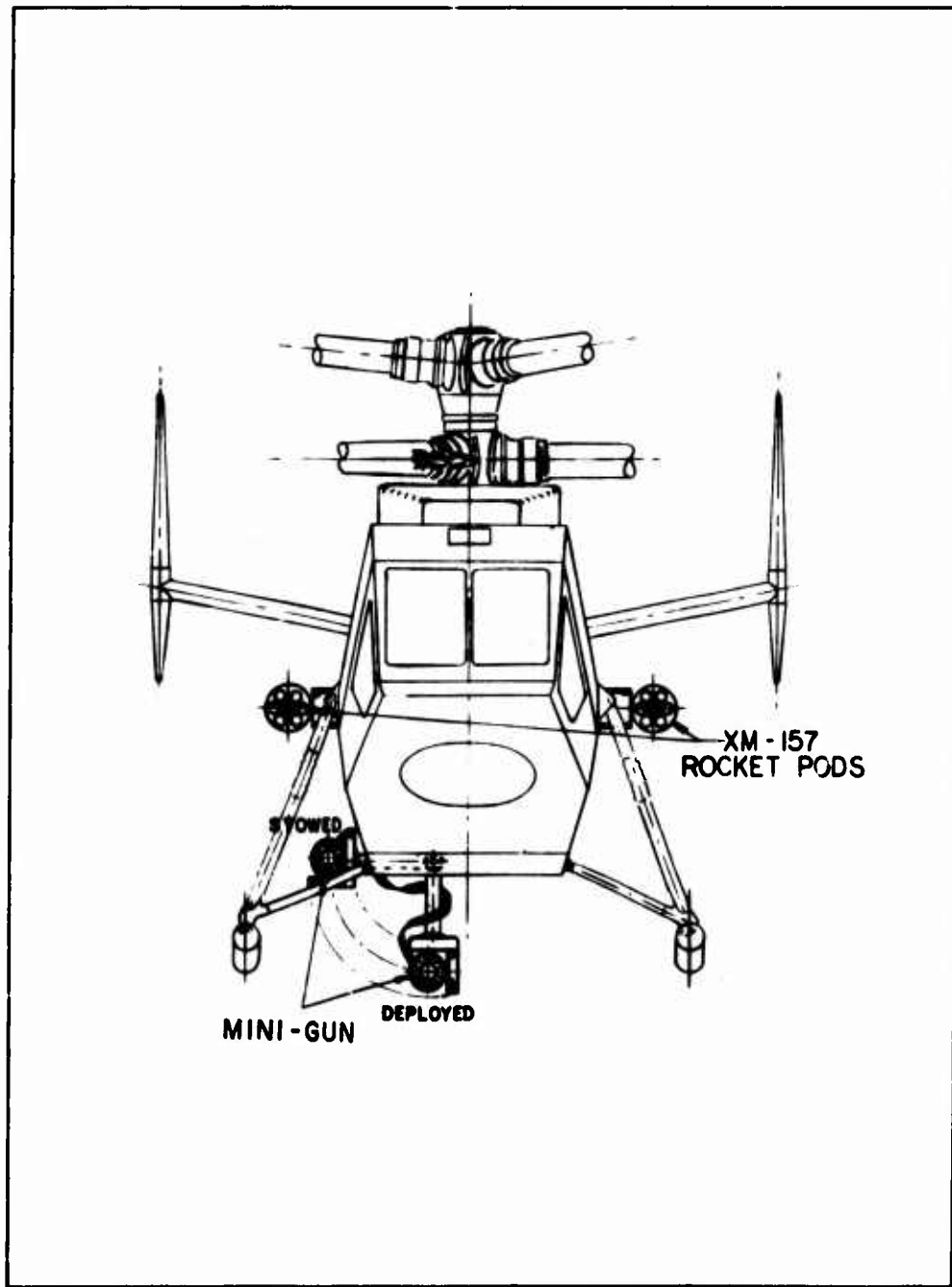


Figure 33. Alternate Armament Configuration at Increased Gross Weight.

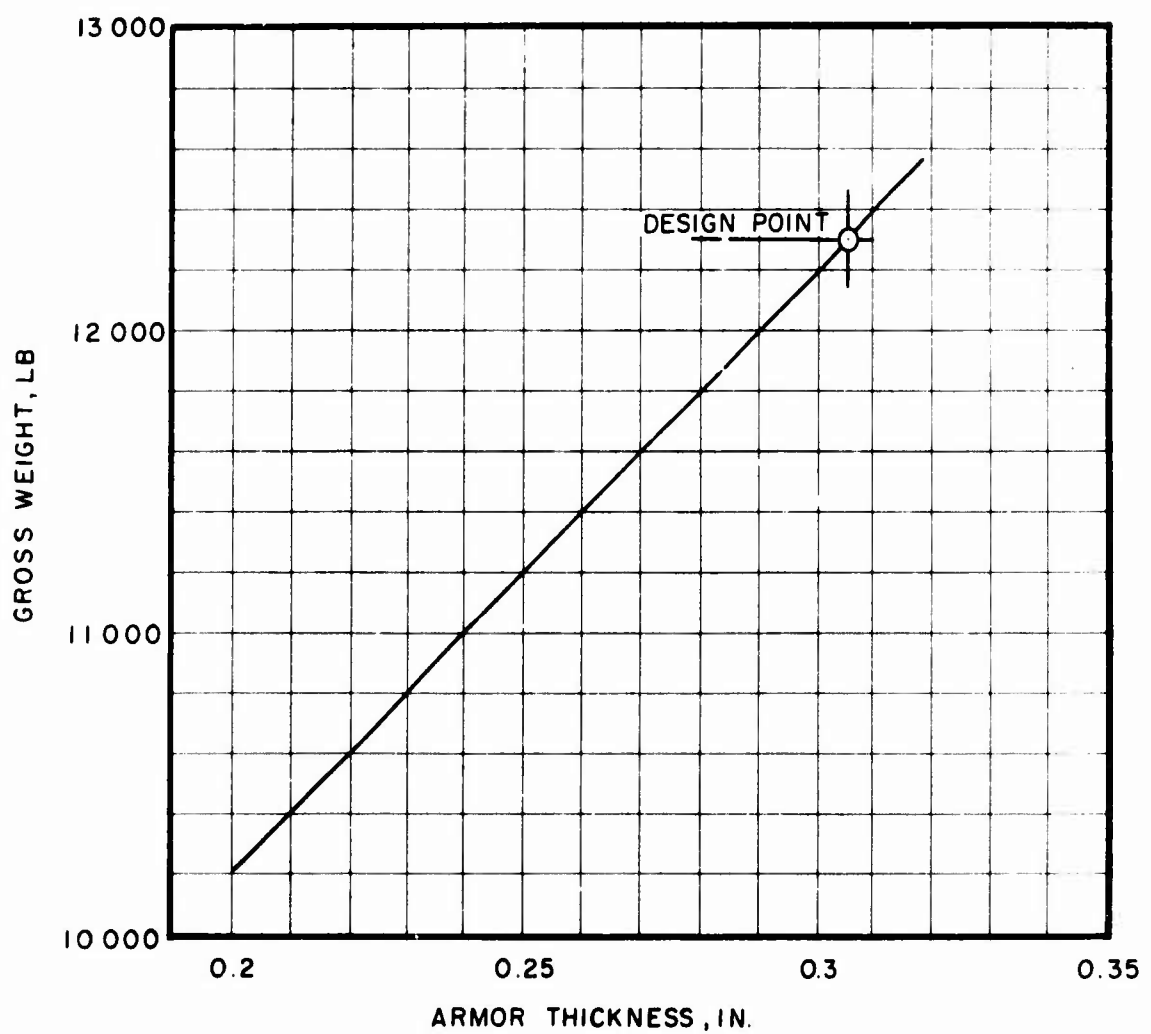


Figure 34. Gross Weight Vs Armor Thickness.

So that symmetric and unsymmetric load conditions could be analyzed, it was necessary to model the entire structure rather than half. As this doubled the number of elements in the structural model, it was necessary to model the regions around the two large access doors with a limited number of beam or bar elements rather than many plate elements. This reduced the total number of degrees of freedom, the band width, and computation time to a value that provided sufficient degrees of freedom for a satisfactory solution to the structure.

From the finite element stress output, critically stressed regions of the fuselage were selected, and the stress and load values were used in fatigue, crack propagation, and fitting analyses. Crack propagation test data were refined by use of a computer program that provides the best statistical fit of Forman's equation through the data points.

All fittings providing attachment of the transmission and landing gear struts to the fuselage were analyzed for fatigue.

DISCUSSION

Finite Element Analysis

A sketch of the center section test specimen is shown in Figure 35. A finite element model of this structure was created to be compatible with NASTRAN. The model included idealizations of simulated landing gear, rotor shaft, and transmission support structures to be used in test. Also modeled were the forward and aft loading tabs and the beams connecting the structure to its reaction points. It was necessary to include this backup structure in the model to represent all stiffness paths to load application and reaction points. These details were included to represent the coupling between the center section and its backup structure.

Rods are used in the model (Figure 36) to represent transmission struts, landing struts, and the forward tension tie. Bars are used for the dummy transmission and rotor shaft, landing skids, and reaction beams. Bars are also used to model the armor plate and associated stiffeners surrounding the transmission and avionics access openings and the upper portion of the aft bulkhead. All large areas of armor plate are modeled by plate elements, as illustrated by the shaded portions of Figure 35. The resulting model consisted of 938 elements connected at 729 nodes, providing 3750 degrees of freedom.

Figure 37 illustrates the detail of bar elements used to represent the armor plate and stiffeners. As indicated by the section drawings, node points are not coincident with the neutral axes of the beams. In the case of section B-B and E-E, there is a substantial offset. This arises from the requirement that node points must be on the skin line to define plate element mid-planes.

To represent these bar elements, the following modeling procedures were followed:

1. Neutral axes of elements were located by offsets from their

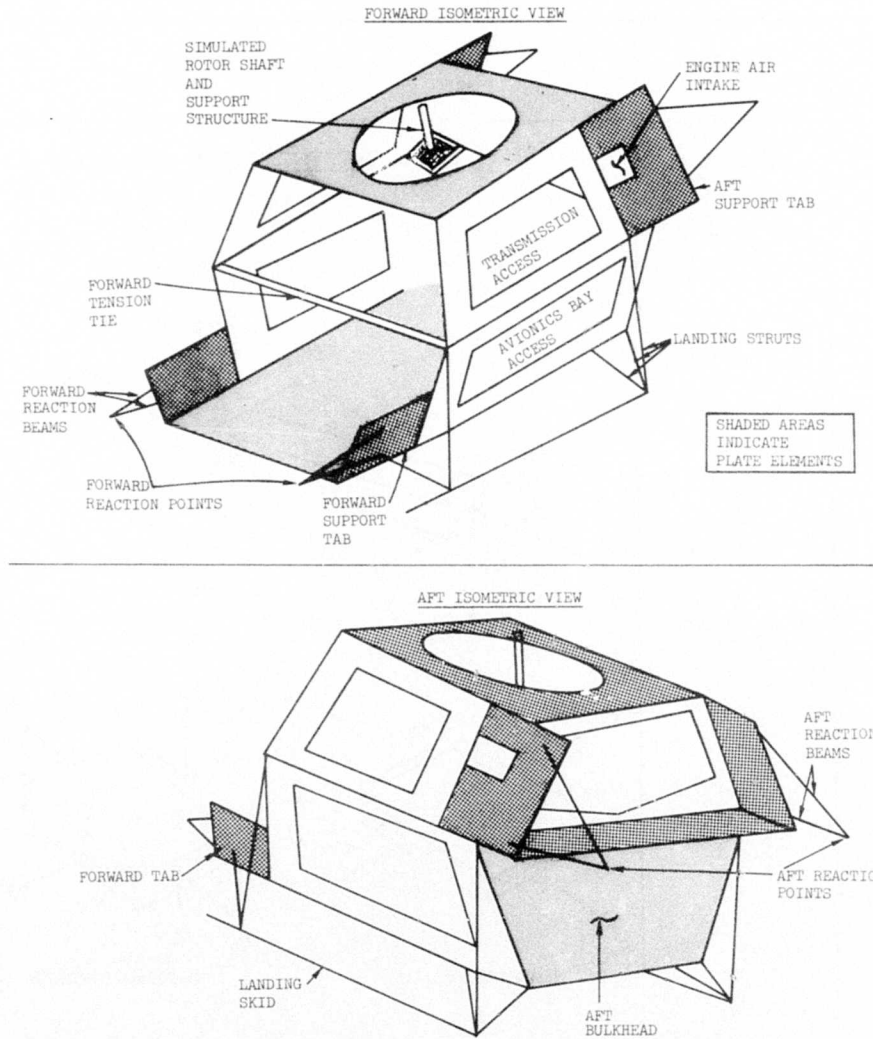


Figure 35. AARS Center Section Test Specimen.

ELEMENT	COORDINATE SYSTEM	ELEMENT FORCES
ROD		
BAR		
PLATE		

Figure 36. NASTRAN Finite Elements in AARS Model.

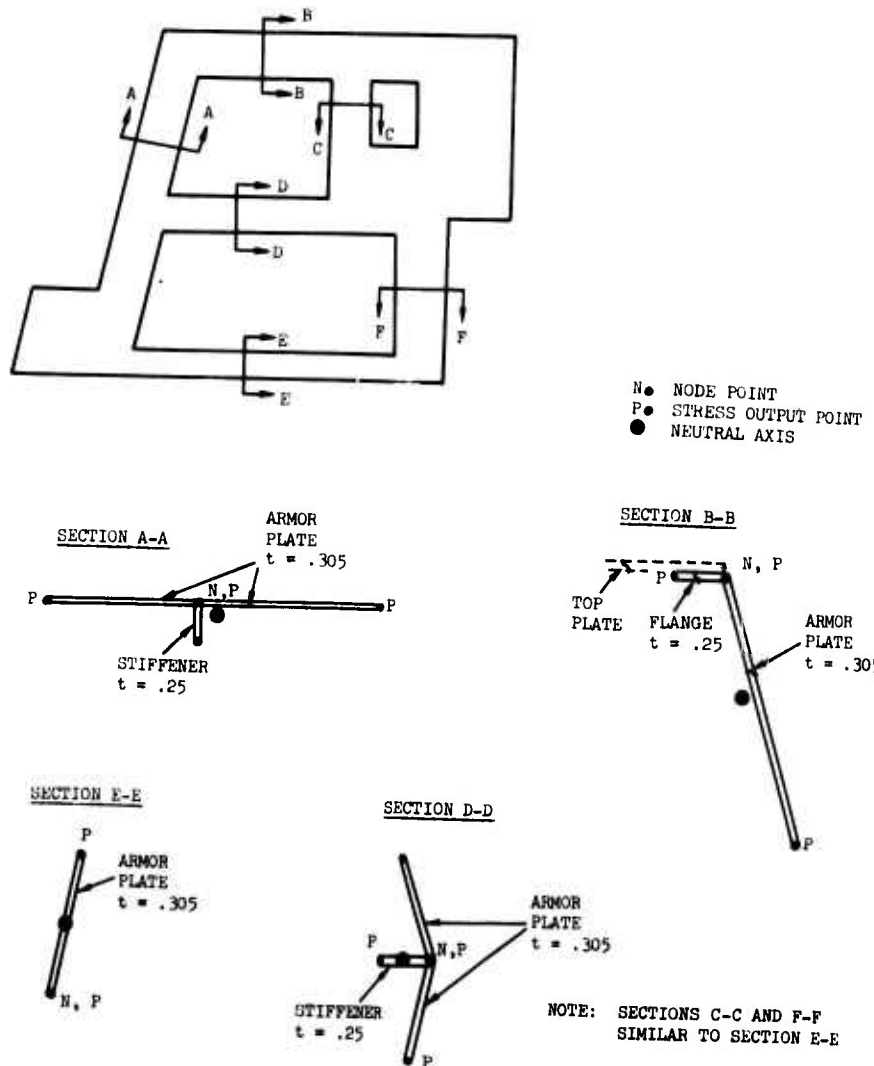


Figure 37. Detail of Beam Elements in AARS Finite Element Model.

node points.

- 2 Bending inertia of the elements was calculated with respect to their respective neutral axes.
3. Fiber distances from neutral axes to critical points in the cross section were measured for the purpose of stress determination. Stress output points are indicated by the symbol P in Figure 37.

Quadrilateral and triangular plate elements were used in modeling the large armor plate areas of the AARS center section (the shaded portions of Figure 35). Quadrilateral elements were used in the majority of these regions for ease of input and output interpretation. Triangular elements were used in areas where the nodal gridwork was refined and where required by the structural geometry. As an example, Figure 38 shows modeling details in the region of the engine air inlet and aft loading tab. Triangular elements are used to refine the nodal gridwork in the region of the reaction beam pickup points. Triangles are also used to introduce a three-element breakup through the depth of the plate running across the top of the air inlet. At least three quadrilateral elements are required to define the inplane bending in this portion of the structure.

After completion of the finite element model, the task of describing this idealization to the NASTRAN computer program was accomplished. Due to a mathematical idiosyncrasy of the finite element plate bending elements, it was necessary to guarantee that the coordinates of all points on a flat plate in the structure be determined accurately. The computer feature of the APS Numerical Control Design program was used to check that the coordinates of all points on a flat plate in the structure were determined accurately. Two coordinates for each node, from projected views of the plates, were supplied to the program, which calculated third coordinates in the structural system (station, waterline, buttline).

Figures 39 and 40 illustrate two portions of the structure before and after editing. Figure 39 shows models of the roof plate of the center section. The error was caused by an incorrect sign on a node point buttline coordinate. Figure 40 shows views of the aft support tab and engine air intake on the left-hand side of the structure. A faulty node point station coordinate was corrected from the Cathode Ray Tube keyboard. After four 1-hour sessions at the tube console, the entire AARS model was visually checked, corrected, and rechecked.

Following completion of the data check, a static stress analysis was performed using the NASTRAN computer program. Results were obtained for a total of 21 load conditions. This included nine maneuver loads plus twelve unit loads to construct additional cases as required. The inclusion of a complete set of unit loads allows stresses to be obtained for new load conditions without costly reruns of the analysis.

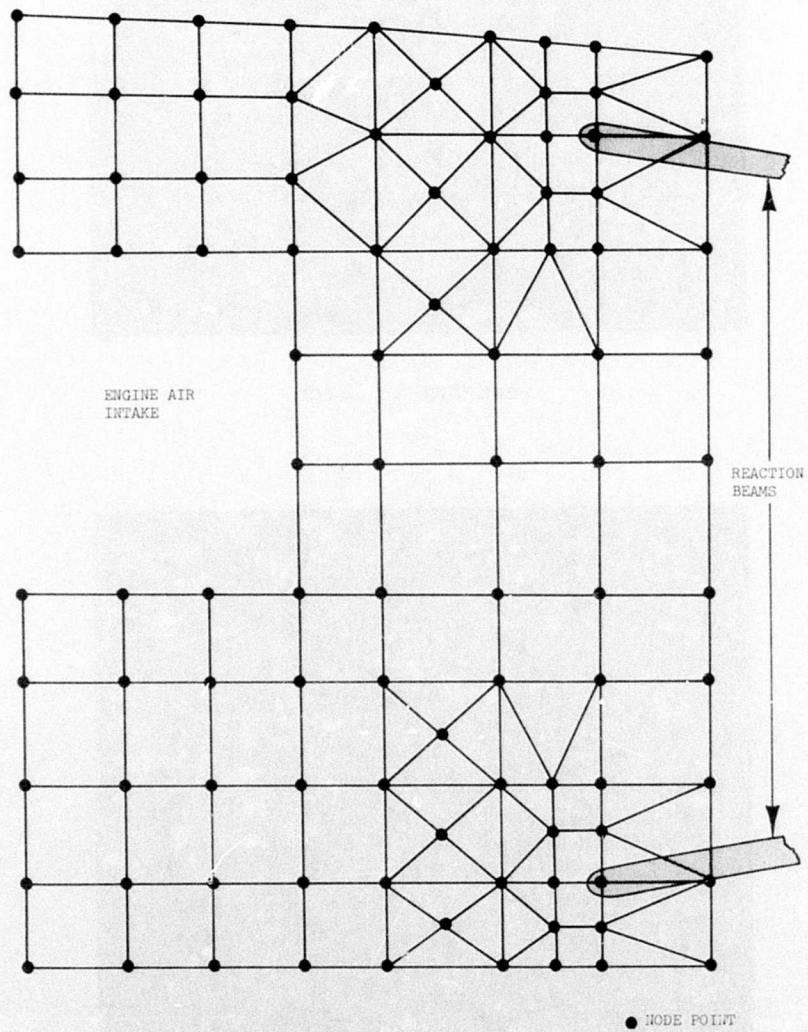
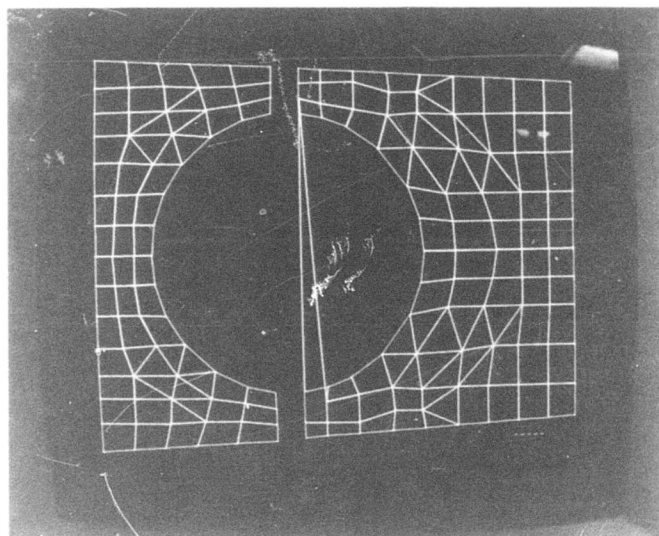
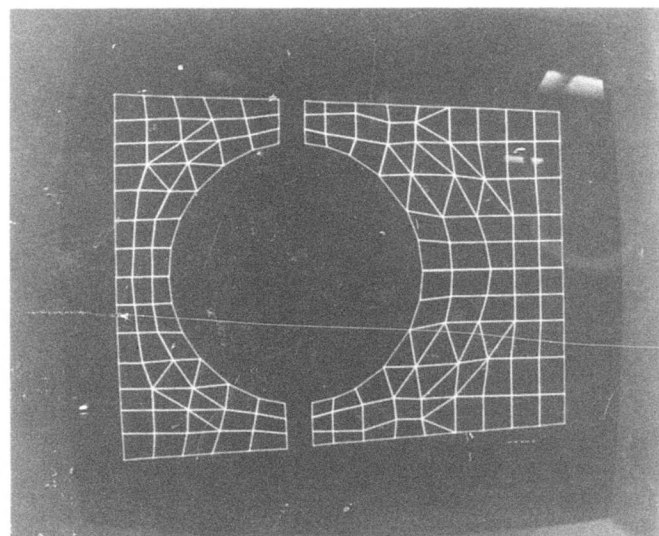


Figure 38. Plate Gridwork in AARS Aft Support Tab Design.

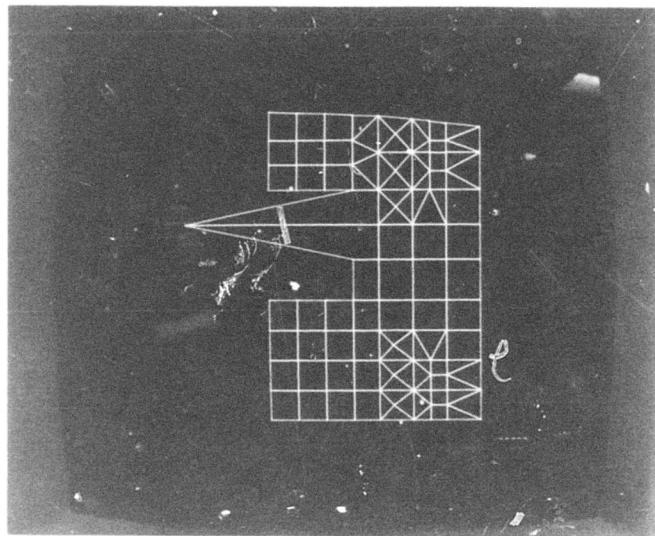


Geometry in Error

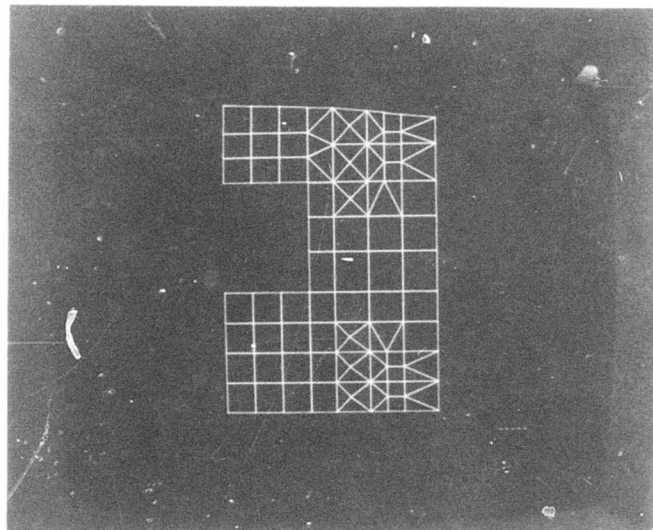


Error Corrected

Figure 39. Structural Model of AARS Roof Plate.



Geometry in Error



Error Corrected

Figure 40. Structural Model of Aft Support Tab and Engine Air Intake.

The NASTRAN program output for the AARS model consisted of the following items:

1. List of inputs
2. Error analysis
3. Reaction loads
4. Nodal displacements
5. Beam shears and moments
6. Beam and plate stresses

Negligible residual loads were obtained for the AARS model, indicating accurate results for the input model of the structure. As an additional check, equilibrium of applied and reaction loads was checked for a few randomly selected load cases. Negligible errors in equilibrium were calculated. As a final check, symmetrical load conditions produced symmetric displacements and reaction loads, and the magnitude and direction of these agreed with anticipated values. Figure 41 illustrates the displaced configuration of the structure for a symmetrical dive and pullout maneuver. Displacements have been magnified for clarity. The shape and continuity of the displaced configuration provide qualitative substantiation of both the model and applied loads.

Principal stresses for plate elements and fiber stresses for beam elements were examined in detail for the following load conditions:

<u>Condition No.</u>	<u>Load Condition</u>
1	Level flight - 180 knots
2	Symmetrical dive and pullout
3	Vertical takeoff
10	Level landing
15	Hovering turn
21	Park

Principal stresses are output at the centroid of each plate element at its inner and outer surface. Beam fiber stresses are output at the points on each beam element defined by the user for this purpose (Figure 37).

The stress distributions in the plate and bar elements for the symmetrical dive and pullout flight case are shown in Figures 42 and 43. This is typical information obtained for all other load cases. The element stresses shown in Figure 43 are not necessarily the maximum values but those at a consistent location of the cross section for continuity.

For every load condition shown above, the maximum stresses were found to occur in the bar elements surrounding the transmission and avionics access doors. Compressive stresses of the same magnitude as the maximum tensile

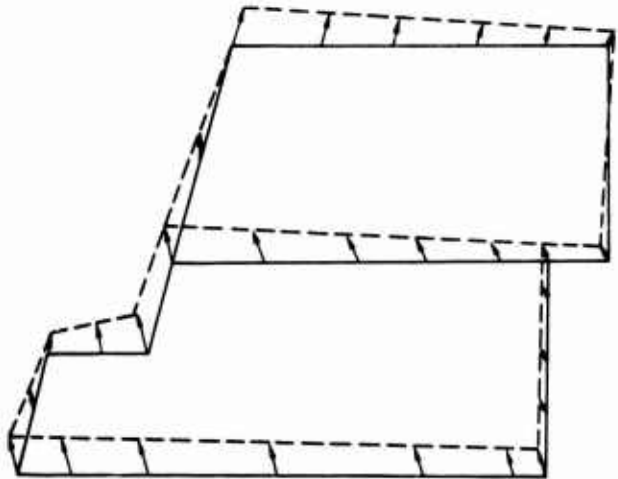


Figure 41. AARS (NASTRAN) Structural Displacements for Symmetrical Dive and Pullout - 216 Knots.

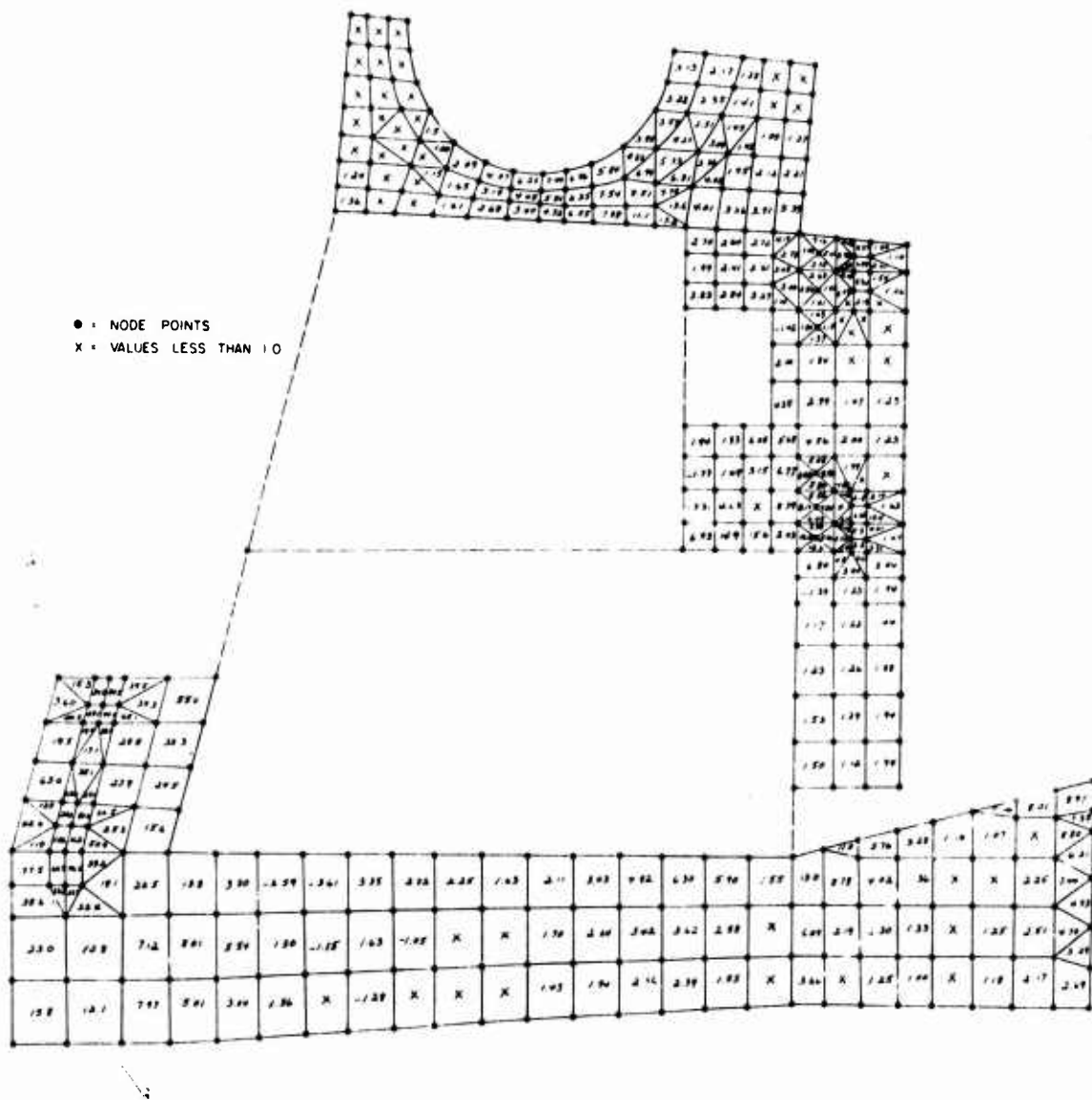


Figure 42. Maximum Principal Stresses (KSI) in Plate Elements, Symmetric Dive and Pullout (216 Knots).

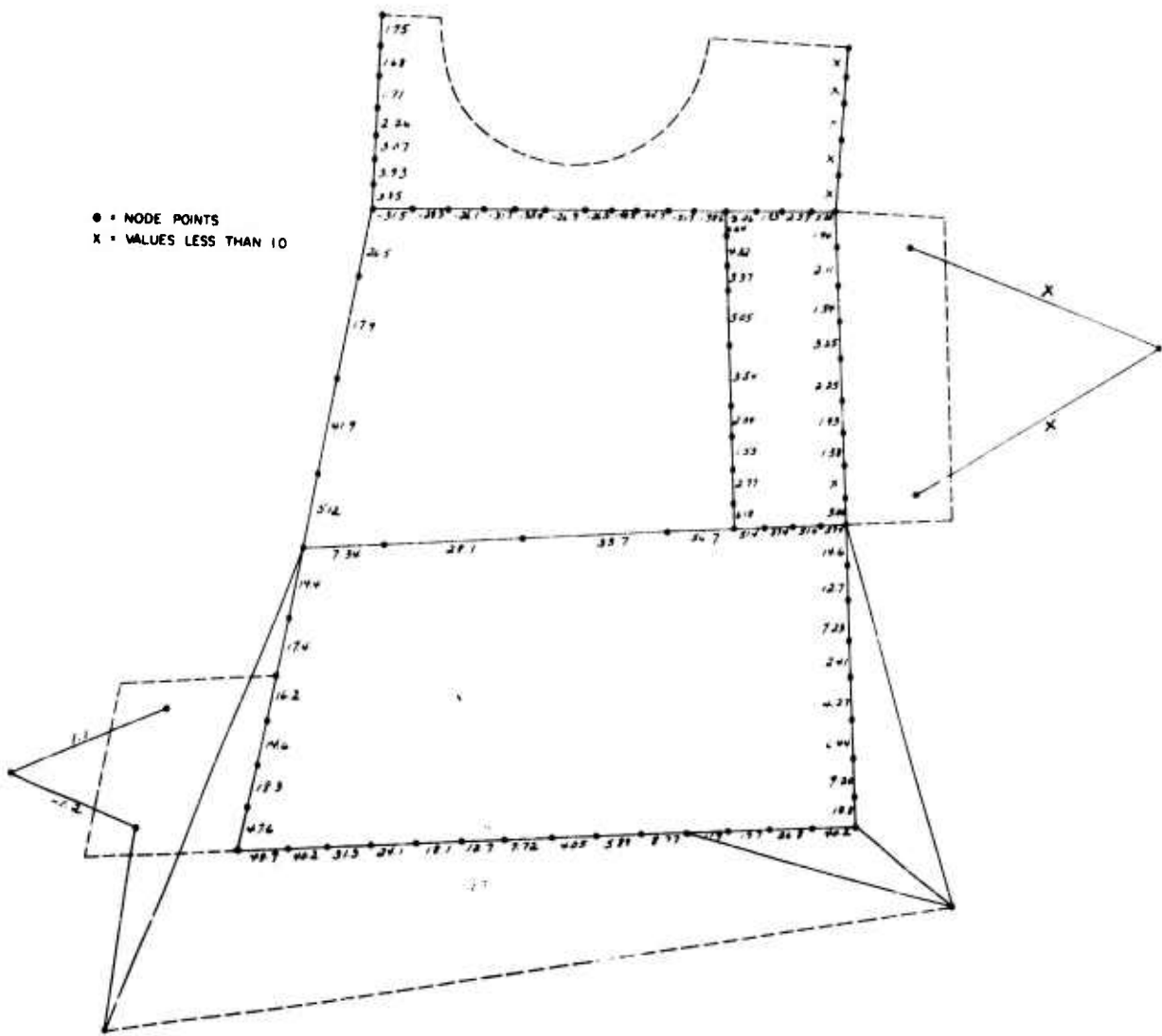


Figure 43. Bending Stresses (KSI) in Bar Elements, Symmetric Dive and Pullout (216 Knots).

stresses were obtained in the analysis. The critical points were selected as being those regions where tensile stresses occurred. At these points the most damaging fatigue spectrum occurred, and fatigue and crack propagation analysis was conducted.

Figure 44 illustrates the location of the eight critical stress points for the fatigue spectrum. Because all critical stresses were obtained in regions modeled by beam elements, no stress concentrations are included in the computer results. Table XVI shows the stresses at the 8 critical points for several flight conditions. These stresses include concentration factors for local geometry effects.

The stresses resulting from level flight, symmetrical dive and pullout, and vertical takeoff are similar at these critical points. This fact may be of advantage in simplifying the fatigue spectrum in test by reducing the number of distinct loads that must be applied.

Fatigue and Fracture Analysis

Critically stressed areas of the AARS airframe, as defined by the NASTRAN finite element analysis, were analyzed to determine the crack initiation time (i.e., fatigue life) of the undamaged structure, and the crack propagation time (i.e., residual life) of the structure after sustaining ballistic damage. These analyses are based on the fatigue and crack propagation data given on pages 126 to 145 of this report. The methodology for fatigue analysis is similar to that presented in Reference 10, and the crack propagation analysis is based on Forman's equation (Reference 11) and the methodology presented in References 12 and 13.

The fatigue methodology presented in Reference 10 is based on fatigue constant life diagrams. Constant life diagrams for the undamaged base and welded materials were therefore constructed from the generated fatigue test data. This was accomplished by fitting a standard fatigue curve shape for steel through the fatigue data for stress ratio $R = 0.1$ (test value) and then using this curve and the material ultimate strength to obtain the straight line constant life diagrams shown in Figures 45 and 46.

The nominal mean and vibratory stresses at each of the eight critical stress site (Figure 44) were determined from the maximum nominal stresses as calculated by the NASTRAN finite element analysis. The nominal mean stress at each stress site was defined as the mean value of the maximum stresses at that site weighted by the percent time of occurrence of each flight condition. The nominal vibratory stress at each stress site for each flight condition was then defined as the difference between the nominal maximum stresses and the calculated mean stress for that stress site. The resulting nominal mean and vibratory stresses are presented in Table XVII.

For a variable stress environment, as exists in the AARS, the fatigue life is calculated by employing Miner's cumulative damage rule. In equation form, Miner's rule is given by

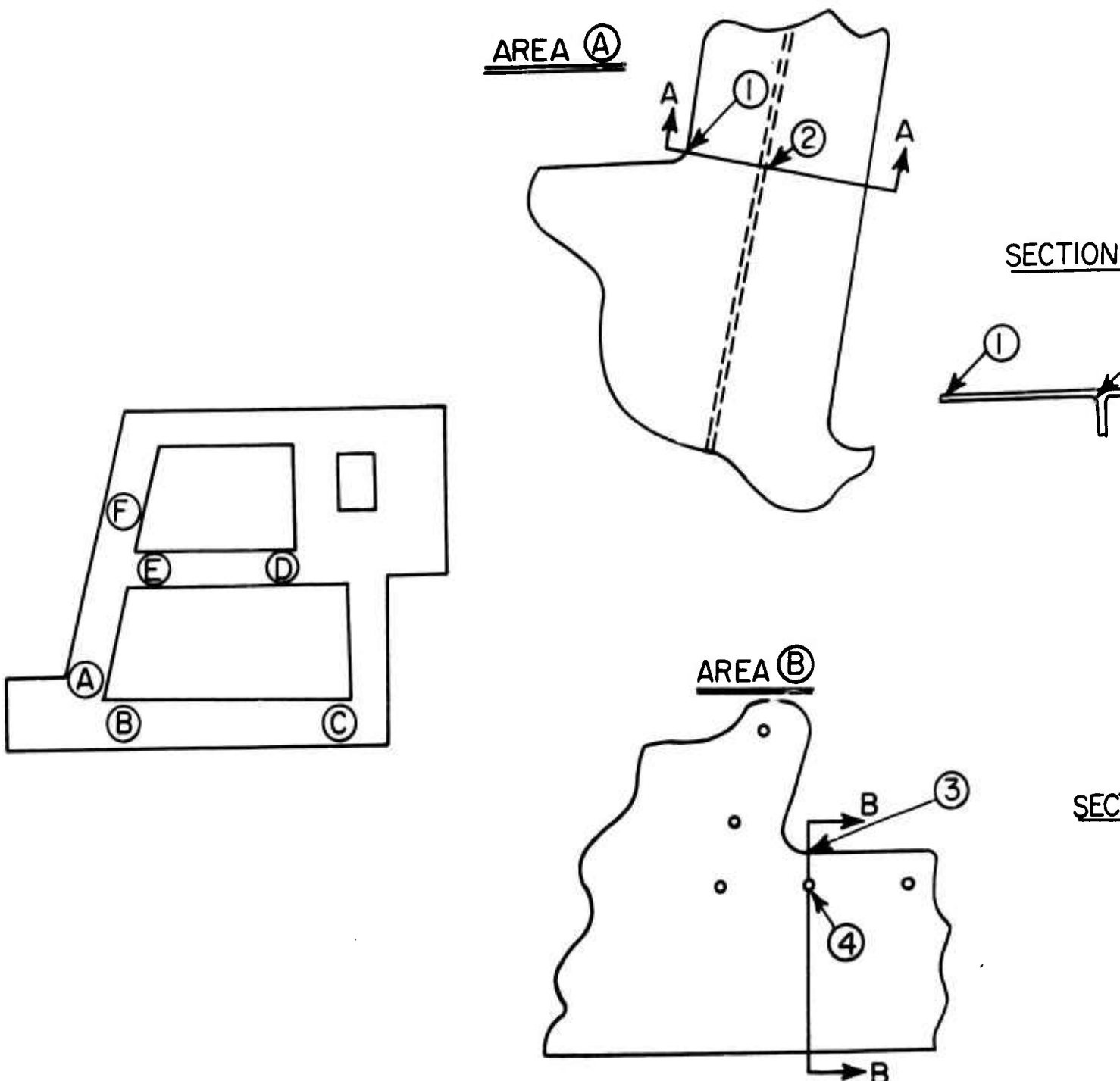
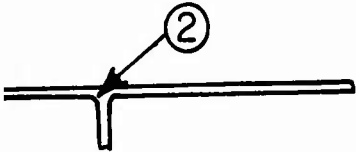
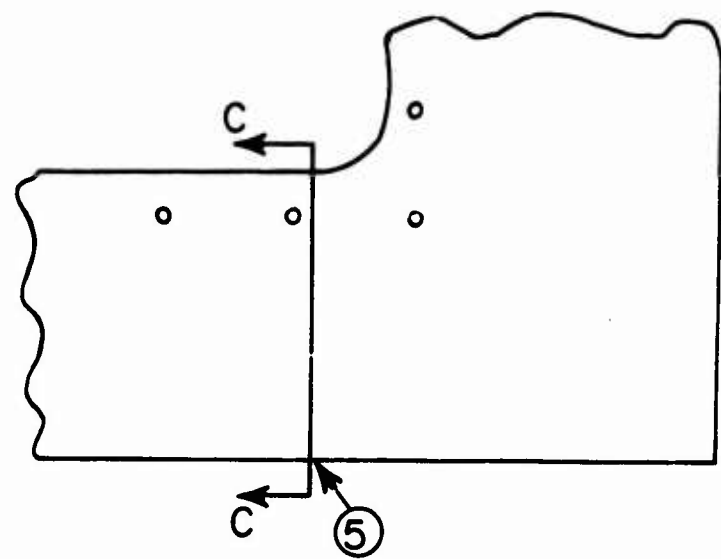


Figure 44. Critical Stress Areas - AARS Center Section.

SECTION A-A



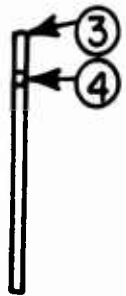
AREA C



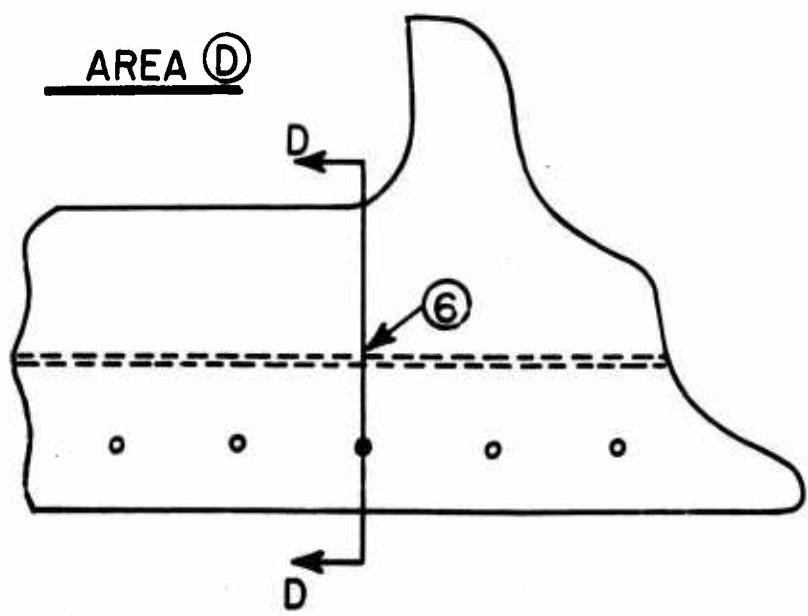
SECTION C-C



SECTION B-B



AREA D



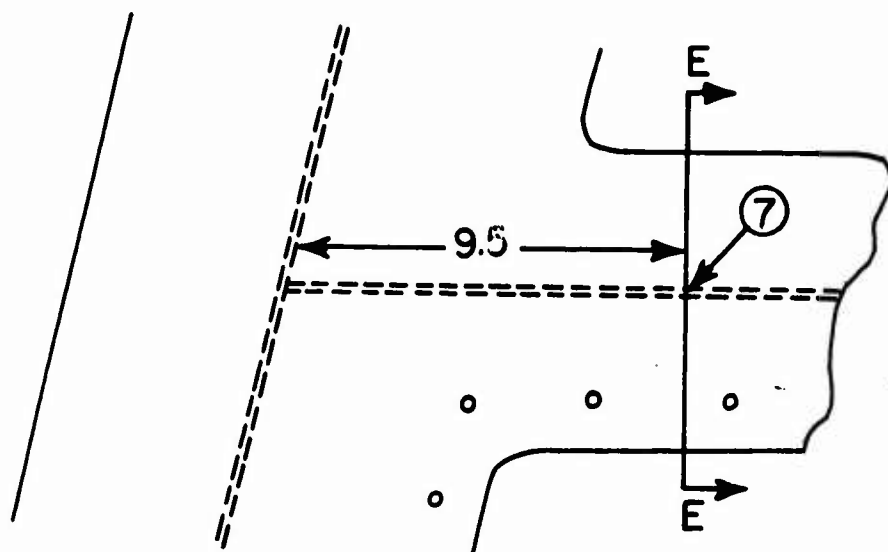
SECTION D-D



AREA E

C

5



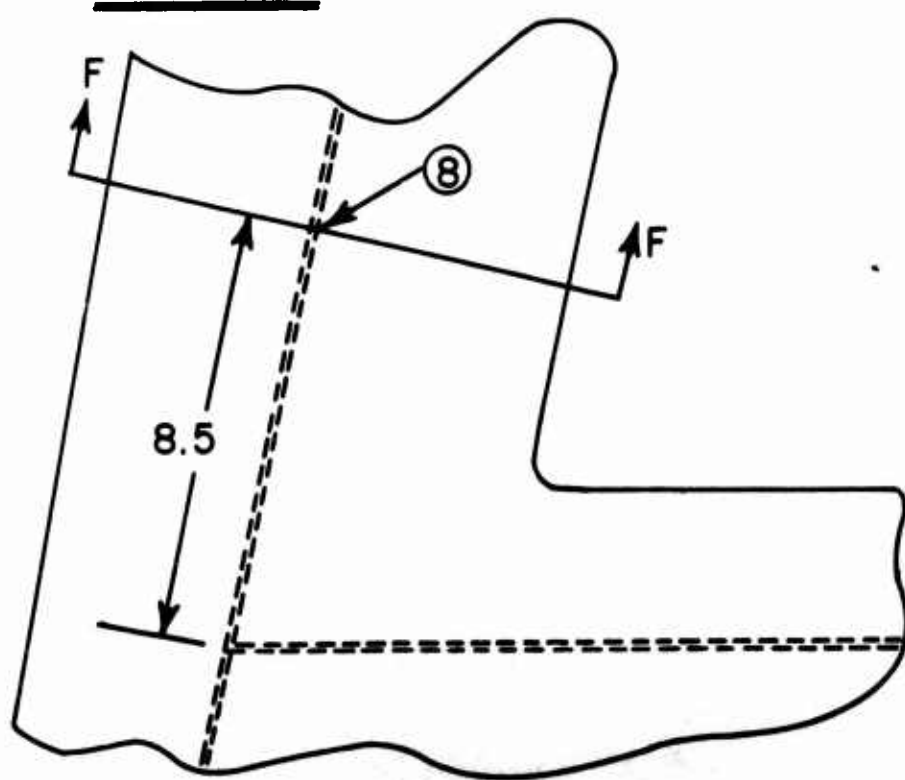
SECTION E-E



AREA F

D-D

6



SECTION F-F

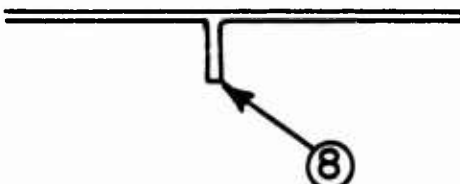


TABLE XVI. STRESSES AT CRITICAL POINTS IN AARS CENTER SECTION (KSI)

Load Condition	Critical Point	(1)*	(2)	(3)*	(4)**	(5)	(6)	(7)	(8)
Level Flight		9.0	2.73	15.8	18.0	4.5	11.2	4.7	5.2
Symmetrical Dive and Pullout		34.8	10.6	63.2	71.4	17.6	26.2	14.5	20.9
Vertical Takeoff		37.0	11.6	67.0	75.6	18.7	27.8	15.1	22.5
Level Landing		36.0	11.6	58.8	66.9	15.4	23.0	12.1	20.6
Hover Turn (Left-Hand Side)		9.6	2.9	12.6	14.4	3.4	4.0	1.9	4.4
Hover Turn (Right-Hand Side)		20.6	8.6	25.6	28.8	7.4	12.3	7.2	9.1
Park		16.0	4.6	2.6	3.9	2.4	4.0	1.4	7.0

* Include corner stress concentration factor 2.0.

** Include hole stress concentration factor 3.0.

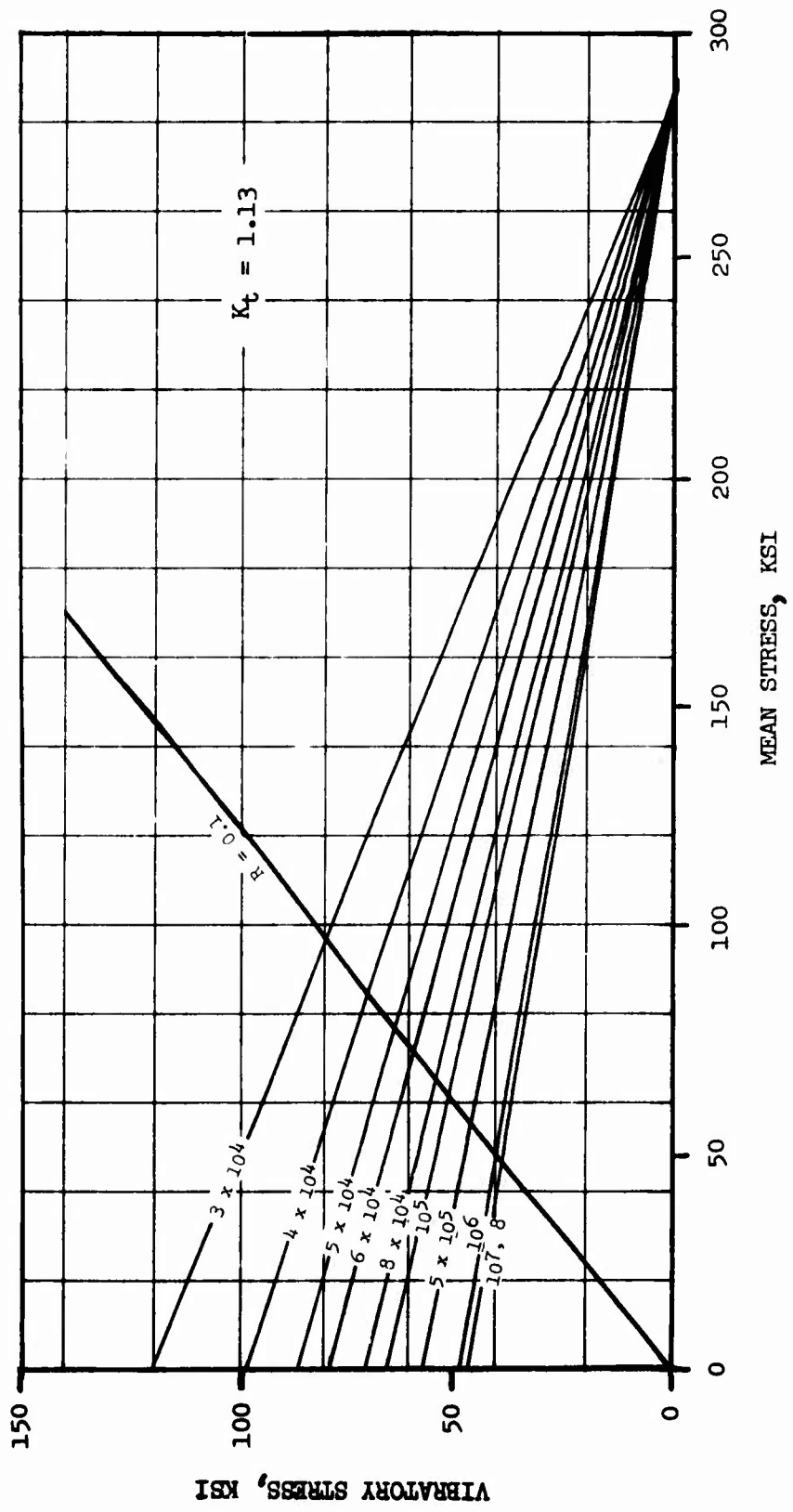


Figure 45. Base Material Constant Life Diagram.

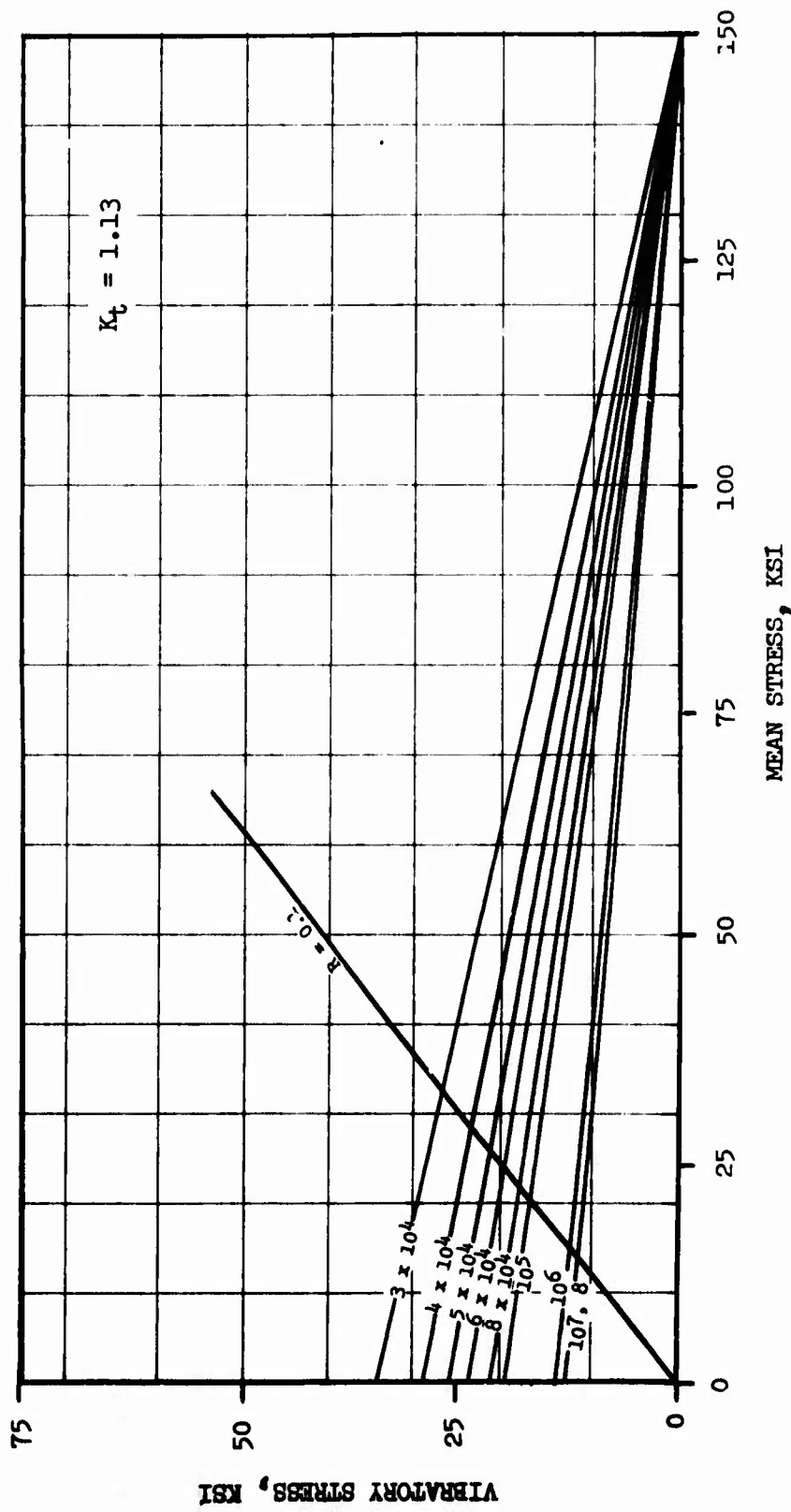


Figure 46. Welded Material Constant Life Diagram.

TABLE XVII. NOMINAL MEAN AND VIBRATORY STRESSES

Flight Cond.	Mean Stress (ksi)	Vibratory Stress (ksi)						Parked
		Level Flight	Dive and Pullout	Takeoff	Landing	Left-Hand Hover Turn	Right-Hand Hover Turn	
1 B	12.33	7.86	5.07	6.17	5.67	7.49	2.03	4.35
2 W	7.86	5.13	2.74	3.74	3.74	5.00	0.77	6.55
3 B	20.14	12.23	11.46	13.36	9.26	13.82	7.34	18.83
4 B	15.21	9.24	8.59	9.99	7.09	10.42	5.57	13.91
5 B	11.31	6.81	6.29	7.39	4.09	7.95	3.91	8.92
6 B	17.86	6.66	8.34	9.94	5.14	13.86	5.56	13.82
7 W	9.46	4.76	5.04	5.64	2.64	7.60	2.26	8.02
8 B	14.02	8.77	6.88	8.48	6.58	9.63	4.92	7.06

B = Stress site in base material.

W = Stress site in welded material.

$$T_h = \frac{1}{\sum_{i=1}^J \frac{n_i}{N_i}} = \text{fatigue life in hours} \quad (23)$$

where n_i = number of cycles at the i^{th} flight condition in 1 hour

N_i = fatigue life for i^{th} flight condition as obtained from the constant life diagram

J = total number of flight conditions

The number of cycles n_i at the i^{th} flight condition occurring in 1 hour can be obtained from the aircraft typical mission spectrum shown in Figure 51.

The fatigue life N_i at each stress site for the i^{th} flight condition is obtained by entering the constant life diagrams with the nominal mean stress (Table XVII) and a modified vibratory stress. This modified vibratory stress $\bar{\sigma}_v$ is defined by the equation

$$\bar{\sigma}_v = \frac{K_f \cdot K_s}{F_r \cdot F_s} \sigma_v \quad (24)$$

where

K_f = fatigue stress concentration factor

K_s = surface finish stress concentration factor

F_r = reliability factor (data scatter)

F_s = size effect factor

$\bar{\sigma}_v$ = nominal vibratory stress (Table XVII)

For the AARS, values for K_f , K_s , F_r , and F_s were conservatively chosen as:

$K_f = K_t$ = theoretical stress concentration factor

$K_s = 1.0$ (since surface finish is included in test data)

$F_r = 0.70$ (standard value of steel at 10^8 cycles)

$F_s = 0.77$ (based on a volume ratio of 50)

The substitution of these values into Equation 24 then yields

$$\bar{\sigma}_v = \frac{K_t}{0.539} \sigma_v \quad (25)$$

The constant life diagrams shown in Figures 45 and 46 are for $K_t = 1.13$, and therefore they must be entered with a further modified vibratory stress σ_v^* defined as

$$\sigma_v^* = \bar{\sigma}_v / 1.13 = \frac{K_t}{(0.539)(1.13)} \sigma_v \quad (26)$$

The theoretical stress concentration factors and the modified vibratory stresses σ_v^* are presented in Table XVIII.

Application of Equation 23 at each critical stress site resulted in the fatigue lives shown in Table XIX, which are all well above the required 3600 hours.

Observation of ballistic damage in good quality armor resulting from a caliber .30 AP projectile at 100 yards revealed the presence of 1/4-inch surface cracks in the base material. In welded areas protected by cover plates, no damage was observed. Crack propagation analysis was therefore required only in the base material.

The bolt hole area at stress site 4 of Figure 44 was considered to be the critical crack propagation region because of the high nominal vibratory stresses (Table XVII) and the high stress concentration $K_t = 3.0$. The model used for crack propagation at this stress site consisted of a 1/4-inch diameter bolt hole with a severe 1/4-inch through crack emanating from the hole as shown in Figure 47.

The Air Force Flight Dynamics Laboratory computer program CRACKS (Reference 14) was used to calculate crack propagation time. The crack propagation analysis in this program is based on Forman's crack propagation equation (Reference 11) which may be written as

$$\frac{d^2a}{dN} = \frac{CAK^n}{(1 - R) K_c - \Delta K} \quad (27)$$

where d^2a/dN = crack propagation rate

ΔK = stress intensity range = $K_{\max} - K_{\min}$

R = stress ratio = $\sigma_{\min}/\sigma_{\max}$

K_c = critical stress intensity

C, n = empirical constants determined from crack propagation data

Table XVIII. THEORETICAL STRESS CONCENTRATION K_t AND MODIFIED VIBRATORY STRESS σ_v^*

Flight Cond. Stress Site	K_t	Modified Vibratory Stress (Ksi)						Parked
		Level Flight	Dive and Pullout	Takeoff	Landing	Left-Hand Hover Turn	Right-Hand Hover Turn	
1 B	2.0	25.2	16.6	20.3	18.6	24.6	6.7	14.3
2 W	1.0	8.4	4.5	6.1	6.1	8.2	1.3	10.8
3 B	2.0	40.2	37.6	43.9	30.4	45.4	24.1	61.8
4 B	3.0	45.5	42.3	49.2	34.9	51.3	27.4	68.5
5 B	1.0	11.2	10.3	12.1	6.7	13.0	6.4	14.6
6 B	1.0	10.9	13.7	16.3	8.4	22.8	9.1	22.7
7 W	1.0	7.8	6.3	9.3	4.3	12.5	3.7	13.2
8 B	1.0	14.4	9.7	13.9	10.8	15.8	8.1	11.8

B = Stress site in base material.

W = Stress site in welded material.

The required values of the critical stress intensity K_c and the empirical constants C and n for the base material (hard side) were determined from the crack propagation test data with the aid of Sikorsky computer program Y124 (Reference 14). The resulting Forman's equation for the hard side of the dual hardness steel is plotted in Figure 48 along with the data in the form of crack propagation rate.

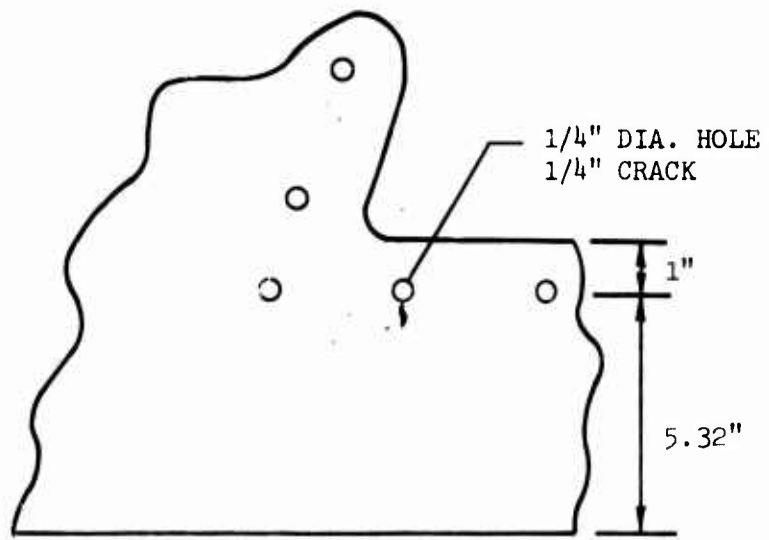
The crack geometry (Figure 47), stress spectrum, critical stress intensity factor, and empirical constants C and n were input to the computer program CRACKS. The output indicated that the crack propagation time in the hard side* of the dual hardness steel exceeds 2400 hours. A factor of safety greater than four is present in the critical crack propagation area, since the required residual life is 600 hours.

TABLE XIX. FATIGUE LIFE IN FLIGHT HOURS

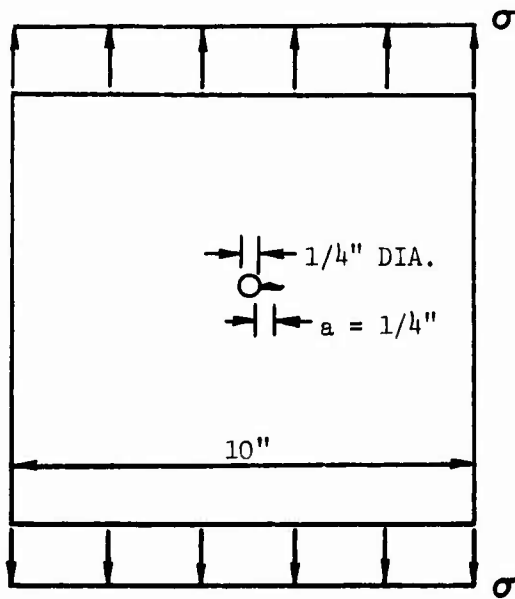
Stress Site	Fatigue Life in Flight Hours
1 B	∞
2 W	∞
3 B	18,500
4 B	15,200
5 B	∞
6 B	∞
7 W	117,800
8 B	∞

* = Indicates that the vibratory stress at this site is below the endurance limit and therefore the fatigue life is infinite.
B = Stress site in base material
W = Stress site in welded material

* Observation of crack propagation indicates that propagation is fastest in the hard side of the dual hardness steel.



a. CRITICAL CRACK PROPAGATION REGION (AREA B)



b. MODEL FOR CRACK PROPAGATION ANALYSIS

Figure 47. Configuration for Crack Propagation Analysis.

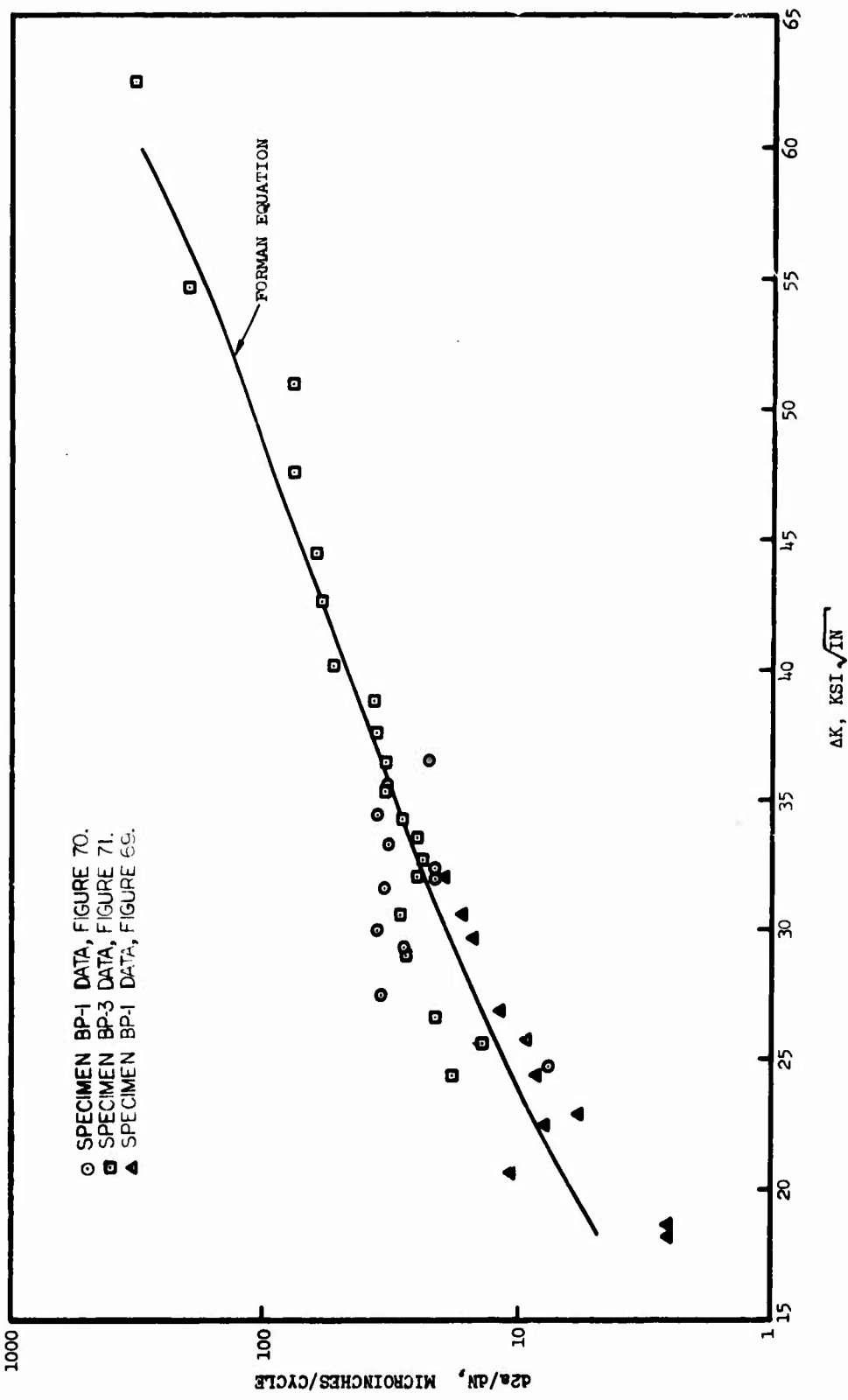


Figure 48. Base Material Crack Propagation Rate, $R = 0.1$.

Fuselage Fitting Analysis

All the transmission attachment fittings and the landing gear attachment fittings have been shown by fatigue stress analysis to be structurally adequate for the anticipated loads and number of cycles. Figure 49 shows the arrangement and designation of the transmission support struts and the location of the forward and aft transmission attachment fittings. Figure 50 shows the arrangement and designation of the landing gear support struts and the location of the upper and forward fittings.

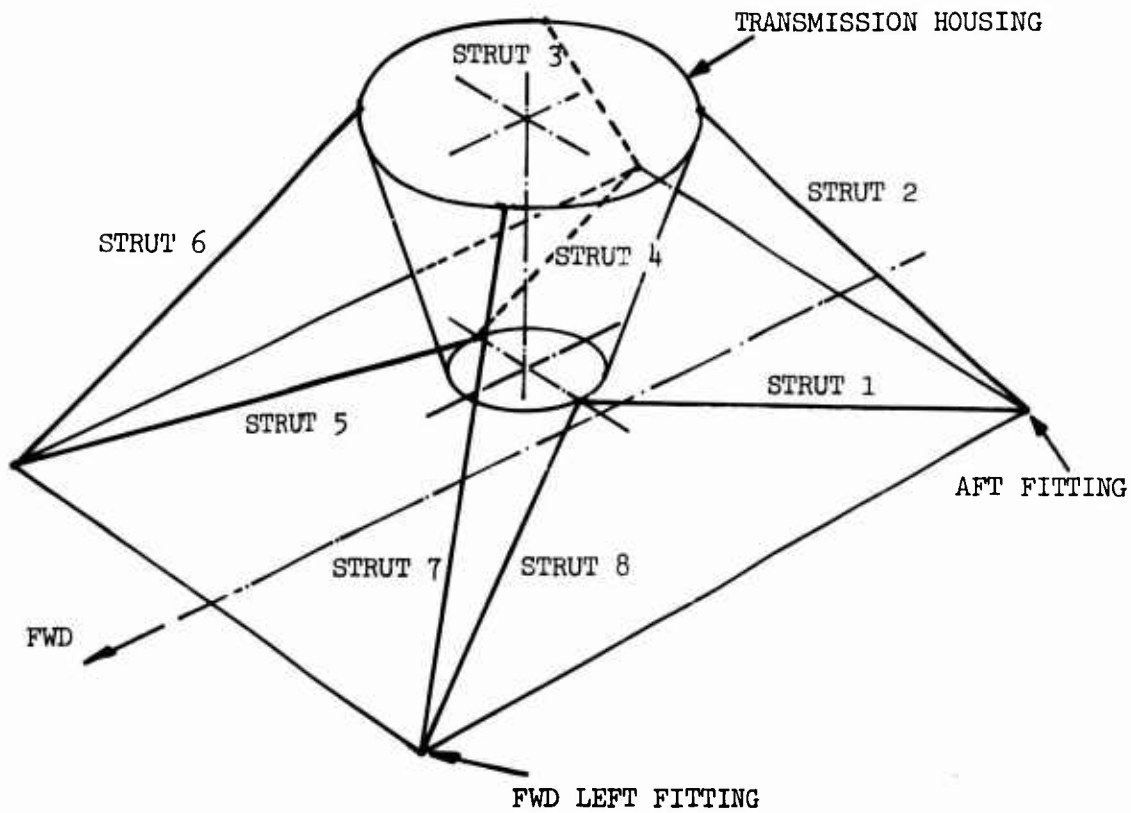


Figure 49. Transmission Support Structure - Strut Designation.

UPPER FORWARD FITTINGS

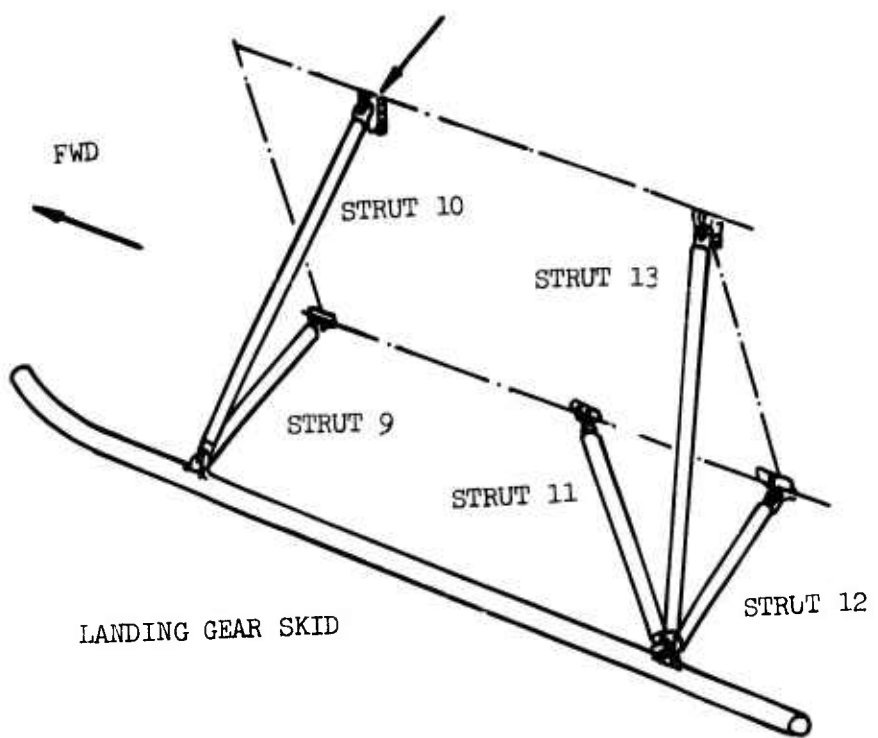


Figure 50. Landing Gear Support Struts.

The loads in the transmission and landing gear support struts for the various load conditions listed are included in Tables XX and XXI respectively.

TABLE XX. TRANSMISSION SUPPORT STRUT LOADS (LB)

Strut Condition	1	2	3	4	5	6	7	8
1. Pull-out	70	6940	7090	90	-9130	20110	20260	-9150
2. Hover Turn	-3460	4810	-410	3350	-5990	8490	3660	790
3. Level Flight	-3160	8710	8670	-3110	730	1650	1620	820
4. Landing	-6490	3670	3710	-6390	-6510	1710	1760	-6330
5. Takeoff	-450	7700	7840	-420	-9420	21320	21460	-9430
6. Parked	-1790	790	750	-1770	-1770	710	670	-1710

TABLE XXI. LANDING GEAR SUPPORT STRUT LOADS (LB)

Strut Condition	9	10	11	12	13
All Flight Conditions	0	0	0	0	0
4. Landing	7520	-16990	4090	2820	-12060
6. Parked	2210	-5000	-3440	4600	-3160

Figure 51 shows the aircraft fatigue test load spectrums used for the substantiation of the fittings.

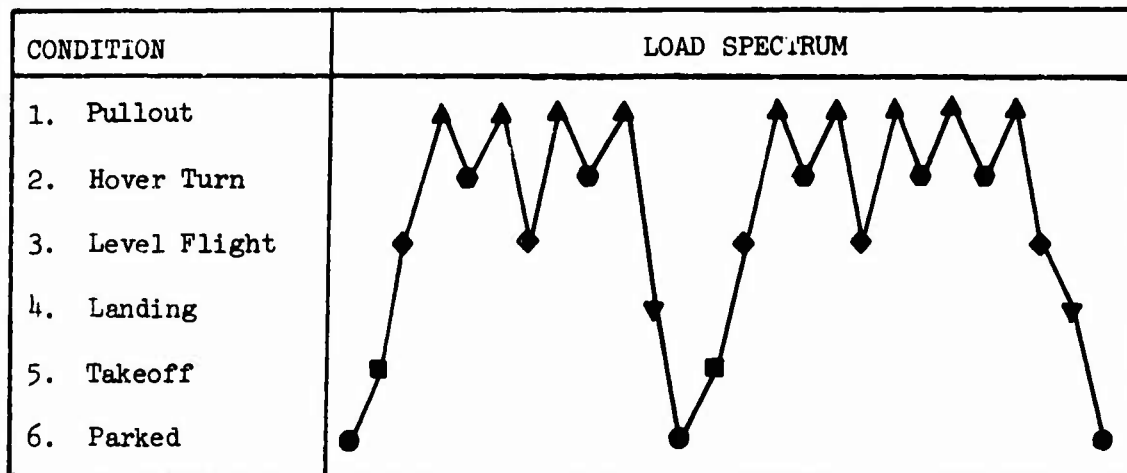


Figure 51. Aircraft Fatigue Test Load Spectrum.

The number of cycles of loading from the above load spectrum is included in Table XXII.

TABLE XXII. NUMBER OF CYCLES PER LOAD BLOCK		
a.	Ground-Air Ground (Max to Min Load)	2
b.	Pullout to Hover Turn	5
c.	Pullout to Level Flight	3 1/2
d.	Parked to Takeoff	1
e.	Takeoff to Level Flight	1
f.	Pullout to Landing	1/2
g.	Landing to Parked	1
h.	Level Flight to Landing	1/2

From Table XX, the amplitude of the repeated loads for the cycles listed in Table XXII are determined and included in Table XXIII.

TABLE XXIII. REPEATED LOAD AMPLITUDES AND CYCLES - TRANSMISSION STRUTS

Strut Loading \	1	2	3	4	5	6	7	8
a	3280	3960	4540	4870	5080	10300	10400	5130
b	1770	1070	3750	1630	1570	5810	8300	4970
c	1620	890	790	1600	4930	9230	9320	4990
d	670	3460	3550	680	3830	10310	10400	3860
e	1360	510	420	1350	5080	9840	9920	5130
f	3280	1640	1690	3240	1310	9200	9250	1410
g	2350	1440	1480	2310	2370	500	550	2310
h	1670	2520	2480	1640	3620	30	70	3580
Design Amplitude	3300	4000	4500	5000	5080	10000	10000	5000
No. of Cycles per Block	2.5	3.0	3.0	2.0	6.5	8.0	8.0	12.5
Applied Cycles	22000 (1)	22000 (1)	22000 (1)	22000 (1)	72000 (2)	72000 (2)	100000 (3)	100000 (3)

(1) 7200 blocks @ 3 cycles/block of loading.
 (2) 7200 blocks @ 10 cycles/block of loading.
 (3) 7200 blocks @ 13 cycles/block of loading.
 (4) Load amplitudes are given in pounds.

The landing gear support strut loads included in Table XXI show that the repeated loads are determined only by the ground-air-ground cycle. The load amplitudes for this condition are included in Table XXIV.

There are two cycles per load block; thus, in 7200 blocks of load application, the number of applied cycles is 14,400.

TABLE XXIV. REPEATED LOAD AMPLITUDES AND CYCLES - LANDING GEAR STRUTS

Strut	9	10	11	12	13
Design Amplitude (lb)	3760	8500	2050	2300	6030
Applied Cycles	14400	14400	14400	14400	14400

From Table XXIII, the forward transmission attachment fittings of struts 7 and 8 are subjected to the highest loads and greatest number of cycles.

From Table XXIV, the forward upper landing gear attachment fitting of strut 10 is subjected to the highest load.

The left-hand forward fitting of the transmission attachment is shown in Figure 52. It sustains the loads in struts 7 and 8. It is seen from Table XX that these loads are out of phase, and the design amplitudes included in Table XXIII are also out of phase.

The upper forward landing gear attachment fitting which is shown in Figure 53 sustains the load in strut 10, as shown in Table XXIV.

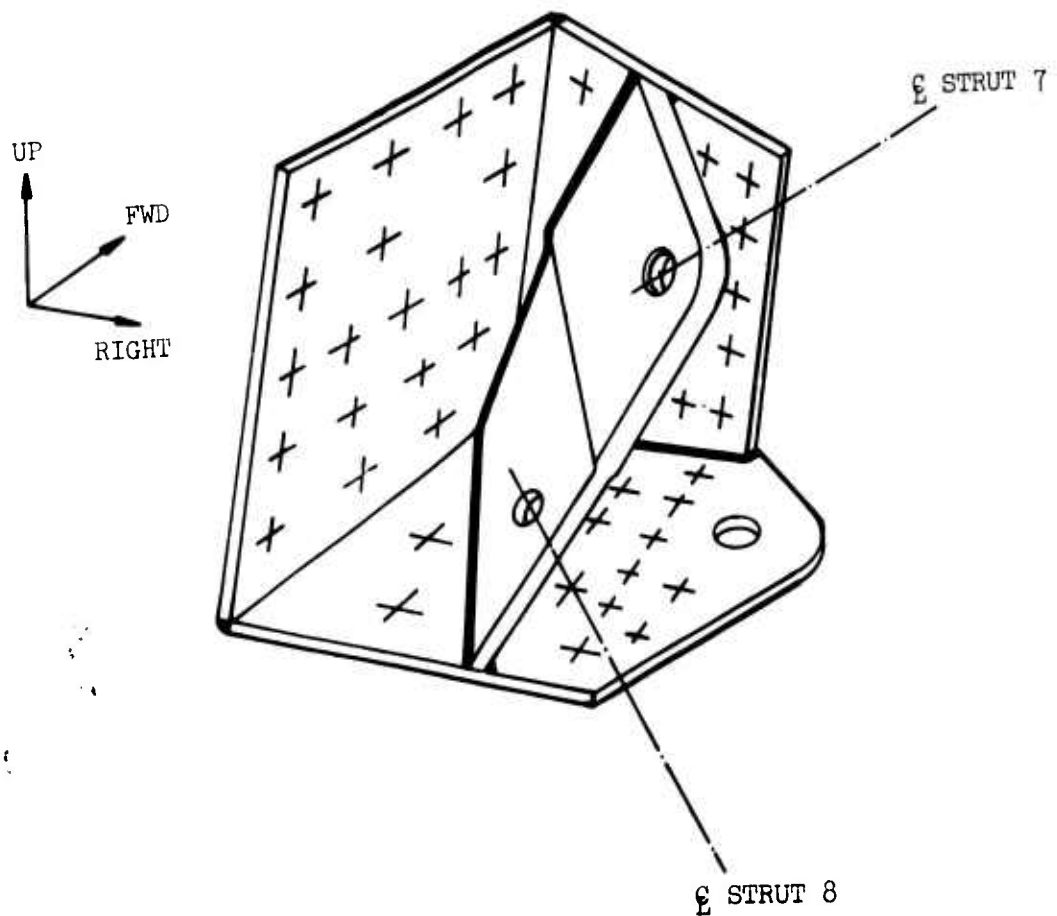


Figure 52. Left-Hand Forward Transmission Support Structure Attachment Fitting.

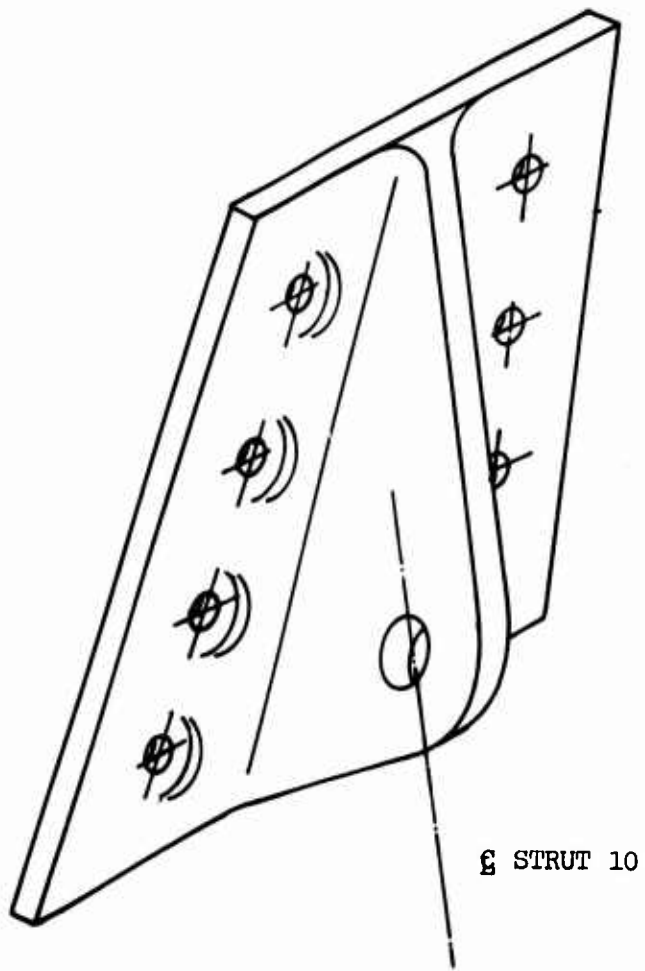


Figure 53. Upper Forward Landing Gear Attachment Fitting.

MATERIALS CHARACTERISTICS

OBJECTIVES

In a previous study (Reference 15), the feasibility of using dual hardness steel armor (DHS) in an integrally armored fuselage application was demonstrated. Various factors were evaluated, such as resistance to fracture under combined static and ballistic impact loads, residual static strength after impact and penetration by caliber .30 ball ammunition, and residual fatigue life and crack propagation rates after the ballistic damage. Full characterization of the engineering properties of the material remained to be performed, especially with respect to crack initiation properties.

In addition, several variables have been changed since the initial feasibility study was performed. The primary ballistic threat has been defined as caliber .30 armor piercing rather than ball ammunition. The hardness of the armor components, and the materials thickness ratio have been altered to provide increased protection at thinner gages of material. Also, the NASTRAN analysis described elsewhere in this report allows a more valid and realistic estimate of stresses to be made than had been available previously.

To take full advantage of the material in aircraft design and to allow valid prediction of its behavior in the fuselage structure, an extensive series of small-scale specimen tests was performed as part of Phase I. These tests were designed to collect new data, refine previous data, and characterize the effect of the changes in material and design that had occurred. Among the properties to be determined were:

- 1) Static tensile strength
- 2) Crack initiation properties and fatigue strength
- 3) Crack propagation rates
- 4) Fracture toughness
- 5) Susceptibility to environmental crack initiation
- 6) Magnitude of residual stresses introduced by welding
- 7) Residual static and fatigue properties after ballistic impact.

APPROACH, PROCEDURES, RESULTS

Material

All testing described in this section was conducted on material supplied by Jessop Steel Company, Washington, Pennsylvania, from Heat K-2060. Dual hardness steel is a roll bonded composite consisting of a face plate (or hard side) with an average hardness of 59-60 on the Rockwell "C" scale and a rear plate (or soft side) of R_c 49-50. The component thickness ratio here was approximately 30:70 to 35:65, hard to soft component, respectively,

as shown in Figure 54. The armor used is fully heat treatable, with the difference in hardenability from side to side due primarily to the difference in carbon content between the two components. The chemical composition of the material tested herein was within the established limits set by Jes-sop for their proprietary armor. Typical microstructure of the front and rear plates may be seen in Figure 55. The nominal thickness of the material tested was 0.305 inch and was chosen on the basis of the ballistic tests de-scribed in the confidential appendix to this report.

Welding Procedure

Welding was performed using the manual gas-tungsten arc weld (GTAW) method (same as TIG) and filler rod per MIL-R-5632, Class 2, Type 1 (heat treatable rod for 4130 type steels). The plates were chamfered (25°) at the abutting edges, and the welds were accomplished in three or four passes using straight polarity on a medium load setting. A 200-ampere, 40-volt Harnesch-feger P&H power supply was used. The primary weld bead was made from the hard side with a final cosmetic pass on the soft side. Copper chill bars were used in all cases to minimize the extent of the heat-affected zone (HAZ). This zone was held to under 1½ inches on the soft side and 2 inches on the hard side, including the weld bead (Figures 56 and 57).

All welded specimens were fluorescent magnetic particle inspected per MIL-M-11473 for the presence of cracks. A small sampling was radiographically inspected. Initial test results revealed the presence of incomplete weld penetration on most of the samples, as shown in Figure 57. Insufficient dwell time to assure complete penetration had been provided, leading to incomplete fusion. The resultant gap acted as a stress raiser, especially in fatigue loading, which resulted in reduced strength.

Attempts to repair several of these welds were not successful, as they led to development of increased internal porosity with little improvement in strength. Preliminary analysis of the data indicated that a fatigue life of 3600 hours or longer would be achieved at the stress levels experienced at the welds. For this reason, the test program was continued as planned. It is certain that more integral welds can be achieved by minor procedural modification. In the interim, all welds were x-rayed and/or the fracture surfaces examined so that the effect of the lack of fusion on measured proper-ties could be analyzed.

Tensile Properties

All tests were conducted in general accordance with American Society for Testing and Materials (ASTM) Method E-8. Depending upon cross-sectional area, either a Satec Systems 400,000-pound capacity, or Riehle 60,000-pound capacity, Universal Testing Machine was utilized. Tensile results for the as-received armor and the as-welded armor are listed in Table XXV.

Welded specimens 1 through 3 were fitted with the adhesively bonded ballis-tic protection plate, while 4, 5 and 6 were without this protection. The presence of the bonded cover appeared to have little or no effect on strength.

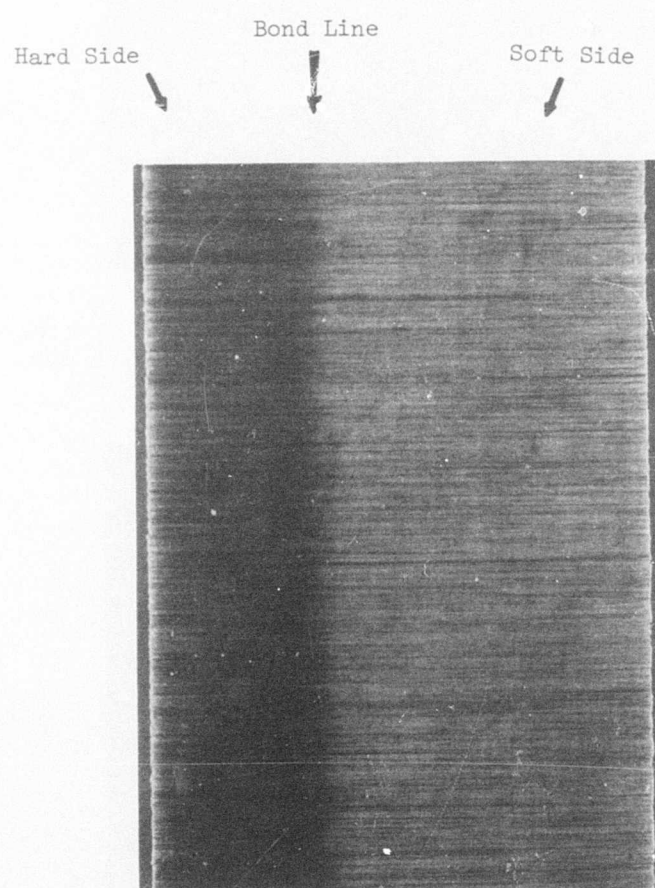
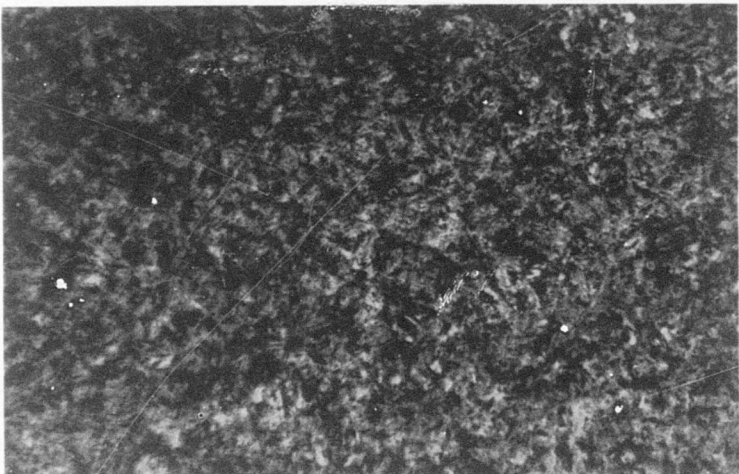
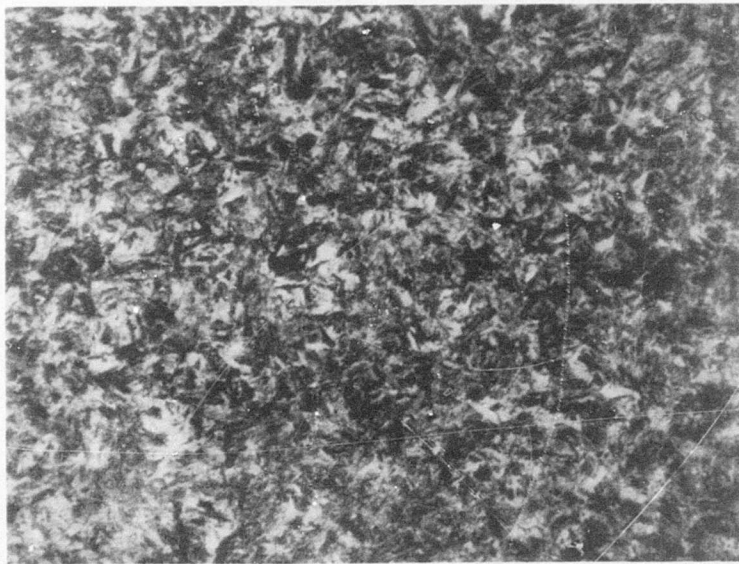


Figure 54. Macrostructural Appearance of DHS Used in All Phases of Material Characterization Testing.
~ 10X



Hard Side

500X Figure 55A. Etchant 2% Nital Photomicrograph of a transverse section normal to direction of rolling taken of the hard side exhibiting a tempered martensitic microstructure.



Soft Side

500X Figure 55B. Etchant 2% Nital Photomicrograph of a transverse section normal to direction of rolling taken of the soft side exhibiting a tempered martensitic microstructure.

Figure 55. Microstructural Appearance of DHS Used in All Phases of Material Characterization Testing.

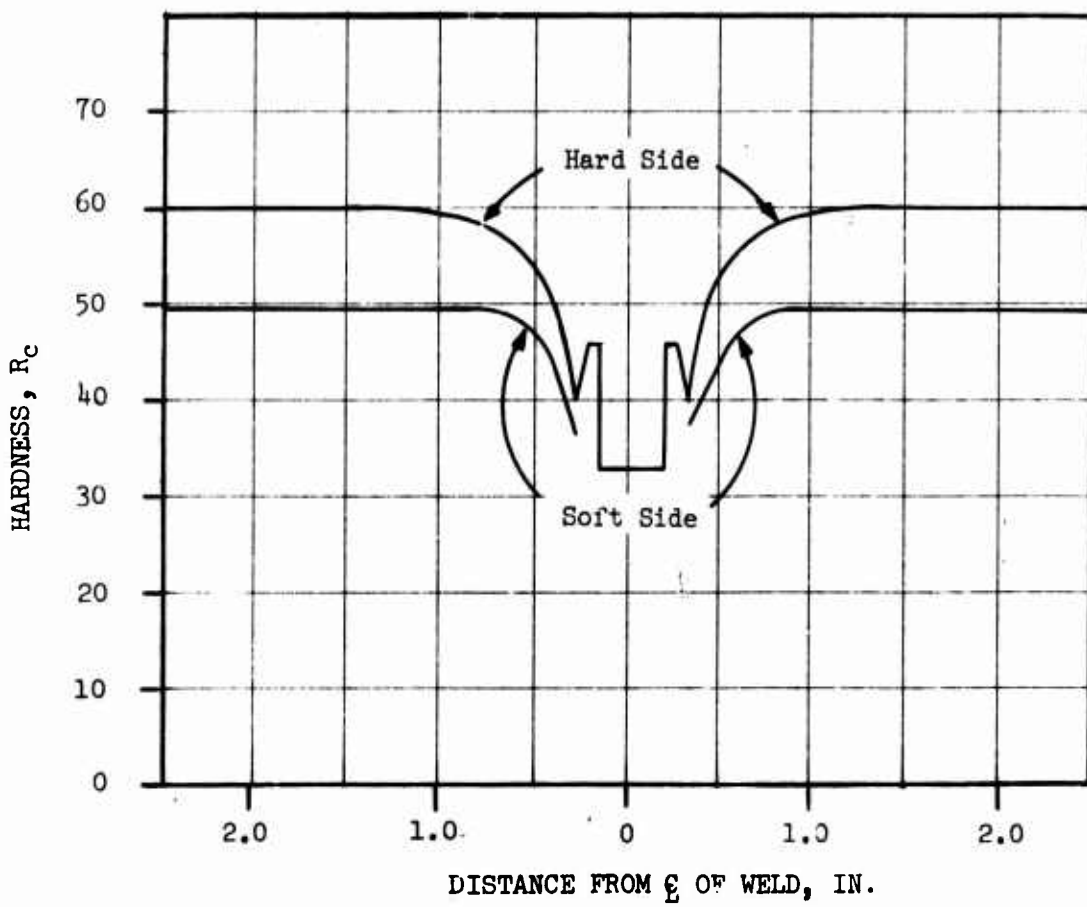
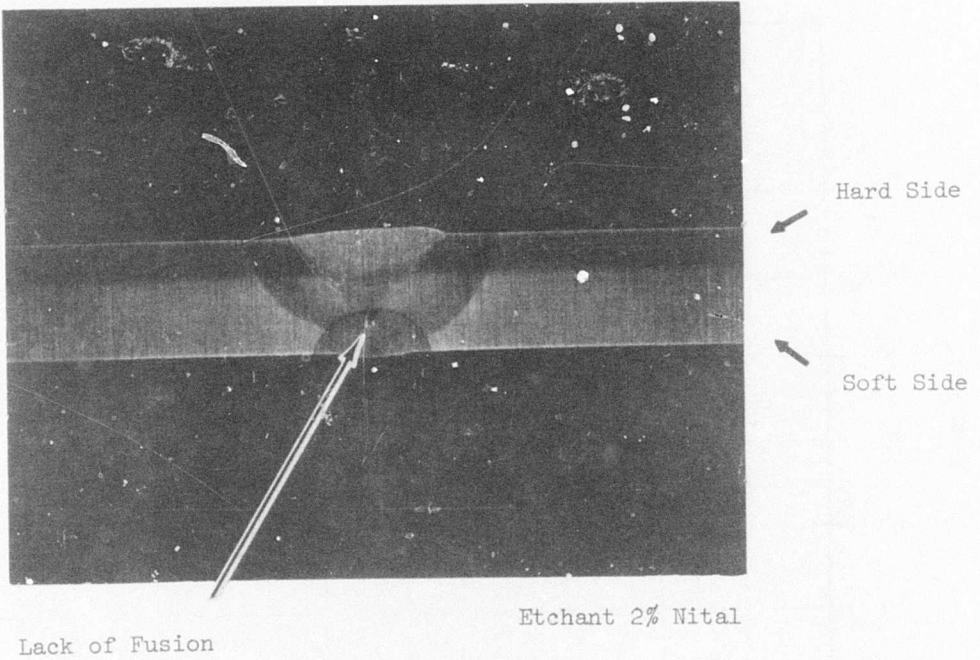


Figure 56. Hardness Profile of Typical Welded Specimen.



Photomicrograph of a transverse section of Dual Hardness Steel Weldment showing a three (3) pass weld with the last pass being made on the soft side. Also noticed was an area of lack of fusion as indicated by the lower arrow.

Figure 57. Macrostructural Appearance of Typical Weld.
~ 2.3X

TABLE XXV. TENSILE TEST RESULTS

Specimen	Ultimate Tensile Strength (psi)	Yield Strength (psi)	Elongation (%)
a) Base Material			
BT-1	285,500	282,300	3.0
BT-2	295,700	291,600	4.0
BT-3	292,000	290,000	3.5
BT-4	288,100	284,000	3.5
BT-5	290,600	287,250	4.5
Average	290,380	287,030	3.7
b) Welded Material			
WT-1	127,950	96,400	3.0
WT-2	103,950	101,000	3.5
WT-3	149,800	110,800	4.0
WT-4	137,300	88,200	2.0
WT-5	147,500	105,400	3.0
WT-6	93,000	81,000	2.0
Average	126,580	97,130	2.9

Variation in strength values result in variation of weld quality.

Fatigue Testing

Twelve 4-inch by 14-inch plates were cut on a high-speed friction saw to an hourglass configuration. A three-hole end grip bolt pattern was then drilled and used to align the specimens for milling to finished shape. The final surface finish preparation consisted of a longitudinal polish of the reduced section with #240 grit silicon carbide abrasive. The base undamaged fatigue initiation specimen configuration is shown in Figures 58 and 60.

Twenty-four 4-inch by 7-inch plates were welded into twelve 4-inch by 14-inch specimen blanks using the process described above. These specimen blanks were then fabricated into twelve fatigue initiation specimens in the same manner as were the base specimens. The welded undamaged fatigue initiation specimen configuration is shown in Figures 59 and 61.

All fatigue testing was axial and utilized spherical bearing grip setups to eliminate bending. Fatigue tests were conducted on an IVY-12 with a 5-to-1 load amplifier ($30,000 \pm 30,000$ pounds capacity) and an IVY-20 ($12,000 \pm 8,000$ pounds load capacity). A Sikorsky calibrated load cell in series with the test specimen and an Ellis BA-12 Bridge, Amplifier and Oscilloscope Console was used as the primary load measuring system. All specimens were tested in the normal laboratory environment at a loading frequency of 1200 cycles per minute (cpm). All tests were conducted at a constant R ratio ($\frac{\sigma_{min}}{\sigma_{max}}$) of 0.10.

Three vibratory stress levels were employed for each specimen condition to obtain specimen failures over the range of 3×10^4 to 2×10^6 cycles. Specimens were tested to failure or to at least 4×10^6 cycles.

Results for the base undamaged and welded undamaged specimens are presented in Tables XXVI and XXVII respectively. Figures 62 and 63 present the S-N results along with log mean curves for the two conditions. The mean vibratory fatigue strength at 10^7 cycles, $R = 0.1$, was found to be ± 34 ksi for base undamaged specimens and ± 11 ksi for welded undamaged specimens.

Soft side surface origins were noted on all base undamaged specimens, as was expected for the polished surface finish employed. The base undamaged specimens had a soft side fatigue crack propagation area which was typically 7 percent of the cross-sectional area. When the propagating crack crossed the bond line into the hard side, brittle fracture of the hard side occurred immediately in the flat, plane-strain mode. This then led to soft side failure, which also was predominantly plane-strain in nature. A small shear lip on the soft side was noted. A typical fracture surface of a base undamaged specimen is shown in Figure 64.

On the welded undamaged specimens, the origins were located at a crack at the intersection of the welded bead and the HAZ on the hard side (2 cases) or at the center of the weld bead in an area of incomplete penetration running the full length of the weld on the soft side (7 cases). A typical fracture surface for this predominant mode of failure of the welded

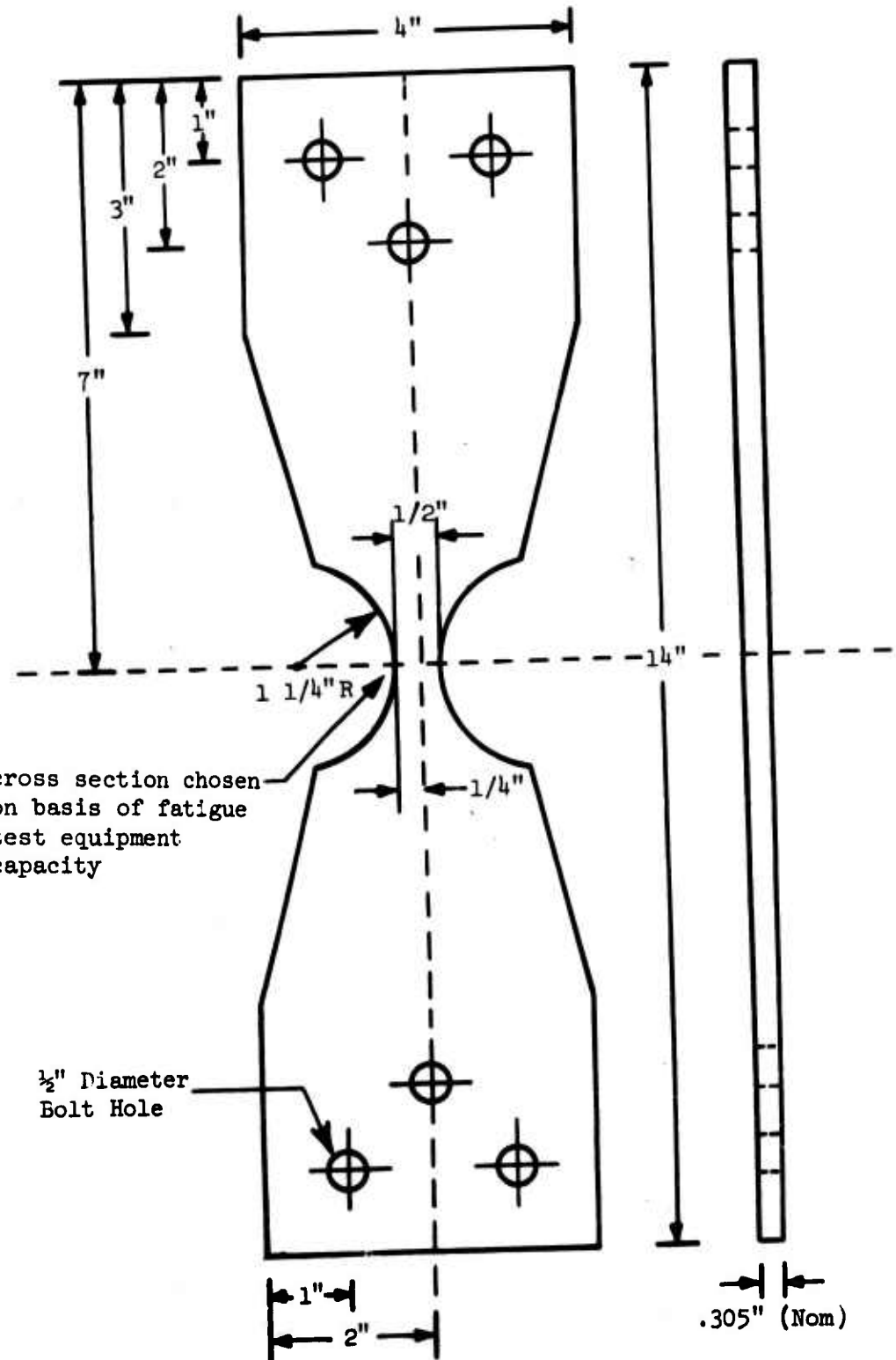


Figure 58. Undamaged Base Fatigue Test Specimen

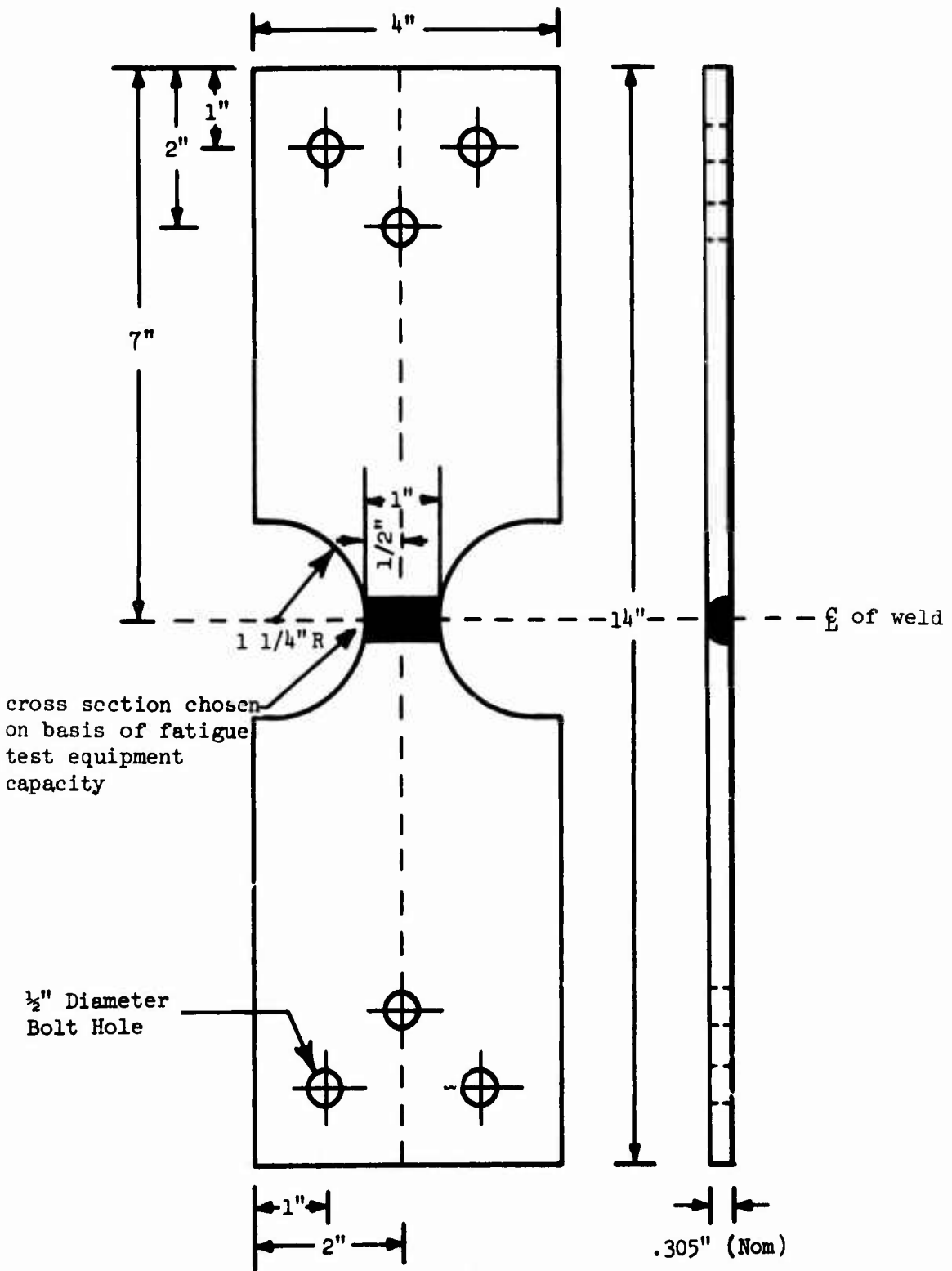
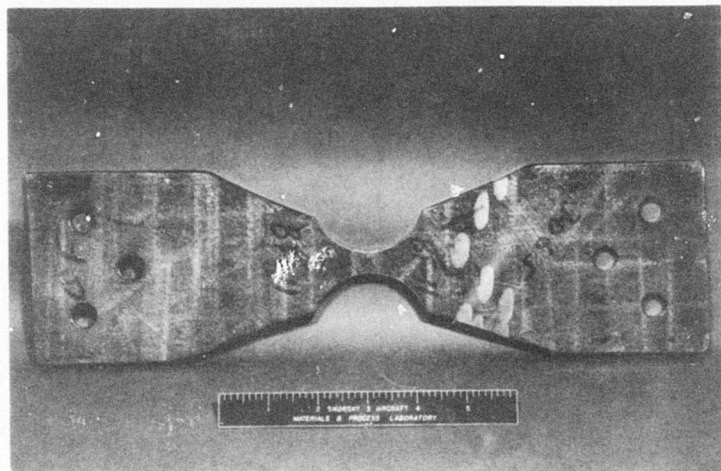


Figure 59. Undamaged Welded Fatigue Test Specimen.



(Marks from Vendor Straightening Operation)

Figure 60. Base Undamaged Fatigue Specimen.

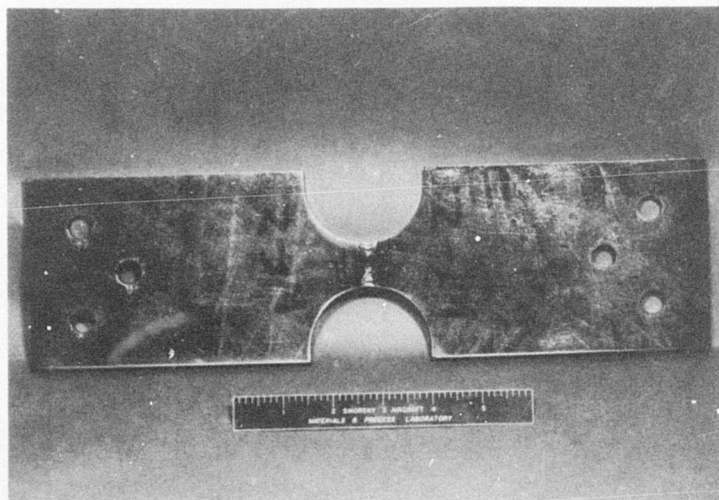


Figure 61. Welded Undamaged Fatigue Specimen.

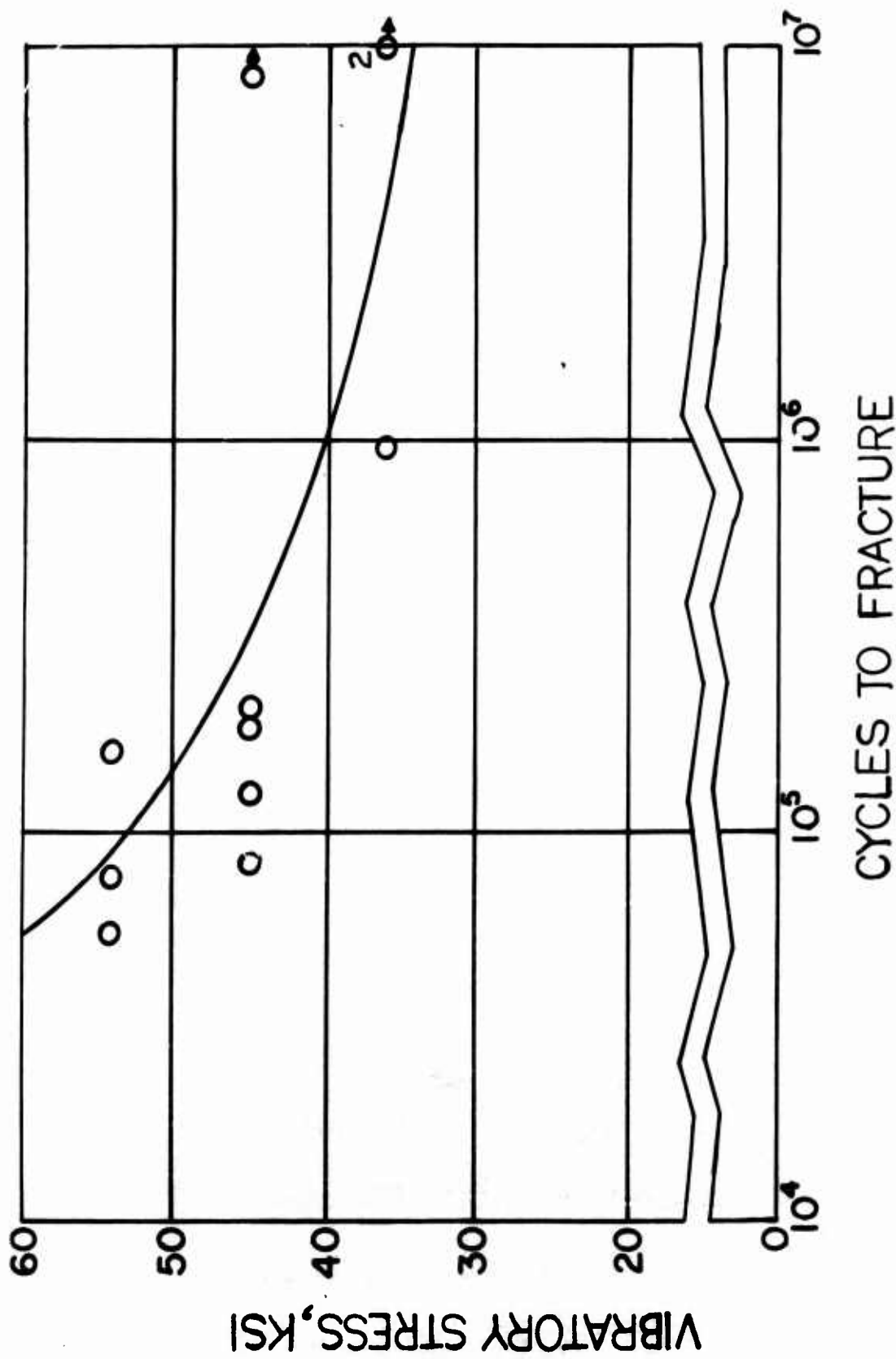


Figure 62. Vibratory Stress Versus Cycles to Fracture, Base Undamaged Material, $R = 0.1$.

TABLE XXVI. FATIGUE TEST RESULTS - BASE UNDAMAGED MATERIAL

T/N	Machine Number	Specimen S/N	+ σ_u^* (ksi)	$\pm \sigma_v$ (ksi)	Cycles to Failure $\tau_x 10^{-6}$	Comments
1	IVY-12-2	BF - 1	55	45	0.210	
2	IVY-12-2	BF - 2	55	45	0.084	
3	IVY-12-2	BF - 3	44	36	0.961	
4	IVY-12-2	BF - 4	66	54	0.162	
5	IVY-12-2	BF - 5	66	54	0.002	Specimen had hard side nick.
6	IVY-12-2	BF - 6	66	54	0.077	
7	IVY-12-2	BF - 7	44	36	10.000 \rightarrow	Did not fail.
8	IVY-12-2	BF - 8	55	45	8.455 \rightarrow	Did not fail.
9	IVY-12-2	BF - 9	66	54	0.056	
10	IVY-12-2	BF - 10	55	45	0.126	
11	IVY-12-2	BF - 11	44	36	10.183 \rightarrow	Did not fail.
12	IVY-12-2	BF - 12	55	45	0.185	

* Uncorrected for Specimen $K_t = 1.13$

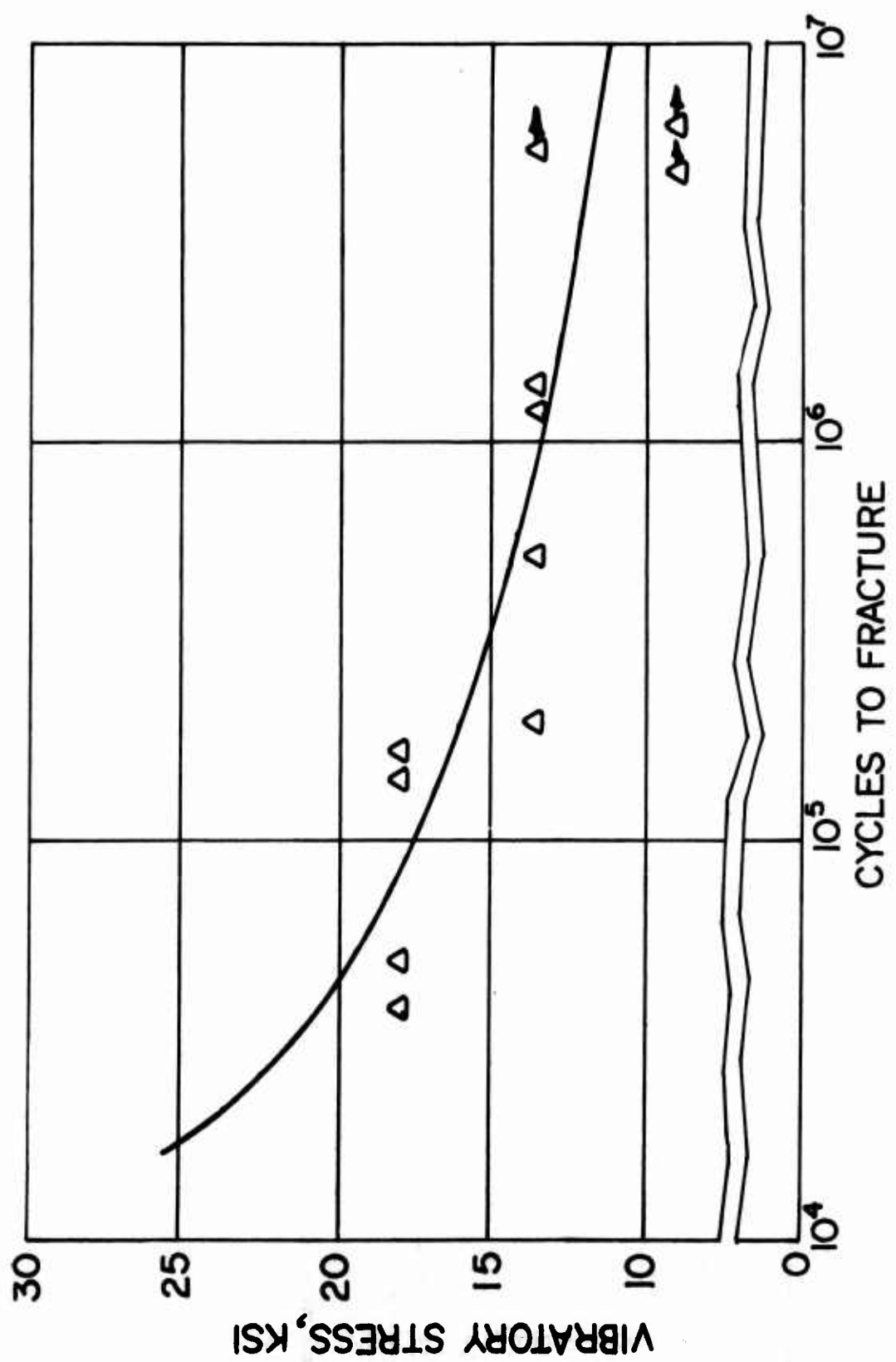


Figure 63. Vibratory Stress Versus Cycles to Fracture, Welded Undamaged Material, $R = 0.1$.

TABLE XXVII. FATIGUE TEST RESULTS - WELDED UNDAMAGED MATERIAL

T/N	Machine Number	Specimen S/N	$\pm \sigma_s$ (ksi)	$\pm \sigma_y$ (ksi)	Cycles to Failure ($\times 10^{-6}$)	Comments
1	IVY-20	WF - 1	68.5	20	<0.001	Overloaded.
	IVY-20	WF - 2	16.5	13.5	5.407 	Did not fail.
2	IVY-20	WF - 3	16.5	13.5	0.204	
	IVY-20	WF - 4	16.5	13.5	0.527	
3	IVY-20	WF - 5	22	18	0.145	
	IVY-12-2	WF - 6	11	9	6.511 	Did not fail.
4	IVY-20	WF - 7	11	9	4.815 	Did not fail.
	IVY-20	WF - 8	22	18	0.051	
5	IVI-12-2	WF - 9	22	18	0.039	
	IVY-12-2	WF - 10	16.5	13.5	1.207	
6	IVY-20	WF - 11	16.5	13.5	1.417	
	IVY-20	WF - 12	22	18	0.172	
* Uncorrected for Specimen $K_t = 1.13$						

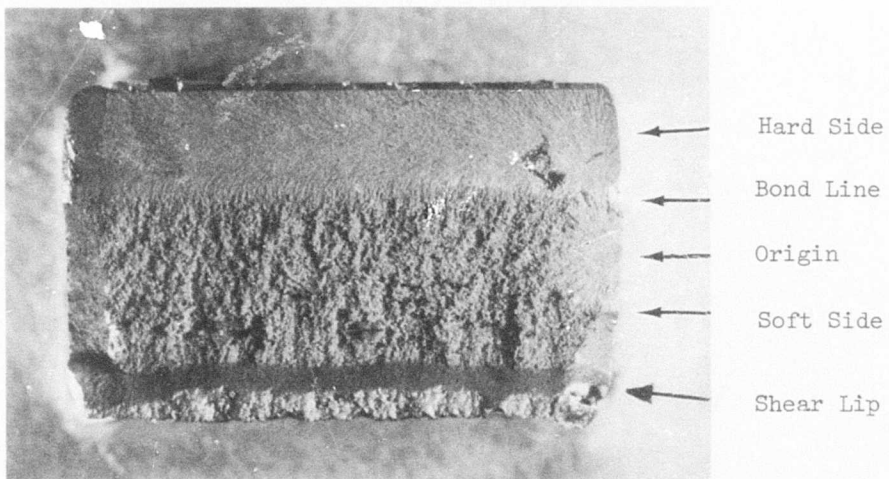


Figure 64. Typical Fracture Surface, Base Undamaged Fatigue Specimen.
~ 6.5X

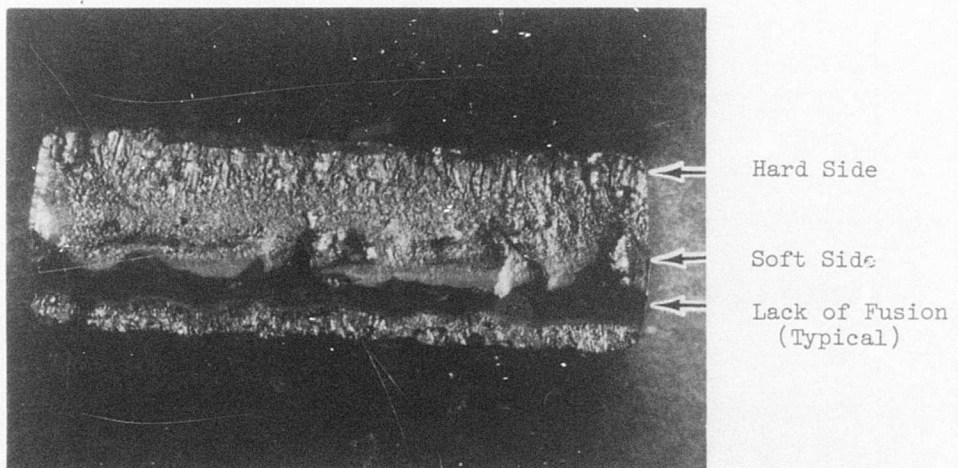


Figure 65. Typical Fracture Surface, Welded Undamaged Fatigue Specimen.
~ 4X

undamaged specimens is shown in Figure 65.

Crack Propagation

Three 4-inch by 14-inch plates, as supplied by Jessop, were fabricated to the configuration shown in Figures 66 and 67. Steel doublers were adhesively bonded to the specimen in order to reinforce the grip section.

Six 4-inch by 7-inch plates were welded into three 4-inch by 14-inch crack propagation specimens using the welding procedure previously described. Steel doublers were bonded to the specimen with 3M EC 1751 adhesive in order to reinforce the grip section. The welded undamaged specimen configuration was similar to that of the base. An actual specimen is shown in Figure 68.

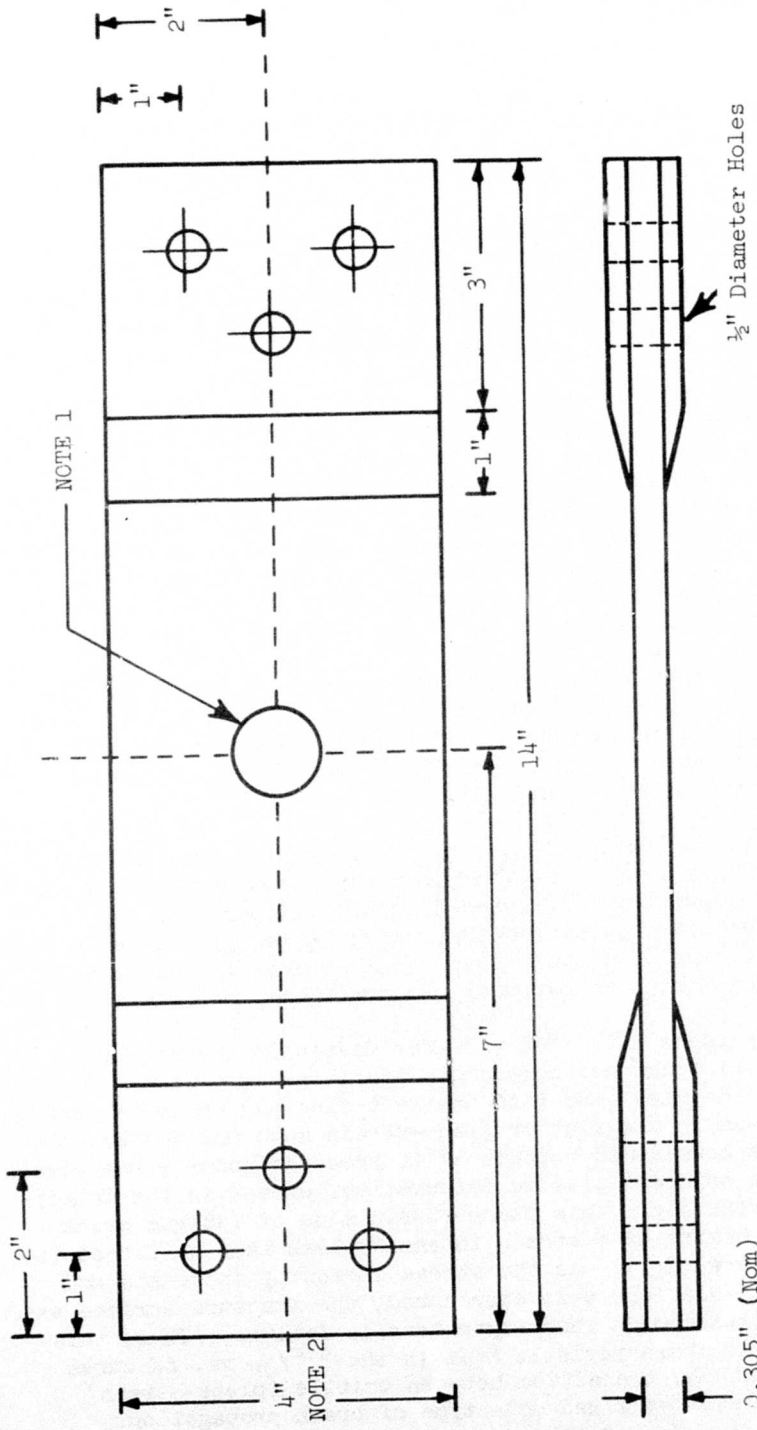
Crack propagation tests were conducted on an IVY-12 fatigue machine with a 5-to-1 load amplifier and a specially designed servo hydraulic test machine equipped with a Nashua closed-loop force feedback system to maintain static and dynamic loads. Loads were determined with a Sikorsky calibrated load cell in series with the test specimen and an Ellis BA-12 Bridge, Amplifier and Oscilloscope Console. Spherical bearing end grip setups were utilized to eliminate bending. Testing was conducted at a loading frequency of 1200 cpm on the IVY-12 and 1000 cpm on the servo-hydraulic machine. All tests were conducted at a constant R ratio ($\sigma_{min}/\sigma_{max}$) of 0.10.

Measurements of crack length versus cycles and general observations were performed visually. Crack length measurements were accomplished by stopping the test at various intervals and, with steady stress still applied, spraying the magnetized specimen with MagnaGlo® solution. The crack length was then measured under ultraviolet light.

A summary of the crack propagation test results is given in Tables XXVIII and XXIX. The total crack length, $2a$, versus cycles for each test specimen is plotted, where possible, in Figures 69 to 74. A curve of $\log \frac{d2a}{dN}$ versus ΔK for the base undamaged crack propagation specimens is shown in the Detail Analysis section of this report. The curve was obtained using Sikorsky Fracture Mechanics Computer Program Y-124, Reference 16.

Cracks in the base specimens initiated and grew faster in the higher strength, lower fracture toughness component, i.e., the hard side. The crack propagated from the hard side into the soft side and became a through crack. Crack growth was in the flat or plane-strain mode and was brittle in nature. A crack is considered brittle if it proceeds under plane-strain conditions with little apparent plastic deformation, except in the immediate vicinity of the crack tip. This plane-strain mode of fatigue crack propagation generally occurs at a stress intensity less than half that required for total fracture (K_{Ic}). As the stress intensity increased and unstable crack growth conditions were approached, the fracture surface exhibited the characteristics of a shear-type tensile failure. Thus, this material should have the characteristic knee in the $\frac{d2a}{dN}$ vs. ΔK curve which is associated with the transition between brittle (plane-strain) and ductile (plane-stress) or mixed mode type of crack propagation.

A typical fracture surface of a failed base undamaged crack propagation



NOTE 1. Crack Starter Area, Notched Hole or Ballistic Damage

NOTE 2 6" for Ballistically Damaged Welded Specimens. Hole Pattern and Relation to θ , Remain Unchanged

Figure 66. Crack Propagation Test Specimen.

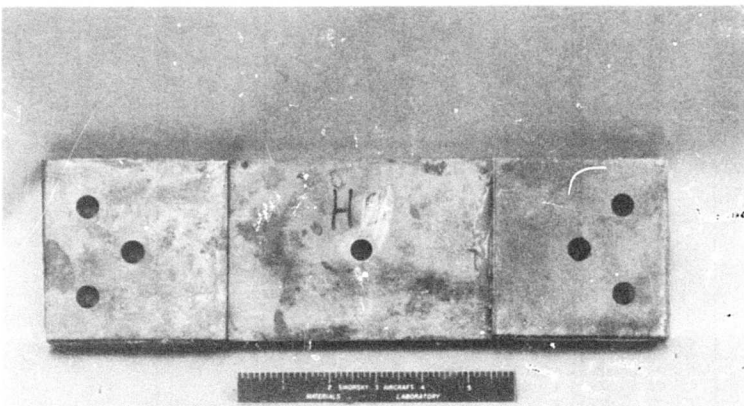


Figure 67. Base Undamaged Crack Propagation Specimen.



Figure 68. Welded Undamaged Crack Propagation Specimen.

TABLE XXVIII. CRACK PROPAGATION RESULTS - BASE UNDAMAGED MATERIAL

T/N	Specimen S/N	Machine Number	Frequency (cpm)	Area (in. ²)	$\pm \sigma_s$ (psi)	$\pm \sigma_v$ (psi)	Cycles to Fracture ($\times 10^{-3}$)	Comments
9	BP - 2	Servo	1000	1.270	12870	10530	439	Grip Failure.
10	BP - 1	Servo	1000	1.277	12870	10530	60	Propagated.
10A	BP - 1	Servo	1000	1.277	6435	5265	271	Fractured.
11	BP - 3	IVY-12-2	1200	1.260	12870	10530	70	Fractured.

TABLE XXIX. CRACK PROPAGATION RESULTS - WELDED UNDAMAGED MATERIAL

T/N	Specimen S/N	Machine Number	Frequency (cpm)	Area (in. ²)	$\pm \sigma_s$ (psi)	$\pm \sigma_v$ (psi)	Cycles to Fracture ($\times 10^{-3}$)	Comments
5	WC-1	Servo	1000	1.248	9900	8100	437	No Propagation.
5A	WC-1	Servo	1000	1.248	12870	10530	187	Fractured.
6	WC-3	Servo	1000	1.250	11880	9720	930	No Propagation.
6A	WC-3	IVY-12-2	1200	1.250	12870	10530	512	Fractured.
7	WC-2	IVY-12-2	1200	1.256	11880	9720	160	Fractured.

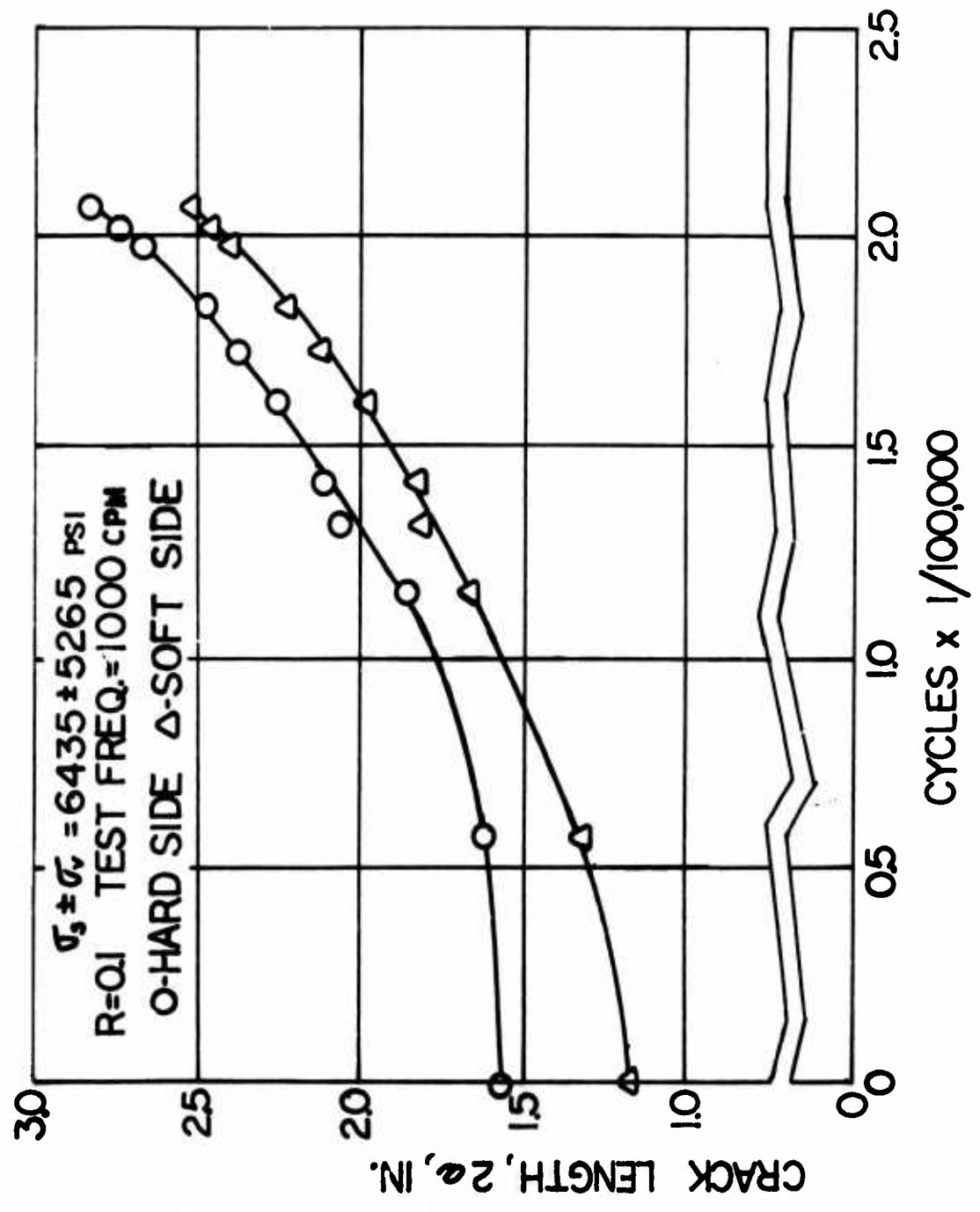


Figure 69. Crack Length Versus Cycles, Base Undamaged Specimen S/N BP-1, Second Stress Level.

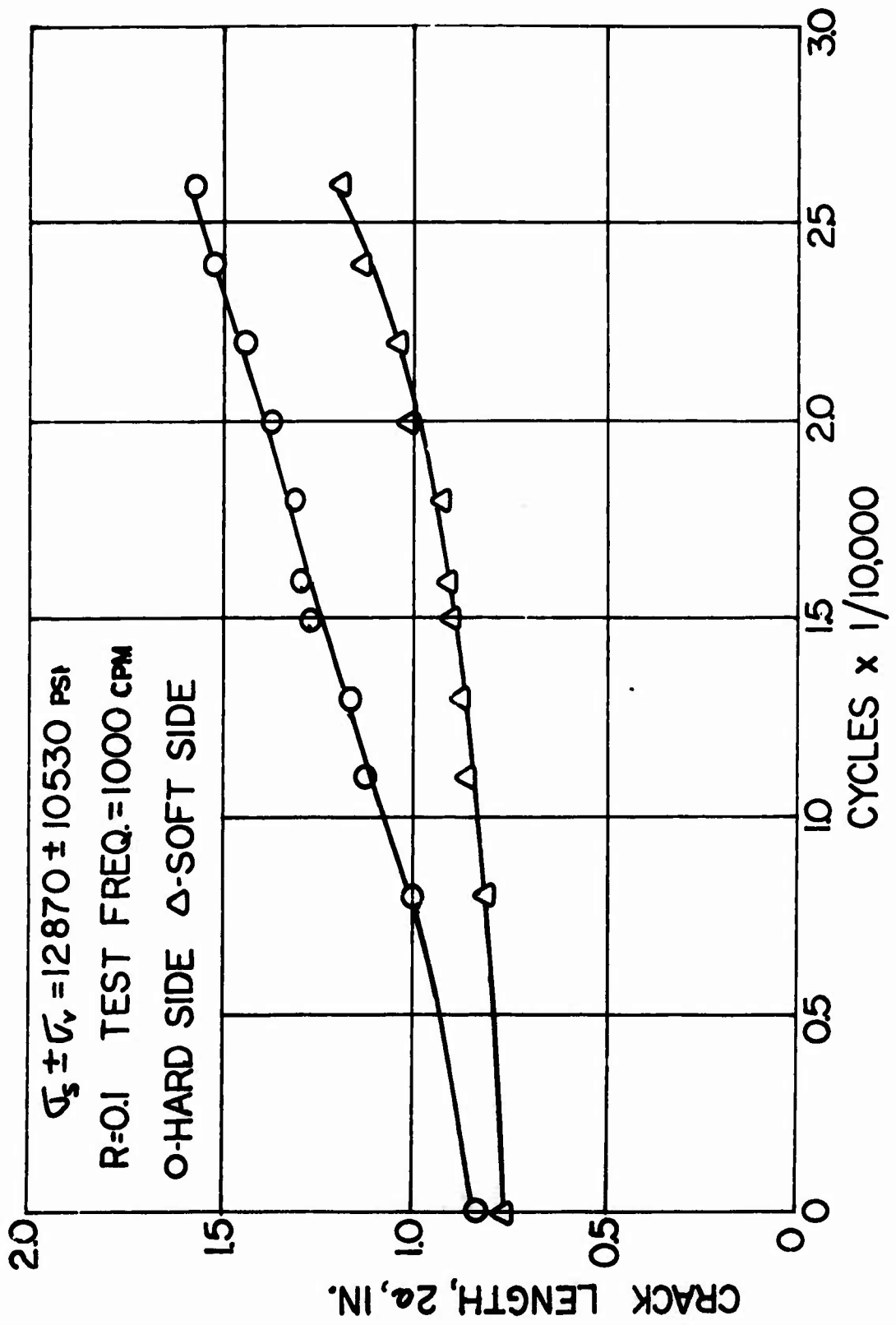


Figure 70. Crack Length Versus Cycles, Base Undamaged Specimen S/N BP-1, First Stress Level.

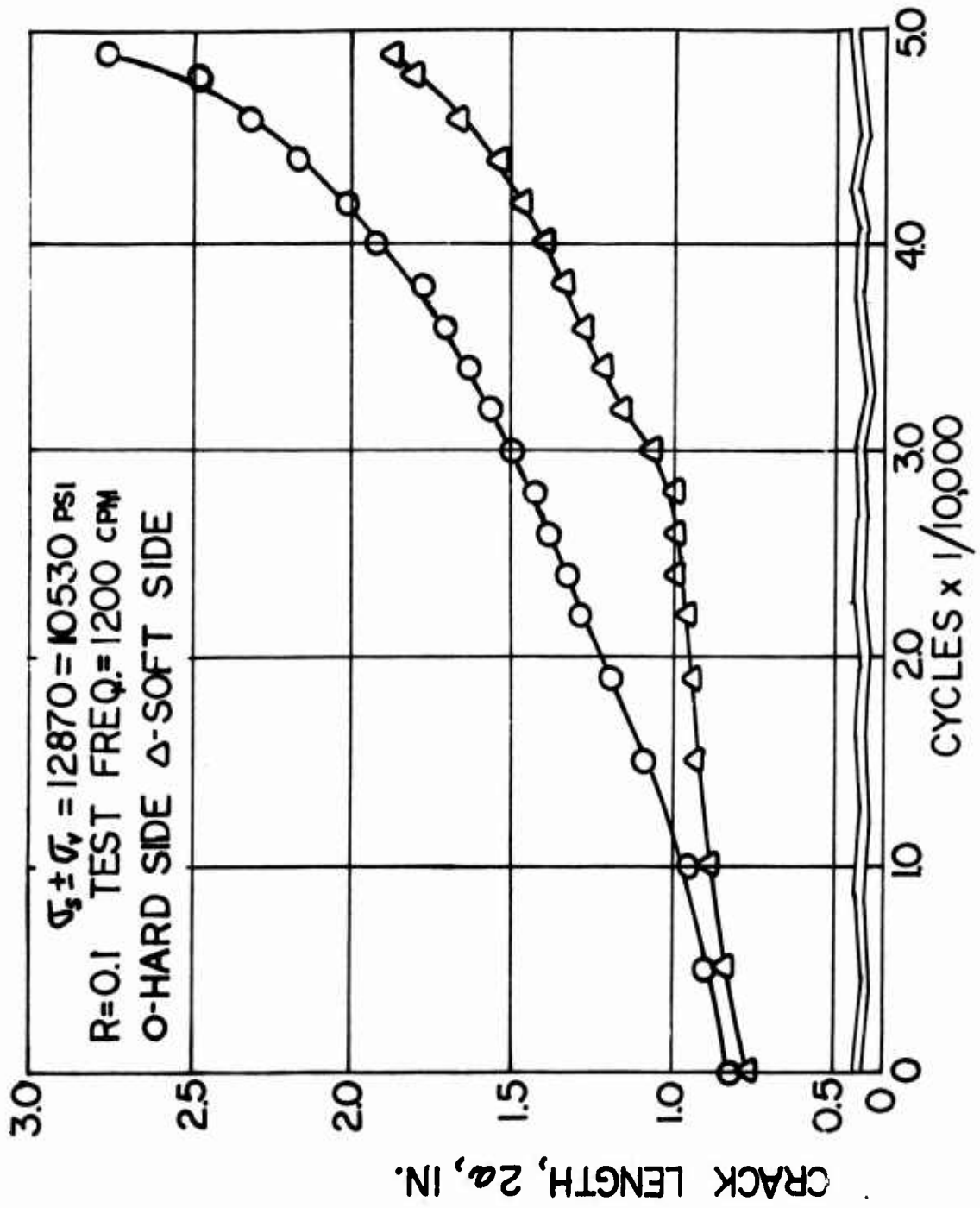


Figure 71. Crack Length Versus Cycles, Base Undamaged Specimen S/N BP-3.

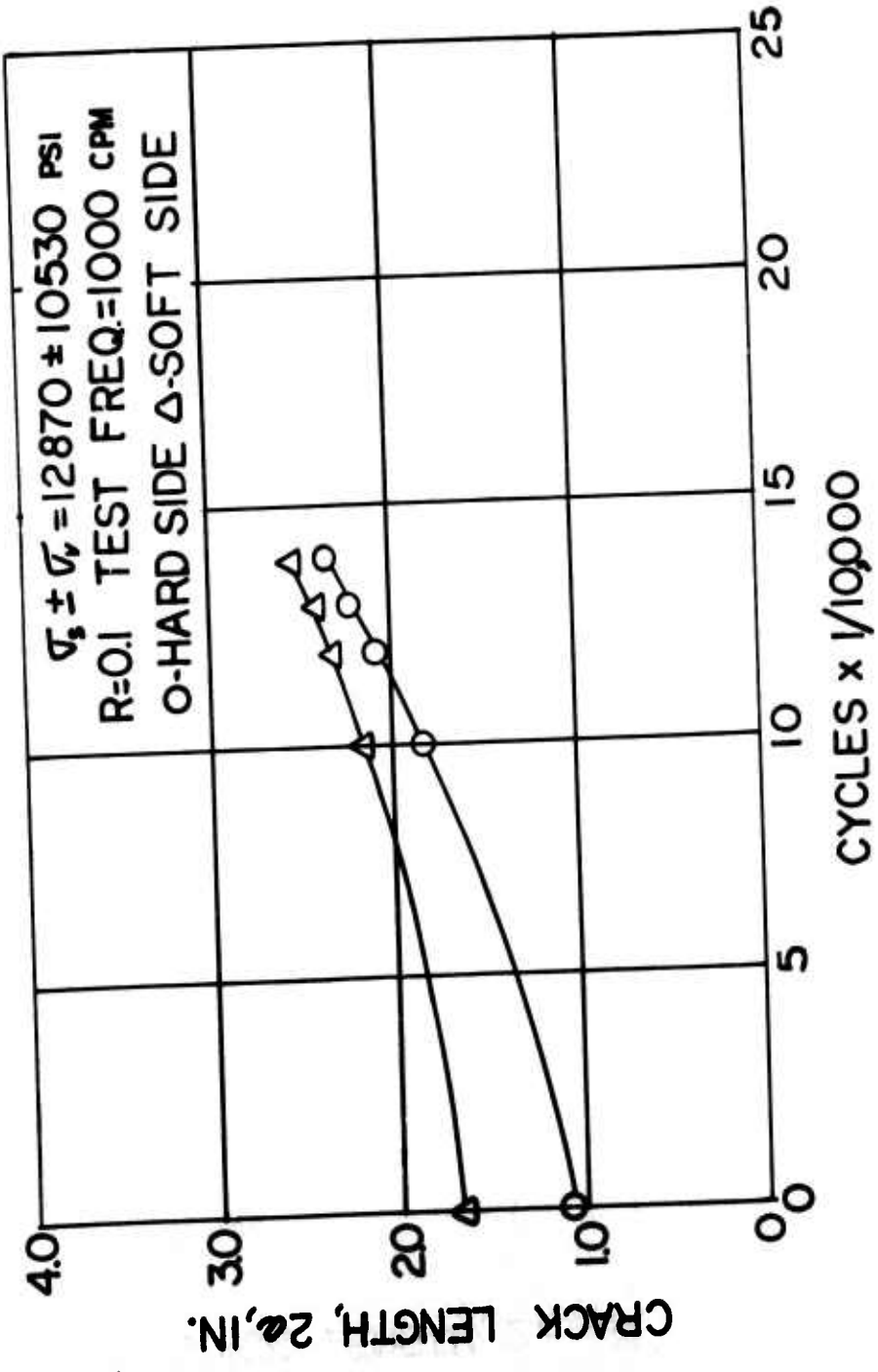


Figure 72. Crack Length Versus Cycles, Welded Undamaged Specimen S/N WC-1.

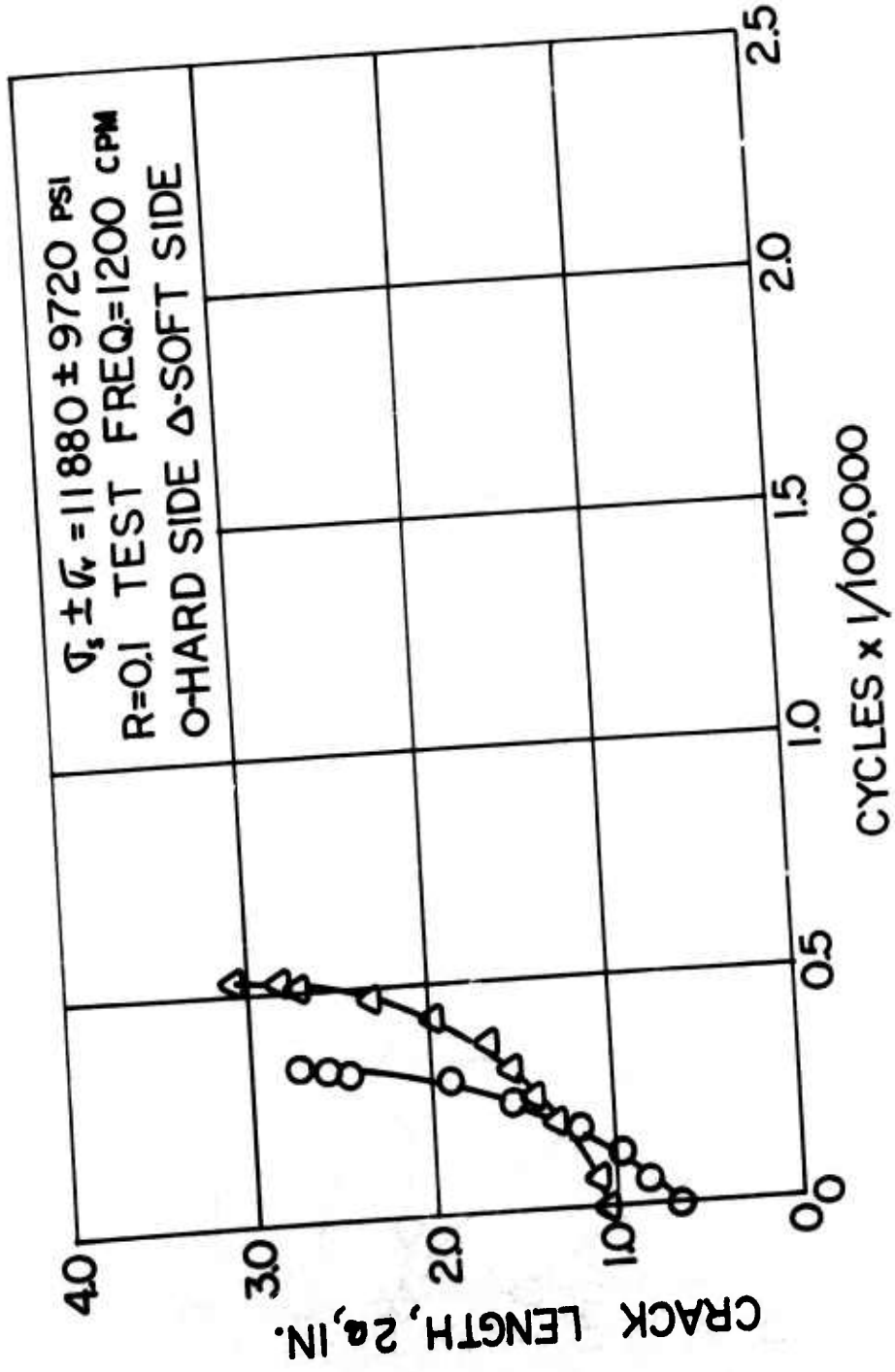


Figure 73. Crack Length Versus Cycles, Welded Undamaged Specimen S/N WC-2.

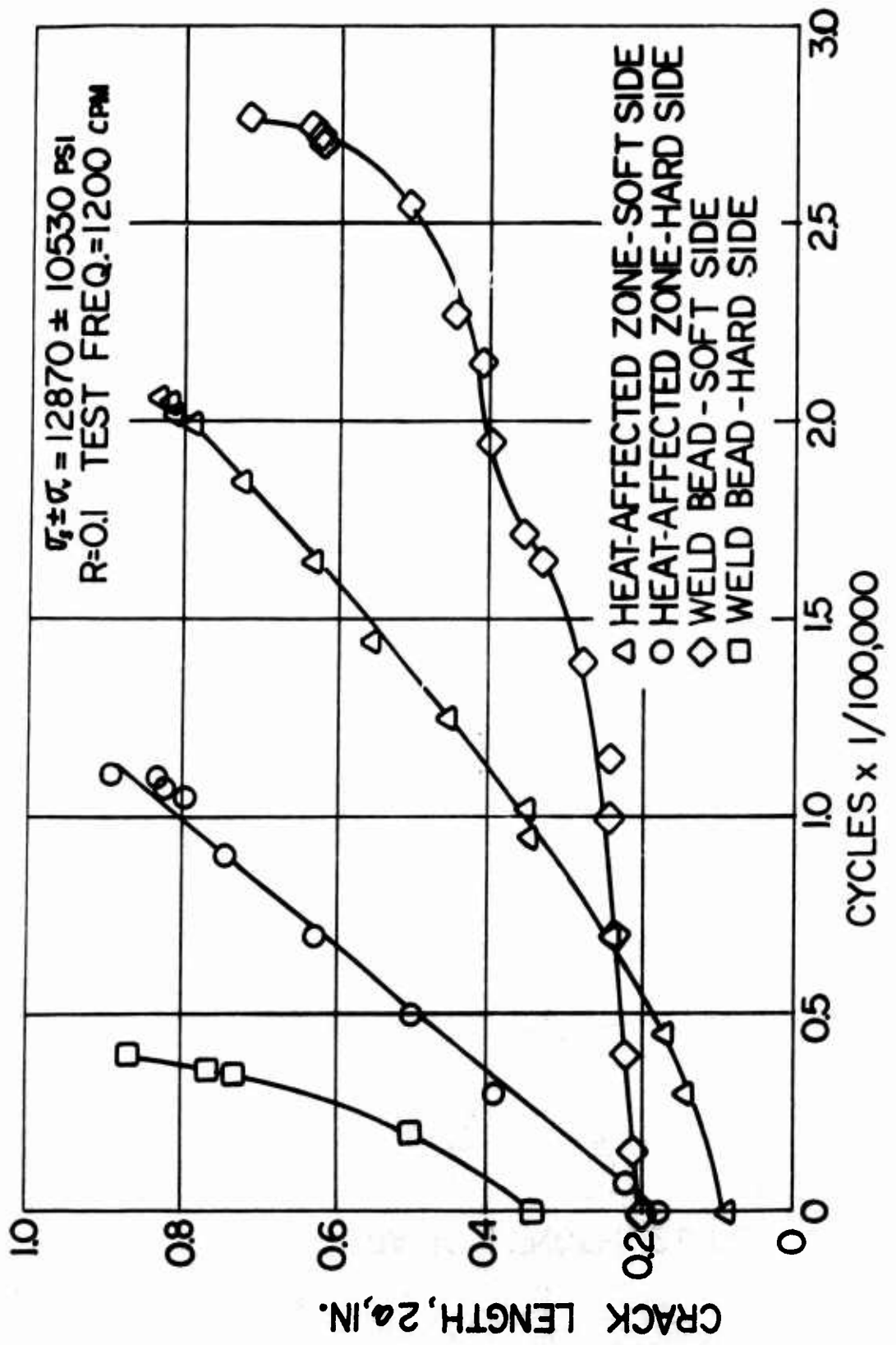


Figure 74. Crack Length Versus Cycles, Welded Undamaged Specimen S/N WC-3.

specimen is shown in Figure 75.

Cracks in the welded specimens initiated subsurface in the fusionless area (due to lack of penetration) in the soft side of the specimen. The crack became visible on the soft side surface, then propagated through the thickness of the material before becoming visible on the hard side. The crack propagated along the path of least resistance, i.e., the fusionless area in the center of the weld bead. The fracture surface of a typical failed welded undamaged crack propagation specimen is shown in Figure 76.

Fracture Toughness

Fracture toughness (K_I) testing was performed using the three-point bend specimen design, test procedures and analysis of the recommended ASTM testing procedure, Reference 17. Although this ASTM standard is not designed for testing of nonhomogeneous material, the test procedure was strictly adhered to in order to provide the most valid results possible.

Specimens having the configuration shown in Figure 77 were prepared. Fatigue precracking was accomplished in the cantilever beam loading setup shown in Figure 78 using a Krouse Fatigue Test Machine (2100 cpm). Reversed bending was used to initiate the crack from the machined notch and to propagate it to the final nominal crack length of 1/2 inch.

Tests were performed on a Riehle PS-20 Universal Testing Machine, using a three-point loading fixture of standardized design. Loads were determined by the output of a calibrated SR-4 type U-1 load cell, 5,000-pound capacity. Deflection across the notch was measured by means of attachable knife edges and an MTS Model 632.01 deflection gage. The ambient specimen testing setup is shown in Figure 79. Load-deflection graphs were automatically plotted using an Electro-Instruments General Purpose Amplifier Model 420 and Moseley X-Y Recorder. A physical calibration of the deflection gage and resistance calibration values for load and deflection were obtained prior to testing. Temperature and humidity at time of testing were recorded. The loading rate was about 3,000 pounds per minute, which is approximately equivalent to a stress intensity rate of 45 ksi - $\sqrt{\text{in.}}$ per minute for these specimens.

Specimens were tested at -65°F , ambient and $+250^{\circ}\text{F}$. Specimens were cooled and heated by use of a Conrad-Missimer Model FTU 3.4 Environmental Chamber, using the same test setup and procedures as for the room temperature tests. Temperature was monitored by use of a thermocouple attached to each specimen being tested. At least 1/2 hour was allowed for each specimen to reach equilibrium after the thermocouple registered the required temperature.

The stringent requirements of ASTM Standard E-399 were not met in several areas. Fracture toughness values were calculated for fatigue crack length-to-width ratios (a/w) of 0.45 to 0.55. Fatigue precracking of some test specimens exceeded the 0.55 value due to the crack running under the micro-wire shutoff system used during precracking. A linearity requirement of the load-deflection graph was exceeded in some tests. Any one of the above,

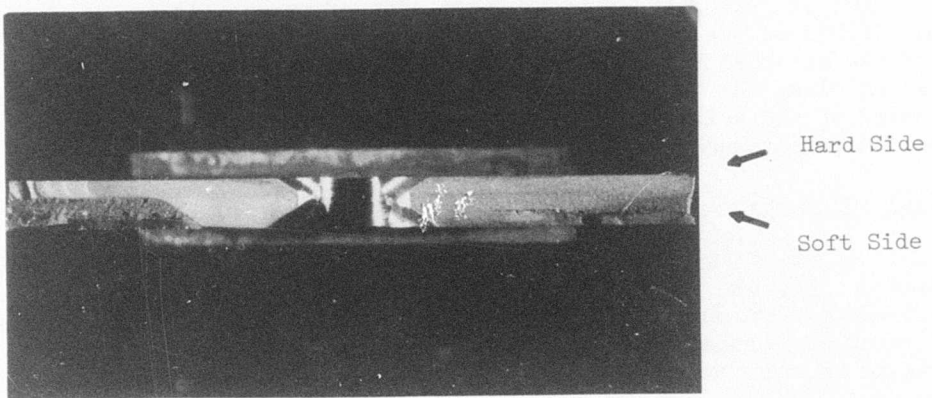


Figure 75. Typical Fracture Surface, Base Undamaged Crack Propagation Specimen.
~ 1X

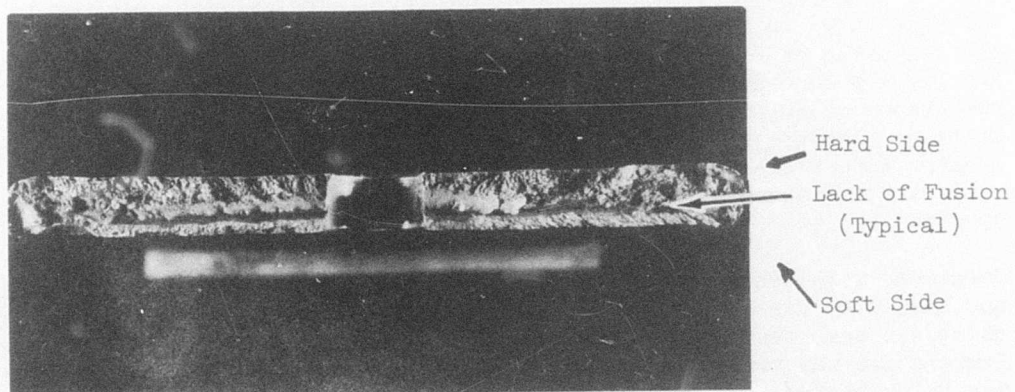
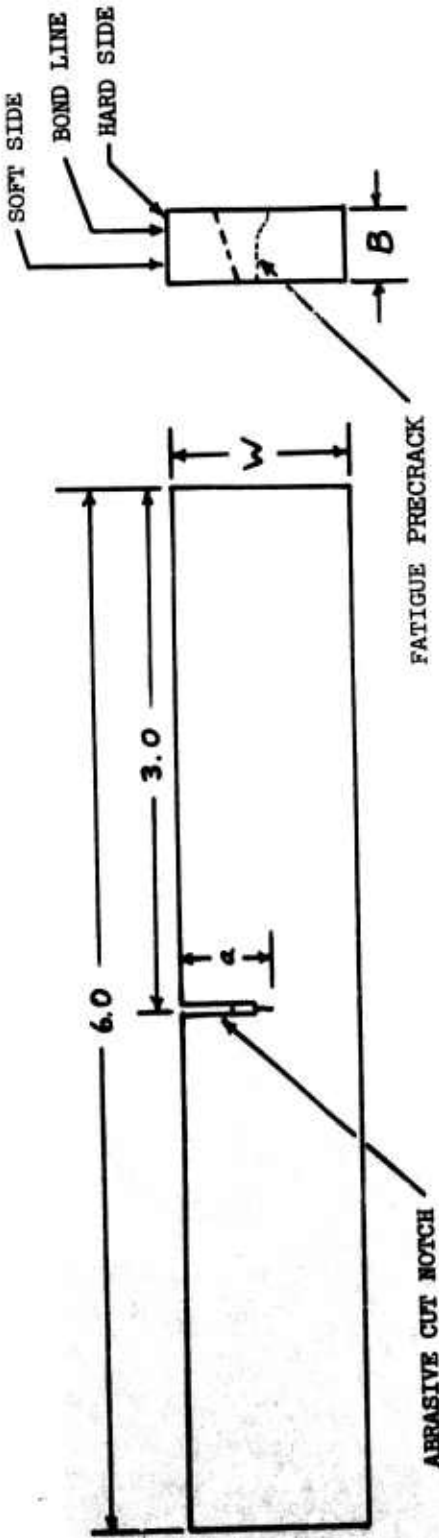


Figure 76. Typical Fracture Surface, Welded Undamaged Crack Propagation Specimen.
~ 1X



B = SPECIMEN THICKNESS, $0.305 \pm .002$ NOMINAL

W = SPECIMEN HEIGHT, $1.100 \pm .100$ NOMINAL

a = LENGTH OF FATIGUE PRECRACK,
 $0.45W$ to $0.55W$

ALL DIMENSIONS IN INCHES

Figure 77. Three-Point Bend Fracture Toughness Specimen.

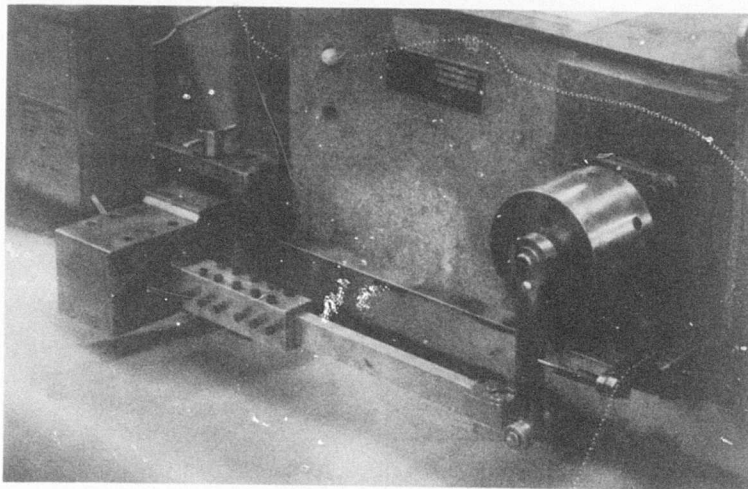


Figure 78. Cantilever Beam Fracture Toughness Precrack Setup.

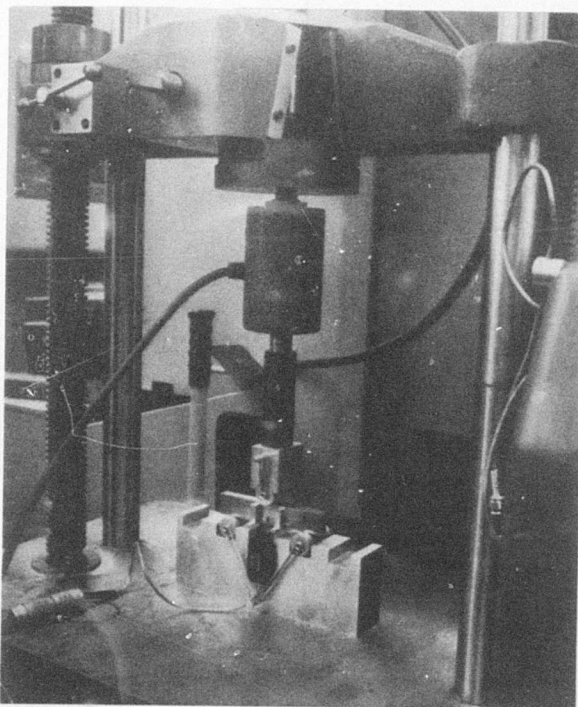


Figure 79. Ambient Fracture Toughness Test Setup.

plus the fact that the material is nonhomogeneous, lead to an invalid test as far as ASTM E-399 is concerned. However, the use of this specification does provide a means for generation of controlled data and permits comparison of the results.

Results for the plane-strain fracture toughness tests conducted are presented in Table XXX. Tests of DHS performed at -65°F resulted in an average value of $K_{IC} = 64 \text{ ksi } \sqrt{\text{in.}}$ as compared to $K_{IC} = 57 \text{ ksi } \sqrt{\text{in.}}$ for the ambient tests and $K_{IC} = 52 \text{ ksi } \sqrt{\text{in.}}$ for tests performed at +250°F.

Stress Corrosion Susceptibility

Since the fuselage will be subject to exposure to the elements, the possibility of crack initiation by environmental mechanisms or weakening of the structure by corrosive attack was investigated. Since the weld is the lowest strength area, and since the presence of the weld bead might permit electrochemical attack, the investigation was restricted to welded samples. The specimens, which were 1 inch by 21 inches, with a weld located 3 inches from one end, were stressed to 10, 30 or 50 ksi by means of the cantilever loading fixture shown in Figure 80. Four specimens were tested for 500 hours at each stress level, two with the hard side up, and two with the soft side up. To accelerate testing, a specially designed cabinet was used to provide a highly corrosive 5% sodium chloride, 95°F salt spray environment.

For a cantilever beam, the stress may be expressed as

$$\sigma = \frac{6PL}{2bt} \quad (28)$$

where σ is the stress on the outer fiber in psi
P is the load applied to the beam end in pounds
L is the beam length in inches
b is the beam width in inches
t is the thickness in inches

However, since the fixture used was not a perfect cantilever beam, and because it is more convenient to measure the maximum deflection of the beam rather than applied load, the calibration curve shown in Figure 81 was established. A strain-gaged specimen was placed in the fixture, various loads applied to the end of the beam, and the beam deflection and resultant outer fiber stress recorded. The calculated deflections were also plotted, from the equation

$$\delta_{max} = \frac{2}{3} \frac{\sigma L^2}{Et} \quad (29)$$

σ , L and t are as in Equation 28
E is Young's modulus
 δ_{max} is the beam deflection at the end in inches

Thereafter, to apply a given stress, the theoretical beam deflection was calculated, and the deflection actually required was read from the

TABLE XXX. FRACTURE TOUGHNESS TEST RESULTS

T/N	S/ $\sqrt{in.}$	K_f (max) (ksi - $\sqrt{in.}$)	Cycles $(\times 10^{-3})$	w (in.)	B (in.)	a(avg)* (in.)	a/v** (in.)	Test Temp. (°F)	Loading Rate (lb/min)	P_Q (1b)	P(max) (1b)	K_{Ic} (ksi - $\sqrt{in.}$)
1	BK-7	30000	34	1.188	.305	.560	.471	+ 72	3000	2440	2640	60.0
2	BK-1	30000	44	1.171	.306	.620	.529	+ 72	3000	1920	2220	57.9
3	BK-4	30000	38	1.145	.306	.665	.581	+ 72	3000	1530	1690	57.8
4	BK-6	30000	112	1.149	.305	.720	.627	+ 72	3000	1180	1320	52.4
5	BK-2	30000	94	1.113	.307	.590	.530	+250	3000	1480	1740	48.1
6	BK-12	30000	44	1.213	.304	.600	.495	+250	3000	2020	2280	52.0
7	BK-3	30000	37	1.069	.304	.485	.454	+250	3000	1730	2110	35.6***
8	BK-5	30000	39	1.109	.306	.545	.491	+250	3000	1930	2010	55.0
9	BK-10	30000	59	1.126	.307	.595	.528	- 65	3000	1960	2060	62.0
10	BK-11	30000	107	1.213	.305	.625	.515	- 65	3000	1680	1840	45.8***
11	BK-9	30000	84	1.208	.306	.565	.468	- 65	3000	2820	2870	67.0

* Fatigue precrack did not meet requirement of Section 7.2.3 of E-399 in all cases.

** For a/w > 0.55, K_{Ic} was determined using the procedures of Reference 19.*** Fatigue crack departed from plane of symmetry of notch ($> 10^{\circ}$).

**** Displacement gage slipped during test.

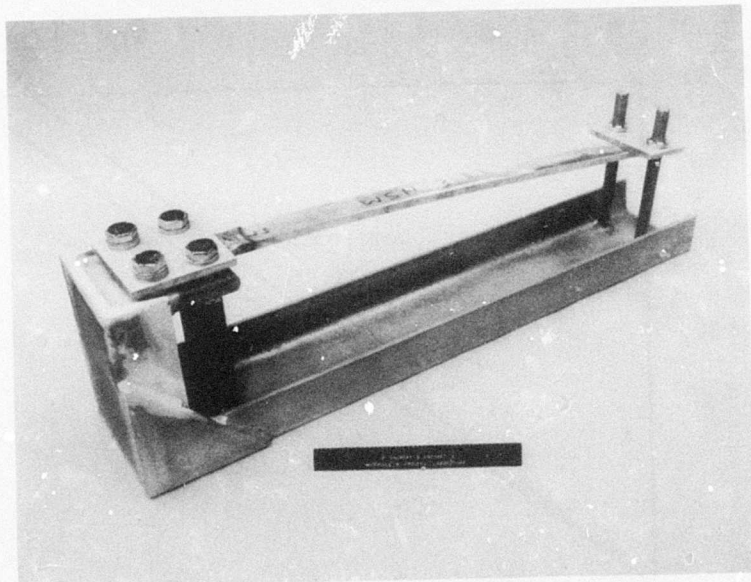


Figure 80. Cantilever Beam Fixture for Environmental Cracking Susceptibility Test.

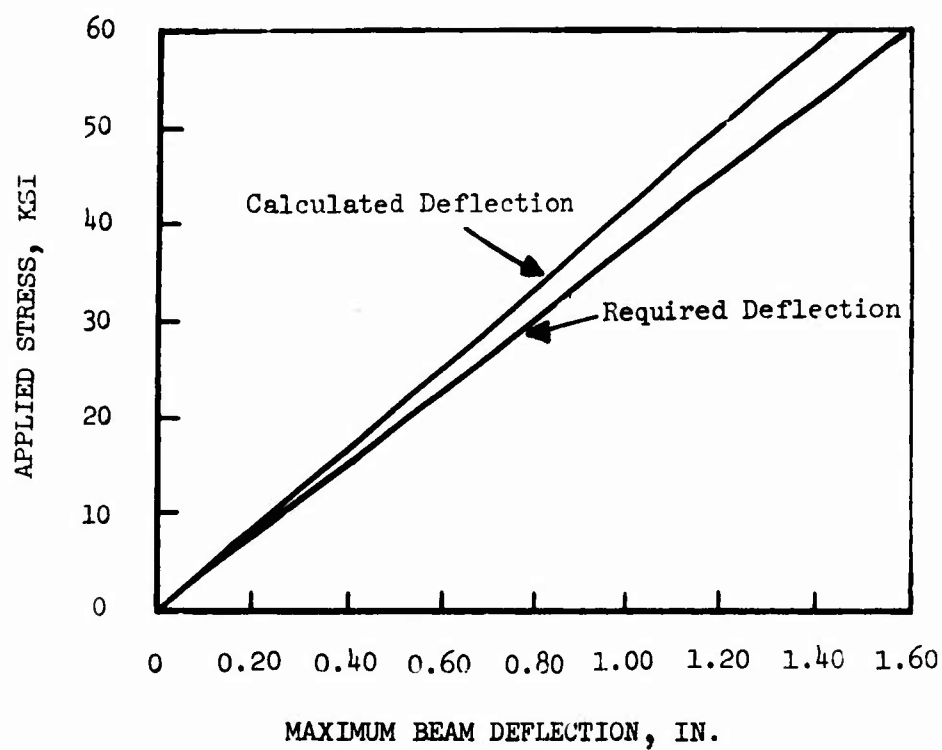


Figure 81. Deflection Calibration for Cantilever Beam Loaded Stress Corrosion Specimens.

calibration curve.

Typical specimen appearance after 500 hours' exposure is shown in Figure 82. Weighing of the specimens before and after exposure showed no discernible trend of percentage weight gain versus applied stress (Figure 83). If the specimens were allowed to dry and then grit-blasted to remove the rust, a trend of weight loss versus stress was found (Figure 84). Since soft side attack was generally less severe than the local deep pitting on the hard side, the differences between hard and soft side up are not unexpected.

The specimens after exposure and grit-blasting are shown in Figure 85. In no case did fracture occur during test, and in only one case was a crack found. Tensile tests conducted after exposure showed a clear trend of decreasing strength with applied stress (Figure 86). All of the test results are shown in Table XXXI.

This testing was performed on the principle of a worst case analysis. The actual fuselage structure will be provided with proper protection so that environmental exposure and corrosive attack do not occur except in highly unusual circumstances.

Residual Stress Measurement

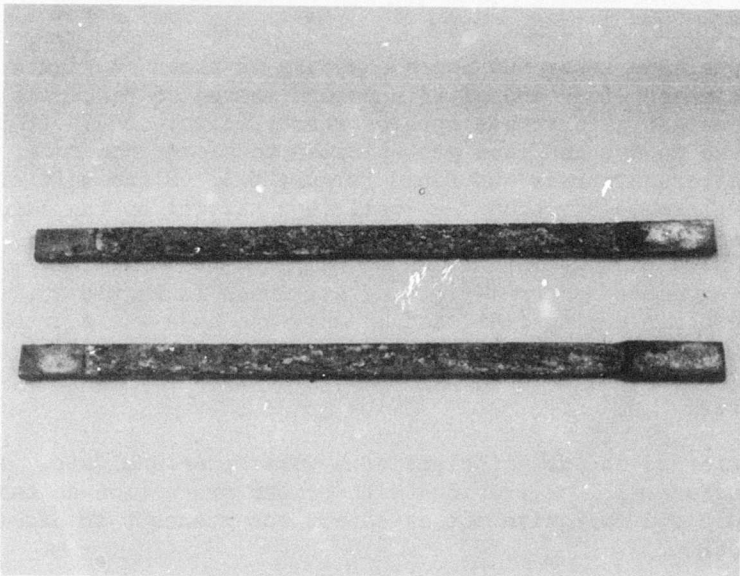
Although they are already present in the fatigue, static and residual strength results, it is of interest to determine the magnitude of the residual stresses introduced into the material by welding and friction cutting, and to examine how changes in procedure might affect engineering properties. For this reason, x-ray diffraction techniques were utilized to allow determination of the magnitude and distribution of stress in the vicinity of the welds. The theory of residual stress measurement by x-ray diffraction, and the derivation of the required equations, are beyond the scope of this report, but may be found in Reference 20.

In practice, the maximum intensity angle is determined for a particular diffraction peak at normal incidence ($\psi = 0^\circ$) and at some angle (in this case $\psi = 45^\circ$). The residual stress is determined from

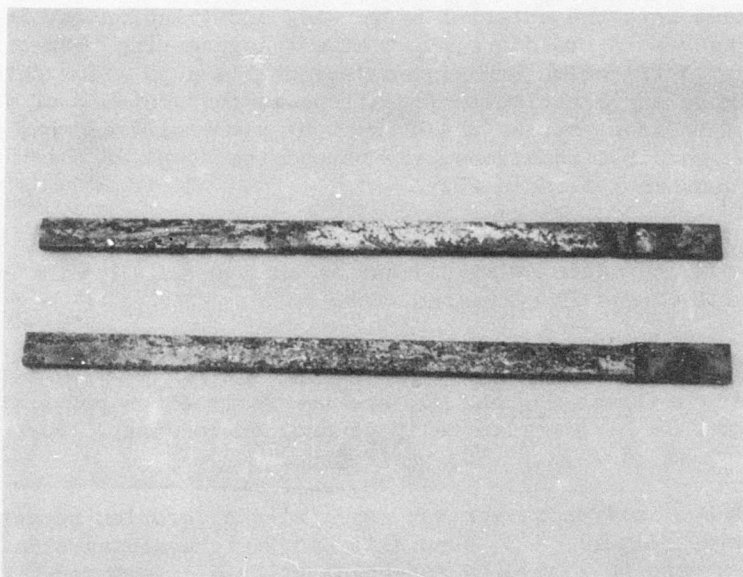
$$\sigma = A (2\theta_0 - 2\theta_\psi) \quad (30)$$

where σ is the residual stress, $2\theta_0$ and $2\theta_\psi$ are the diffraction peaks at 0° and 45° incidence, and A is an experimentally determined constant. For steel, the accepted value of A is 86,300 psi/degree.

A General Electric XRD-6 Diffractometer was used, with a chromium target tube and vanadium oxide filter. A 3° beam slit and 0.2° receiving slit were used. Power settings were 40 kilovolts potential at 20 milliamperes. Measurements of intensity of the 211 plane were performed at $2\theta = 155, 156$ and 157° . These intensity values were then corrected for absorption and Lorentz polarization factors, and the peak located by means of the three-point parabola technique (Reference 21). This technique results in an uncertainty in measurement of ± 3 ksi.



Exposed
Side



Down
Side

Figure 82. Typical Specimen Appearance After 500-Hour Exposure.

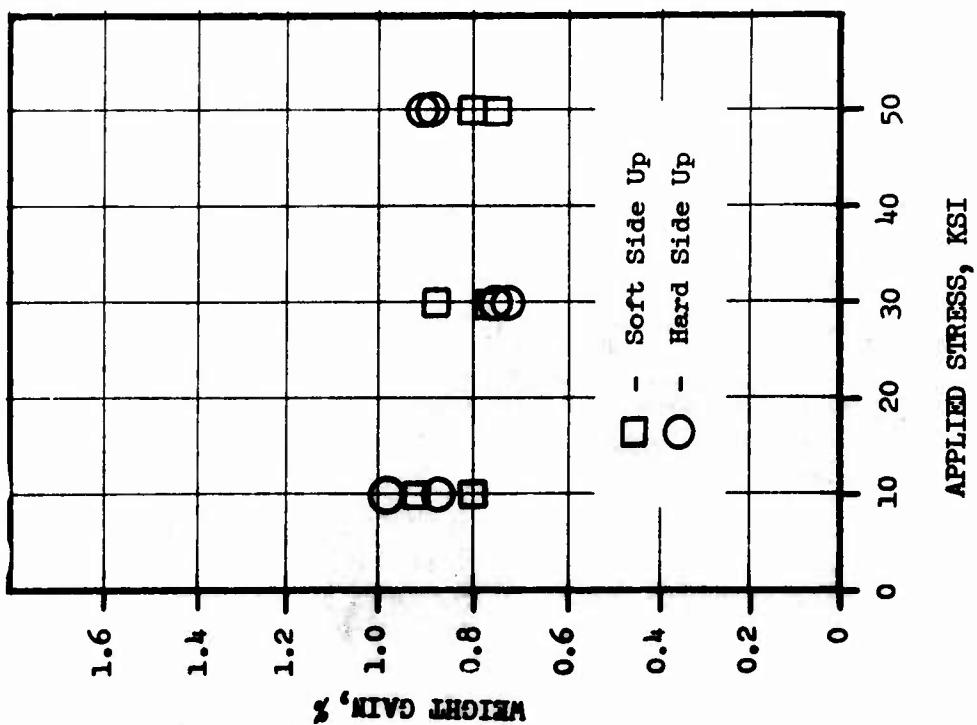
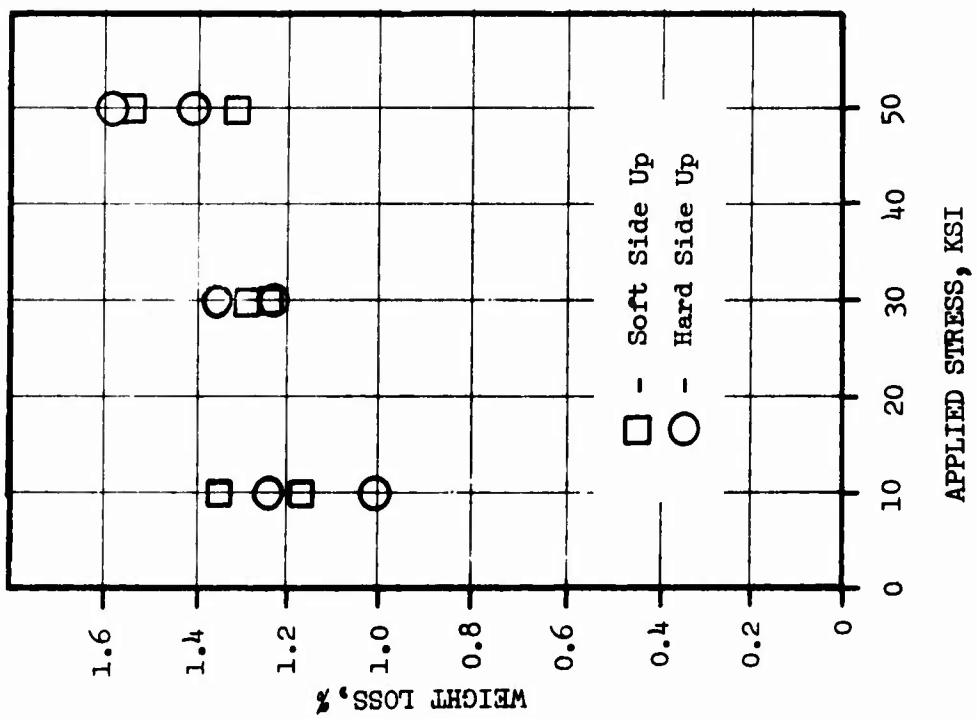
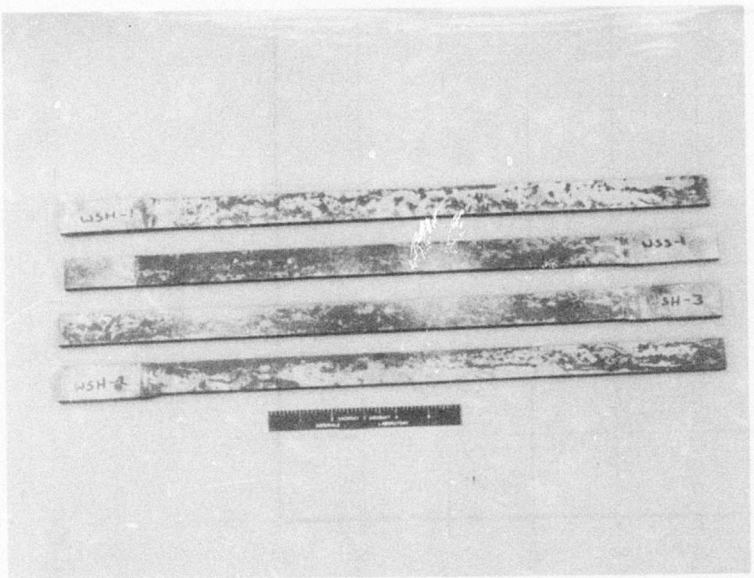


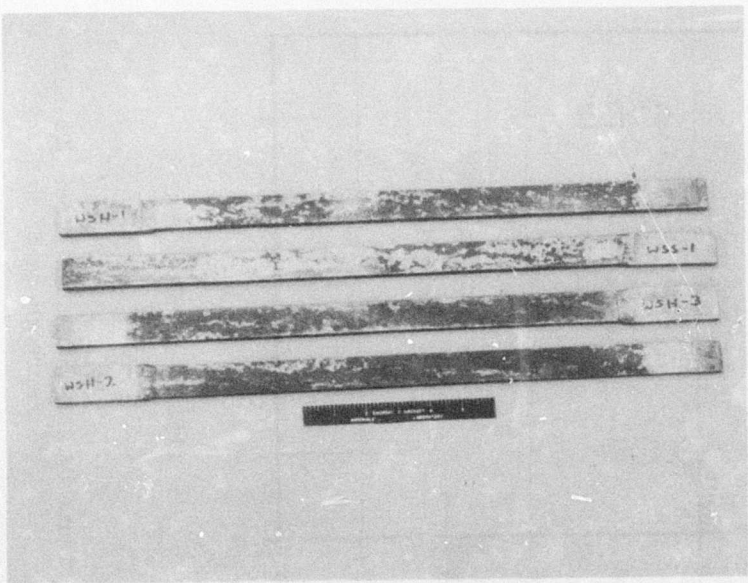
Figure 83. Weight Gain After 500-Hour Exposure to 5% NaCl, 95°F.

Figure 84. Weight Loss After Removal of Corrosion Product.



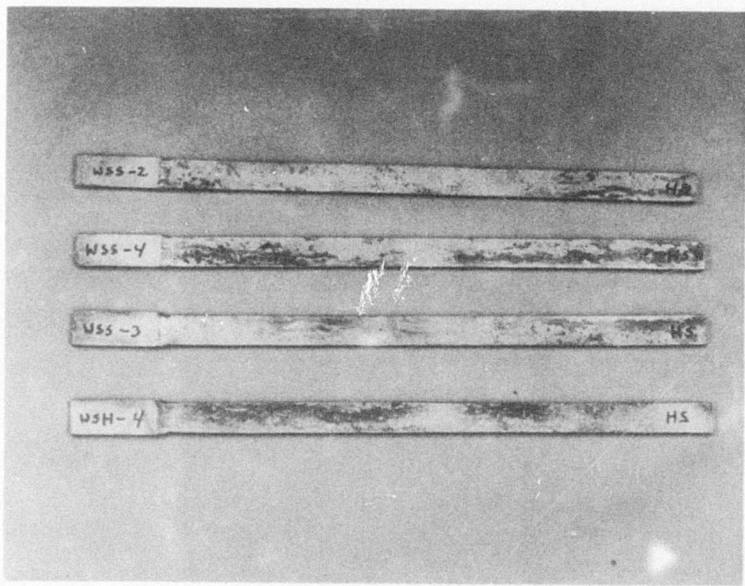
Soft
Sides

Tests 1 to 4



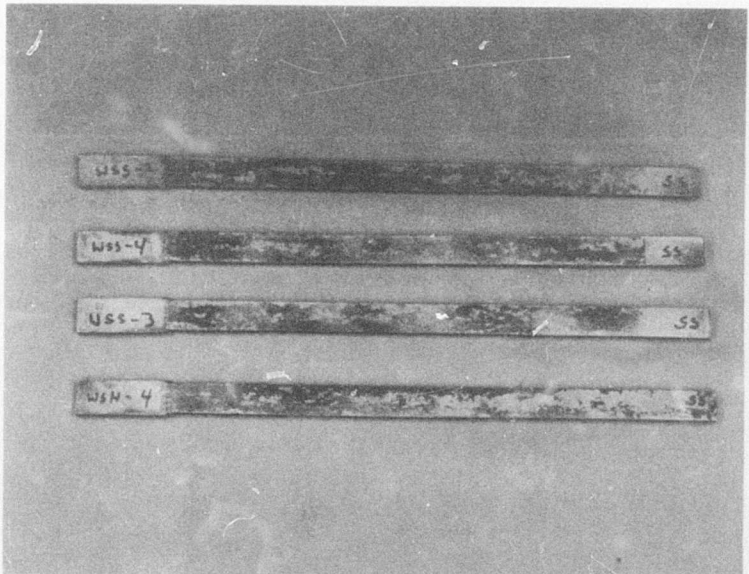
Hard
Sides

Figure 85. Specimen Appearance After Removal of Corrosion Product.



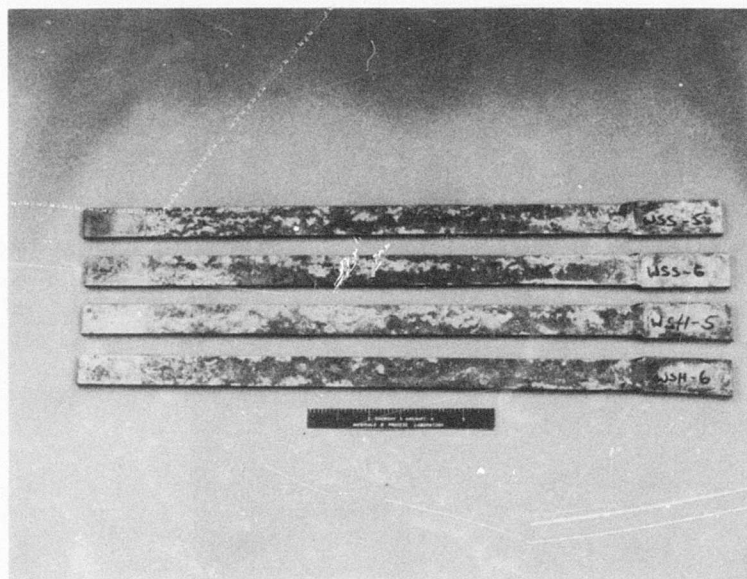
Hard
Sides

Tests 5 to 8



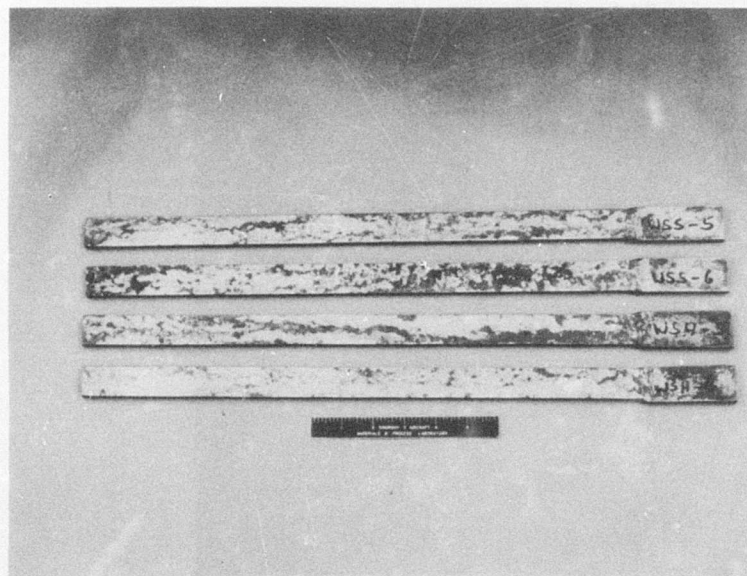
Soft
Sides

Figure 85. (Continued).



Exposed
Side

Tests 9 to 12



Down
Side

Figure 85. (Continued).

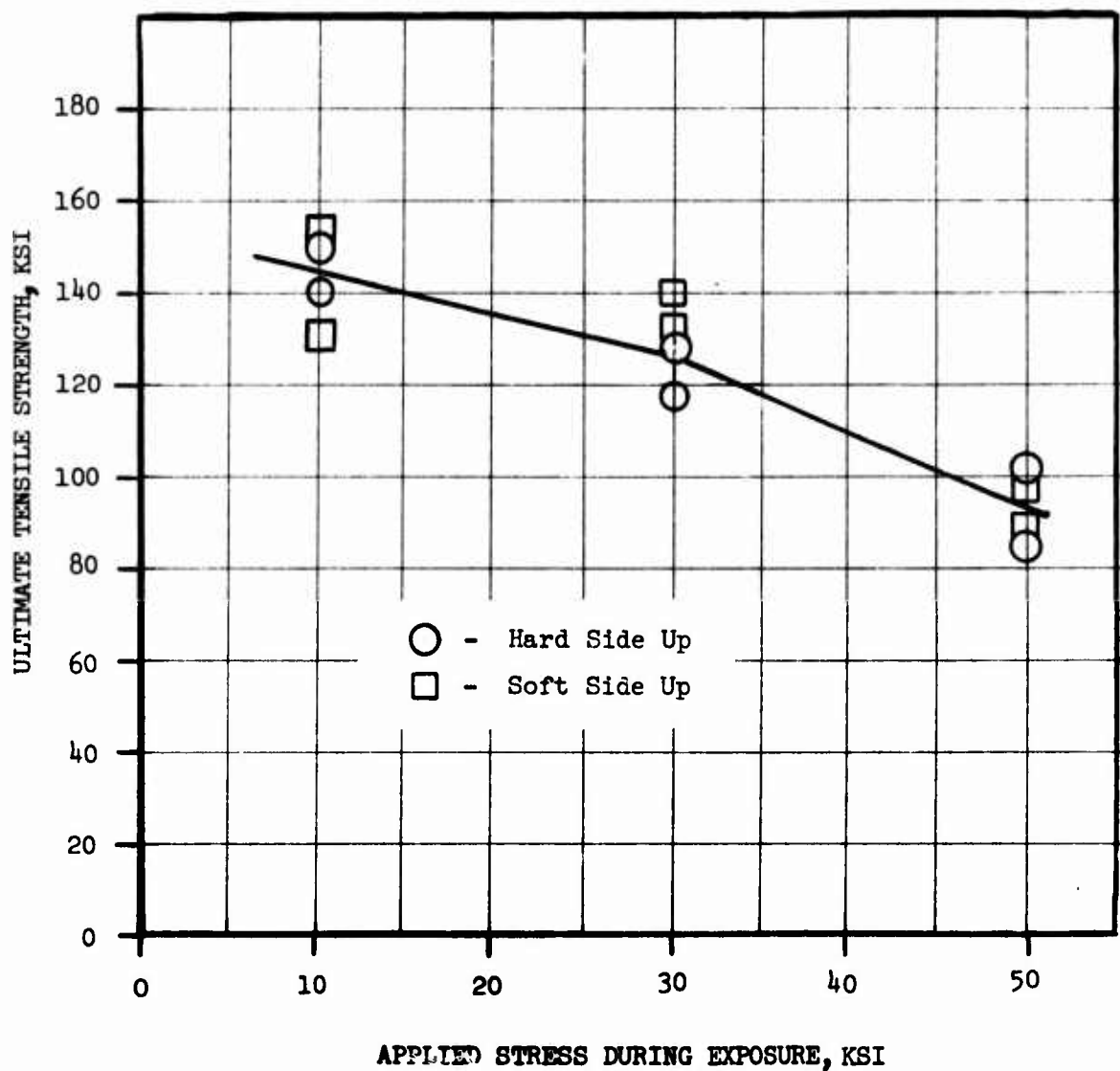


Figure 86. Remnant Tensile Strength After 500-Hour Exposure to 5% NaCl at 95°F.

TABLE XXXI. STRESS CORROSION SUSCEPTIBILITY RESULTS

Specimen	Side Exposed	Stress (psi)	Initial Weight (grams)	Weight Gain (%)	Weight Loss (%)	Tensile Strength After Exposure (psi)
WSH - 1	Hard	10,000	829.4	0.87	1.01	149,500
WSH - 2	Hard	30,000	835.0	0.74	1.23	129,500
WSH - 3	Hard	50,000	833.2	0.90	1.58	86,500
WSH - 4	Hard	50,000	840.8	0.89	1.41	102,000
WSH - 5	Hard	10,000	843.9	0.99	1.23	140,500
WSH - 6	Hard	30,000	834.2	0.74	1.36	118,500
WSS - 1	Soft	50,000	821.3	0.80	1.32	89,300
WSS - 2	Soft	50,000	834.2	0.75	1.55	96,000
WSS - 3	Soft	30,000	850.3	0.78	1.24	139,000
WSS - 4	Soft	30,000	834.0	0.88	1.25	132,000
WSS - 5	Soft	10,000	839.6	0.92	1.36	149,000
WSS - 6	Soft	10,000	843.9	0.80	1.18	132,500

* After 500-hour exposure to 5% NaCl at 95°F.

** After removal of corrosion product by grit blasting.

The measured residual stresses are mapped in Figure 87. In general, both tensile and compressive stresses were fairly low in magnitude and do not appear to present any difficulties. Friction sawing was found to have a negligible effect beyond 1/4 inch from the location of the cut. As expected, stress magnitude increased as the measurement location neared the weld, and also as the end of the weld bead was approached. The latter effect was due to lesser annealing time from the heat of welding. The stresses appeared to reach steady state of ± 10 ksi approximately 1 inch from the end of the weld.

Residual Static Strength

Sixty 6-inch by 14-inch specimens, 27 welded and 33 base, were impacted at zero stress, on the hard side, with a single caliber .30 AP round at 0° obliquity at the velocity specified in the contract. Full ballistic test data may be found in the separate Confidential Appendix to this report. Ballistic tests were conducted at the Army Materials and Mechanics Research Center, Watertown, Massachusetts.

The welded specimens were equipped with an adhesively bonded protector plate and, generally, were not penetrated. Except for three cases of impingement through the cover, damage was restricted to the protector. Temperature at time of impact was of little or no effect.

However, the temperature of impact determined the type of damage observed on the base specimens. Cratering, or penetration with cracking, occurred at ambient temperature, penetration without cracking at $+250^{\circ}\text{F}$, and cratering with extensive cracking at -65°F . Typical resultant damage to these specimens is shown in Figures 88 to 91. The cracks have been brought out by photographing the specimens under ultraviolet light after fluorescent magnetic particle inspection.

Five base and five welded from each temperature were tensile tested to determine residual static strength. Test procedure was the same as for the tensile tests described previously. The results are shown in Tables XXXII and XXXIII.

Analysis of the welded specimen data showed no clear effect of ballistic impact or of temperature. The range of strength values is identical to that shown for undamaged welds. Again, most of these specimens showed internal lack of fusion due to the welding problems discussed above. No clear trend is apparent after analysis. Almost 100% residual strength was always found. This is to be expected since the protector plate prevented penetration.

The as-received specimens, however, strongly showed the effect of impact, with only 25-30% residual strength after impact. Interestingly, there was only a slight difference observed between penetrated (69-81 ksi) and cratered specimens (75-91 ksi) as compared to the loss from the undamaged strength (290 ksi). If the values for the penetrated specimens are corrected for loss of area, they become 74 to 87 ksi, essentially identical to that found for cratered (i.e., impacted but unpenetrated) specimens. This suggests that the cracking and shock wave effects occurring on impact have a much

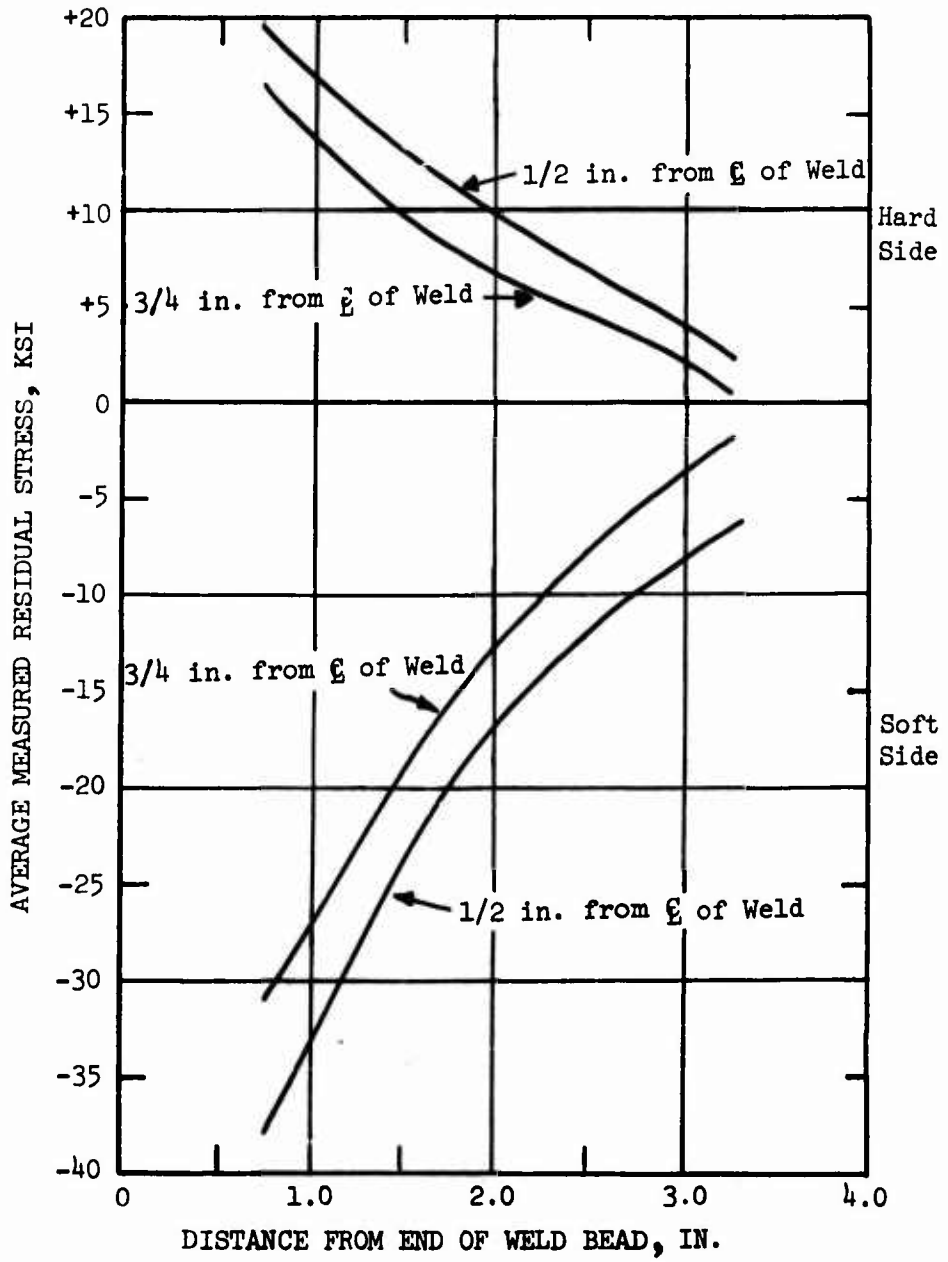
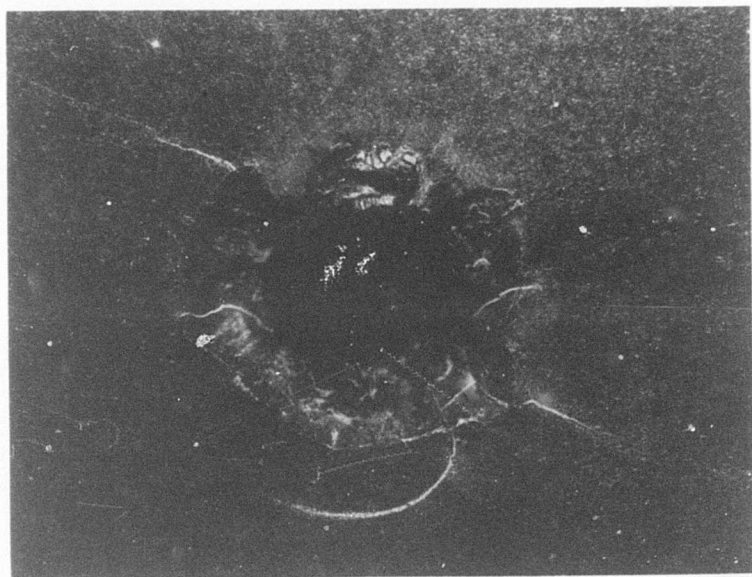
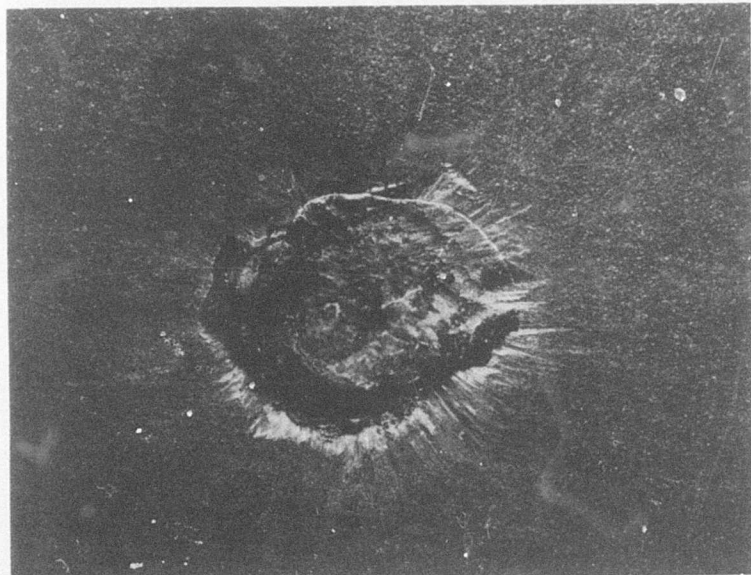


Figure 87. Residual Stress Distribution.



~ 4X

Figure 88. Ballistic Penetration, Ambient Temperature.



~ 4X

Figure 89. Impact Cratering, Ambient Temperature.

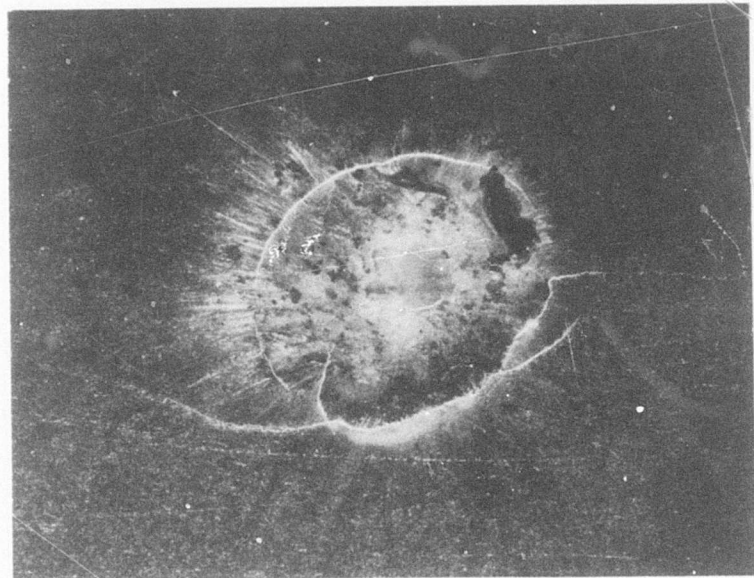


Figure 90. Impact Cratering, -65°F .

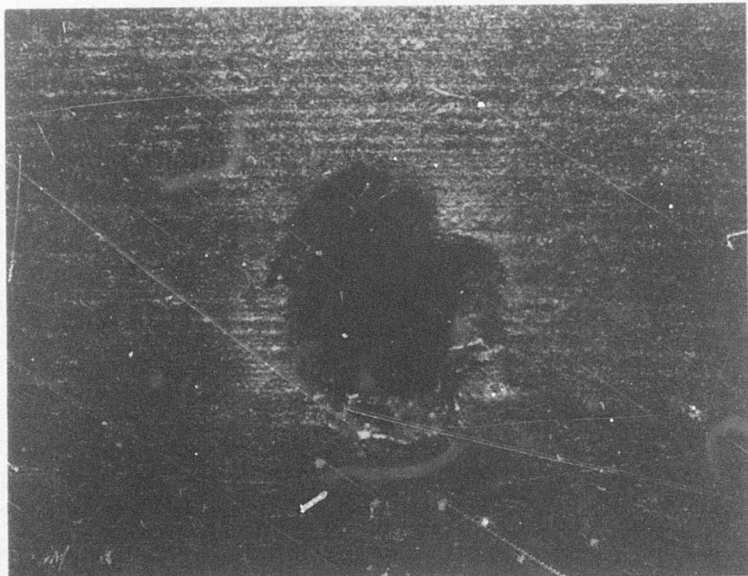


Figure 91. Ballistic Penetration, $+250^{\circ}\text{F}$.

TABLE XXXII. RESIDUAL STRENGTH, BALLISTICALLY IMPACTED BASE SPECIMENS

Specimen	Temperature During Impact	Type of Damage *	Ultimate Tensile Strength	
			Gross (psi)	Corrected ** (psi)
BDA - 5	Ambient	S	87,750	--
BDA - 7	Ambient	S	72,700	--
BDA - 11	Ambient	S	82,750	--
BDL - 3	- 65°F	S	86,150	--
BDL - 4	- 65°F	S	89,400	--
BDL - 9	- 65°F	S	75,800	--
BDL - 10	- 65°F	S	83,300	--
BDL - 11	- 65°F	S	91,500	--
BDA - 1	Ambient	H	75,250	80,400
BDA - 9	Ambient	H	74,800	80,100
BDE - 1	+ 250°F	H	109,750	117,450
BDE - 2	+ 250°F	H	77,100	83,900
BDE - 8	+ 250°F	H	70,700	76,950
BDE - 10	+ 250°F	H	81,300	87,600
BDE - 11	+ 250°F	H	69,950	74,650

* H - Through penetration hole.

S - Surface damage without penetration.

** Corrected for lost area of through hole.

Note: No yielding evident; elongations were 2 - 3%.

TABLE XXXIII. RESIDUAL STRENGTH, BALLISTICALLY IMPACTED WELDED SPECIMENS

Specimen	Temperature During Impact	Ultimate Tensile Strength (psi)
WDA - 2	Ambient	141,200
WDA - 4	Ambient	110,400
WDA - 5	Ambient	97,100
WDA - 8	Ambient	143,850
WDA - 9	Ambient	151,000
WDE - 1	+ 250°F	147,050
WDE - 2	+ 250°F	137,300
WDE - 3	+ 250°F	114,400
WDE - 6	+ 250°F	97,700
WDE - 8	+ 250°F	118,450
WDL - 2	- 65°F	131,200
WDL - 6	- 65°F	153,100
WDL - 7	- 65°F	109,400
WDL - 8	- 65°F	135,100
WDL - 9	- 65°F	126,450

Note: Yield strength and elongation were not recorded, but behavior appears to be similar to that of undamaged welded specimens (Table XXV).

more important effect on residual strength than does penetration. The adhesive bond line on the welded specimens appears to provide protection from such effects.

Residual Fatigue Properties

After ballistic impacting, fourteen of the base panels were returned to Sikorsky for specimen fabrication and testing. The plates were cut on a high speed friction saw to 4 inches by 14 inches with ballistic damage located at the center of the plate. The three-hole bolt pattern was then drilled and used to align the specimens for milling to finished shape. The final surface finish preparation consisted of a longitudinal polish of the reduced section with #240 grit silicon carbide abrasive. The base damaged residual fatigue life specimen configuration is shown in Figures 92, 94 and 95.

Nine of the welded specimens were returned to Sikorsky from AMMRC after ballistic impacting for specimen fabrication and testing. The weld protector plates and adhesive were removed from the specimen blanks to expose any damage to magnetic particle inspection prior to fabrication and testing. The nine specimen blanks were cut on a high speed friction saw to 4 inches by 14 inches. The three-hole bolt pattern was then drilled and used to align the specimens for milling to finished shape. The final surface finish preparation consisted of a longitudinal polish of the reduced section with #240 grit silicon carbide abrasive. The welded damaged residual fatigue life specimen configuration is shown in Figures 93 and 96.

All fatigue testing was axial in nature and utilized spherical bearing grip setups to eliminate bending. Fatigue tests were conducted on an IVY-12 with a 5-to-1 load amplifier (30,000 \pm 30,000 pounds load capacity) and an IVY-20 (12,000 \pm 8,000 pounds load capacity). A Sikorsky calibrated load cell in series with the test specimen and an Ellis BA-12 Bridge, Amplifier and Oscilloscope Console was used as the primary load measuring system. All specimens were tested in the normal laboratory environment at a loading frequency of 1200 cpm. All tests were conducted at a constant R ratio ($\sigma_{min}/\sigma_{max}$) of 0.10.

Four vibratory stress levels were employed for the base damaged specimen condition, and three vibratory stress levels were employed for the welded damaged specimen condition to obtain specimen failures over the range of 1×10^4 to 1.5×10^6 cycles. Specimens were tested to failure or at least 5×10^6 cycles.

Results for the base damaged and welded damaged specimens tested are presented in Tables XXXIV and XXXV respectively. Figures 97 and 98 present the S-N results along with log mean S-N curves for the two conditions.

As shown in the figures, the mean vibratory fatigue strength at 10^7 cycles, R = 0.1, is ± 6.5 ksi for base damaged specimens and ± 7.5 ksi for welded damaged specimens.

A comparison of the log mean S-N curves for the damaged material properties and previously determined undamaged properties is shown in Figure 99.

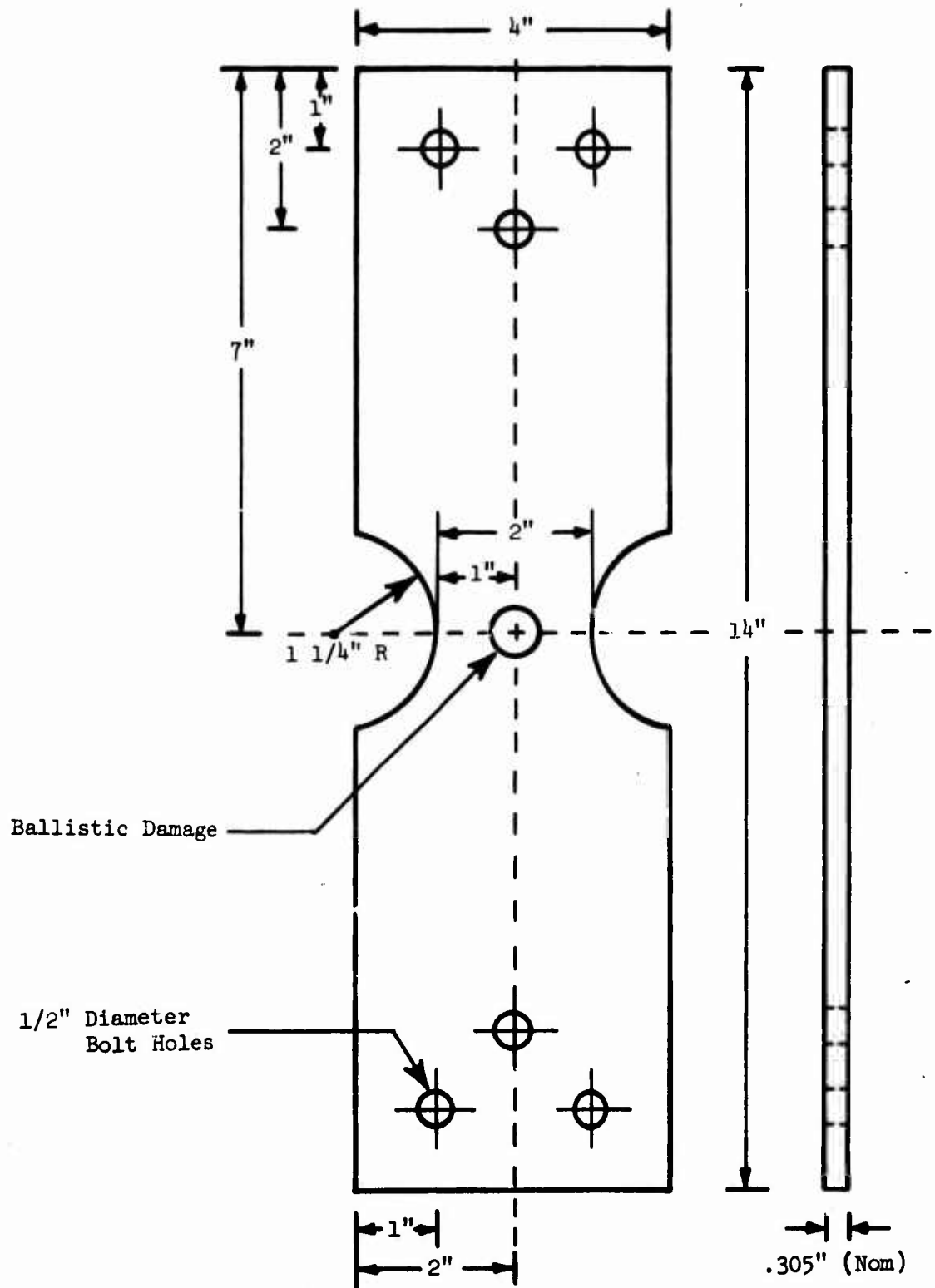


Figure 92. Ballistically Damaged Base Fatigue Test Specimen.

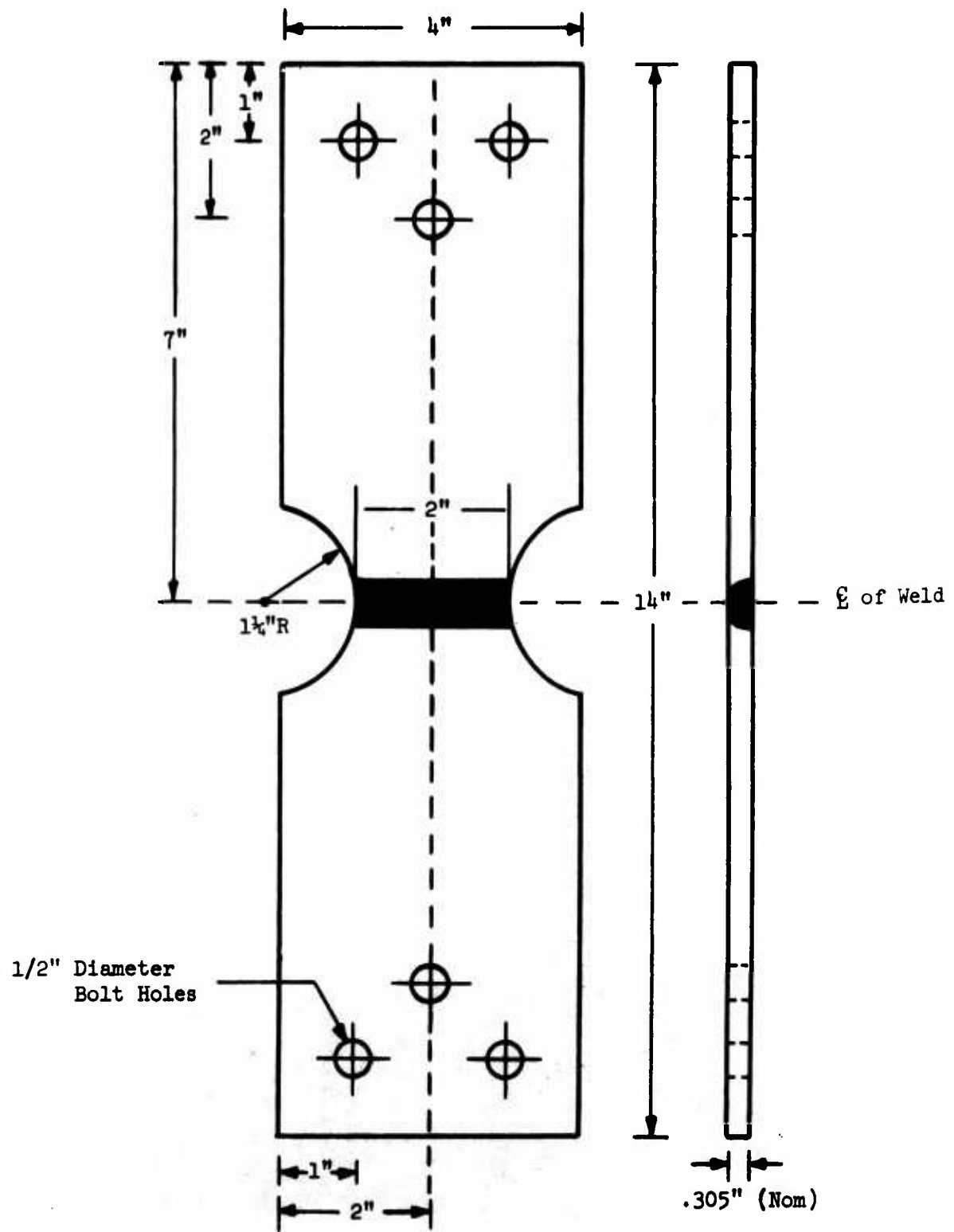


Figure 93. Ballistically Damaged Welded Fatigue Test Specimen.

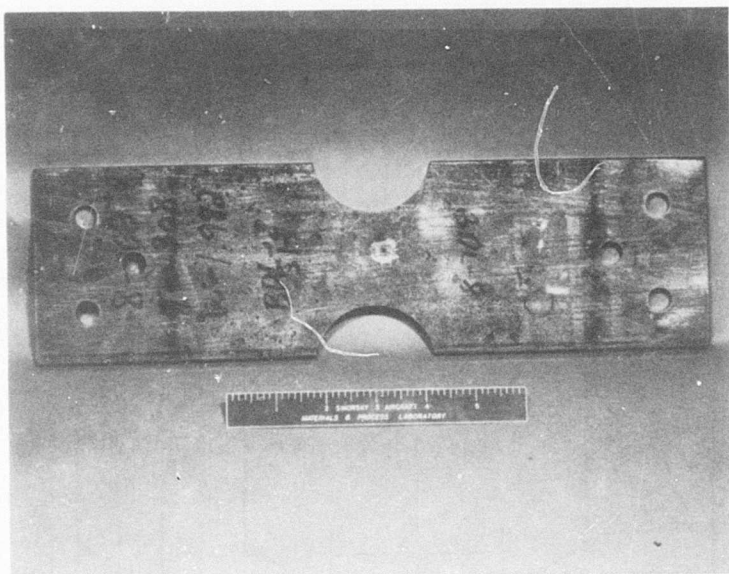


Figure 94. Base Damaged Fatigue Specimen With Hard Side Surface Damage.

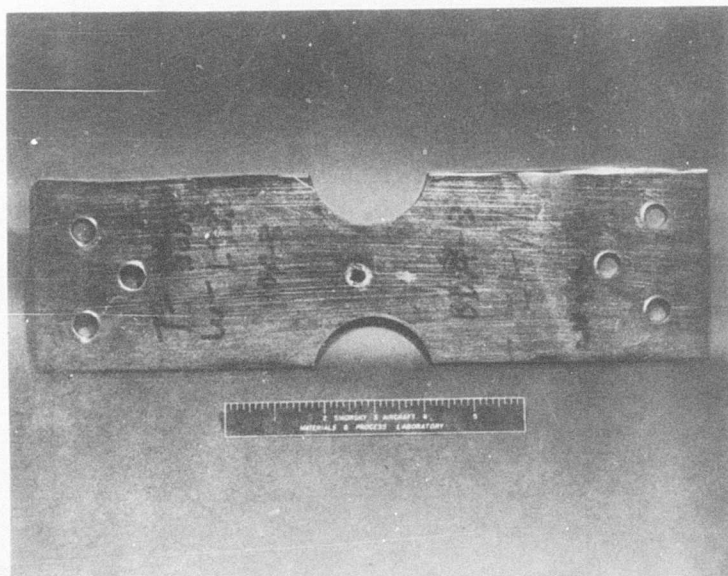
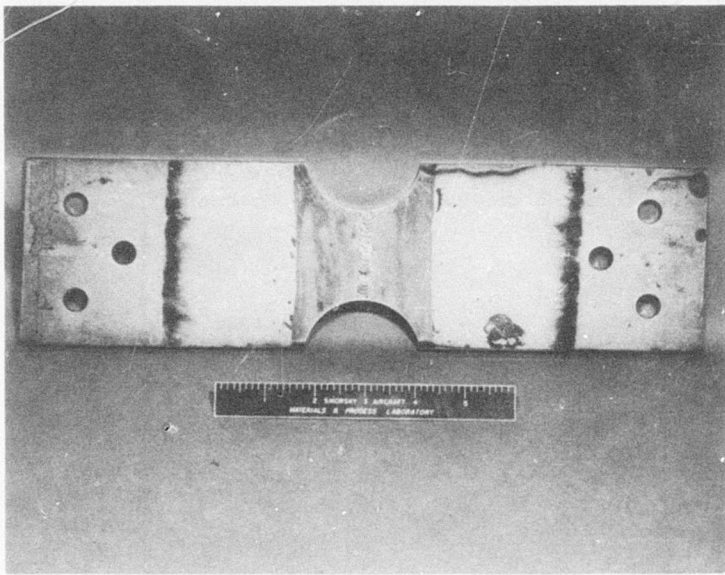


Figure 95. Base Damaged Fatigue Specimen With Through Hole.



Typical specimen showing no damage due to defeat of projectile by protective plate.

Figure 96. Welded Damaged Fatigue Specimen.

TABLE XXXIV. FATIGUE TEST RESULTS - BASE DAMAGED MATERIAL

T/N	Machine Number	Specimen S/N	$\pm \sigma_s$ (ksi)	$\pm \sigma_v$ (ksi)	Cycles to Failure ($\times 10^{-6}$)	Comments
1	IVY-12-2	BDE - 9	11	9	0.209	Thru hole.
2	IVY-20	BDE - 5	11	9	0.662	Thru hole.
3	IVY-12-2	BDA - 1	16.5	13.5	0.460	H.S. surface damage.
4	IVY-12-2	BDL - 7	16.5	13.5	0.294	H.S. surface damage.
5	IVY-20	BDE - 7	11	9	1.335	Thru hole.
6	IVY-12-2	BDA - 3	8.25	6.75	5.056 →	Thru hole.
7	IVY-20	BDL - 8	8.25	6.75	5.031 →	Did not fail. H.S. surface damage.
8	IVY-12-2	BDE - 3	16.5	13.5	0.132	Did not fail.
9	IVY-20	BDA - 6	11	9	1.080	Thru hole.
10	IVY-12-2	BDA - 2	22	18	0.010	H.S. surface damage.
11	IVY-20	BDE - 6	11	9	0.612	Thru hole.
12	IVY-12-2	BDE - 4	16.5	13.5	0.147	Thru hole.
13	IVY-12-2	BDL - 5	22	18	0.212	H.S. surface damage.
14	IVY-12-2	BDL - 2	22	18	0.210	H.S. surface damage.

*Uncorrected for specimen $K_t = 1.13$

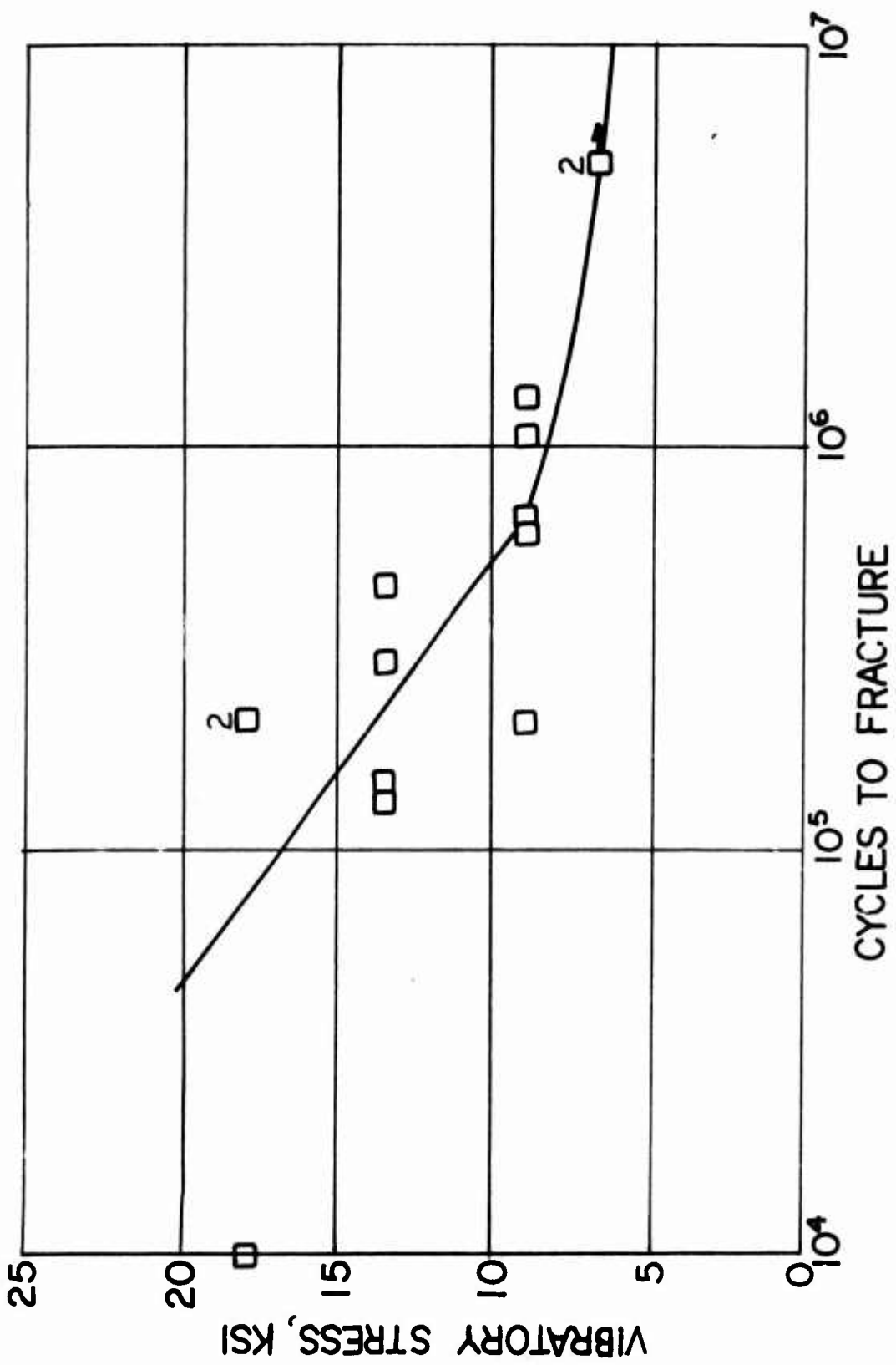


Figure 97. Vibratory Stress Versus Cycles to Fracture, Base Damaged Material, $R = 0.1$.

TABLE XXXV. FATIGUE TEST RESULTS - WELDED DAMAGED MATERIAL

T/N	Machine Number	Specimen S/N	+ σ_s (ksi)	$\pm \sigma_y$ (ksi)	Cycles to Failure ($\times 10^{-6}$)	Comments
1	IVY-20	WDL - 1	11	9	8.370 →	Did not fail.
2	IVY-12-2	WDL - 5	22	18		0.046
3	IVY-12-2	WDE - 5	16.5	13.5		0.307
4	IVY-12-2	WDA - 6	22	18		0.053
5	IVY-12-2	WDA - 1	22	18		0.079
6	IVY-12-2	WDL - 3	11	9		1.135
7	IVY-12-2	WDA - 3	16.5	13.5		0.047
8	IVY-20	WDL - 4	11	9		0.592
9	IVY-12-2	WDE - 4	16.5	13.5		0.312

* Uncorrected for Specimen $K_t = 1.13$

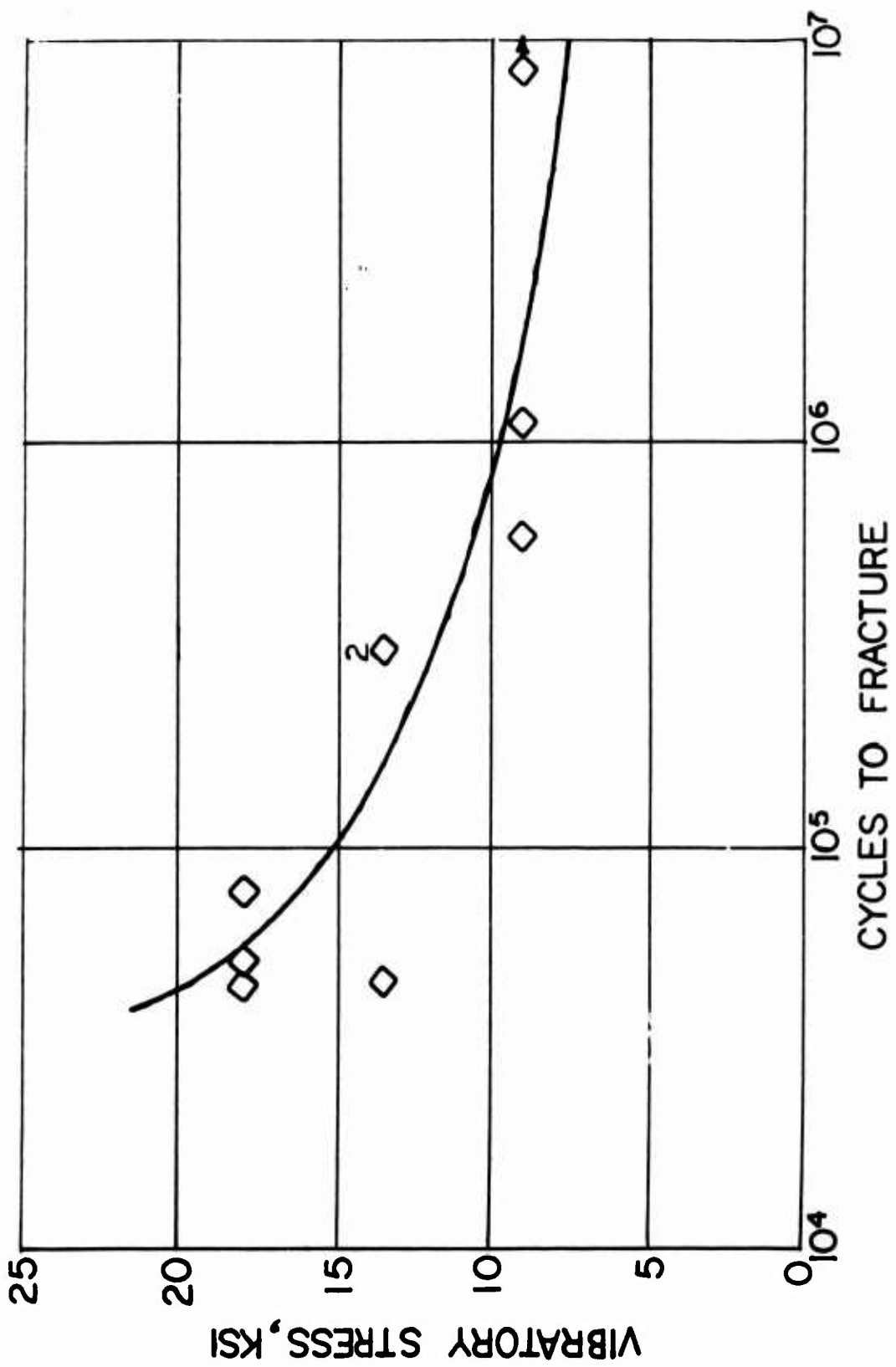


Figure 98. Vibratory Stress Versus Cycles to Fracture, Welded Damaged Material, $R = 0.1$.

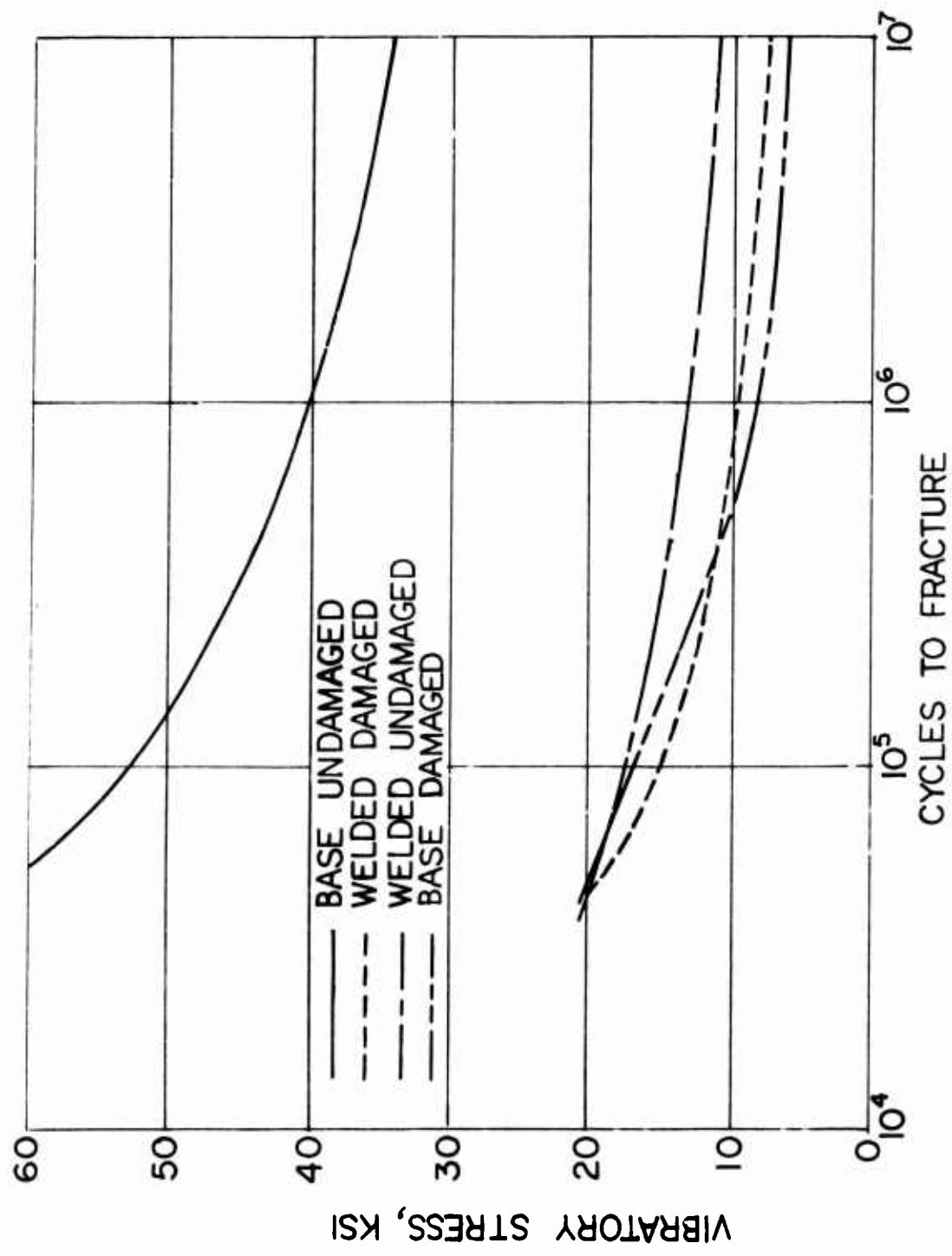


Figure 99. Vibratory Stress Versus Cycles to Fracture, Mean Curve Comparison, $R = 0.1$.

The typical base damaged microstructural appearance of the hard and soft sides of the DHS used is shown in Figure 100. White streaks (adiabatic shear bands) and associated cracks were found on both the hard and soft sides of the material. They probably are formed by one or both of the following mechanisms: (1) adiabatic heating and rapid quenching in concentrated areas of high shear deformation; or (2) severe local plastic deformation and heating in tempered martensite (containing carbides and a high dislocation density), which cause the carbides to dissolve and to migrate to new dislocation sites (Reference 21).

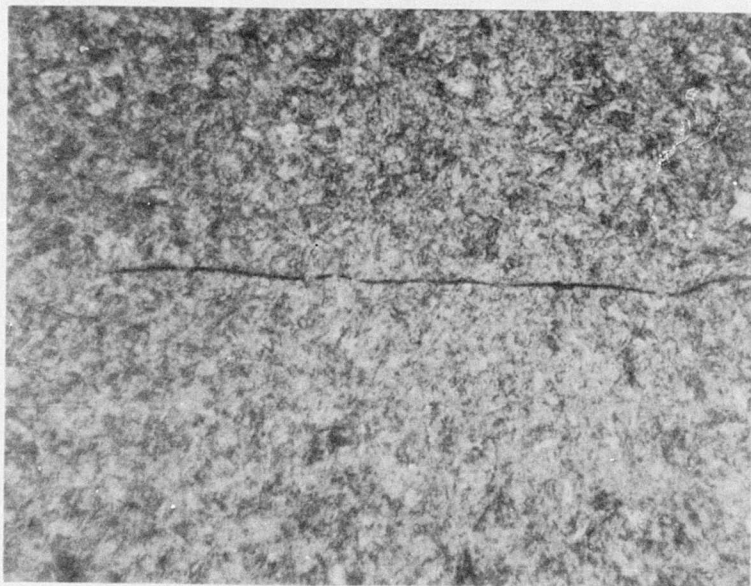
The base residual fatigue life specimens exhibited hard side surface cracking or a through hole from ballistic impacting. Through hole specimens exhibited residual fatigue life comparable to those with surface cracks, except at the highest test stress level. Crack origins of through hole specimens were located at hard side microcracks around the hole. Crack origins of surface damaged specimens were located at the base of one or more surface cracks in the hard side. In both types of base specimens, the crack initiated and grew faster in the higher strength, lower fracture toughness hard side. The crack propagated from the hard side into the soft side and stayed subsurface on the soft side. Crack growth was predominantly in the flat or plane-strain mode and brittle in nature. The base specimens exhibited a fatigue crack propagation region which was typically 70 percent of the cross-sectional area. Figure 101 shows typical fracture surfaces of both surface-damaged and through hole base residual fatigue life specimens.

Crack origins and propagation occurred subsurface in the fusionless area (due to lack of penetration) in the soft side of the welded damaged specimens. The crack propagated along the path of least resistance, i.e., the fusionless area in the center of the weld bead. The welded damaged specimens had a fatigue crack propagation area which was typically 50 percent of the cross-sectional area. The typical fracture surface of a welded residual fatigue life specimen is shown in Figure 102.

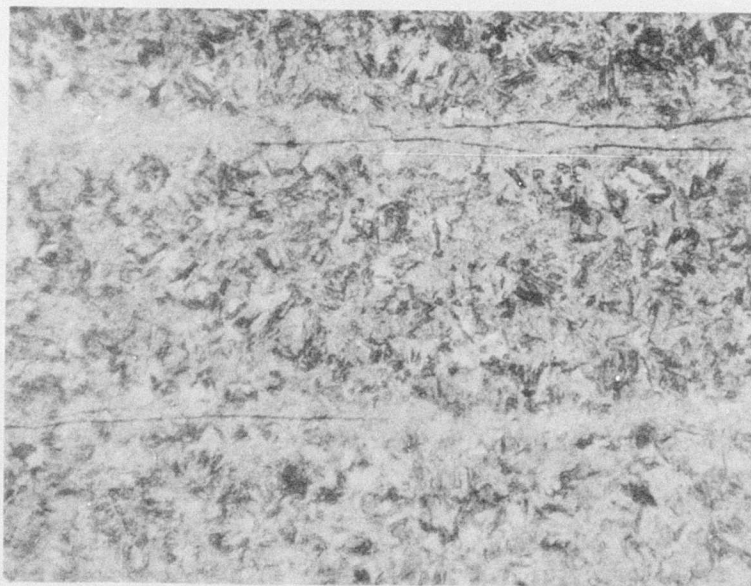
Crack Propagation From Ballistic Damage

After ballistic impacting, the remaining four base plates were returned to Sikorsky for specimen fabrication and testing. The plates were cut on a high speed friction saw to 4 inches by 1 $\frac{1}{4}$ inches with the ballistic damage located at the center of the plate. Four base damaged crack propagation test specimens were fabricated to the configuration shown in Figures 66 and 103. Steel doublers were bonded to the specimens with 3M EC 1751 adhesive in order to reinforce the grip section.

After ballistic impacting, the remaining 3 welded plates were also returned to Sikorsky for specimen fabrication and testing. The weld protector plates and adhesive were removed from the specimen blanks to expose any damage to magnetic particle inspection prior to fabrication and testing. The three welded damaged specimen blanks were then fabricated to the configuration shown in Figures 66 and 104. Steel doublers were bonded to the specimens with 3M EC 1751 adhesive in order to reinforce the grip section.



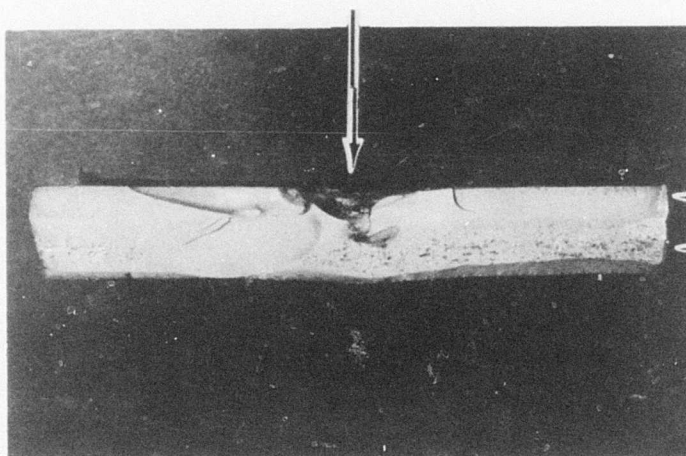
Hard Side



Soft Side

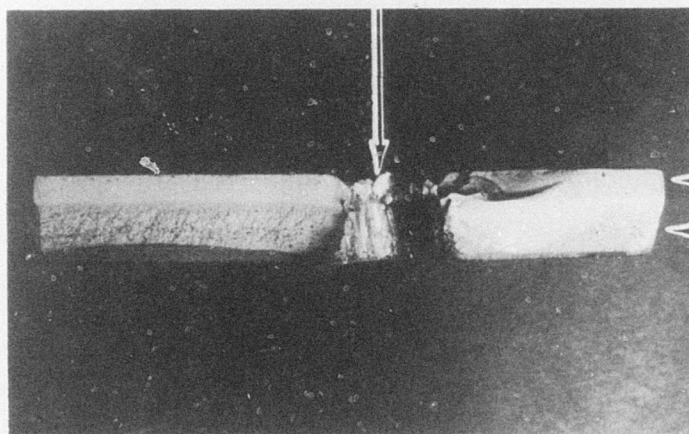
Figure 100. Typical Base Damaged Microstructural Appearance
Showing White Streaks and Associated Cracks.
~500X

Hard Side Surface Damage



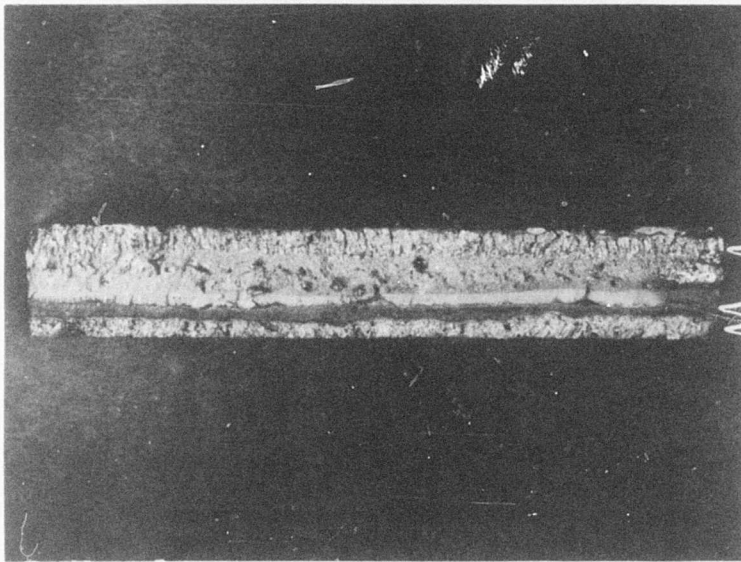
Hard Side
Soft Side

Through Hole



Hard Side
Soft Side

Figure 101. Typical Fracture Surfaces of Base Damaged Fatigue Specimens.
~1.7X



Hard Side
Lack of Fusion
Soft Side

Figure 102. Typical Fracture Surface, Welded Damaged Fatigue Specimen.
~2.2X

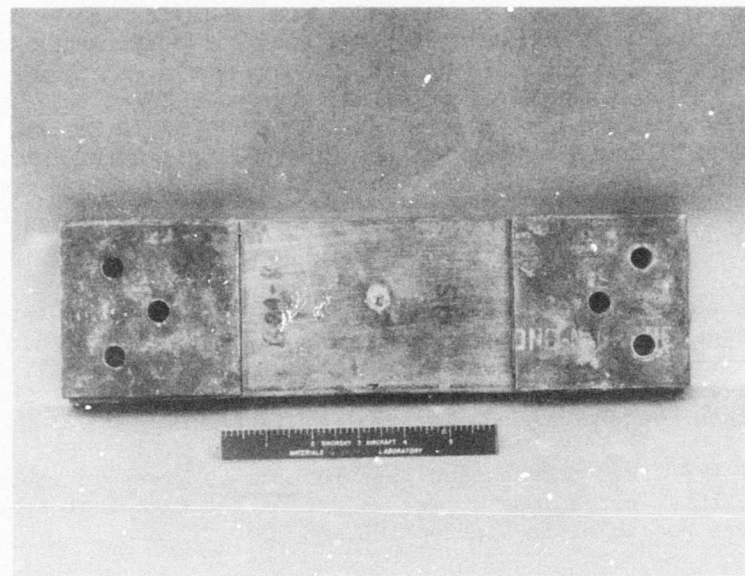


Figure 103. Base Damaged Crack Propagation Specimen.



Figure 104. Welded Damaged Crack Propagation Specimen.

Crack propagation tests were conducted on an IVY-12 fatigue machine with a 5-to-1 load amplifier and a specially designed servo-hydraulic test machine equipped with a Nashua closed-loop force feedback system to maintain static and dynamic loads. Loads were determined with a Sikorsky calibrated load cell in series with the test specimen and an Ellis BA-12 Bridge, Amplifier and Oscilloscope Console. Spherical bearing end grip setups were utilized to eliminate bending. Testing was conducted at a loading frequency of 1200 cpm on the IVY-12 and 1000 cpm on the servo-hydraulic machine. All tests were conducted at a constant R ratio ($\sigma_{min}/\sigma_{max}$) of 0.10.

Measurements of crack lengths versus cycles and overall observations were performed visually. Crack length measurements were accomplished by stopping the test at various intervals and, with the steady stress still applied, spraying the magnetized specimen with MagnaGlo® solution. The crack length was then measured under ultraviolet light.

A summary of the crack propagation test results is given in Tables XXXVI and XXXVII. The total crack length, 2a, vs cycles for each test specimen, is plotted, where possible, in Figures 105 and 106.

Testing of the base damaged crack propagation specimens at the stress levels specified in Table XXXVI resulted in grip failures in all four cases even though the specimen exhibited hard side surface cracking from ballistic impacting in three cases and a through hole in the fourth case. Fretting was evident in the attachment areas and was probably the precipitating cause of failure. A small amount of crack propagation from the ballistic impact was noted prior to end grip failure.

Initiation and propagation in the damaged welded specimens took place from and at the boundary of the weld bead and HAZ on the hard side of the material. The crack propagated through the thickness of the material and propagated in the HAZ of the soft side weld bead from a partial penetration from ballistic impacting. Crack growth was in the flat or plane strain mode and brittle in nature. Grip failures occurred in two specimens. The fracture surface of the failed welded damaged crack propagation specimen is shown in Figure 107.

These tests indicate that drilled bolt holes with fretting in this material are more detrimental to fatigue life than are cracks or through holes caused by ballistic impact.

DISCUSSION

The combined results of the various materials characteristics tests have further demonstrated the feasibility of the use of dual hardness steel in an integrally armored fuselage structure application. As shown in the Detail Analysis section of this report, the properties of the material, even after ballistic impact, permit achievement of the required life at the stress levels predicted by the NASTRAN analysis. The only problem area identified, the lack of complete weld penetration, could be overcome by minor procedural modifications. These modifications resulted in the higher life specimens,

TABLE XXXVI. CRACK PROPAGATION RESULTS - BASE DAMAGED MATERIAL

T/N S/N	Specimen Number	Machine Number	Frequency (cpm)	Area (in. ²)	+ σ _s (psi)	- σ _v (psi)	Cycles to Fracture (x 10 ⁻³)	Comments
3	BDA - 4	Servo	1000	1.199	9900	8100	609	No C.P.
3A	BDA - 4	Servo	1000	1.199	11880	9720	364	No C.P.
3B	BDA - 4	Servo	1000	1.199	14256	11664	178	Grip failure.
4	BDL - 1	IVY-12-2	1200	1.224	9900	8100	437	No C.P.
4A	BDL - 1	IVY-12-2	1200	1.224	12870	10530	215	Grip failure.
8	BDA - 8	IVY-12-2	1200	1.245	11880	9720	545	Little C.P.
8A	BDA - 8	IVY-12-2	1200	1.245	12870	10530	133	Little C.P.
13	BDL - 6	Servo	1000	1.233	12870	10530	280	Grip failure.
								Grip failure.

Note: C. P.=Crack Propagation

TABLE XXXVII. CRACK PROPAGATION RESULTS - WELDED DAMAGED MATERIAL

T/N S/N	Specimen Number	Machine Number	Frequency (cpm)	Area (in. ²)	+ σ _s (psi)	- σ _v (psi)	Cycles to Fracture (x 10 ⁻³)	Comments
1	WDE - 9	Servo	400	1.896	9900	8100	185	Grip failure.
2	WDA - 7	Servo	400	1.890	9900	8100	992	Fracture.
12	WDE - 7	IVY-12-2	1200	1.889	12870	10530	32	Grip failure.

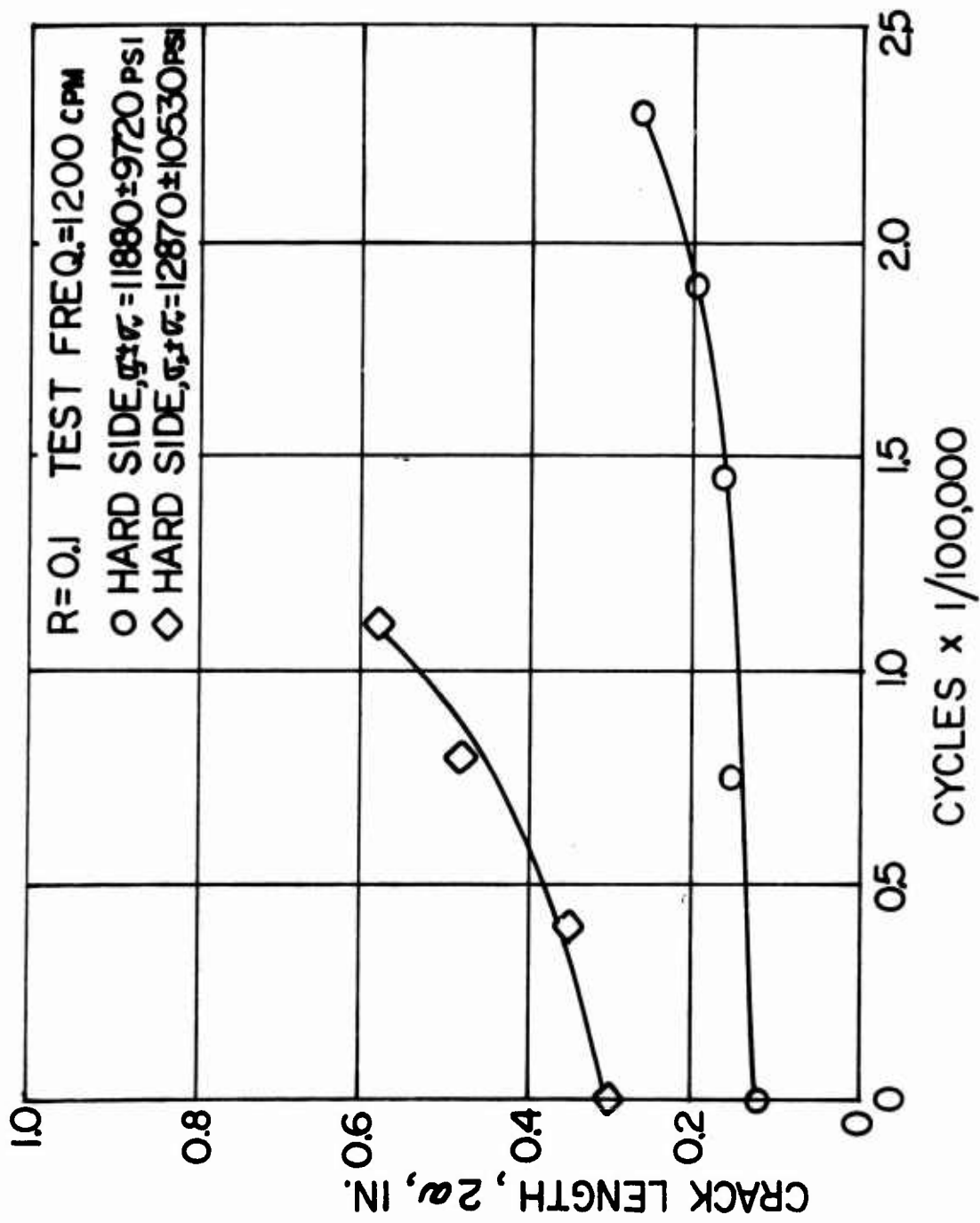


Figure 105. Crack Length Versus Cycles, Base Damaged Specimen S/N BDA-8.

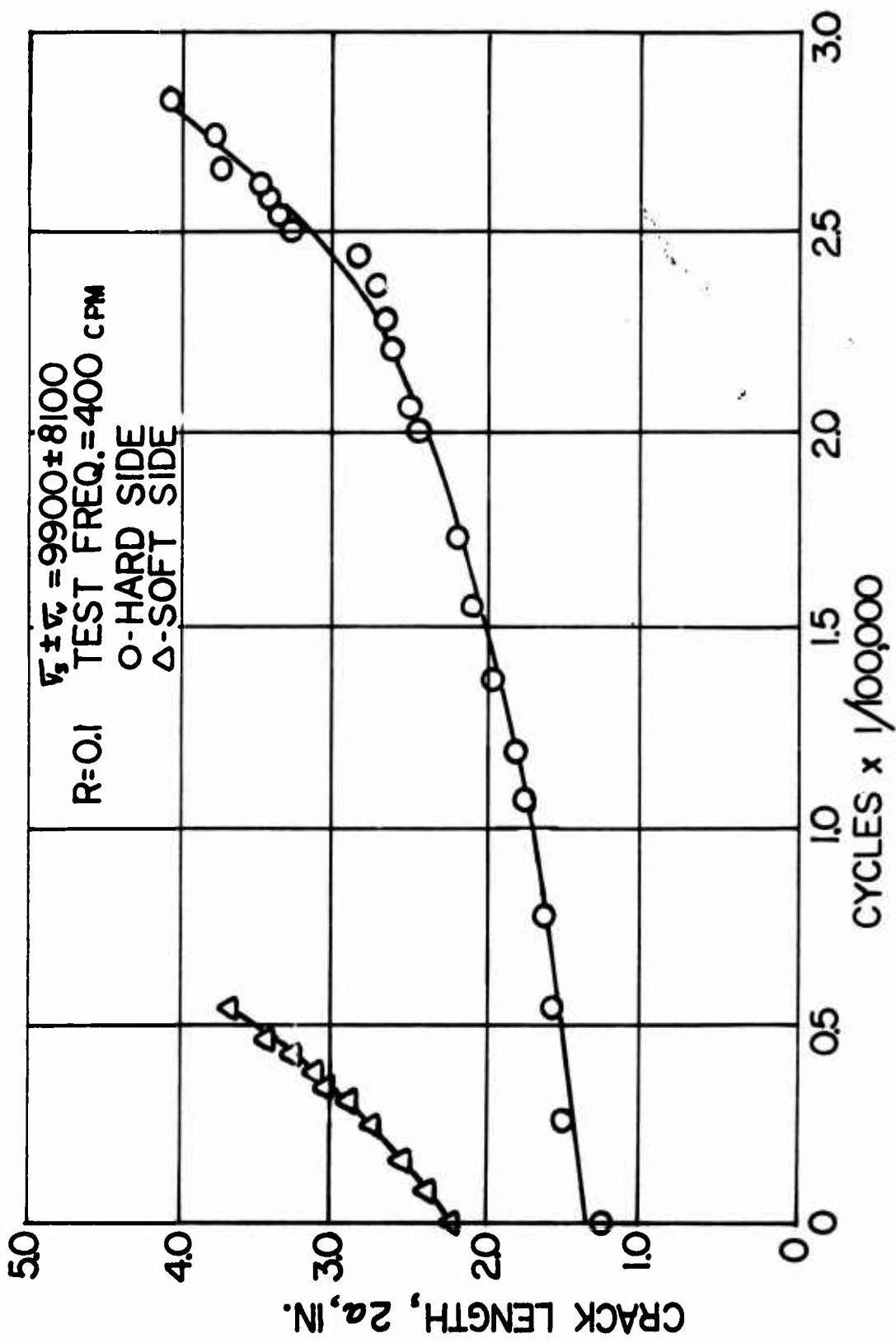


Figure 106. Crack Length Versus Cycles, Welded Damaged Specimen S/N WDA-7.

such as the runout at the intermediate level, shown in Figure 63. However, as the analysis shows, even the comparatively low strength welds are capable of supplying the required structural integrity.

Although the fatigue and static strengths of the base material are significantly higher than those of the welds, several additional factors must be considered in this comparison. Under conditions of axial loading, fatigue crack initiation on base undamaged specimens occurred on the soft side. This is to be expected from a consideration of the comparative strengths of the components. Under different conditions of stress distribution, hard side origins could occur, although probably at higher stress levels. However, when notches or cracks from ballistic impact are present, crack propagation tends to occur more rapidly in the harder component. Since fatigue life is a combination of both the initiation and propagation times, different stress distributions would be expected to result in different observed fatigue properties. In the vicinity of a weld, of course, cross-sectional properties are more uniform, so that a lesser effect of stress distribution would be expected, leading to a different picture of relative weld and base fatigue strengths.

Another factor affecting this comparison is the presence of stress raisers, such as drilled holes or ballistic impacts. Since fittings for the most part attach to the base armor, the presence of bolt holes will increase the local stress intensity and lower the observed fatigue strength. This is considered more fully in the Detail Analysis. Based on the repeated grip failures during crack propagation tests of ballistically damaged armor, the drilled holes (along with observed fretting) lower the undamaged fatigue strength to a value comparable to that of ballistically damaged material.

Ballistic impact had a much smaller effect on the strength of the welds than on that of the base material. This is to be expected due to the presence of the adhesively bonded protector. The small drop in strength appears to be due only to the effect of the impact shock wave. However, the residual properties of the base material were reduced to values below that of the welds. The residual strength values were similar for both penetrated and cratered base specimens, indicating that the shock damage and cracking occurring on impact are more significant than the presence or absence of a through hole.

Some comment is required on the validity of the crack propagation and fracture toughness test results. To facilitate measurement, propagation testing was performed in the presence of MagnaGlo[®] solution. The effect of this solution is not known and will depend on the crack growth mechanism, which has not been identified. Any effect is expected to be small and in no way would invalidate the results.

Because cracks propagate at a different rate in the hard and soft components of the material, it was not possible to achieve the flat crack front required for a valid fracture toughness measurement. Other requirements for validity were met. Since there is no generally accepted method for determination of the fracture toughness of composite materials, the ASTM method was selected as providing close control of test variables and as a basis

for some comparison. The reported value is the closest approximation to a valid K_{IC} possible under these conditions.

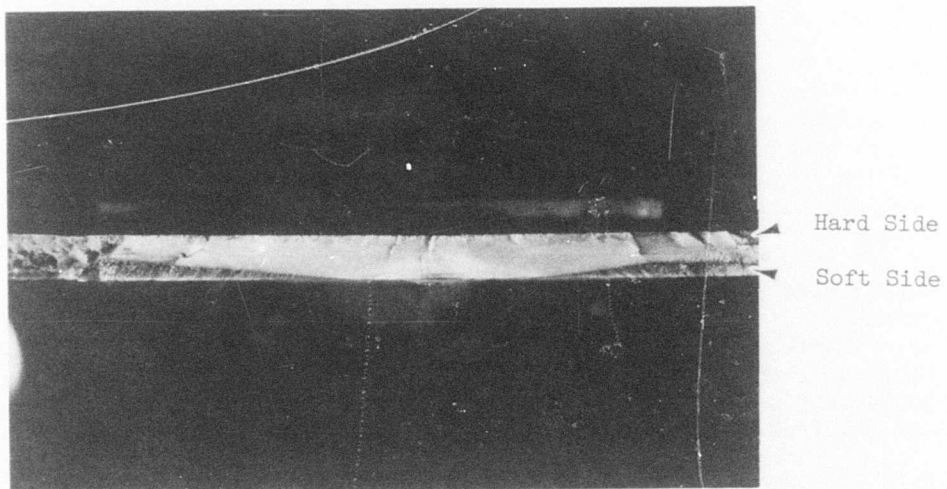


Figure 107. Fracture Surface, Welded Damaged Crack Propagation Specimen.
~1X

TEST SPECIMEN FABRICATION

SUMMARY

Fabrication of the two center section test articles was accomplished despite the occurrence of several different types of cracking. The procedures used in fabrication were based on those developed under previous contracts (References 1 and 15), as well as Phase I of the present program. All cracks in highly stressed areas (and others where feasible) were repaired. The locations of those which were not corrected have been noted for attention during the test phase. The applicability of laser weld technology to dual hardness steel was also briefly evaluated.

FABRICATION PROCEDURES

Armor

All of the dual hardness steel (DHS) used in fabrication was supplied by Jessop Steel. Several lots of material were used, all of which were similar in composition and properties to that qualified during the Phase I testing, reported in the preceding section and the confidential appendix. In general, armor details were supplied to final size and configurations, to drawings and templates furnished by Sikorsky Aircraft. Simple flat panels were sheared to size prior to heat treatment. More complex parts, such as the attachment tab or center panel cutout shown in Figure 108, were flame-cut prior to heat treatment and ground or milled, if necessary, to final form. Contoured components, such as the weld protective strips or the air scoops, were partially formed prior to heat treatment, with any required final shaping accomplished afterwards.

In most cases, a flattening operation was required after heat treatment, usually by cold hammering. This resulted in the introduction of significant residual stresses. A number of parts were cracked during manufacturing, and had to be repaired or replaced prior to shipment. However, some parts were received with cracks which either had not been detected or had occurred after inspection.

Some minor modifications were performed at Sikorsky. These included trimming of the weld protective strips to final length, and the addition of holes for the test fixture interface, door tracks, hinges and fittings, using carbide tipped drills. All of these procedures were performed in accordance with practices developed in References 1 and 15.

Fittings

The remainder of the test article details, other than standard hardware items, such as bolts, were supplied by Sikorsky Aircraft. The majority of these were fittings for the transmission support structure, landing gear attachments and access doors. Welded fittings, such as those shown in Figure 109, were 4130 plate per MIL-S-18729, welded per MIL-W-6811, using MIL-R-5632, Class 2, Type 3 filler wire. One piece fittings, such as those for landing gear attachment, were 4340 bar per MIL-S-5000. All

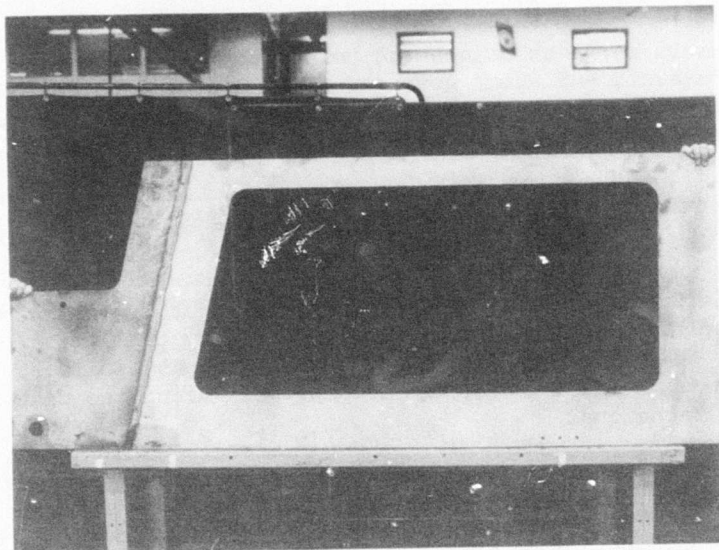


Figure 108. Typical Center Section Subassembly.

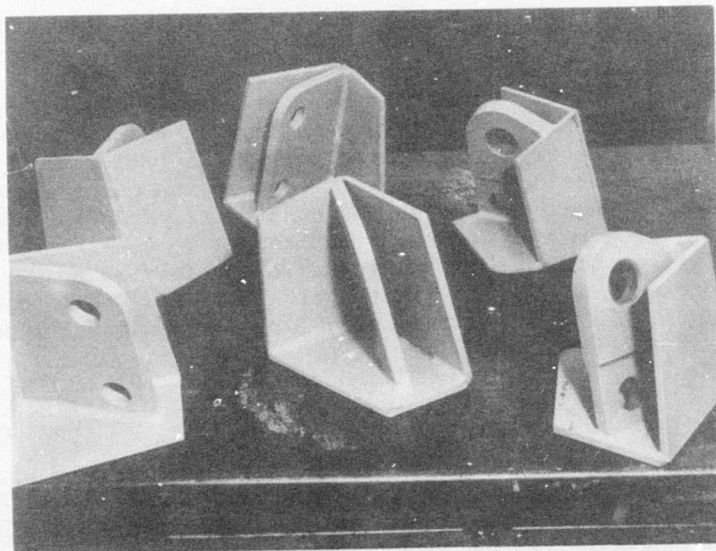


Figure 109. Welded Attachment Fittings.

fittings were heat treated to a minimum tensile strength of 150 ksi per MIL-H-6875, and were cadmium plated per QQ-P-416 and given two coats of MIL-P-8585 primer for protection against corrosion.

These fittings serve as attachment points for struts leading to the test fixture framework and dummy gearbox. They are used to introduce the loads generated by the fixture into the armor fuselage. More detail on the test fixture and dummy gearbox may be found in the Test Facility section

ASSEMBLY PROCEDURES

Welding

The welding procedures are discussed first, since they are common to the entire assembly process. Edges were prepared by chamfering (20°) for butt joints, or edge grinding for lap and fillet joints, followed by vapor blast cleaning. All welding was accomplished using the manual gas tungsten arc (GTAW) technique.

Generally, the pieces to be joined were first fitted together and tack welded. Copper chill bars were used in all cases to minimize the heat-affected zone. Multiple pass welds were generally required, made predominantly from the hard side and usually from the center of the joint to the ends. Where geometry permitted, a cosmetic pass was made on the opposite side to assure full penetration.

An AC-DC welding machine and standard support equipment were used. Power was varied by an operator-controlled foot switch. Amperage was not measured. The power rating of the welding equipment was 18 to 320 amps on medium range and 38 to 500 amps on high range.

Most of the welds on the first specimen were made with 4130-type filler wire, conforming to MIL-R-5632, Class 2, Type 1, which had been used for the Phase I test specimens and previous programs (Reference 15). However, due either to the residual stresses present in the material, or to geometric factors such as panel size and constraint, frequent fusion line cracking was encountered. A concurrent change to a slightly different weld geometry and to 310-type welding wire, conforming to MIL-R-5031, used in the Reference 1 study, alleviated this problem. The more ductile, but lower strength, 310 wire was then used for all repair welds and for most of the second specimen joints.

Subassembly

The first step of the fuselage assembly consisted of welding armor detail parts into subassemblies. A typical example is the lower side, shown in Figure 108, consisting of a lower side panel and a forward attachment tab. The various subassemblies are shown in exploded view in Figure 110.

Except for the aft bulkhead assembly, all were flat, butt joints. Fixturing was limited to chill bars and such plates and clamps as were required to keep the assembly flat during welding. The slightly more

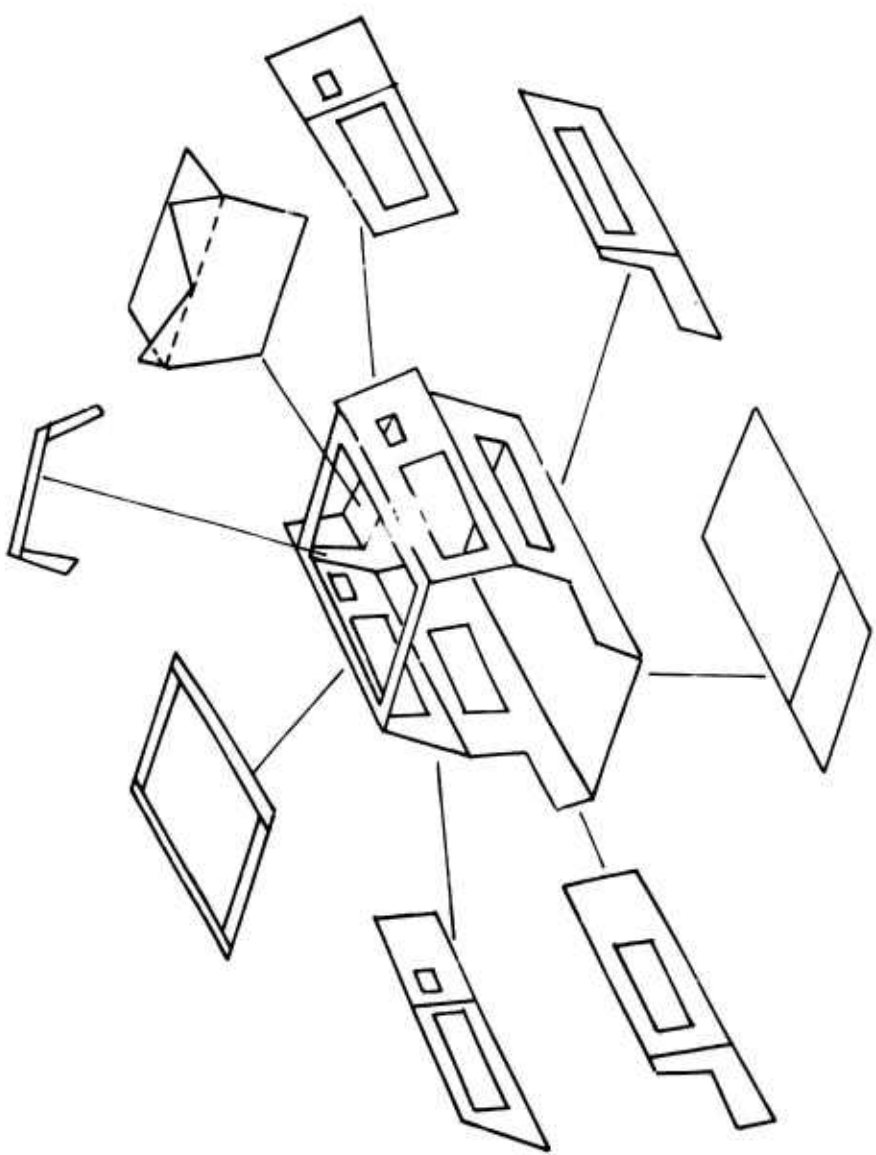


Figure 110. Exploded View of Center Section Showing Major Structural Subassemblies.

complex fixturing required for the aft bulkhead, a 90° joint, is shown in Figures 111 and 112.

Next, the four lower subassemblies (sides, floor and aft bulkhead) were joined together to form the lower center section. Fixturing (Figure 113) consisted of a wood and steel framework to position the parts. The sub-assemblies were clamped to the fixture and chill bars positioned prior to welding. The finished lower center section is shown in Figure 114.

The upper center section panels, with the aft attachment tabs, were then joined, using additional fixturing. The roof panels were also added at this time, as were the air scoops on the second specimen.

Final Assembly

The test specimen assembly procedure was completed by the addition of those parts which were bolted on rather than welded. These included the various transmission, gun pod, and landing gear fittings, the forward fuselage brace and the removable swashplate fairing and protective cover. The location of these may be seen in Figure 125. In addition, the second specimen was fitted with track assemblies and hinges for the access doors. The completed assembly is shown in Figure 115. At a later time, the joint protective strips were bonded on with EC-1675 adhesive. Only those strips required for ballistics protection and others which did not interfere with strain gage locations were installed during testing.

MANUFACTURING PROBLEMS

The only major difficulties encountered during fabrication were the presence of cracks in the as-received material, and the occurrence of other cracks during welding. Three separate types of cracking occurred - those due to residual stress, those due to welding, and those due to a combination of both factors.

Residual Stress Cracking

The first type of cracking was noted in the armor details prior to any welding. During flattening, cracks up to 11 inches in length had occurred in several panels, which were either replaced or repaired prior to shipment. However, a number of panels were received with cracks which generally started at an edge and ran perpendicularly for distances up to 5 inches. most occurred on the hard side only, although a few through cracks were noted.

All of these cracks were repaired prior to assembly. The repair procedure consisted of stop-drilling the ends of the crack (Figure 116), grinding out the crack (Figure 117) and puddling a weld into the resulting groove. Dye penetrant inspection was conducted after grinding to assure that the crack had been removed, and again after welding. The majority of these repairs were made with the 4130-type wire.

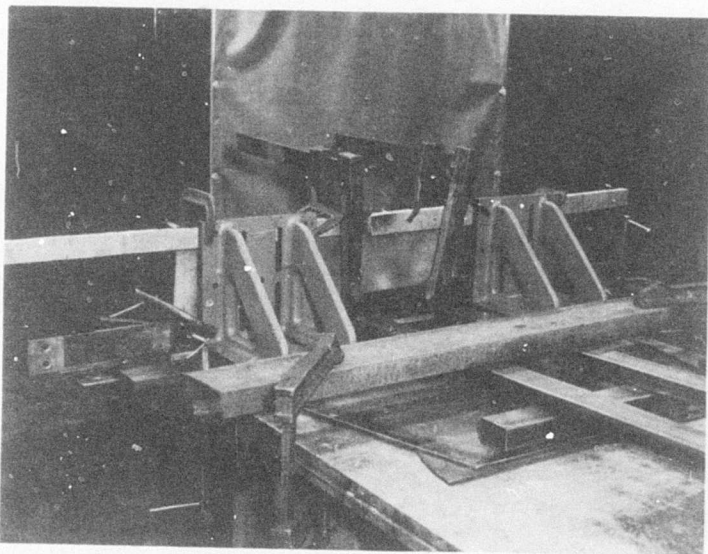


Figure 111. Aft Bulkhead Assembly Fixture.



Figure 112. Welding of Aft Bulkhead Assembly.

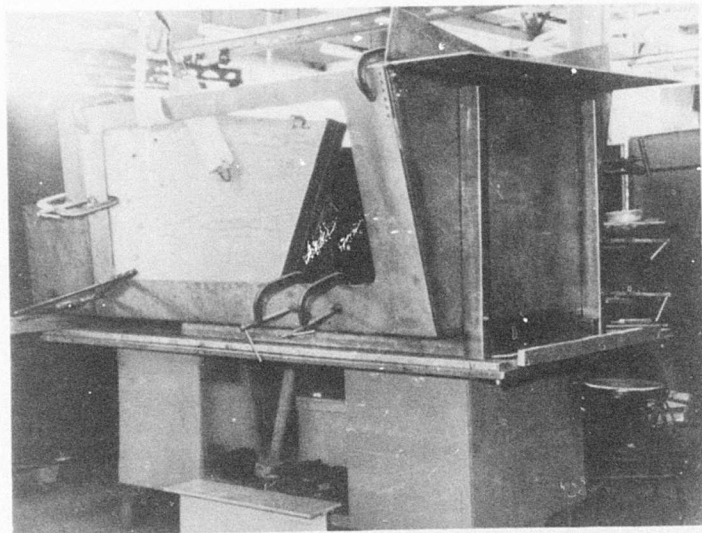


Figure 113. Lower Center Section Assembly Fixture.

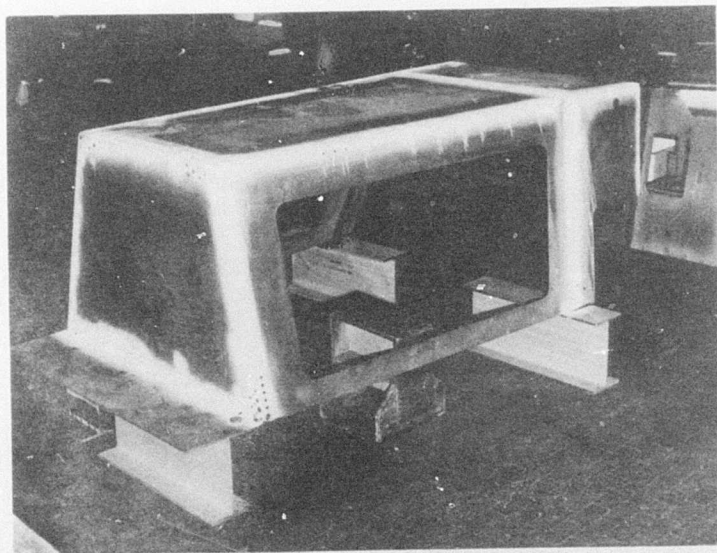
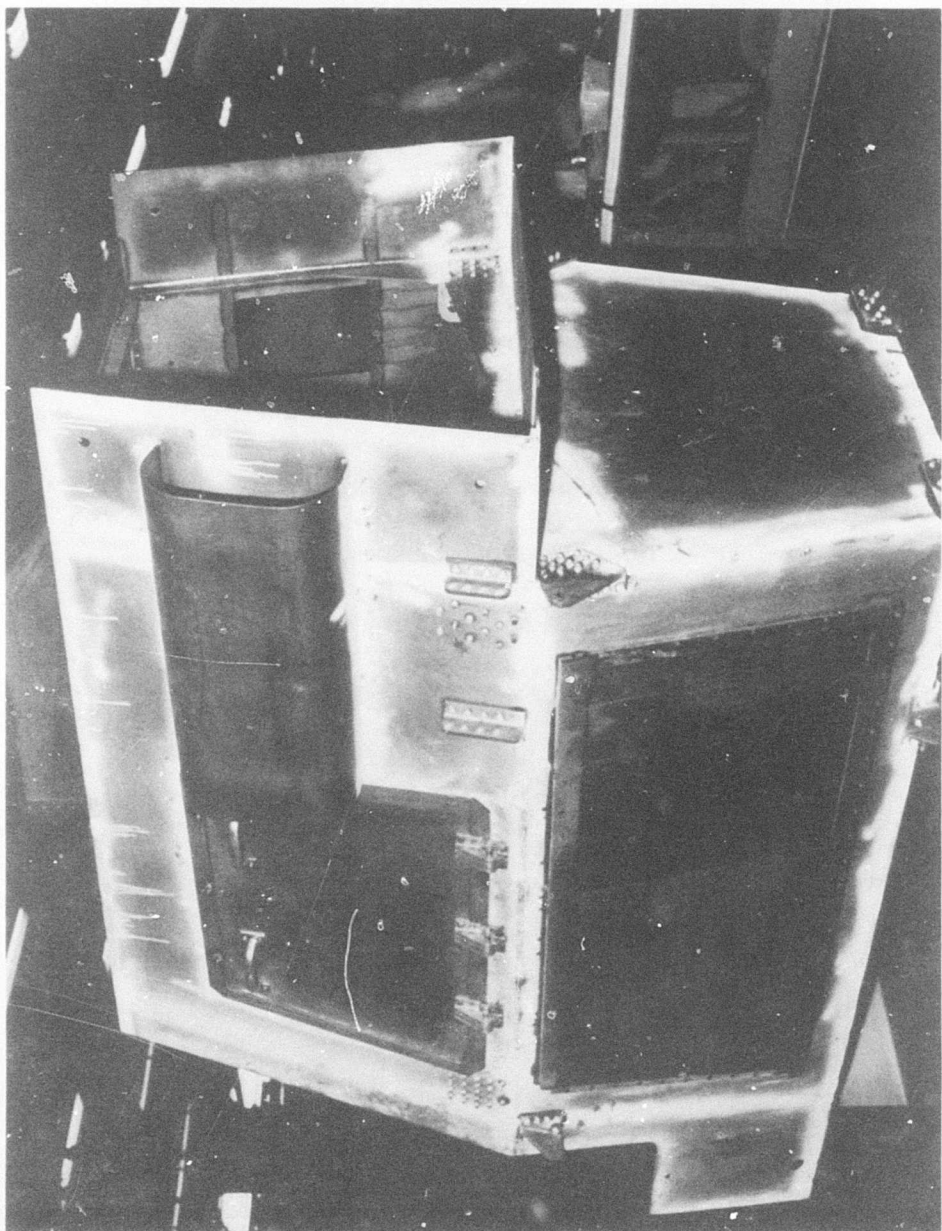


Figure 114. Completed Lower Center Section.

Figure 115. Completed Center Section.



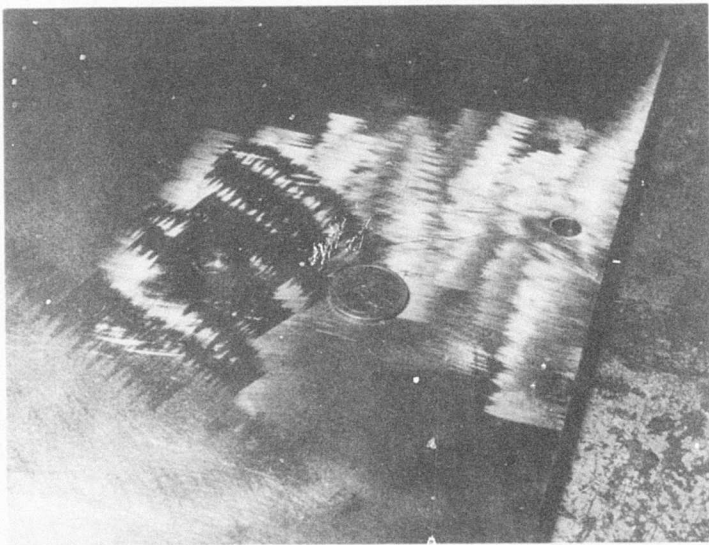


Figure 116. Typical Residual Stress Crack After Stop-Drilling.

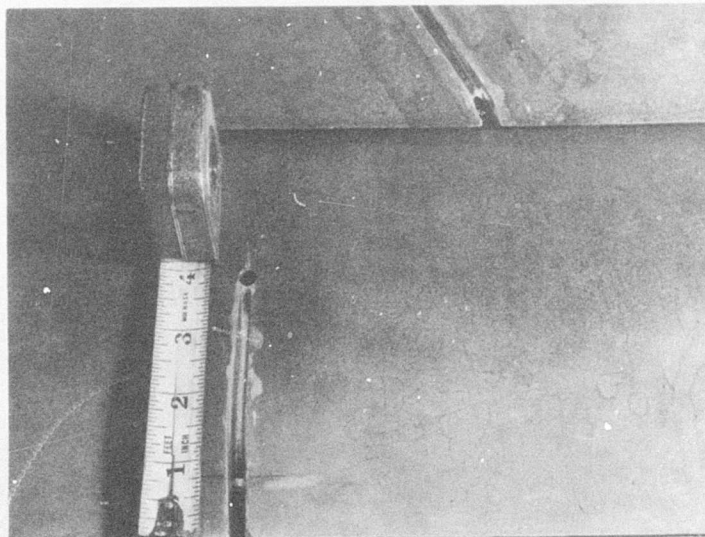


Figure 117. Crack Removed and Ready for Weld Repair.

Similar cracks occasionally occurred during welding, either spontaneously, or from very small edge cracks (Figure 118). These were similarly repaired by stop-drilling, grinding and welding (Figure 119).

Fusion Line Cracking

The second type of cracking (Figure 120) occurred parallel to the weld joint at the edge of the weld bead. Similar cracks occurred around a plug weld made to fill a mispositioned hole in one of the attachment tabs (Figure 121). These cracks have been an occasional problem in welding armor, since conventional practices, such as preheating and postheating, cannot be followed without detrimental effects on ballistic properties. It is considered to be a form of "hot-shortness", where the weld bead pulls away from the parent metal during cooling. The problem seems to have been aggravated by the residual stresses in the material.

The incidence of this type of cracking was sharply reduced by a change from the higher strength 4130-type wire to more ductile 310-type, and a concurrent change to a higher weld bead crown. This procedure was followed on the second specimen, resulting in a significant reduction in cracking. On the first specimen, however, most of the welds showed this type of cracking. It should be noted that these cracks occurred most often in flat, butt joints.

Some repair of the cracks by grinding and rewelding was attempted, but because the cracking was so extensive, especially on the first specimen, very wide heat-affected zones occurred. This technique was discarded in favor of providing an alternate load path by placement of soft side beads where required.

Heat-Affected Zone Cracking

These cracks also occurred parallel to the weld, but were typically located approximately 0.1 inch away from the edge of the bead. They occurred only where plates were welded together at an angle to form an edge, such as side to floor, or aft bulkhead to side (Figures 122 and 123).

Reference to Figure 56 shows that the location of these cracks corresponds to the point of minimum hardness (and strength) of the heat-affected zone. Their presence appears to be directly related to the presence of adverse residual stresses in the material, possibly aggravated by the constraints of joining at an angle. Attempts to grind out and reweld these cracks also proved impractical due to the resultant wide heat-affected zone, as well as the appearance of new cracks at the same relative location to the repair welds. Where required, soft side beads were used to provide alternate load paths.

Corrective Action

Several approaches were considered to eliminate the cracking problems. Welding from the lower carbon soft side was suggested; however, this would

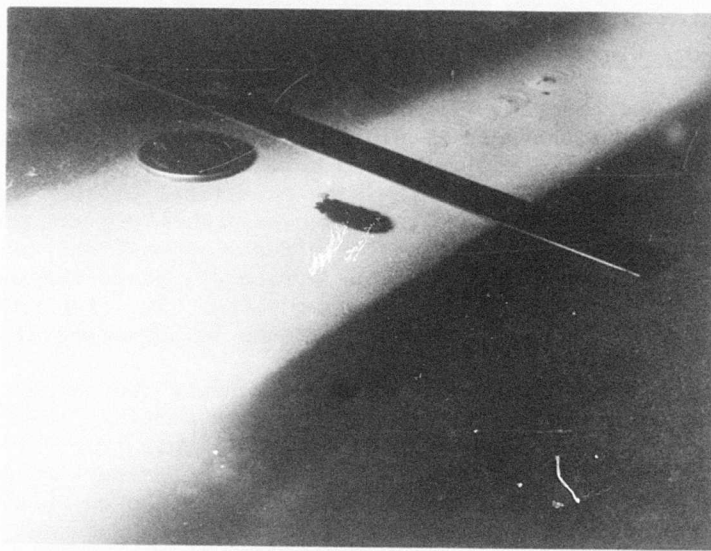


Figure 118. Secondary Residual Stress Crack.

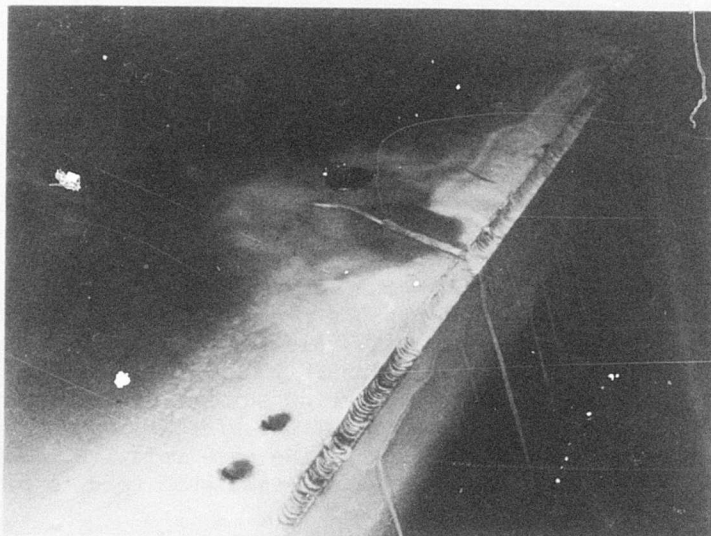


Figure 119. Secondary Crack During Weld Repair.

Figure 120. Typical Fusion Line Cracking.
Forward Attachment Tab

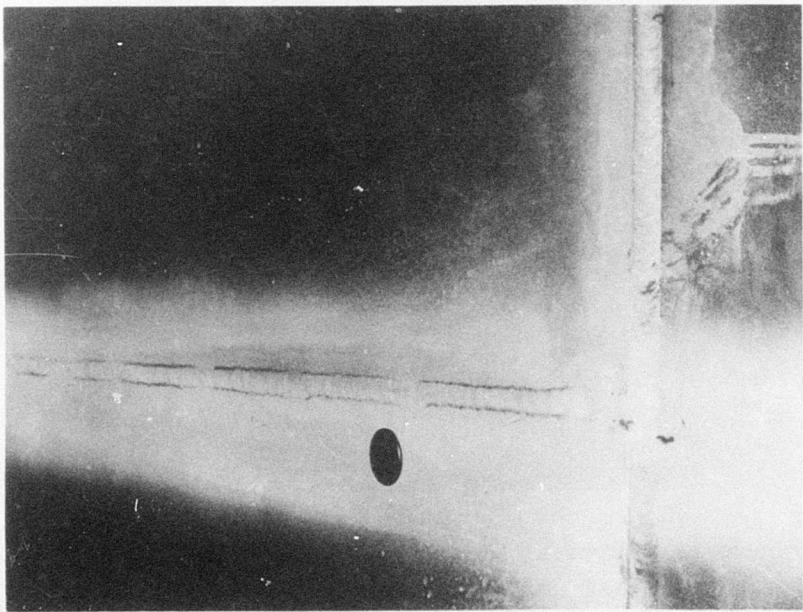


Figure 121. Fusion Line Cracking Around Repair Plug Weld.

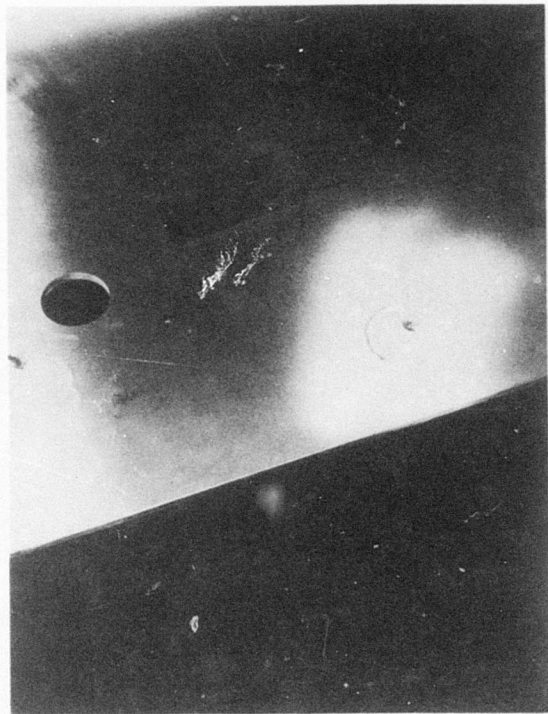




Figure 122. Typical Corner Heat-Affected Zone Crack.

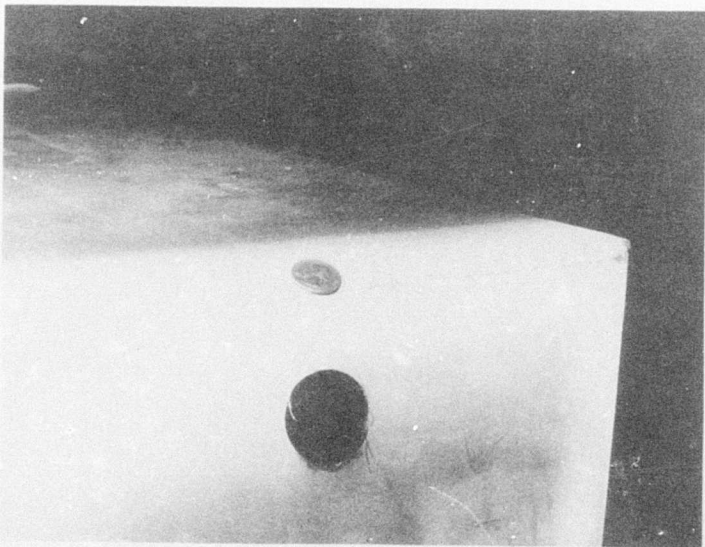


Figure 123. Typical Edge Heat-Affected Zone Crack.

greatly limit the use of automated welding techniques, which have always been an aim in these development programs. Welding from the ends of the joint to the center was also tried, in order to provide greater heat flow from the weld, and did seem to somewhat reduce the extent of cracking. However, since most of the subassembly welding had been completed, full use of this approach could not be made. Replacement of the armor with material having lower residual stresses was also considered. This, however, implied extensive development of heat-treating and forming techniques and would have resulted in increased costs and/or a long program delay.

Attention was given instead to methods of improving structural integrity, rather than preventing the occurrence of cracks. Since the amount of repair welding required to totally eliminate the cracks would have resulted in extensive degradation of the armor, ways to minimize this repair were sought. All cracked areas were examined to determine the level of induced stresses during test, and repairs were made only where structurally necessary. These repairs were made by grinding and rewelding where feasible. In other cases, a weld bead was placed along the inside of the joint to provide an alternate load path and bypass the cracked area.

At the completion of this repair procedure, the specimens were dye penetrant inspected and the location and extent of all cracks noted. The second specimen, where improved techniques were used, proved to have numerically more indications than the first (155 vs 117) but a reduced total crack length (186 inches vs 267 inches). All cracks are listed in Tables XXXVIII and XXXIX. As may be seen from Figure 124, 60% of the cracks in the second specimen were under 1 inch in length, many of them only spotty or hazy indications. The locations of the cracks are noted in Figures 125 and 126 by reference to the tables. For clarity, only those over 2 inches in length have been shown.

With the possible exception of the fusion line cracking, which was correctable by changes in technique, all cracks were related to the presence of residual stresses. It is probable that the fusion line cracking was also affected by this factor. Further development of material processing techniques to eliminate these stresses would greatly reduce the incidence of cracking. The problems experienced are related to the material, rather than to fabrication procedures, and do not invalidate the concept of integrally armored structure.

LASER WELDING

A brief study was made which indicated that laser welding technology may be applicable to dual hardness steel for future production considerations. A number of "bead-on-plate" welds were made on dual hardness steel samples, using a 5-kilowatt carbon dioxide (CO_2) laser operated by United Aircraft Research Laboratories. Welds were made from both hard and soft sides at speeds of 40 to 80 inches per minute. Based on the information derived from these tests, several butt welds were made on both .220 and .305 inch thick material, from the hard side, at 50 to 60 inches per minute.

TABLE XXXVIII. CRACK DOCUMENTATION, SPECIMEN #1

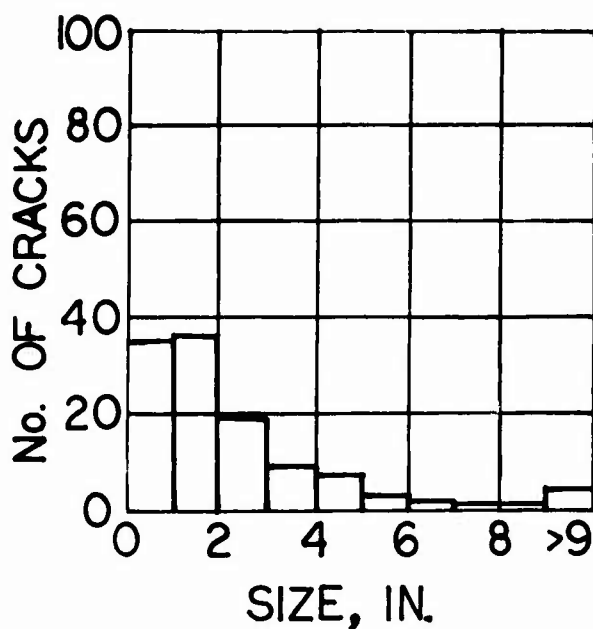
Crack Number	Length (in.)	Crack Number	Length (in.)	Crack Number	Length (in.)
1	1	41	1/2	81*	7-1/4
2*	2	42	1/8	82	1-1/2
3*	4-1/4	43*	2	83*	15
4*	6	44*	2-1/8	84	1-1/2
5*	5	45	3/4	85*	14
6*	3-1/2	46	1	86	1-7/8
7*	3-1/2	47	1-1/8	87	1/8
8	1	48*	2-1/2	88*	9-3/8
9	1	49*	4-1/2	89	1-1/8
10	3/8	50	1-1/8	90	2-1/4
11*	2-1/4	51	3/4	91*	16-3/8
12*	2	52	1/2	92	1-1/2
13	1-1/8	53*	2-3/8	93*	2
14	3/4	54	1/8	94	1/4
15*	3-1/2	55	1/4	95*	2-5/8
16	3/4	56*	6-1/4	96	5/8
17	1-1/2	57	1/4	97*	4
18*	2-1/4	58	3/16	98	3/4
19	3/4	59	1/8	99	1-1/4
20	1/2	60	1-3/4	100*	2-3/4
21	5/8	61*	5-1/8	101	1/4
22	3/4	62	1/4	102	SPOT
23	5/8	63*	4-5/8	103	1
24	1	64*	2-1/16	104	1
25	1/2	65*	2	105	1-1/2
26*	2	66	1-1/8	106	1
27*	3	67*	5-1/16	107	1/2
28*	4-1/2	68*	2	108	1
29	1	69*	3-1/2	109	1
30	1-1/2	70	1-3/4	110*	4
31*	2-1/8	71*	3	111*	2
32	5/8	72*	2-1/2	112*	8
33	1-1/2	73	5/8	113	1/2
34	1-3/8	74	1-5/8	114	1-1/4
35	1-3/8	75*	4-3/4	115*	3
36	3/4	76*	4	116	3/4
37	1-7/8	77	1-1/2	117	1-5/8
38	1-1/8	78	3/4		
39	3/4	79*	2-3/8		
40	1	80*	3-3/4		

Location shown in Figure 125.

TABLE XXXIX. CRACK DOCUMENTATION, SPECIMEN #2

Crack Number	Length (in.)						
1*	7-1/4	40	1-3/4	79	1	118	1/2
2*	9	41	3/4	80	SPOT	119	SPOT
3	3/4	42	1/2	81	SPOT	120	SPOT
4	1/2	43	1/4	82	1-3/4	121	1/8
5	1/2	44	3/4	83	1-1/2	122	SPOT
6*	2-1/2	45	SPOT	84	1/4	123	5/8
7	1/2	46	SPOT	85	1-1/2	124	1-1/2
8	1	47	SPOT	86*	4	125*	3
9*	2-1/4	48	1/2	87	1/4	126	SPOT
10	1	49	SPOT	88	SPOT	127*	21-1/2
11*	4	50	SPOT	89*	9	128	1/2
12*	2-1/2	51	1/4	90	1	129	1
13*	2-3/8	52	1/4	91	SPOT	130	1-1/2
14*	2	53	SPOT	92	1/4	131	1/4
15	1-1/2	54	SPOT	93	1-1/2	132	5/8
16	1	55	SPOT	94	1/4	133	5/8
17*	3	56	1	95	1/2	134	1-1/8
18*	2-1/2	57	SPOT	96	1-1/8	135*	2-1/4
19*	2	58*	4	97	1-7/8	136	1/2
20*	2-1/2	59	1/2	98	1-1/2	137	5/16
21*	2-1/2	60	3/16	99	SPOT	138	5/8
22*	2-5/8	61	1/4	100	SPOT	139	SPOT
23	1-1/2	62	1	101	SPOT	140	SPOT
24*	2-1/2	63	1/4	102	1/4	141	SPOT
25	7/8	64	1/2	103	SPOT	142	SPOT
26	1-3/4	65*	2-5/8	104	1/2	143	1/8
27	7/8	66	1	105	1/2	144	3/4
28	1-3/4	67	SPOT	106	1/8	145	1-7/8
29	1/4	68	1/4	107	SPOT	146*	2
30	5/8	69	SPOT	108	SPOT	147*	2-1/2
31	1/8	70	1-1/4	109	9/16	148	1-3/4
32	1/8	71	SPOT	110	SPOT	149*	2-3/4
33*	2	72	SPOT	111	1/8	150	1-1/2
34	1/2	73	SPOT	112	1/4	151	1-3/4
35*	2-1/2	74	3/8	113	3/16	152	1-1/2
36	SPOT	75	1/4	114	7/8	153	1-1/4
37	1-3/8	76	1/4	115	SPOT	154	1-3/4
38	1	77	1/4	116	1/2	155	1
39*	2	78	1/4	117*	10-1/2		

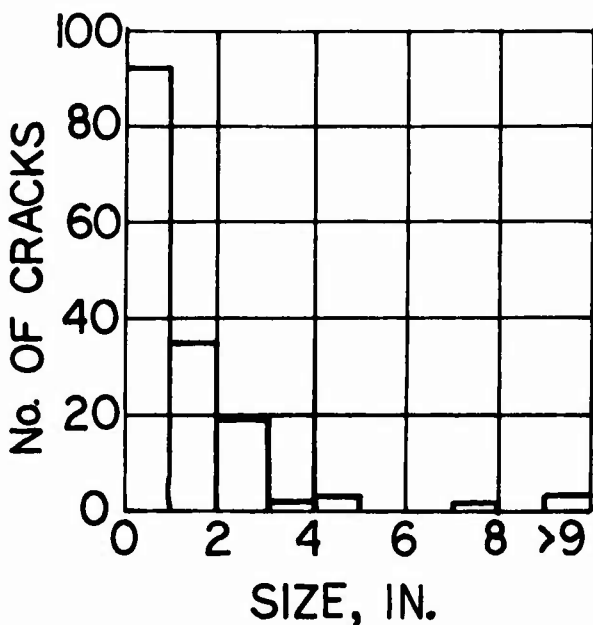
Location shown in Figure 126.



SIZE (IN.)	No.	PCT
< 1	35	29.9
1-2	36	30.8
2-3	19	16.4
3-4	9	7.7
4-5	7	6.0
5-6	3	2.5
6-7	2	1.7
7-8	1	0.8
8-9	1	0.8
> 9	4	3.4

TOTAL No.-117
TOTAL LENGTH - 267 IN.

SPECIMEN No. 1



SIZE (IN.)	No.	PCT
< 1	92	59.3
1-2	35	22.7
2-3	19	12.3
3-4	2	1.3
4-5	3	1.9
5-6	0	0.0
6-7	0	0.0
7-8	1	0.6
8-9	0	0.0
> 9	3	1.9

TOTAL No.-155
TOTAL LENGTH - 186 IN.

SPECIMEN No. 2

Figure 124. Crack Size Distribution.

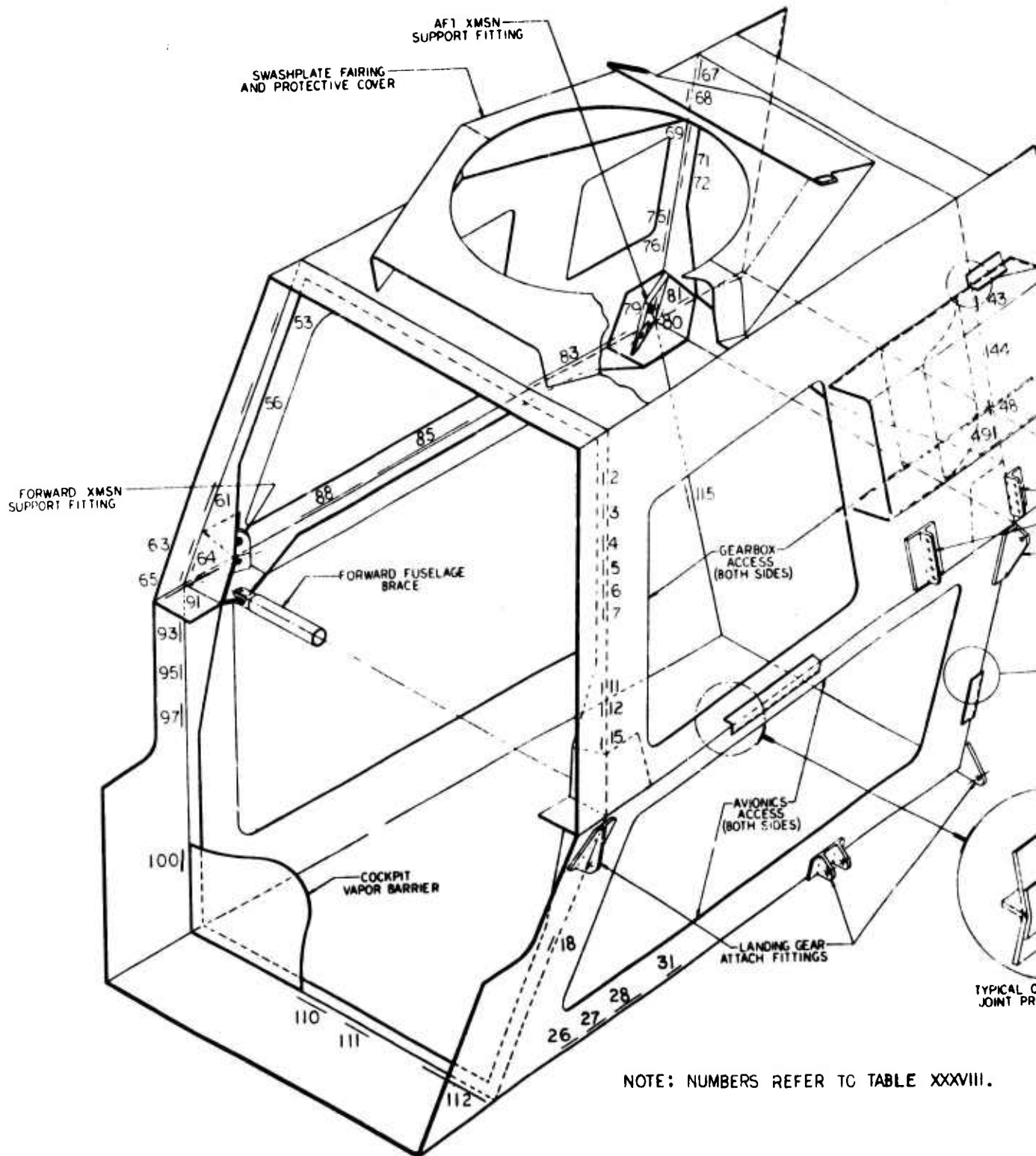
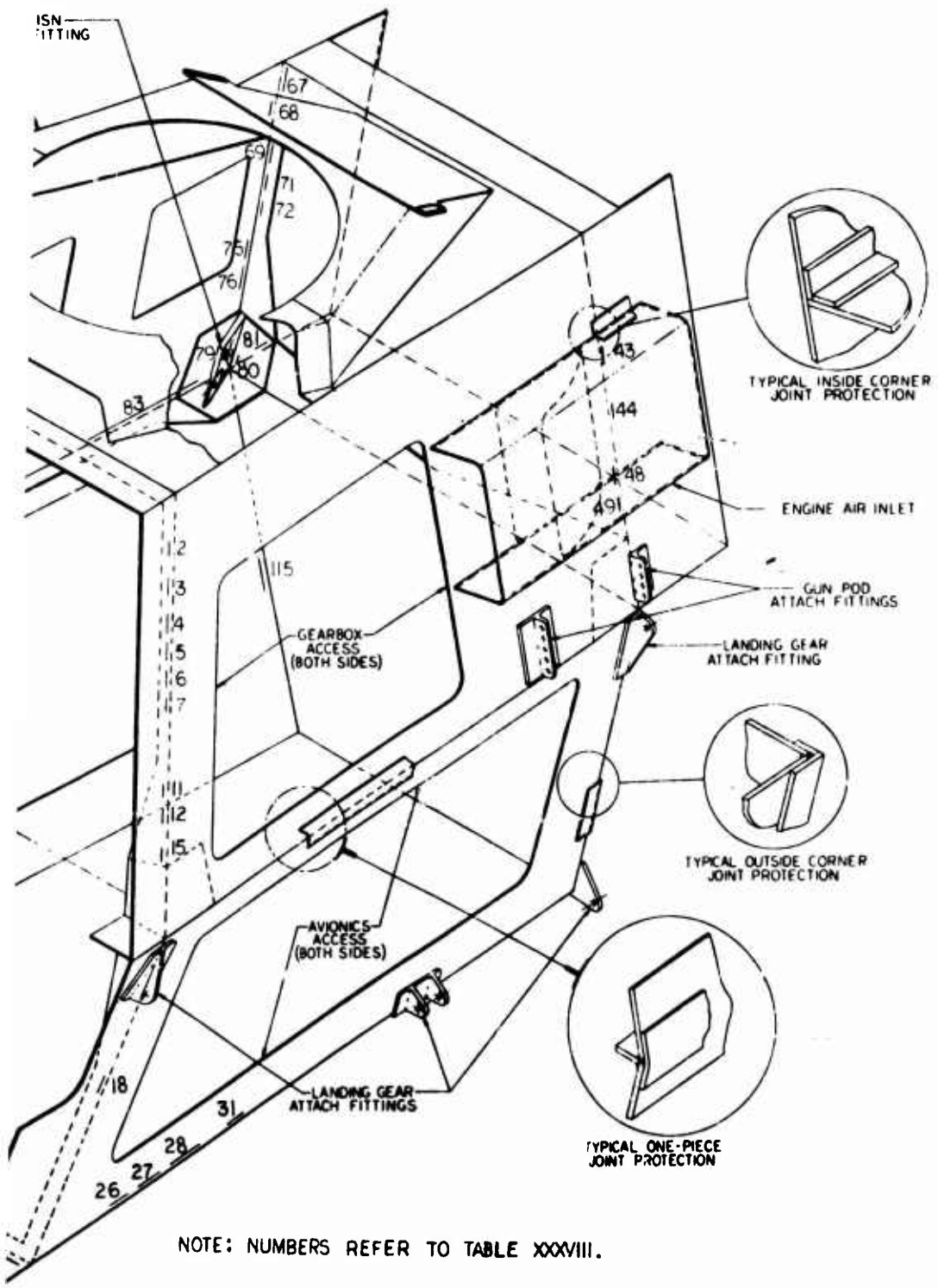


Figure 125. Crack Locations, Specimen 1.



lons, Specimen 1.

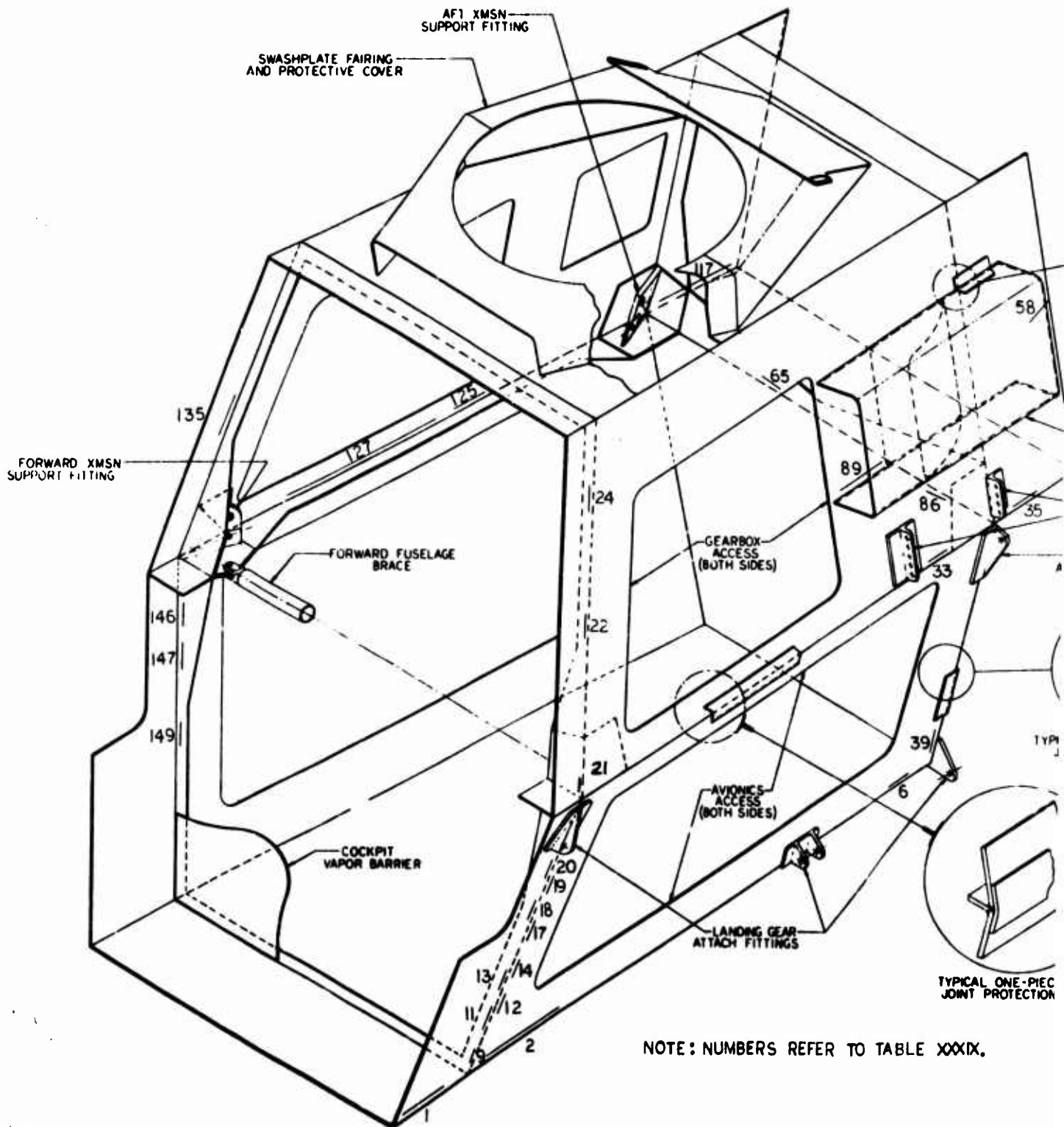
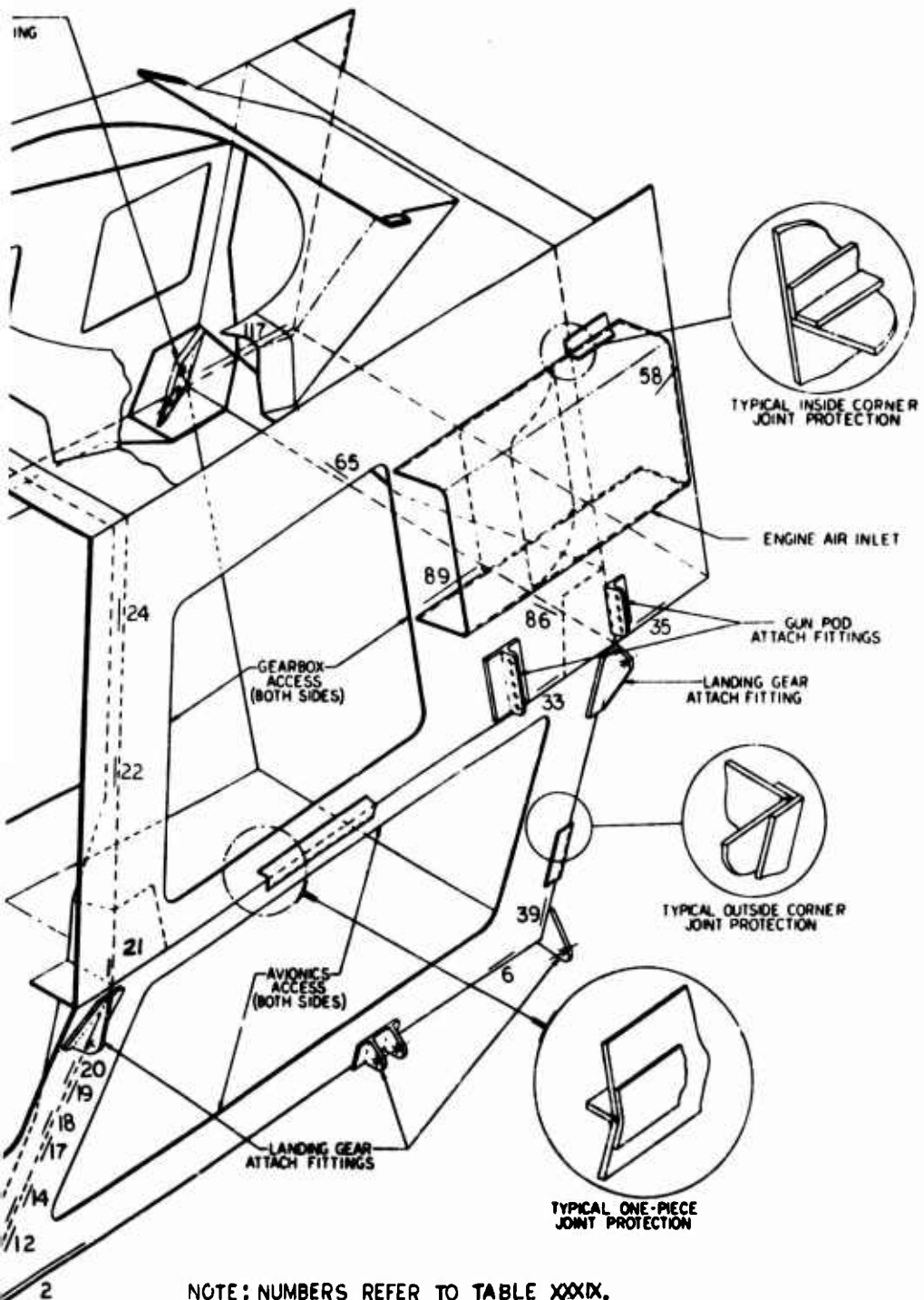


Figure 126. Crack Locations, Specimen 2.

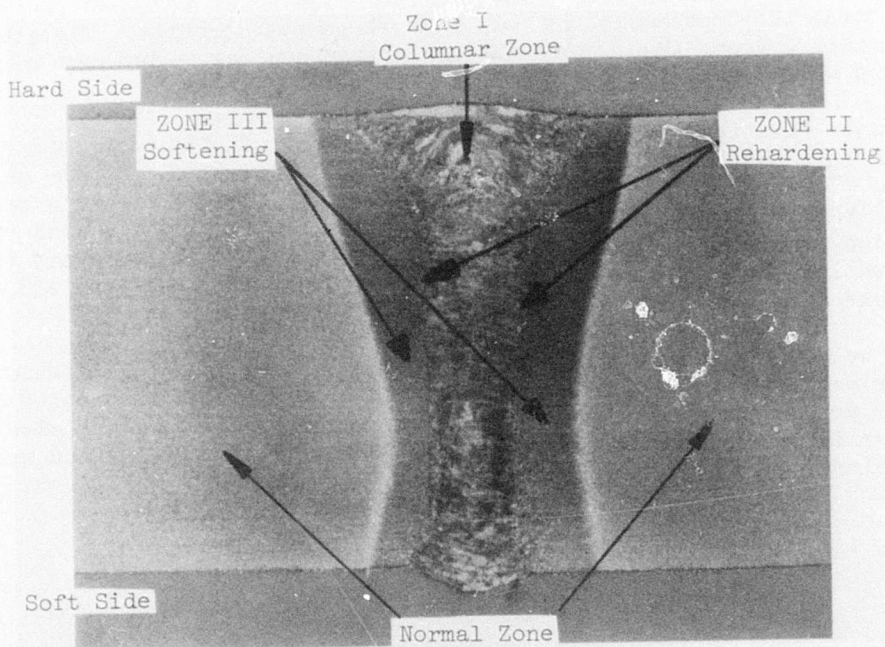


Metallurgical examination revealed full penetration in all cases. Microscopic examination showed three distinct zones (Figure 127) — a columnar central zone where melting had occurred, a narrow rehardened zone, and a small softened zone. One of the most promising features was the hardness profile shown in Figure 128. The total heat-affected zone was typically less than 0.5 inch, with a minimum face hardness of R_c 43. By comparison (Figure 129), GTA welding typically results in a heat-affected zone of up to 2 inches, and a minimum face hardness of R_c 32. These properties suggest that laser welded armor might not require additional joint protection.

Although some tendency toward fusion line cracking up to 0.040 inch deep was noted, this appears to be only a developmental problem. The achieved properties suggest that preheating and/or postheating techniques could be used while retaining acceptable ballistic resistance.

The major advantages of laser welding are the speed, the high equivalent temperature and energy density, the resultant properties, and the elimination of filler wire. While these may also be found in electron beam welding (laser welding does not require a vacuum) there are no secondary X-ray emission problems, and the laser beam can be directed with mirrors to the desired location. Also, the laser beam is essentially massless and does not tend to drive shield gas impurities into the weld bead.

Laser welding is a comparatively new process and equipment limitations presently exclude its use in current programs. However, in an armored helicopter production time frame, the process shows considerable promise. Further investigations of ballistic and mechanical properties and welding variables should be pursued.



See Figure 128 for Hardness Profile

Figure 127. Laser Weld Cross Section, 9X.

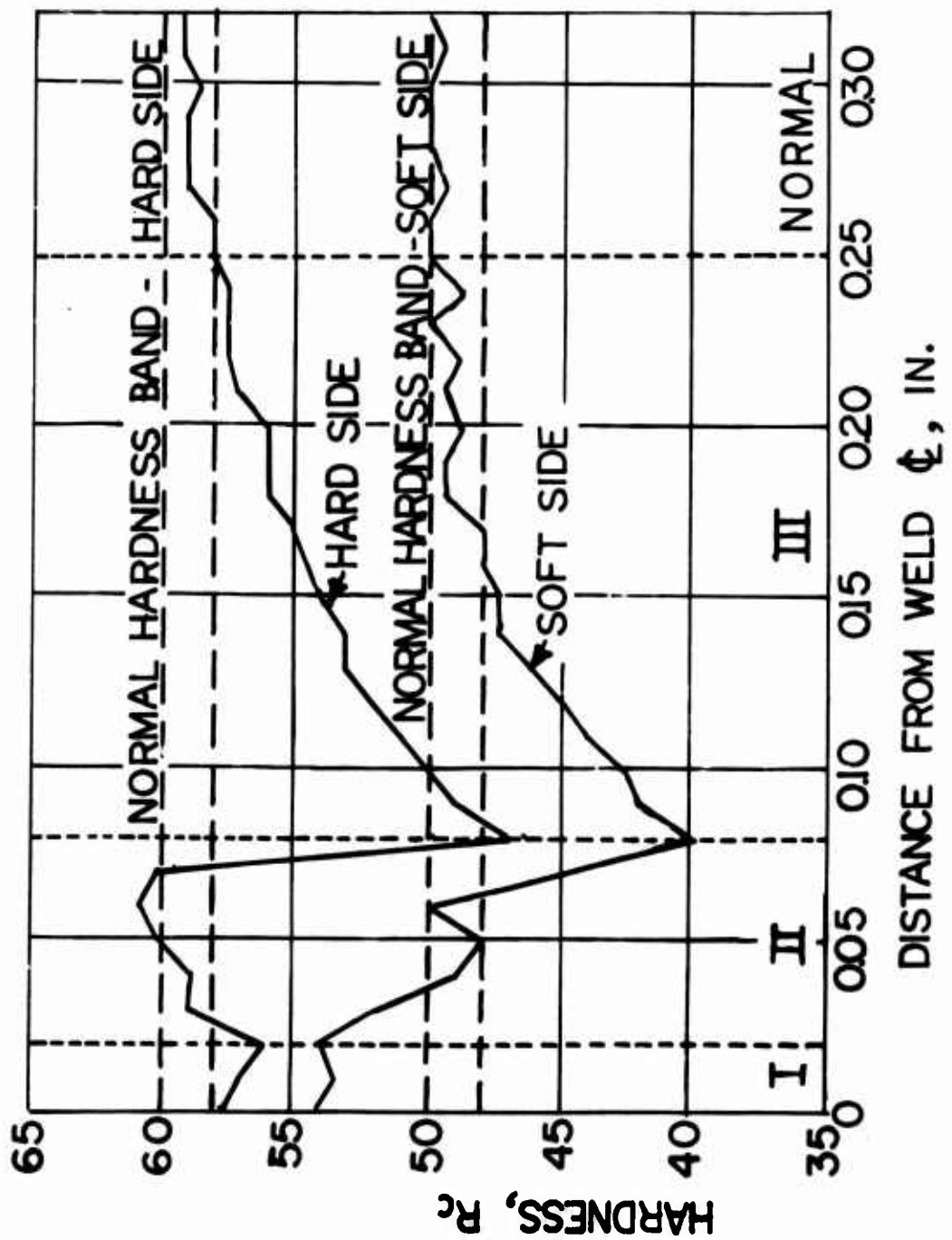


Figure 128. Typical Laser Weld Hardness Profile, Thickness 0.305 Inch, Speed 50 Inches per Minute.

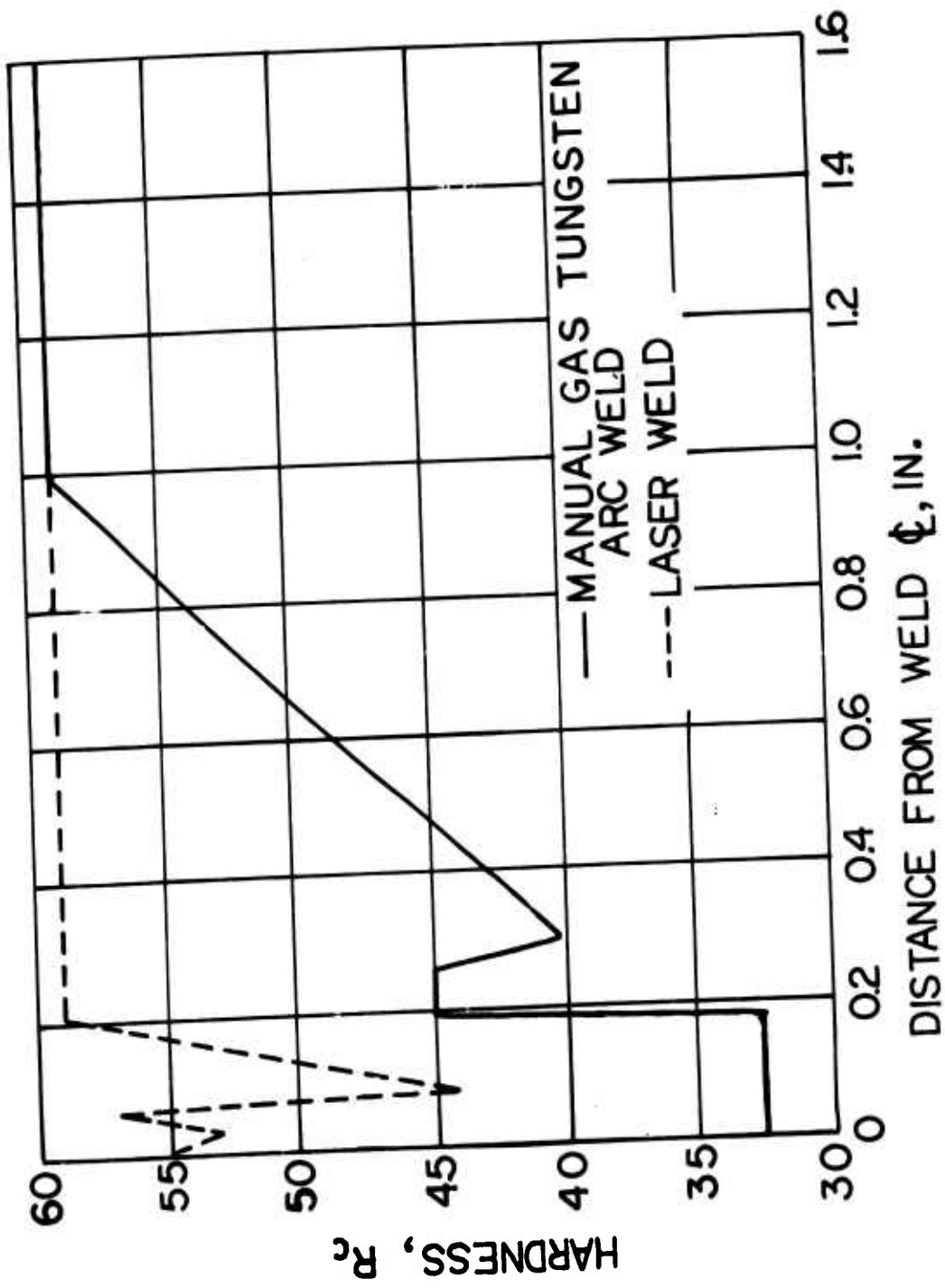


Figure 129. Weld Hardness Profile Comparison.

ARMORED FUSELAGE TEST FACILITY

GENERAL

The armored fuselage test facility consisted of a support frame, a dummy gearbox, a dummy landing gear, a load control system capable of applying the loading as specified in the approved test plan, and an instrumentation system capable of reading out the critical stress locations and the applied loads.

CONFIGURATION DEFINITION

The armored fuselage test facility is designed to subject the fuselage center section specimens to a spectrum of load conditions representative of normal flight.

Load Type Selection

The ballistic survivability design criteria for the fuselage resulted in an extremely strong, rigid structure. High frequency, low amplitude loads resulting from rotor harmonic loads and motions are nondamaging. The test facility is designed to apply the relatively low cycle, high level loads resulting from takeoffs, maneuvers, and landings which occur in the course of normal helicopter operations.

Load Simulation

Representative thrust, moments, inertia and drag loads are applied through a dummy gearbox/rotor assembly and dummy landing skids. Reaction to these loads is provided by extending the fuselage and mounting it at forward and aft locations chosen to provide optimum simulation of fuselage inertia loads.

Mission Spectrum

Table XL shows the design operational usage spectrum for the aircraft, and summarizes the maneuvers and steady flight conditions experienced by the aircraft together with their estimated frequency of occurrence. The aerodynamic and inertia loads resulting from each condition were calculated and the spectrum was simplified to a degree where simulation in the laboratory was practical. Table XLI shows loads calculated for significant maneuvers.

TABLE XL. OPERATIONAL USAGE SPECTRUM

Item	Occurrences (100 Hours)	Occurrence Aircraft Life (3600 Hrs.)	Occurrence % of Aircraft Life
Steady Hovering			9.32
Sideward Flight			.932
Rearward Flight			.466
Forward Level Flight			
Speed = 20% V_H			4.66
40% V_H			4.66
50% V_H			1.86
60% V_H			7.46
70% V_H			9.32
80% V_H			14.00
90% V_H			16.80
V_H			9.32
115% V_H			.932
Takeoff Power Climb			.932
Full Power Climb			2.8
Power Dives			2.33
Right Turns	1050	37800	2.330
Left Turns	1050	37800	2.330
Autorotation	-	-	1.860
Takeoff (Equal No. of Landing)	400	14400	.667
Hovering Turns	1000	36000	3.333
Control Reversals - Hovering	1000	36000	.278
Landing Approach	500	18000	.556
Partial Power Descents	500	18000	2.220
Control Reversals	800	28800	.333
Pull-ups	250	9000	.208
Power to Autorotation	40	1440	.022
Autorotation to Power	40	1440	.044
Autorotation Pull-ups	40	1440	.044
Ground-Air-Ground Cycles	100	1440	.044
V_H is maximum level flight speed.			

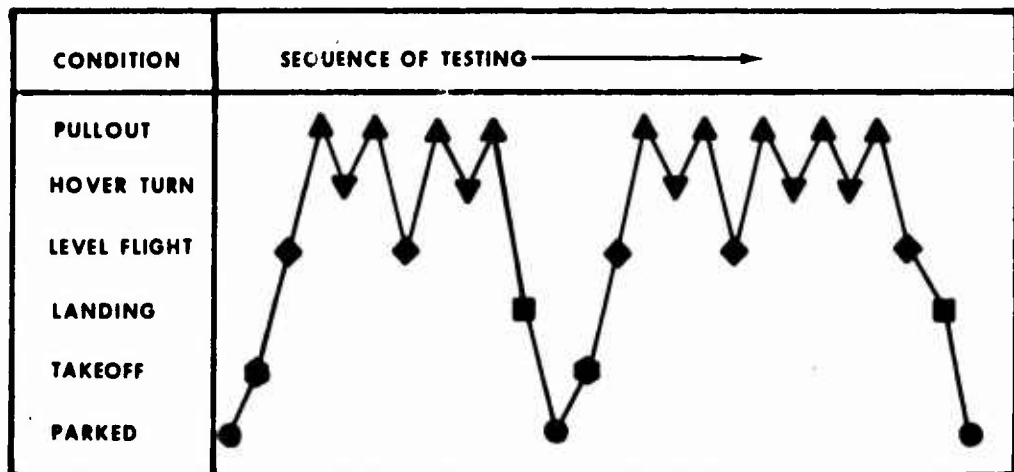
TABLE XLI. APPLIED LOADS						
Condition	Rotor Aerodynamic & Inertia Loads				Skid Loads	
	Thrust (in.)	Drag (in.)	Pitching Moment (in.-lb)	Yaw Moment (in.-lb)	Vertical (lb)	Drag (lb)
Parked	0	0	0	0	4930	0
Take off	42000	0	342900	0	0	0
Landing	8000	0	0	0	17550	8040
Level Flight	15360	1080	-210300	0	0	0
Hover Turn	12000	0	98000	114000	0	0
Pullout	39790	760	375400	0	0	0

Load Application Scheme

Fatigue damage is a result of cyclic changes of stress level, so the percentage time spent at any given steady flight condition is unimportant. Fatigue damage is accrued when a large change in stress occurs such as when an aircraft takes off and the vertical thrust load and the resulting stresses increase from a 1g to a 2g level, then return to a 1g level as the aircraft settles into a hover or forward level flight condition. The sequence in which maneuvers occur is therefore of importance, and Figure 130 shows the fatigue test spectrum selected as being representative of design usage using the criteria outlined.

SUPPORT FRAME

The support frame shown in Figure 131 supported the fuselage and reacted the applied loads. The loads are tabulated in Table XLII for each cylinder. The frame consisted of low grade structural steel I-beams and machined cylinder attachment fittings. The frame, as well as the gearbox and landing gear, was designed to the quasi-static loading as listed in Table XLII with a safety factor of 4.



CONDITION	NUMBER OF OCCURRENCES	
	per SPECTRUM BLOCK	per 100 HOURS
PULLOUT	9	1800*
HOVER TURN	5	1000
LEVEL FLIGHT	5	1000
LANDING	2	400
TAKEOFF	2	400
PARKED	2	400

*Includes conservative allowance for high-speed banked turns etc.

Figure 130. Fatigue Test Load Spectrum.

TABLE XLII. LOADING SYSTEM RANGES

Channel	Load Applied	Remarks	Load Range (lb)	
1	Pitch Moment and Thrust	Works in conjunction with #2	0	to 13,213
2	Pitch Moment and Thrust	Works in conjunction with #1	-984	to 20,114
3	Rotor Drag	-	0	to 2,049
4	Yaw Moment	Use two parallel plumbed cylinders	0	to 1,188
5	Landing	Use two parallel plumbed cylinders	0	to 19,304
6	Parked	Use two parallel plumbed cylinders	0	to 4,930

DUMMY GEARBOX

The dummy gearbox shown in Figure 132 provides the means of applying the rotor loads (thrust, drag, pitch, and yaw) to the test article through the transmission pickup points.

The dummy gearbox consisted of a large I-beam with fitting hubs welded to it. The fitting hubs are attached to the test article by short links.

The gearbox weight of 1300 pounds was removed from the test article by adjusting the applied loads.

DUMMY LANDING GEAR

The dummy landing gear shown in Figure 133 permitted the parked and landing loads to be applied to the test article through the landing gear pickup points. The landing gear consisted of two I-beams (one on each side) attached to long rods from the landing load cylinders and the parked load cylinder. The dummy landing gear weight of 700 pounds each was removed by attaching weights to pulleys as shown in Figure 133.

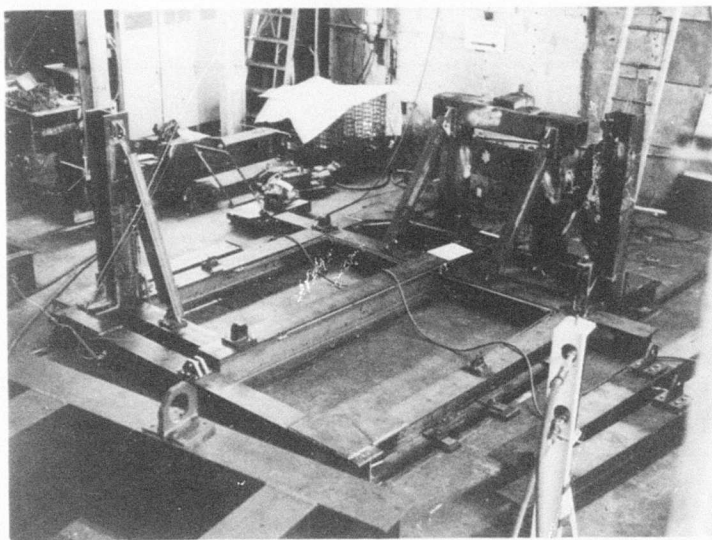


Figure 131. Support Frame.

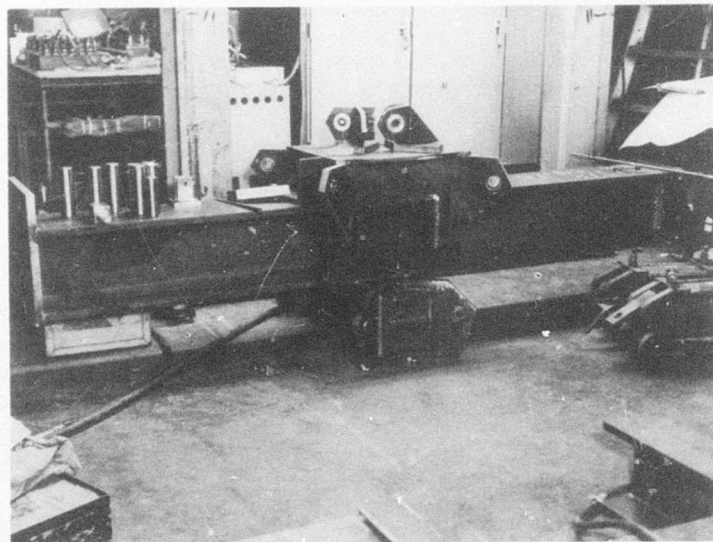
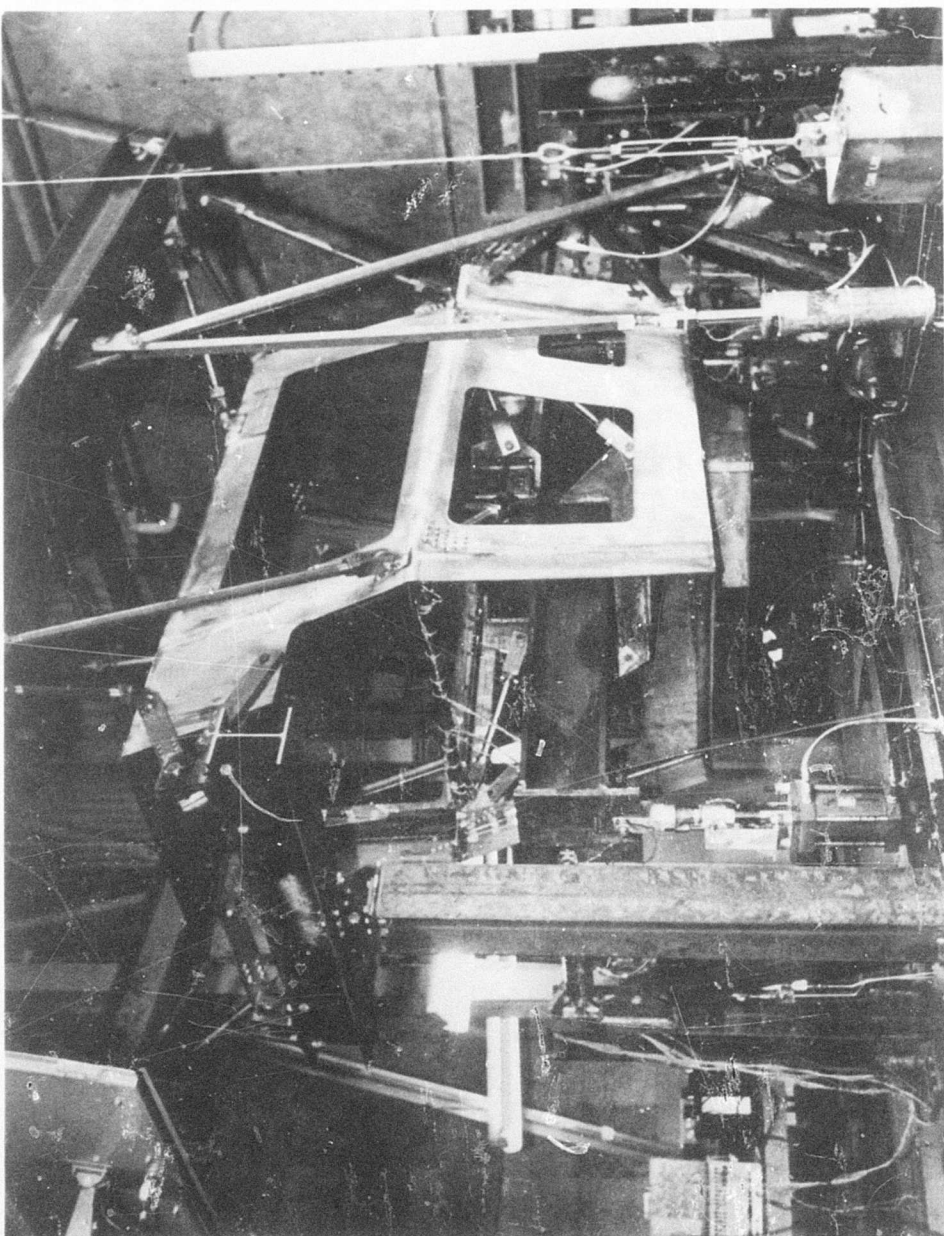


Figure 132. Dummy Gearbox.

Figure 133. Test Article Installed in Test Facility.



CONTROL SYSTEM

The control system performs the function of applying the loads, maintaining the load, automatically shutting down on load error, and automatically sequencing through the load spectrum. Figure 134 shows the control console.

The loads are applied by hydraulic cylinders. The cylinders are generally in tension throughout the spectrum. The system pressure is 2000 psi for normal operation.

Feedback System

The loads are maintained and applied by nulling the command load with load feedback from a load cell. Figure 135 shows schematically the load control feedback system. The error signal (difference between commanded and actual load) is amplified and filtered by the servo amplifier. The servo amplifier in turn drives a servo valve. The servo valve applies a pressure differential across the cylinder piston. The resultant force is applied to the test specimen through the dummy gearbox and dummy landing gear. The load is measured by a load cell in series mechanically (see Figure 136) with the cylinder piston. This load cell output signal is amplified and used for the error determination. There are six systems to apply load. Table XLII lists the six systems and their functions.

The six servos are all low bandwidth systems. This is suitable since only quasi-static inputs are desired. Since the specimen was deemed "very stiff", load feedback seemed a suitable and convenient method for controlling load.

Error Detection

Each servo loop has a safety shutoff system built in. The load error is sensed and applied to a relay amplifier. When the load error exceeds a preset level for 2.5 seconds, the hydraulic supply is shut down. The shutdown mode turns off the pump, and dumps the pressure.

In addition to the error detect shutdown, limit switches were installed on the test fixture. These switches will shut down the hydraulic supply, without a delay, whenever any overtravel by critical pistons occurs.

Programmer

The error signal, as previously discussed, is the difference between the desired load and the actual load. The desired load or command load is a DC voltage proportional to the load. This voltage originates in the programmer. The programmer shown schematically in Figure 137 is a step-per switch which sequences (manually or automatically) through a set of

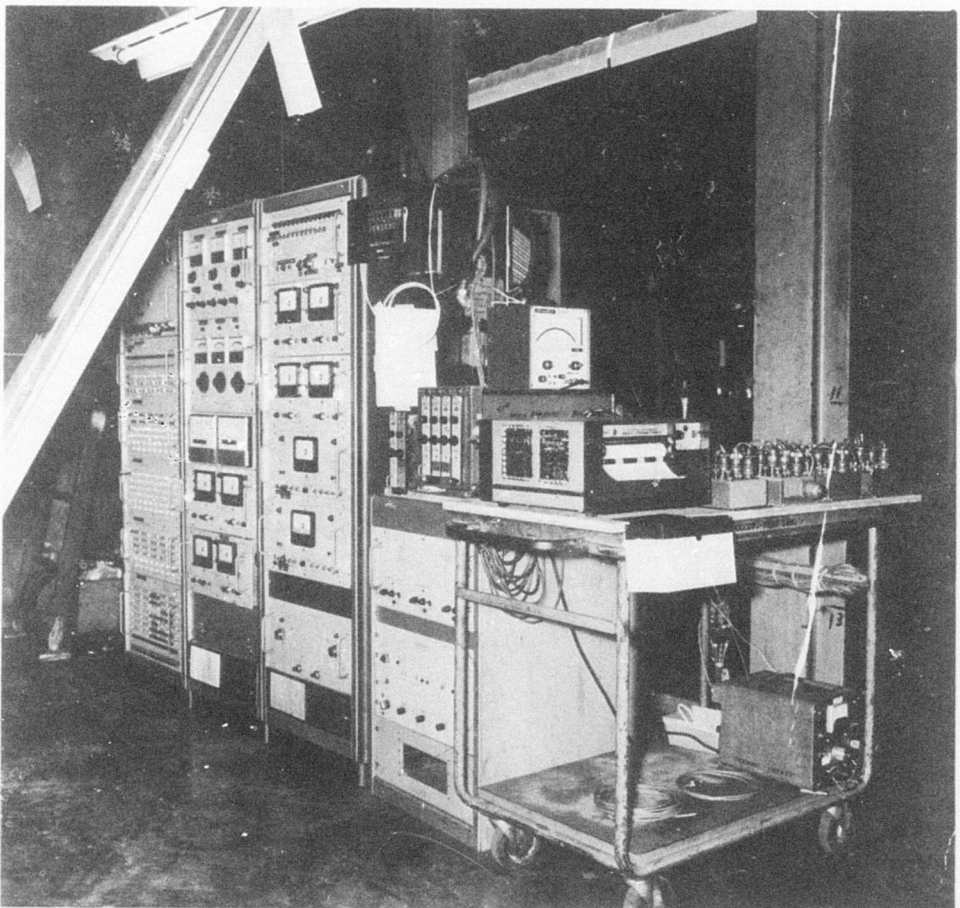


Figure 134. Control Console.

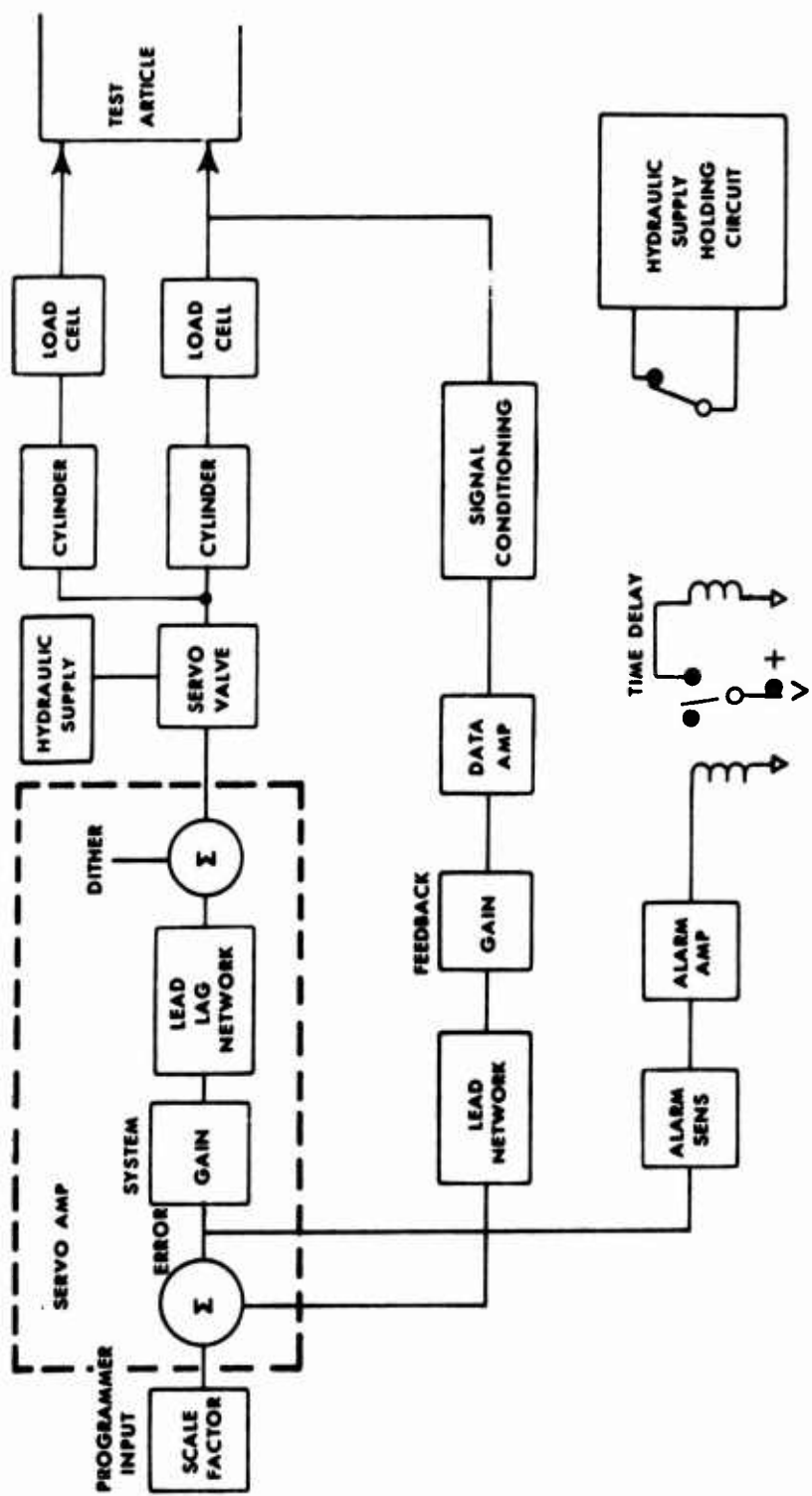


Figure 135. Control System Block Diagram.

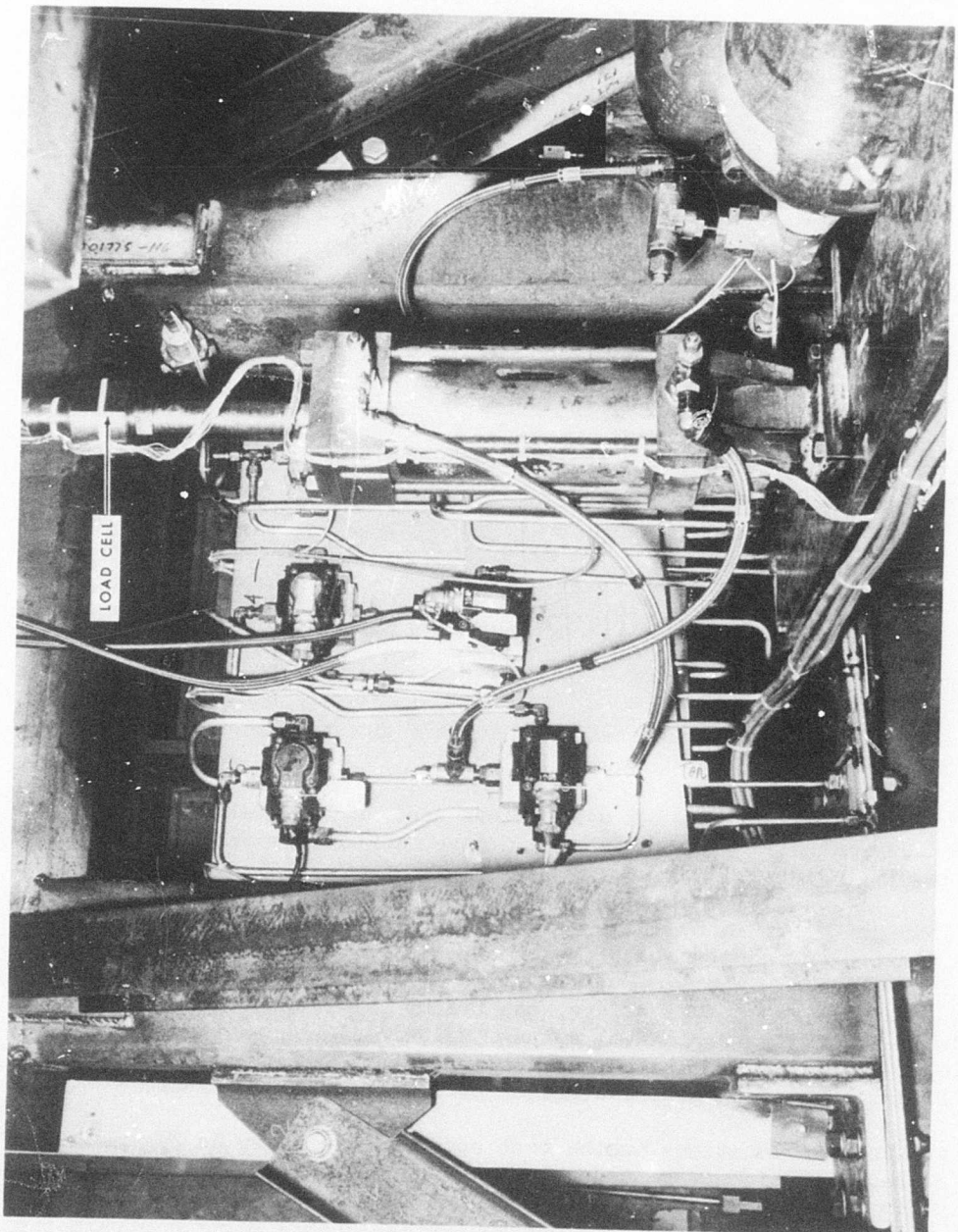


Figure 136. Loading System.

voltages patched into a program board. This stepper switch has seven decks of contacts of which six are used (one deck for each channel). The voltages patched into the board represent the six flight conditions. The sequence (25 different steps allowed before repeating) that these voltages are stepped through represents the load spectrum as shown in Figure 130.

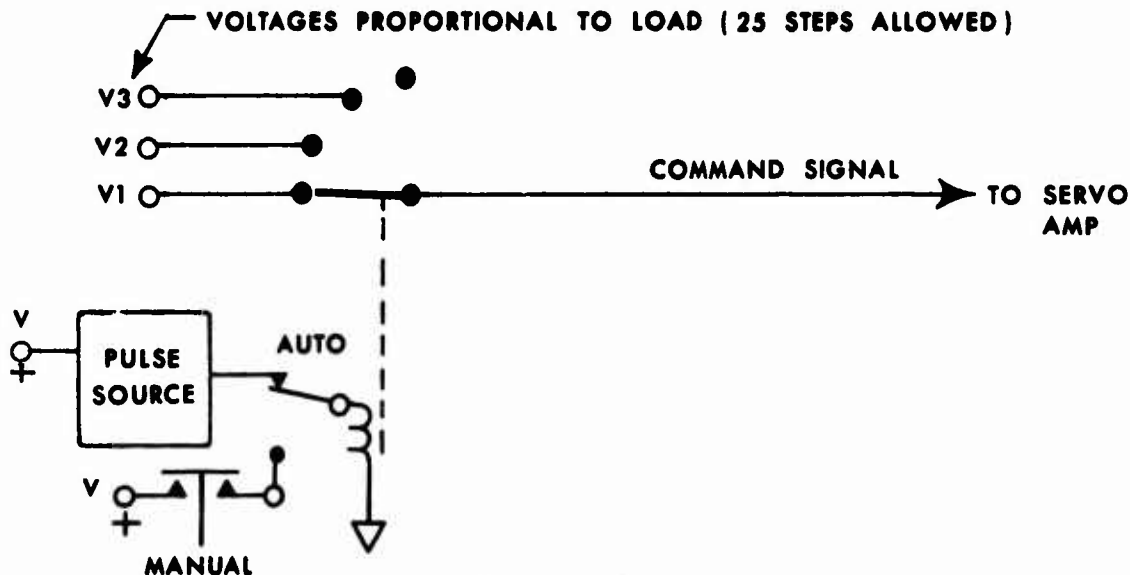


Figure 137. Programmer Schematic.

INSTRUMENTATION SYSTEM

The instrumentation system enables the loads and strains to be read out and recorded.

Two types of instrumentation systems are used, a load cell transducer recorded on an oscillosograph, and strain gage transducers read out on a digital strain indicator.

The load cells are installed and calibrated on a Baldwin test machine for both tension and compression. Figure 136 shows a typical load cell cylinder installation. The linearity of the calibration data is $\pm 1\%$ full scale. Each load cell has a dual bridge, one bridge for readout and the other for feedback signal in the control system. Figure 133 shows the load cell cylinder locations. All nine load cell readouts are tied to an 18-channel oscillosograph which permits evaluation of the transient response.

The strain gage locations on the test specimen are shown in Figure 143. The 30 gage locations were determined by analysis of critical strain values. The gages were electrically calibrated and have a readout accuracy of $\pm 2\%$ full scale. The gages are read out sequentially on a digital strain indicator. Nine of the most important gages were put on the oscillosograph to permit parallel readout.

TESTING OF THE STRUCTURAL ARMOR FUSELAGE SPECIMENS

INTRODUCTION

A series of tests were performed to demonstrate the structural integrity and the ballistic survivability of the structural armor fuselage. Static tests provided stress measurement at critical locations on the fuselage for comparison with stress values predicted by finite element analysis, and for determination of fatigue test acceleration factors. A spectrum of fatigue loading, simulating actual flight, was applied to the fuselage to simulate 3600 hours of service life. Ballistic tests were performed to demonstrate the capability of the fuselage, under simulated level flight loading, to withstand multiple impacts of ball and armor-piercing projectiles. Subsequent to ballistic testing, a fatigue test was performed simulating a further 600 hours of service life. Finally a static test was performed to demonstrate the residual strength of the fuselage.

TESTING THE FIRST SPECIMEN

Static tests were performed to provide stress measurements at critical locations on the first specimen for comparison with finite element analysis and for fatigue methodology damage calculations. The fuselage was installed in the test facility as shown in Figures 138-142. Non-structural components, such as access doors, hinges, sliding tracks, engine air intake scoops, etc., were not fabricated for the first specimen. Strain gages were located on the fuselage where high stresses were predicted by the NASTRAN finite element analysis. These locations are shown in Figure 143. A series of incremental loading static tests were performed. The load control console was used to apply incremental loads up to 100% of the design limit load for each of the following conditions:

- Park
- Takeoff
- Level Flight
- Symmetrical Pullout
- Hover Turn
- Land

Strain gage outputs were monitored on a digital strain indicator, checked for linearity vs applied load, and compared with analytical predictions. These data are presented in Table XLIII. During these tests, specimen manufacturing defects, including weld cracks, etc., were inspected and no changes were observed.

At this point manufacture and assembly of the second specimen was completed using an improved welding technique. This specimen appeared superior to the first specimen in terms of weld and material cracks.

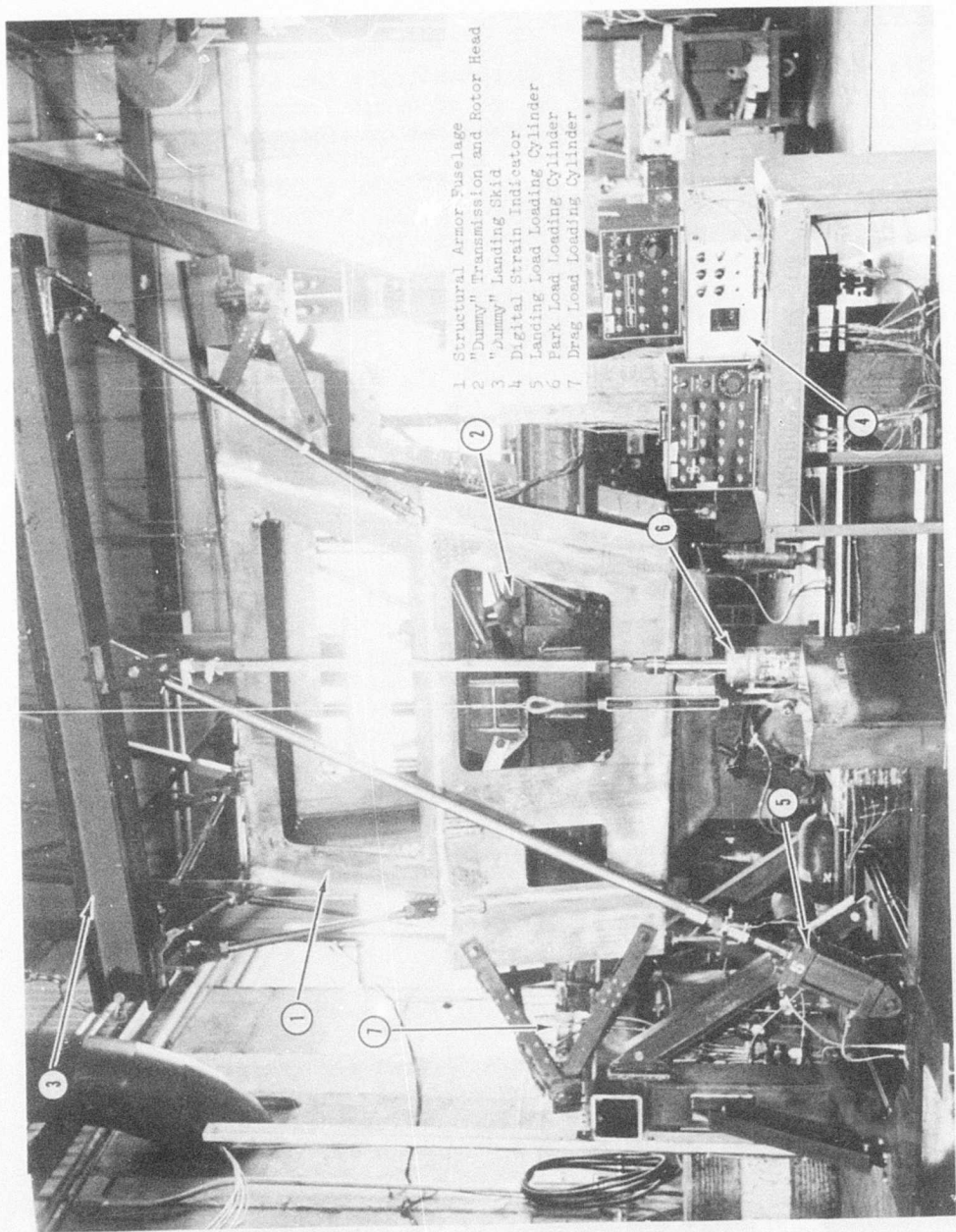


Figure 138. Structural Armor Fuselage Test Setup, Specimen S/N-1.

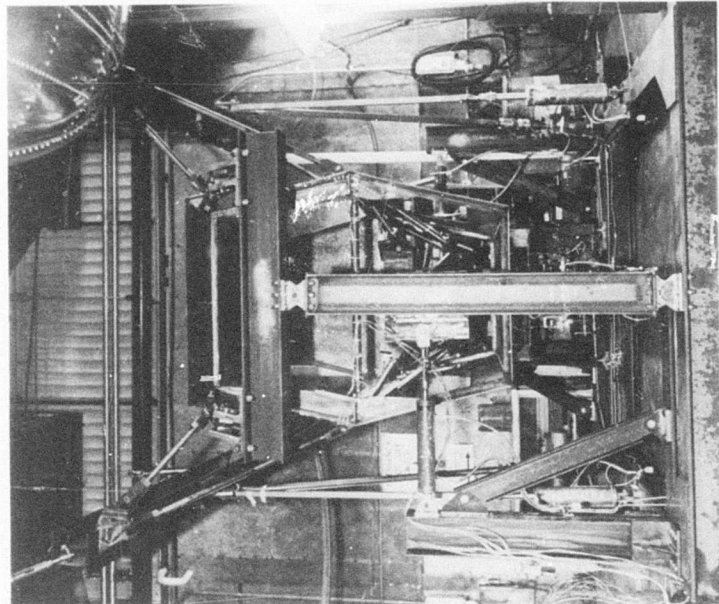


Figure 140. Structural Armor Fuselage Test Setup, Specimen S/N-1.

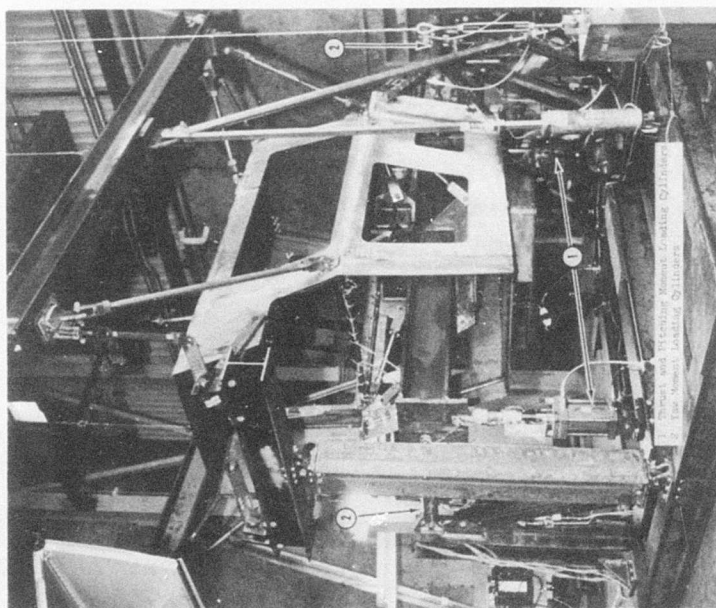


Figure 139. Structural Armor Fuselage Test Setup, Specimen S/N-1.

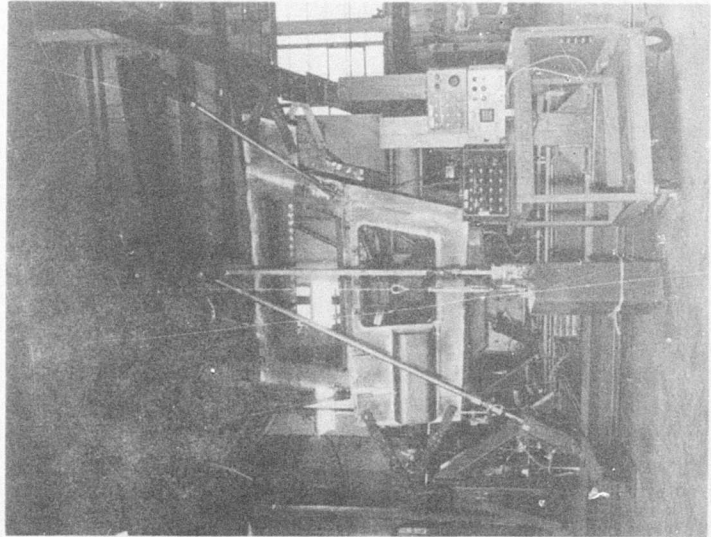


Figure 141. Structural Armor Fuselage
Test Setup, Specimen S/N 2.

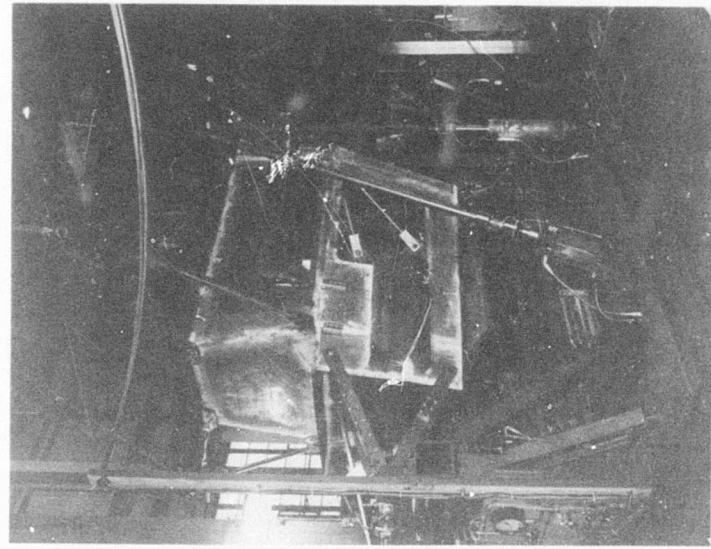
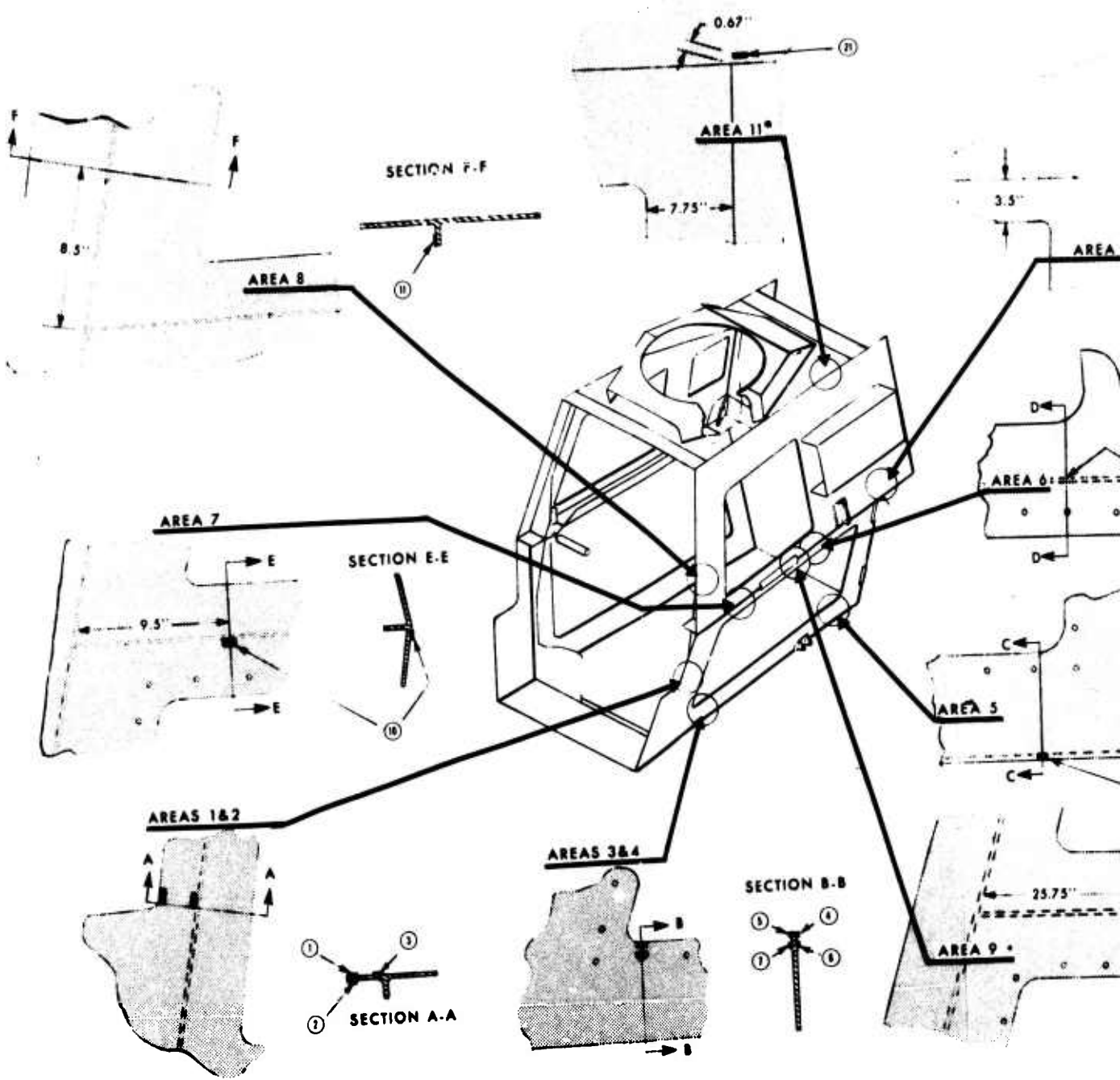
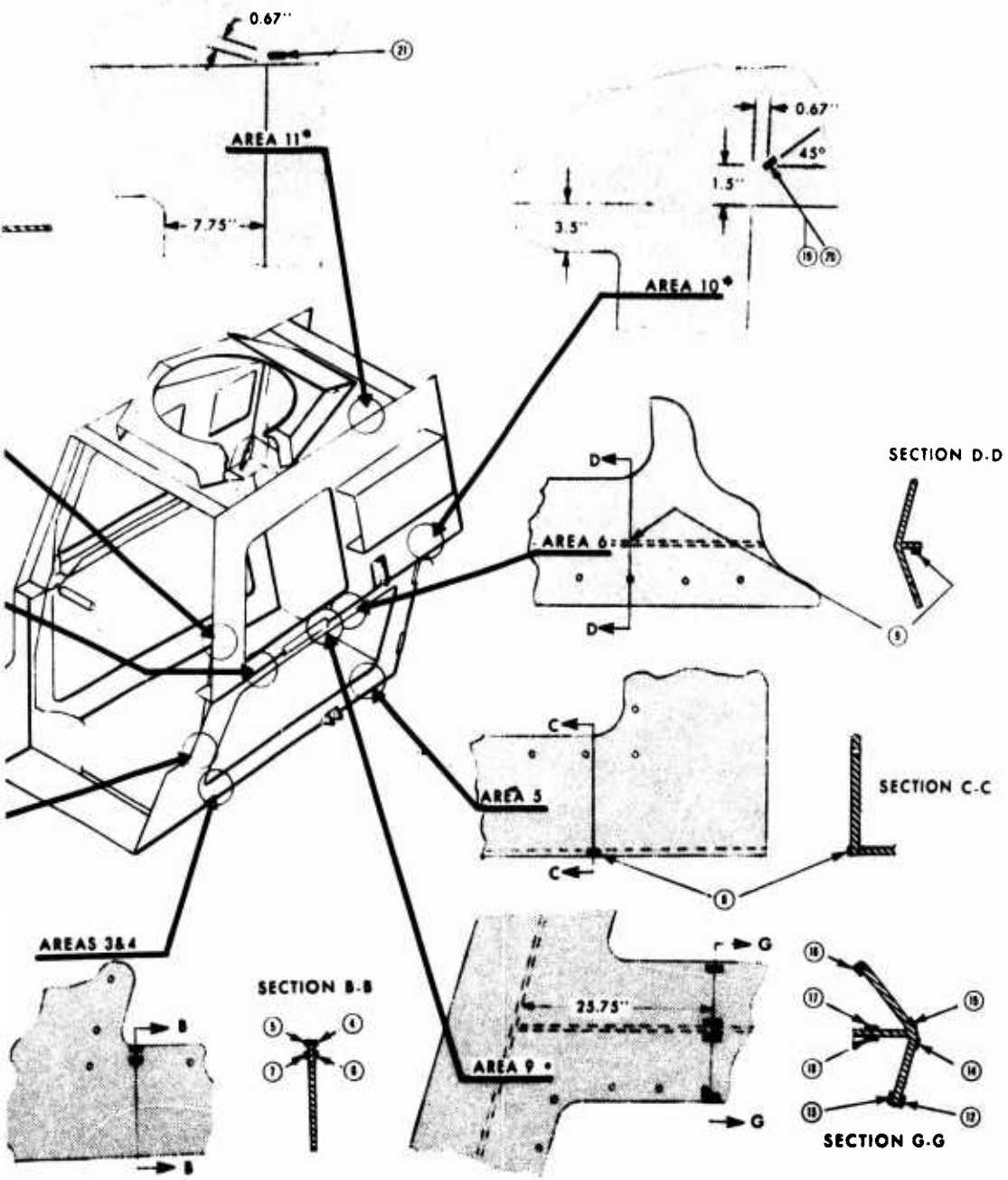


Figure 142. Structural Armor Fuselage
Test Setup, Specimen S/N 2.



^aGages 12 through 21 located on left side

Figure 143. Structural Armor Fuselage, Strain Gage Locations.



*Gages 12 through 21 located on left side of specimen S/N 2 only.

age, Strain Gage Locations.

TABLE XLIII. A
 S

Loading Condition	Park			Takeoff			Level	
	Specimen S/N-1	Specimen S/N-2	Analytical Stress	Specimen S/N-1	Specimen S/N-2	Analytical Stress	Specimen S/N-1	Specimen S/N-2
Left Side Strain Gages	12.4	10.30	7.98	18.7	19.00	18.5	3.9	4.3
	9.5	8.76	7.98	17.9	18.40	18.5	3.5	4.1
	2.0	12.90	4.64	3.3	3.21	11.6	0.6	-0.0
	3.5	3.48	1.31	38.1	36.20	33.5	7.9	7.6
	7.3	5.97	1.31	28.5	37.30	33.5	5.3	7.5
	2.0	2.16	1.30	28.2	27.30	25.2	5.8	5.6
	5.3	3.96	1.30	19.0	23.60	25.2	3.5	4.7
	1.2	0.93	2.39	7.8	7.71	18.7	1.3	1.5
	2.8	2.73	4.04	10.0	11.30	27.8	2.9	3.3
	1.6	1.38	1.44	5.9	8.40	15.1	0.9	1.6
	1.4	0.48	6.96	1.6	1.59	22.5	0.5	0.6
	-	0.15	-	-	3.72	-	-	-1.2
	-	-0.06	-	-	6.18	-	-	-1.8
	0.9	0.75	-	4.1	4.92	-	-	0.6
	-	0.63	-	-	5.37	-	-	0.8
	-	0.42	-	-	1.02	-	-	-0.2
	-	-0.54	-	-	-7.77	-	-	-2.1
	-	-0.33	-	-	-7.77	-	-	-2.1
	0	0.06	2.25	2.1	2.04	17.4	-	0.1
	0.2	0.39	2.25	2.7	4.35	17.4	-	0.9
	0.9	0.30	4.08	1.3	1.35	16.0	0.9	0.7
Right Side Strain Gages								
1	-	12.70	7.98	18.6	22.80	18.5	3.50	5.3
2	-	10.50	7.98	17.1	22.40	18.5	3.60	4.9
3	-	1.29	4.64	3.2	3.09	11.6	0.45	0.6
4	-	2.85	1.31	35.7	36.70	33.5	5.40	6.6
5	-	5.28	1.31	21.2	36.80	33.5	3.30	6.6
6	-	1.32	1.30	26.3	23.60	25.2	3.90	4.2
7	-	3.84	1.30	32.0	24.40	18.7	5.00	4.6
8	-	0.27	2.39	7.3	7.56	27.8	0.9	1.2
9	-	1.41	4.04	7.7	7.83	15.1	2.3	2.1
10	-	0.57	1.44	7.6	6.39	22.5	1.8	8.7

THIS PAGE IS BLANK-NOT FILMED

E XLIII. AARS STRUCTURAL ARMOR FUSELAGE
STATIC STRESS SURVEY RESULTS

Level Flight			Pullout			Hover Turn				
Item	Specimen	Analytical	Specimen	Specimen	Analytical	Specimen	Specimen	Analytical	S/N-1	S/N-2
	S/N-2	Stress (ksi)	S/N-1	S/N-2	Stress (ksi)	S/N-1	S/N-2	Stress (ksi)	(ksi)	(ksi)
9	4.38	4.47	18.0	17.60	17.4	5.50	5.61	4.84	21.3	22
5	4.17	4.47	17.0	16.80	17.4	4.80	4.74	4.84	19.6	18
6	-0.09	2.73	3.3	3.24	10.6	0.48	0.57	2.86	4.6	4
9	7.62	7.91	36.2	33.80	31.6	4.50	4.20	6.32	31.6	30
3	7.53	7.91	27.8	34.60	31.6	4.50	4.83	6.32	28.8	38
8	5.67	5.97	26.3	25.30	23.8	3.20	3.24	4.79	22.1	22
5	4.71	5.97	14.7	22.00	23.8	3.00	3.12	4.79	19.6	25
3	1.56	4.50	6.3	6.96	17.6	0.69	0.72	3.36	4.2	5
9	3.30	11.20	9.0	10.10	26.2	-0.63	-0.09	4.0	6.2	7
9	1.62	4.70	5.3	7.65	14.5	-	0.39	1.86	3.0	4
5	0.69	5.25	1.8	1.59	20.9	2.40	2.61	4.39	3.5	3
-	-1.20	-	-	-3.42	-	-	-0.18	-	-	-4
-	-1.80	-	-	-5.76	-	-	-0.48	-	-	-6
-	0.63	-	3.6	4.65	-	-	0.69	-	1.7	2
-	0.81	-	-	5.16	-	-	0.63	-	-	2
-	-0.24	-	-	1.02	-	-	0.30	-	-	-1
-	-2.10	-	-	-7.32	-	-	-0.69	-	-	-7
-	-2.16	-	-	-7.17	-	-	-0.69	-	-	-7
-	0.12	5.57	-	1.80	16.5	-	0.24	3.51	-	0
-	0.90	5.57	2.7	3.63	16.5	-	0.69	3.51	-	2
9	0.78	10.90	1.2	0.93	15.1	0.18	0.06	2.62	1.4	1
50	5.34	4.47	18.0	20.90	17.4	4.50	4.89	10.30	19.7	26
60	4.92	4.47	16.5	20.60	17.4	4.40	5.43	10.30	17.0	22
45	0.69	2.73	3.0	2.64	10.6	1.30	1.41	8.65	4.5	1
40	6.69	7.91	34.4	33.70	31.6	14.40	15.20	12.80	29.6	29
30	6.63	7.91	20.1	32.60	31.6	8.00	13.90	12.80	20.9	33
90	4.29	5.97	24.9	21.50	23.8	11.20	10.10	9.64	20.9	18
00	4.68	5.97	30.3	22.30	23.8	11.50	9.15	9.64	30.7	21
9	1.23	4.50	6.9	6.42	17.6	3.10	3.24	7.40	4.5	1
13	2.40	11.20	6.9	6.63	26.2	4.70	5.37	12.30	4.5	1
8	8.70	4.70	5.3	5.50	14.5	2.90	4.02	7.20	2.2	1

FUSELAGE
RESULTS

Pullout			Hover Turn			Land		
Specimen	Specimen	Analytical	Specimen	Specimen	Analytical	S/N-1	S/N-2	Analytical
N-1	S/N-2	Stress	S/N-1	S/N-2	Stress	(ksi)	(ksi)	(ksi)
(si)	(ksi)	(ksi)	(ksi)	(ksi)	(ksi)			
1.0	17.60	17.4	5.50	5.61	4.84	21.3	22.60	18.0
1.0	16.80	17.4	4.80	4.74	4.84	19.6	18.20	18.0
1.3	3.24	10.6	0.48	0.57	2.86	4.6	4.47	11.6
1.2	33.80	31.6	4.50	4.20	6.32	31.6	30.60	29.4
1.8	34.60	31.6	4.50	4.83	6.32	28.8	38.30	29.4
1.3	25.30	23.8	3.20	3.24	4.79	22.1	22.60	22.3
1.7	22.00	23.8	3.00	3.12	4.79	19.6	25.10	22.3
1.3	6.96	17.6	0.69	0.72	3.36	4.2	5.61	15.4
1.0	10.10	26.2	-0.63	-0.09	4.0	6.2	7.89	23.0
1.3	7.65	14.5	-	0.39	1.86	3.0	4.47	12.1
1.8	1.59	20.9	2.40	2.61	4.39	3.5	3.33	20.6
-	-3.42	-	-	-0.18	-	-	-4.77	-
-	-5.76	-	-	-0.48	-	-	-6.51	-
1.6	4.65	-	-	0.69	-	1.7	2.37	-
-	5.16	-	-	0.63	-	-	2.49	-
-	1.02	-	-	0.30	-	-	-1.29	-
-	-7.32	-	-	-0.69	-	-	-7.77	-
-	-7.17	-	-	-0.69	-	-	-7.89	-
-	1.80	16.5	-	0.24	3.51	-	0.96	12.3
1.7	3.63	16.5	-	0.69	3.51	-	2.97	12.3
1.2	0.93	15.1	0.18	0.06	2.62	1.4	1.56	15.2
1.0	20.90	17.4	4.50	4.89	10.30	19.7	26.10	18.0
1.5	20.60	17.4	4.40	5.43	10.30	17.0	22.90	18.0
1.0	2.64	10.6	1.30	1.41	8.65	4.5	4.83	11.6
1.4	33.70	31.6	14.40	15.20	12.80	29.6	29.50	29.4
1.1	32.60	31.6	8.00	13.90	12.80	20.9	33.50	29.4
1.9	21.50	23.8	11.20	10.10	9.64	20.9	18.80	22.3
1.3	22.30	23.8	11.50	9.15	9.64	30.7	23.70	22.3
1.9	6.42	17.6	3.10	3.24	7.40	4.5	4.47	15.4
1.9	6.63	26.2	4.70	5.37	12.30	4.5	3.42	23.0
1.3	5.50	14.5	2.90	4.02	7.20	2.2	2.37	12.1

It was therefore decided to utilize the second specimen for all further tests.

TESTING THE SECOND SPECIMEN

Static Tests

The series of incremental loading static tests performed on the first specimen were repeated with the second specimen. Resultant data are shown in Table XLIII. No changes in specimen manufacturing defects were observed as a result of testing.

Comparison of the finite element analytical stresses with test results from the second specimen are presented in Table XLIII. In the more highly stressed areas (Areas 1, 3 and 4), excellent correlation was obtained as shown in Figures 144 through 146. In the lower stressed areas, correlation was not as good. However, in these areas the finite element predictions were generally conservative (higher than measured).

Stress correlation could be improved in the lower stressed regions by improved finite element modeling techniques. The technique used to model suspected high stress areas utilized a large number of small model elements, while modeling techniques on the suspected lower stressed areas resulted in a reduction of model elements to meet budget and schedule constraints and in turn resulted in insufficient detail to obtain good correlation.

3600-Hour Fatigue Test

The fuselage specimen was subjected to a spectrum of fatigue loads simulating 3600 hours of service to demonstrate the structural integrity of the fuselage.

In order to define the loading levels and duration of the proposed accelerated fatigue test, the stresses measured during static tests together with established fatigue methodology were used to calculate the fatigue damage which would be accrued during 3600 hours of service life. Appropriate stress concentration factors were applied to the stress data in those areas where the strain gage, due to its physical size, could not be located at the precise point of maximum stress. Figure 147 shows a typical strain gage installation, and Figure 148 presents a typical stress concentration factor calculation.

Since in-flight load magnitudes vary widely as a function of pilot technique, it was unrealistically severe to apply the maximum stress resulting from 100% of design limit load to each maneuver damage calculation. Figures 149 through 152 show the frequency of occurrence of each maneuver vs maneuver severity based on flight histories of similar aircraft. These data were used to define the number of occurrences at



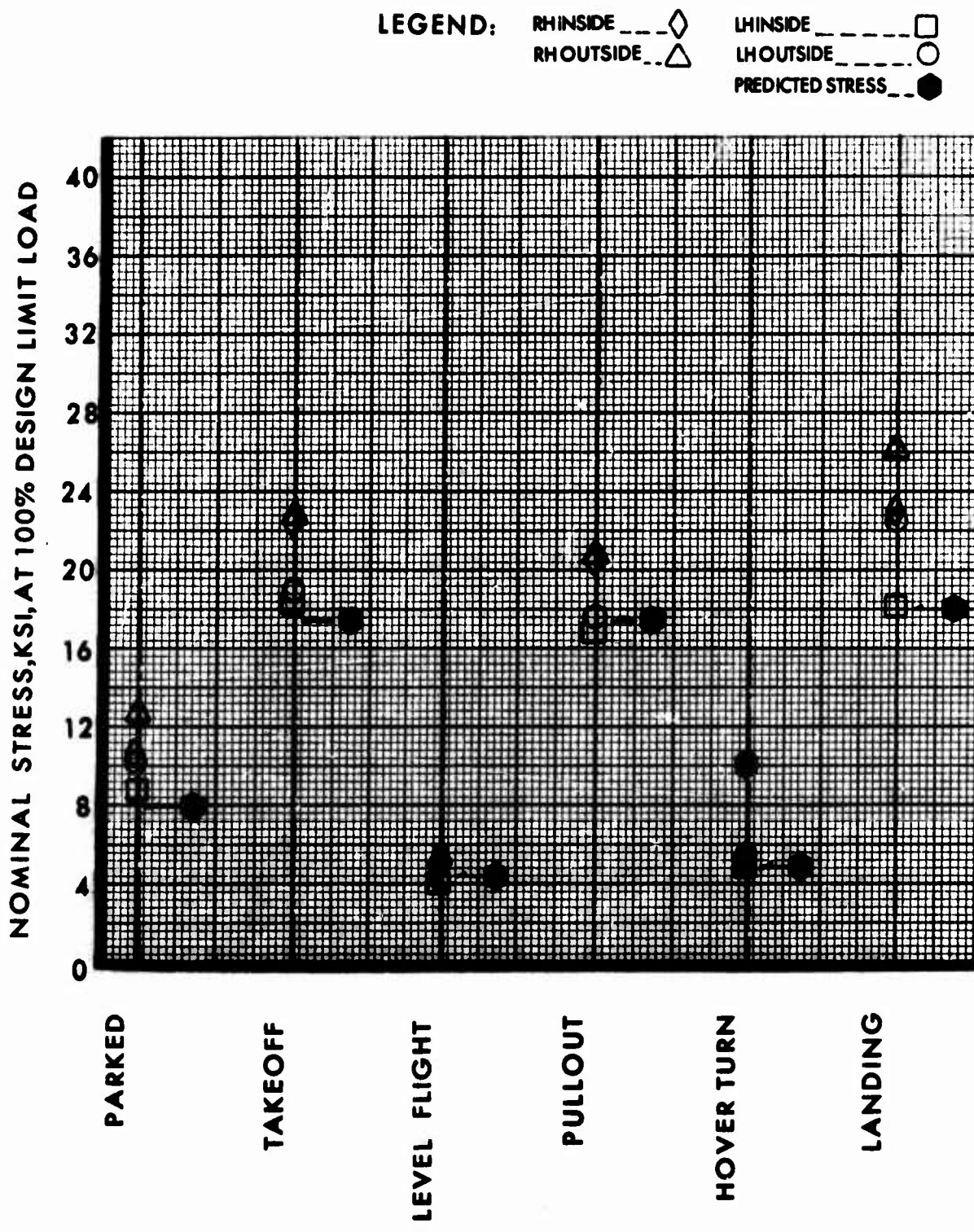


Figure 144. Structural Armor Fuselage, Static Stress Correlation,
Specimen S/N-2, Area 1.

LEGEND: RH INSIDE \square
 RH OUTSIDE \triangle
 LH INSIDE \square
 LH OUTSIDE \circ
 PREDICTED STRESS \blacksquare

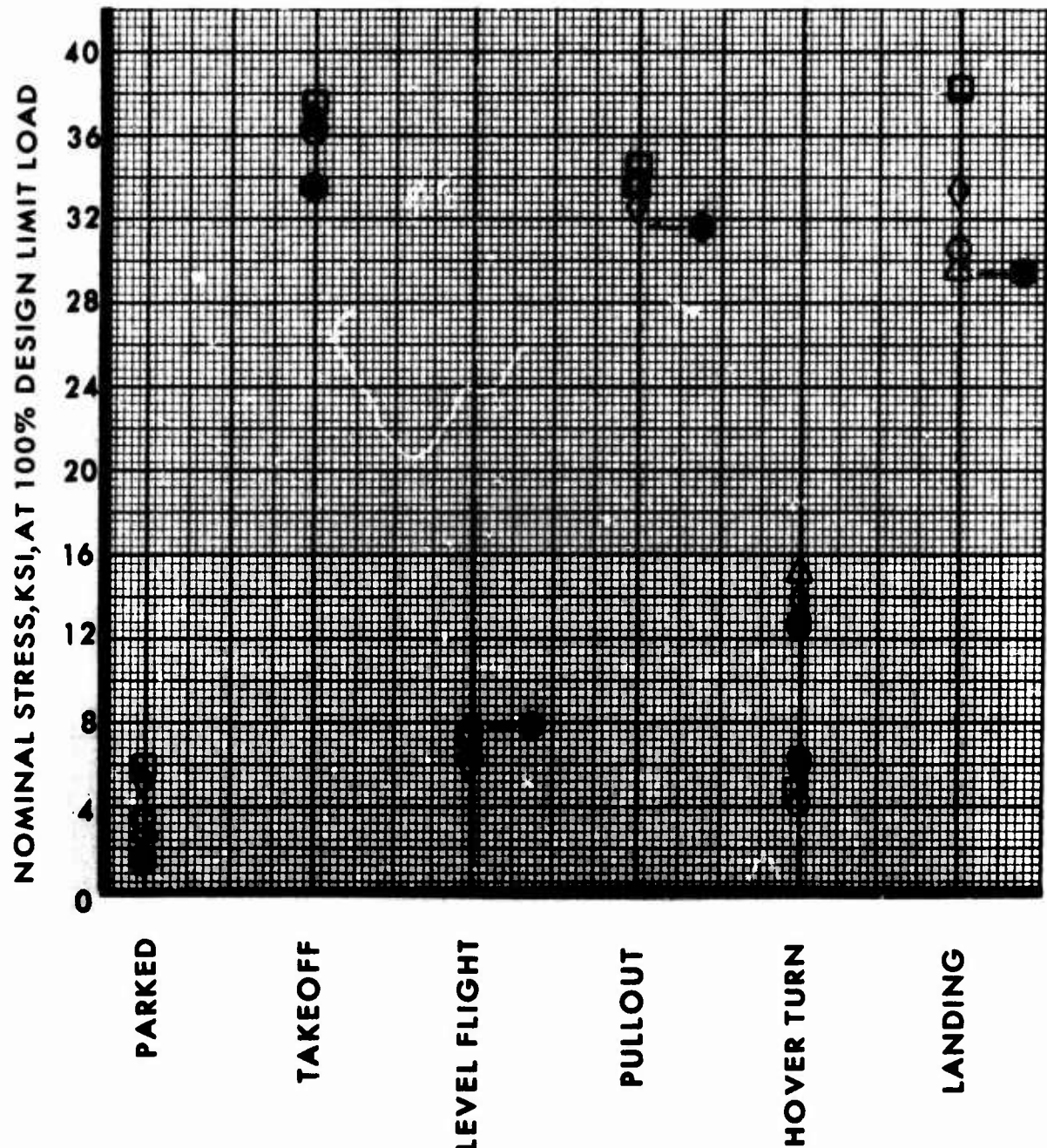


Figure 145. Structural Armor Fuselage, Static Stress Correlation, Specimen S/N-2, Area 3.

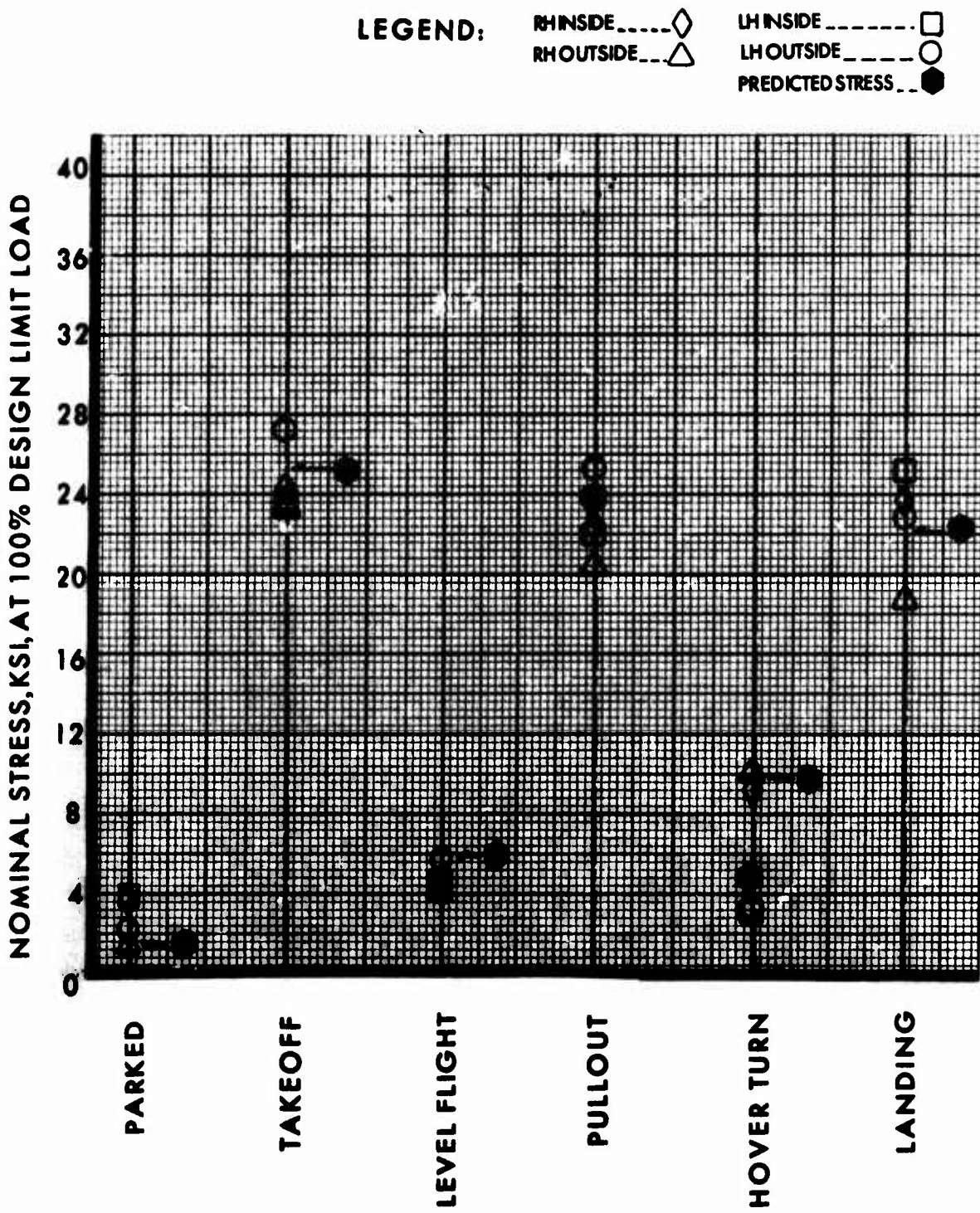


Figure 146. Structural Armor Fuselage, Static Stress Correlation, Specimen S/N-2, Area 4.

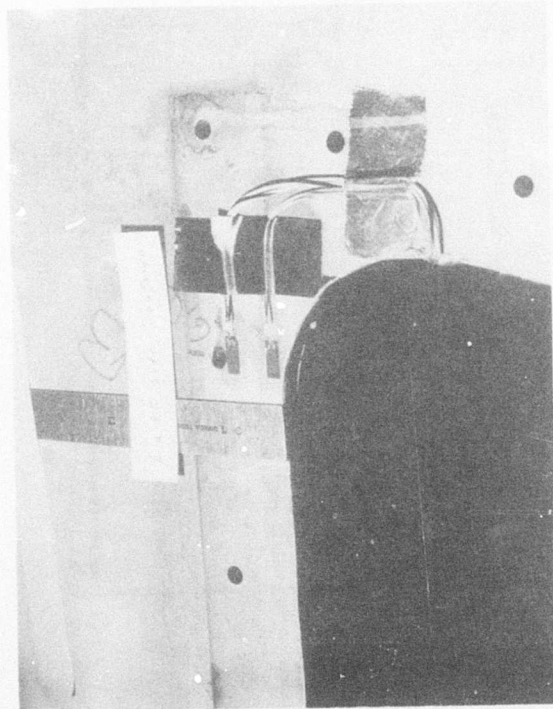
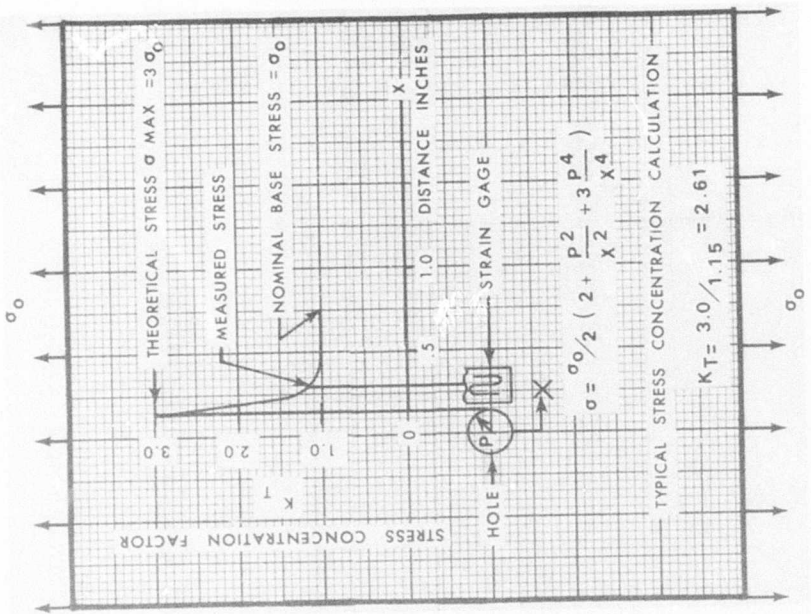


Figure 147. Structural Armor Fuselage, Typical Strain Gage Installation, Specimen S/N-2, Areas 3 and 4.

X DISTANCE FROM CENTER OF HOLE
P RADIUS OF HOLE
 σ_0 BASE STRESS

Figure 148. Typical Stress Concentration Calculation, Area 1.

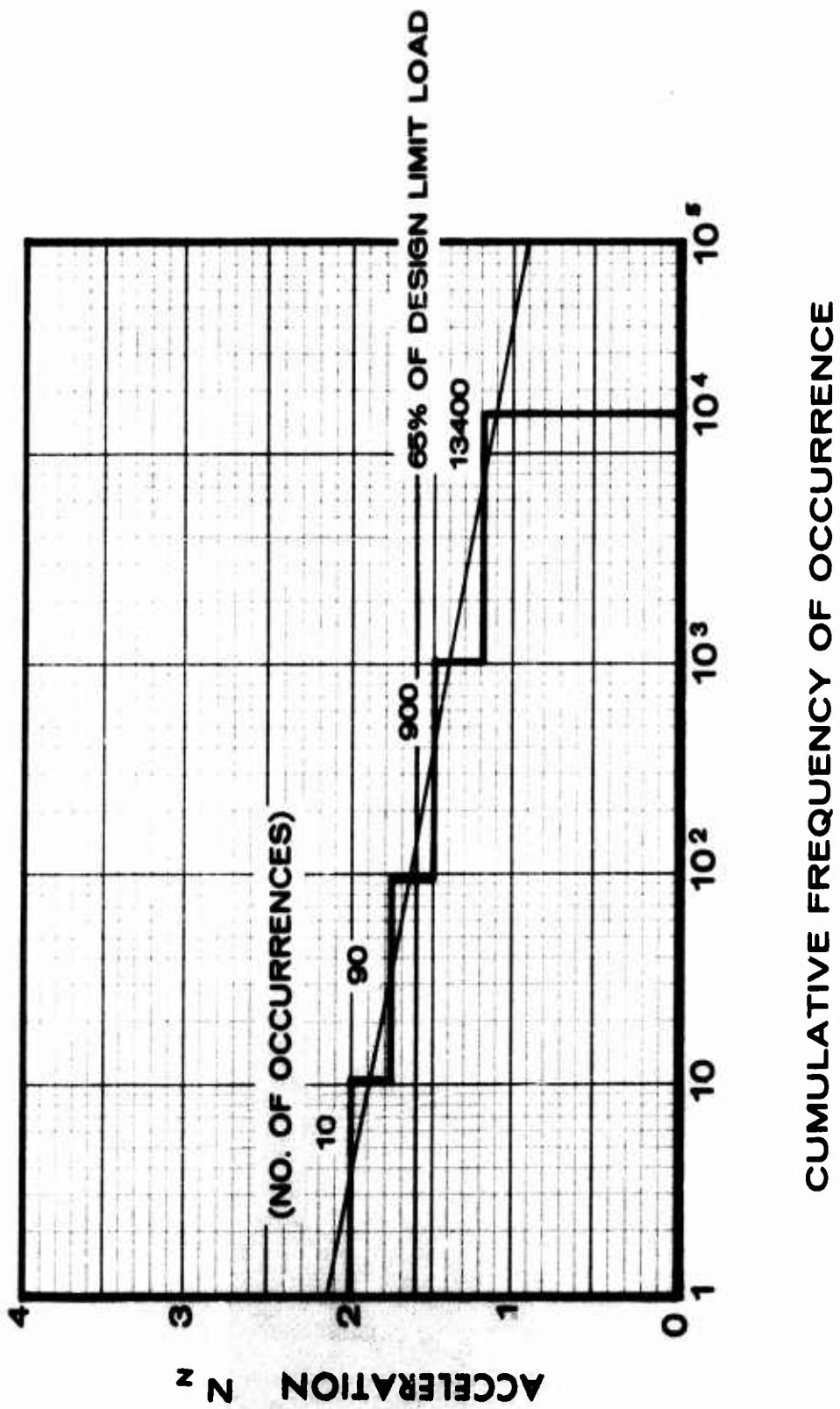
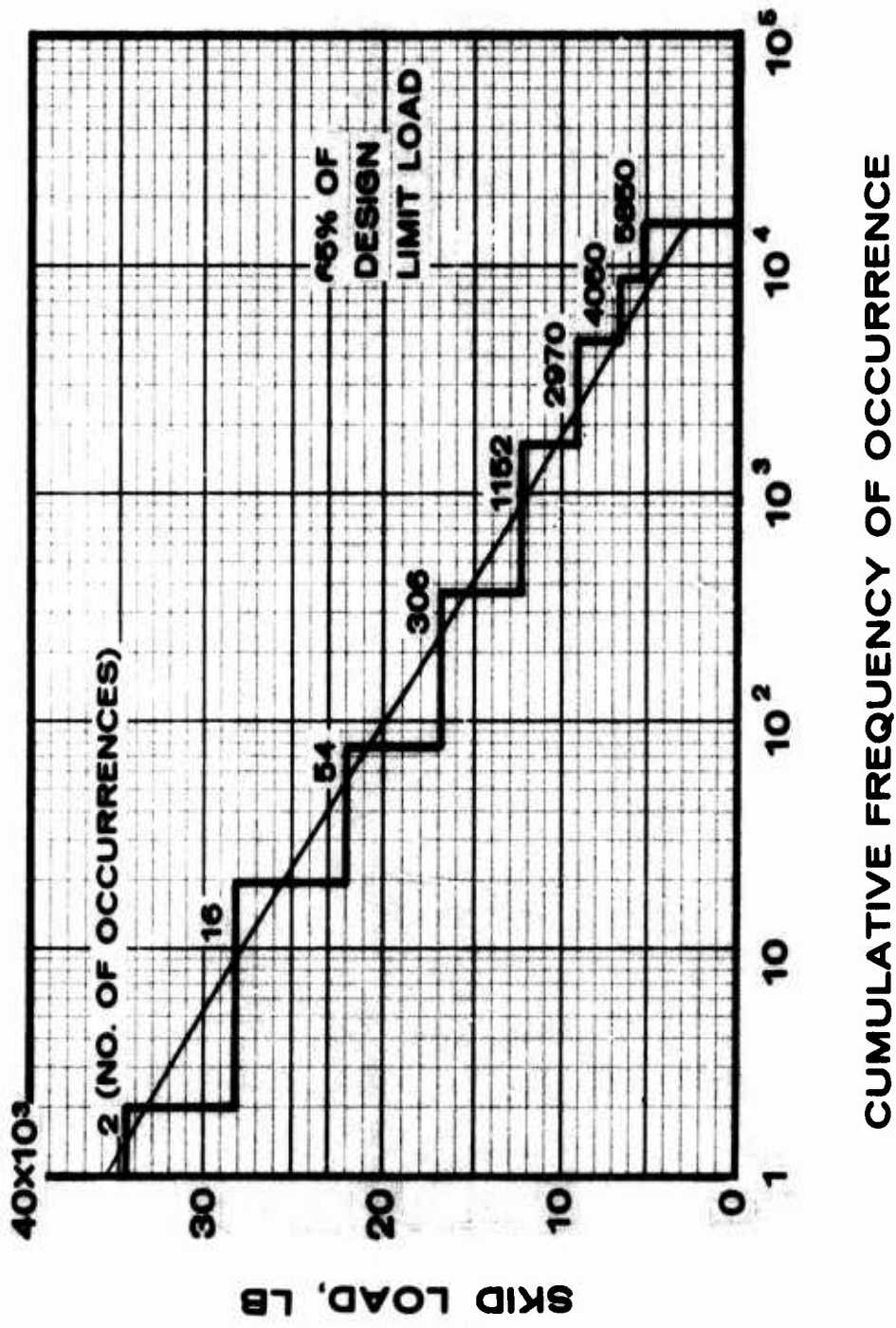


Figure 149. Structural Armor Fuselage, Load Factor Distribution - Cumulative Frequency of Occurrences in Vertical Takeoff Maneuvers for Aircraft Life of 3600 Hours.



CUMULATIVE FREQUENCY OF OCCURRENCE

Figure 150. Structural Armor Fuselage, Impact Landing Load Distribution - Cumulative Frequency of Occurrence for Aircraft Life of 3600 Hours.

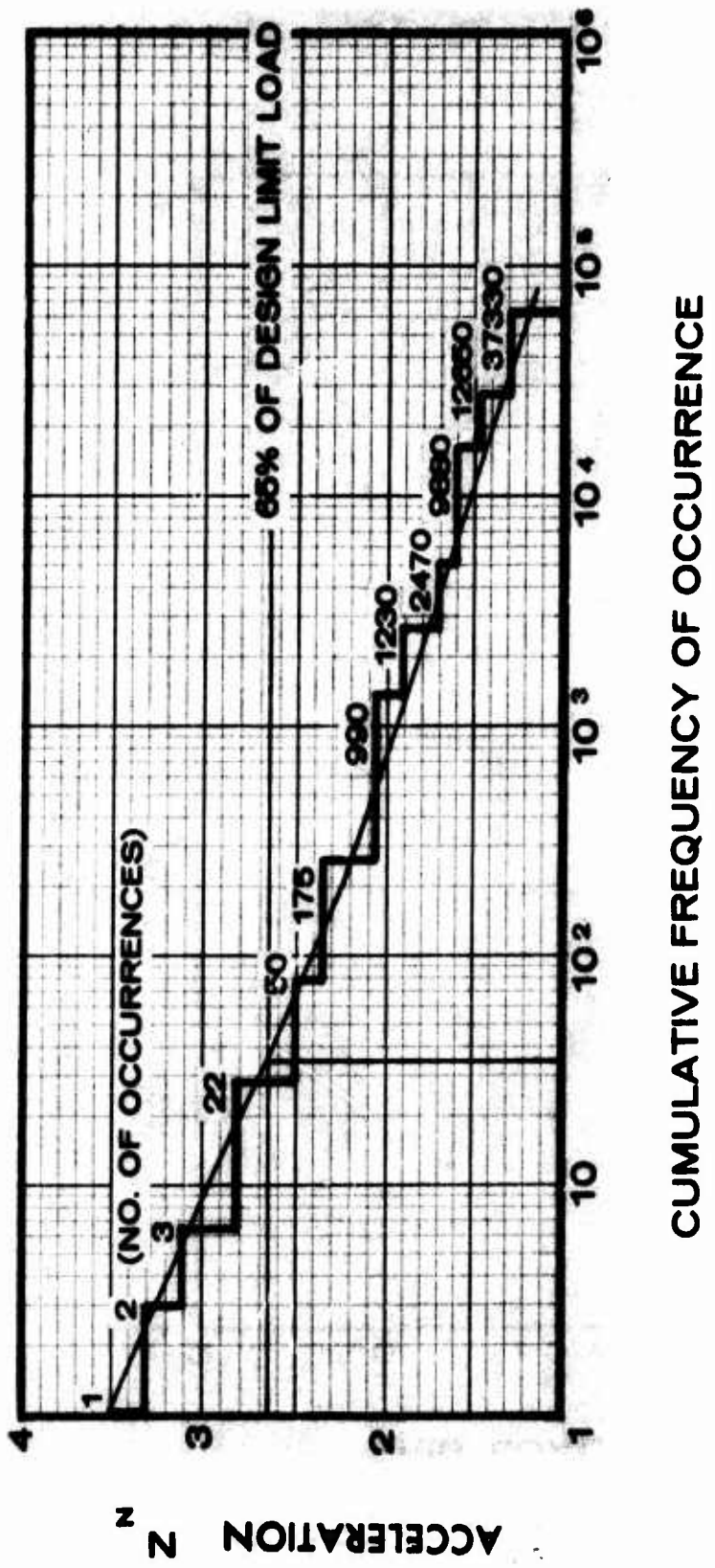


Figure 151. Structural Armor Fuselage, Maneuver Load Factor Distribution - Cumulative Frequency of Occurrence for Aircraft Life of 3600 Hours.

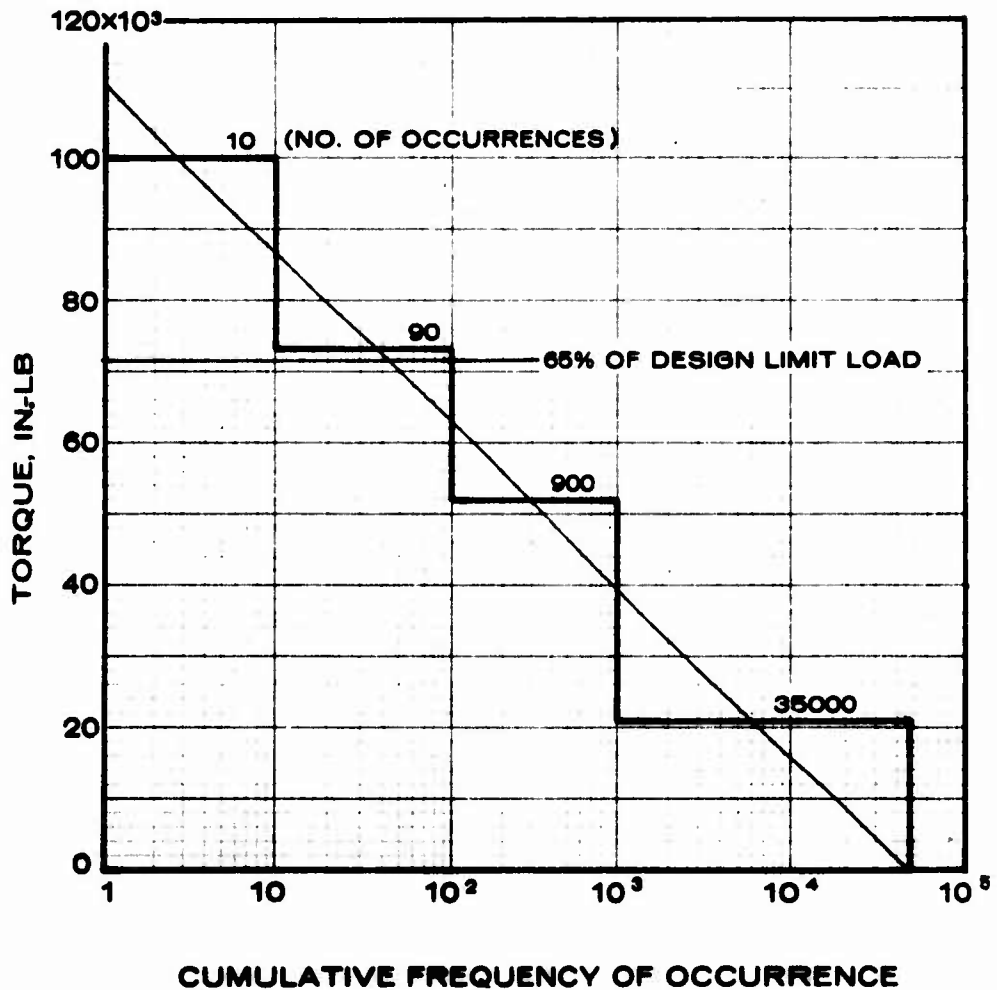


Figure 152. Structural Armor Fuselage, Hover Turn Torque Distribution - Cumulative Frequency of Occurrence for Aircraft Life of 3600 Hours.

each severity level for each maneuver, and provided the basis for the in-service damage calculations in Tables XLIV, XLV, and XLVI.

Vibratory stresses for each maneuver load were calculated using level flight as a base and used to perform fatigue damage calculations based on the dual hardness steel S-N curve shown on Figure 153. This curve was reduced by the appropriate size factor relating fuselage size to the size of the small specimens used for S-N data evaluation.

Employing Miner's Cumulative Damage Theory which states

$$\text{Damage} = \sum n/N$$

where n = the number of cycles at a given level
 N = the allowable cycles at that level

and that crack initiation theoretically occurs when $\sum n/N = 1.0$ the in-flight damage, accumulated in 3600 service hours, was calculated in Tables XLIV, XLV, and XLVI.

The results of these calculations showed that 100% design limit loads resulted in equivalent vibratory stresses below the material endurance limit at all except two locations. At these locations the equivalent vibratory stresses were only marginally over the material endurance limit. Calculated in-flight fatigue damage at these locations due to 3600 hours of service was negligible and was, in fact, exceeded by the 100% design limit load static testing. The calculations of damage accrued during static tests are shown in Tables XLVII, XLVIII and XLIX.

The requirement to subject the specimen to the equivalent of 3600 hours service life had thus been met by loading during static tests, but in order to further increase confidence in the structural integrity of the fuselage, a fatigue test was performed at 65% of design limit loads, which represented loads higher than the 99½ percentile load levels occurring in service.

The specimen was subjected to 300 blocks of the fatigue load spectrum shown in Figure 130. Weld protection strips were bonded to all welded joints except those where critical strain gages were located or where the bonded strip would interfere with observation of any crack propagation. The cylinder loads were applied automatically by the servo controlled hydraulic loading system and monitored continuously to verify correct functioning of the load control programmer. Selected strain gages, on the more highly stressed areas of the fuselage, were monitored periodically during load cycling. Microwire circuits were used to detect crack initiation in critical areas. Periodic visual inspections of the entire fuselage for fatigue cracks supplemented the microwire detection system.

The 300 spectrum blocks were completed without initiation of new cracks or any propagation of existing material processing cracks.

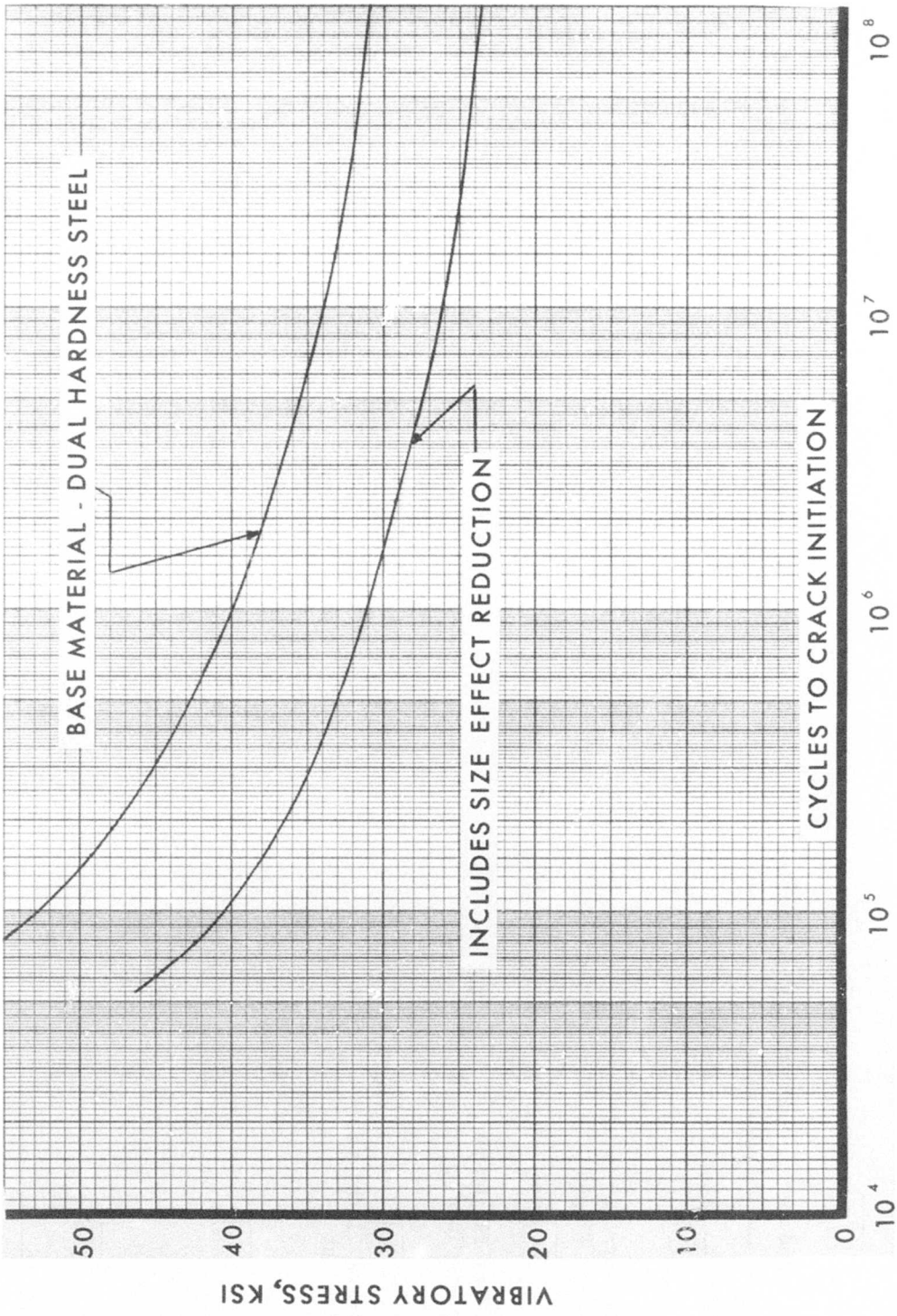


Figure 153. Structural Armor Fuselage, Dual Hardness Steel Material S/N Curve.

TABLE XLIV. IN-FLIGHT DAMAGE CALCULATIONS, SPECIMEN 2, AREA 1 (GAGES 1 & 2)

Maneuver	Item	Acceleration	Cycles in 3600 Hrs.	Equivalent Vibratory Stress (±ksi)	Allowable Cycles (X10 ⁻⁶)	Damage
Park to Takeoff	1	2.00	5	9.17	0	
	2	1.75	45	nondamaging	0	
	3	1.50	450	nondamaging	0	
	4	1.20	4700	nondamaging	0	
Takeoff to Level Flight	1	2.00	5	14.51	0	
	2	1.75	45	nondamaging	0	
	3	1.50	450	nondamaging	0	
	4	1.20	6700	nondamaging	0	
Level Flight to Hover Turn	1	3.50	10	0.24	0	
	2	2.70	45	nondamaging	0	
	3	2.00	450	nondamaging	0	
	4	1.00	17500	nondamaging	0	
Level Flight to Pullout	1	3.50	1	12.99	0	
	2	3.30	2	nondamaging	0	
	3	3.10	3	nondamaging	0	
	4	2.80	22	nondamaging	0	
	5	2.50	50	nondamaging	0	
	6	2.35	175	nondamaging	0	
	7	2.05	990	nondamaging	0	
	8	1.90	1230	nondamaging	0	
	9	1.70	2470	nondamaging	0	
	10	1.60	9880	nondamaging	0	
	11	1.45	12650	nondamaging	0	
	12	1.30	37330	nondamaging	0	

TABLE XLIV - Continued

Maneuver	Item	Acceleration	Cycles in 3600 Hrs.	Equivalent Vibratory Stress (±ksi)	Allowable Cycles (X10-6)	Damage
Level Flight to Land	1	3.50	1	16.15	0	nondamaging
	2	2.90	8		0	nondamaging
	3	2.40	27		0	nondamaging
	4	2.00	153		0	nondamaging
	5	1.70	576		0	nondamaging
	6	1.30	1485		0	nondamaging
	7	1.20	2025		0	nondamaging
	8	1.00	2925		0	nondamaging
Land to Park	1	3.50	1	10.81	0	nondamaging
	2	2.90	8		0	nondamaging
	3	2.40	27		0	nondamaging
	4	2.00	153		0	nondamaging
	5	1.70	576		0	nondamaging
	6	1.30	1485		0	nondamaging
	7	1.20	2025		0	nondamaging
	8	1.00	2925		0	nondamaging
TOTAL IN-FLIGHT DAMAGE IN 3600 HRS.						
						0

TABLE XLV. IN-FLIGHT DAMAGE CALCULATIONS, SPECIMEN 2, AREA 3 (GAGES 4 & 5)

Maneuver	Item	Acceleration	Cycles in 3600 Hrs.	Equivalent Vibratory Stress (\pm ksi)		Allowable Cycles ($\times 10^{-6}$)	Damage
				2.00	5		
Park to Takeoff	1	2.00	5	29.45	1.9	.000003	
	2	1.75	45	22.09	∞	0	
	3	1.50	450	nondamaging	∞	0	
	4	1.20	6700	nondamaging	∞	0	
Takeoff to Level Flight	1	2.00	5	26.97	6.8	.0000007	
	2	1.75	45	20.23	∞	0	
	3	1.50	450	nondamaging	∞	0	
	4	1.20	6700	nondamaging	∞	0	
Level Flight to Hover Turn	1	3.50	10	6.77	∞	0	
	2	2.70	45	nondamaging	∞	0	
	3	2.00	450	nondamaging	∞	0	
	4	1.00	17500	nondamaging	∞	0	
Level Flight to Pullout	1	3.50	1	24.40	40.0	0	
	2	3.30	2	22.45	∞	0	
	3	3.10	3	∞	∞	0	
	4	2.80	22	nondamaging	∞	0	
	5	2.50	50	nondamaging	∞	0	
	6	2.35	175	nondamaging	∞	0	
	7	2.05	990	nondamaging	∞	0	
	8	1.90	1230	nondamaging	∞	0	
	9	1.70	2470	nondamaging	∞	0	
	10	1.60	9980	nondamaging	∞	0	
	11	1.45	12650	nondamaging	∞	0	
	12	1.30	37330	nondamaging	∞	0	

TABLE XLV - Continued

Maneuver	Item	Acceleration	Cycles in 3600 Hrs.	Equivalent Vibratory Stress (±ksi)	Allowable Cycles (X10-6)	Damage
Level Flight to Land	1	3.50	1	23.54	2	
	2	2.90	8	nondamaging	0	
	3	2.40	27	nondamaging	0	
	4	2.00	153	nondamaging	0	
	5	1.70	576	nondamaging	0	
	6	1.30	1485	nondamaging	0	
	7	1.20	2025	nondamaging	0	
	8	1.00	2925	nondamaging	0	
Land to Park	1	3.50	1	26.01	10.0	
	2	2.90	8	19.77	0	
	3	2.40	27	nondamaging	0	
	4	2.00	153	nondamaging	0	
	5	1.70	576	nondamaging	0	
	6	1.30	1485	nondamaging	0	
	7	1.20	2025	nondamaging	0	
	8	1.00	2925	nondamaging	0	
TOTAL IN-FLIGHT DAMAGE IN 3600 HRS.						.0000037

TABLE XLVI. IN-FLIGHT DAMAGE CALCULATIONS SPECIMEN 2 AREA 4 (GAGES 6 & 7)

Maneuver	Item	Acceleration	Cycles in 3600 Hrs.	Equivalent Vibratory Stress (\pm ksi)	Allowable Cycles ($\times 10^{-6}$)	Damage
Park to Takeoff	1	2.00	5	28.59	3.0	.000002
	2	1.75	45	21.44	∞	0
	3	1.50	450	nondamaging	∞	0
	4	1.20	6700	nondamaging	∞	0
Takeoff to Level Flight	1	2.00	5	25.96	10.0	.0000005
	2	1.75	45	nondamaging	∞	0
	3	1.50	450	nondamaging	∞	0
	4	1.20	6700	nondamaging	∞	0
Level Flight to Hover Turn	1	3.50	10	6.25	0	
	2	2.70	45	nondamaging	0	
	3	2.00	450	nondamaging	0	
	4	1.00	17500	nondamaging	0	
Level Flight to Pullout	1	3.50	1	23.44	0	
	2	3.30	2	nondamaging	0	
	3	3.10	3	nondamaging	0	
	4	2.80	22	nondamaging	0	
	5	2.50	50	nondamaging	0	
	6	2.35	175	nondamaging	0	
	7	2.05	990	nondamaging	0	
	8	1.90	1230	nondamaging	0	
	9	1.70	2470	nondamaging	0	
	10	1.60	9880	nondamaging	0	
	11	1.45	12650	nondamaging	0	
	12	1.30	37330	nondamaging	0	

TABLE XLVI - Continued

Maneuver	Item	Acceleration	Cycles in 3600 Hrs.	Equivalent Vibratory Stress (\pm ksi)	Allowable Cycles ($\times 10^{-6}$)	Damage
Level Flight				23.12	0	
to Land	1	3.50	1	nondamaging	0	
	2	2.90	8	nondamaging	0	
	3	2.40	27	nondamaging	0	
	4	2.00	153	nondamaging	0	
	5	1.70	576	nondamaging	0	
	6	1.30	1485	nondamaging	0	
	7	1.20	2025	nondamaging	0	
	8	1.00	2925	nondamaging	0	
Land to Park	1	3.50	1	25.75	13.0	.0000001
	2	2.90	8	nondamaging	0	
	3	2.40	27	nondamaging	0	
	4	2.00	153	nondamaging	0	
	5	1.70	576	nondamaging	0	
	6	1.30	1485	nondamaging	0	
	7	1.20	2025	nondamaging	0	
	8	1.00	2925	nondamaging	0	
TOTAL IN-FLIGHT DAMAGE IN 3600 HRS.						
.0000026						

TABLE XLVII. STATIC TEST DAMAGE CALCULATIONS,
SPECIMEN S/N-2,
AREA 1 (GAGES 1 & 2)

Test Condition	Change in Stress (ksi)	Equivalent Vibratory Stress (±ksi)	Actual Cycles	Allowable Cycles (x10 ⁻⁶)	Accumulated Damage
Parked	19.24	9.62	4	∞	0
Takeoff	37.58	18.79	2	∞	0
Level Flight	8.57	4.28	2	∞	0
Pullout	34.54	17.27	2	∞	0
Hover Turn	9.43	4.72	2	∞	0
Land	40.86	20.43	3	∞	0
Total Damage					0

TABLE XLVIII. STATIC TEST DAMAGE CALCULATIONS,
SPECIMEN S/N-2,
AREA 3 (GAGES 4 & 5)

Test Condition	Change in Stress (ksi)	Equivalent Vibratory Stress (±ksi)	Actual Cycles	Allowable Cycles (x10 ⁻⁶)	Accumulated Damage
Parked	-8.00	4.00	4	∞	0
Takeoff	-66.90	33.45	2	0.45	0.0000044
Level Flight	12.95	6.48	2	∞	
Pullout	61.75	30.87	2	1.10	0.0000018
Hover Turn	26.48	13.24	2	∞	
Land	60.02	30.01	3	1.50	0.0000020
Total Damage					0.0000082

TABLE XLIX. STATIC TEST DAMAGE CALCULATIONS,
SPECIMEN S/N-2,
AREA 4 (GAGES 6 & 7)

Test Condition	Change in Stress (ksi)	Equivalent Vibratory Stress (\pm ksi)	Actual Cycles	Allowable Cycles ($\times 10^{-6}$)	Accumulated Damage
Parked	7.36	3.68	4	∞	0
Takeoff	64.54	32.27	2	0.66	0.0000030
Level Flight	12.63	6.32	2	∞	0
Pullout	59.51	29.76	2	1.75	0.0000011
Hover Turn	25.13	12.57	2	∞	0
Land	58.86	29.43	3	1.95	0.0000015
Total Damage					0.0000056

Ballistic Test

The ballistic survivability characteristics of the fuselage were demonstrated by exposing the fuselage, under static load, to ballistic impact of caliber .30 ball and armor-piercing (AP) projectiles. The target areas, including one landing skid attachment area, were located where relatively high stresses were measured during the static stress survey. Six target areas were selected on each side of the fuselage as shown in Figures 154 and 155. One side was exposed to AP projectiles and the other to ball projectiles.

Each selected target area was marked and a wood-lined, heavy steel tube fitted over the target area to contain debris and spall. A .020 gage 6 inch x 6 inch 2024-T3 aluminum alloy witness plate was located inside the fuselage $4\frac{1}{2} \pm \frac{1}{2}$ inches behind and parallel to the target area surface to detect any penetration. The weapon was aligned, bore sighted through the spall containment tube, and clamped in place as shown in Figures 156 through 159. Wood blocks and sandbags, required for protection of personnel, equipment, and the test fixture, were placed behind the target area and around the end of the spall containment tube to seal it to the fuselage. The level flight static load condition was applied to the specimen and a chronograph, required to measure the velocity of the projectile, activated. A single round caliber .30 AP or ball ammunition was fired at the target area at normal incidence. The load was dropped, the protective blocks and spall containment tube removed, and the target area and witness plate examined for ballistic impact damage.

Thirteen rounds of caliber .30 ammunition (6 ball and 7 AP) were fired at the designated target areas on each side of the specimen. No projectile penetrations or material cracks were experienced. One round of AP (Round 1) was below minimum projectile impact velocity requirements. This shot was repeated at a target area shifted slightly from the original area. Photographs of each impact zone are shown in Figures 160 through 173. The values of projectile velocity for each round are tabulated in Table XI of the separate confidential appendix to this report.

600-Hour Fatigue Test

A fatigue test simulating an additional 600 service hours was performed on completion of ballistic testing. The specimen was cycled from no load to 100% of design limit load for each flight condition. This cycling accumulated fatigue damage in excess of that incurred in 600 hours of service. An additional 64 fatigue test spectrum loading blocks at 65% of design limit loads (in excess of the 99 $\frac{1}{2}$ percentile flight loads for each condition) were accumulated to provide further confidence in the design.

Posttest inspection showed no evidence of damage, either new cracking, or propagation of existing material processing cracks, as a result of these tests.

Ballistic Test Target Areas,
Ball Projectiles.

Figure 155. Structural Armor Fuselage,

Ballistic Test Target Areas,
Ball Projectiles.

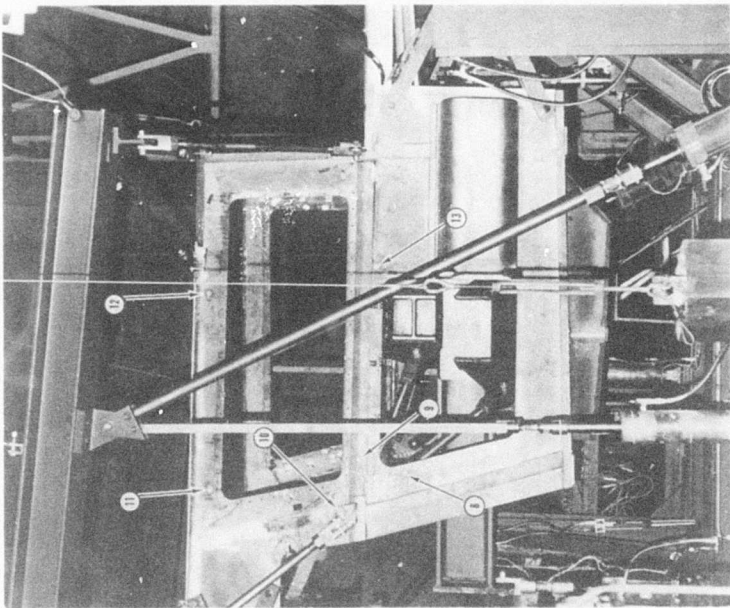


Figure 154. Structural Armor Fuselage,
Ballistic Test Target Areas,
Armor-Piercing Projectiles.

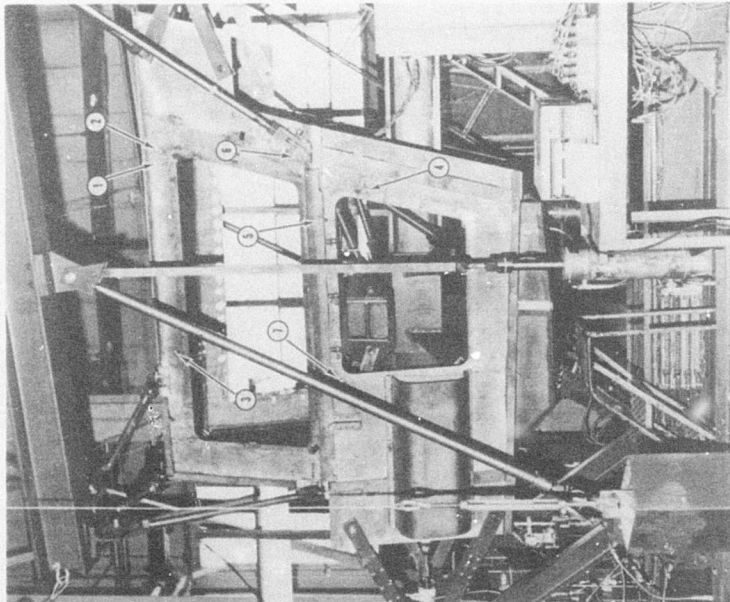


Figure 157. Structural Armor Fuselage,
Ballistic Test Setup Showing
Weapon and Chronograph.

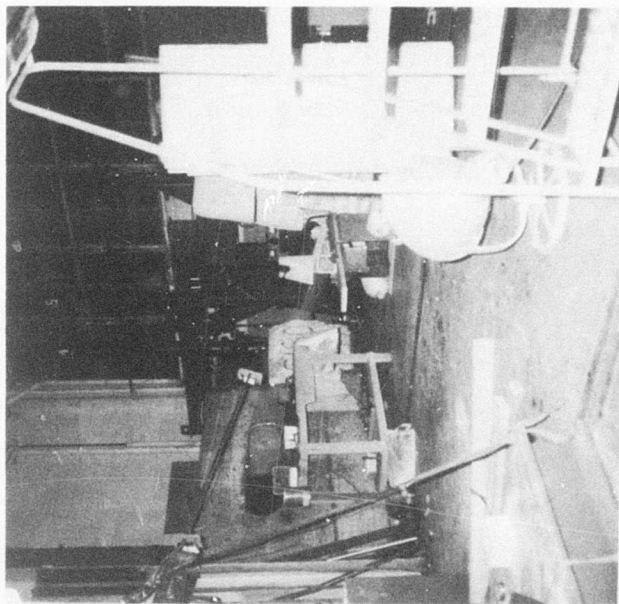
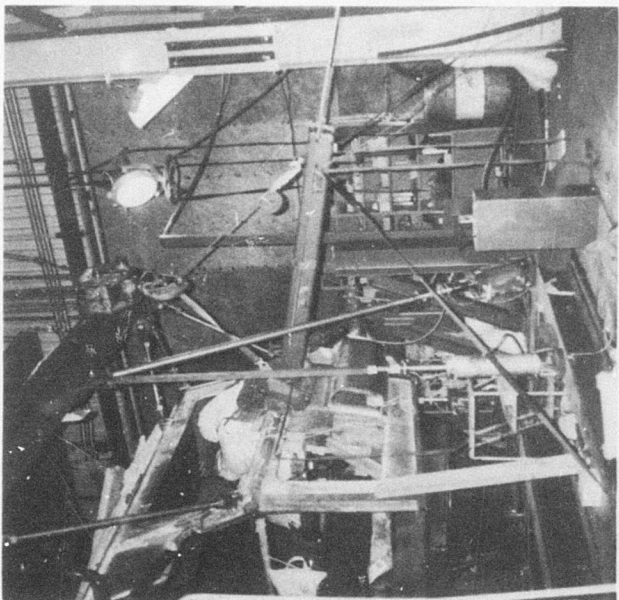


Figure 156. Structural Armor Fuselage,
Ballistic Test Setup Showing
Typical Spall Containment
Arrangements.



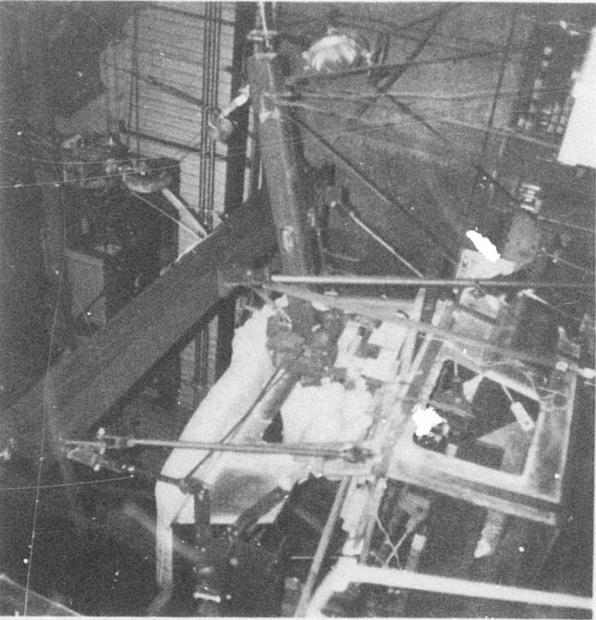


Figure 158. Structural Armor Fuselage, Ballistic Test Setup Showing Typical Spall Containment Arrangements.

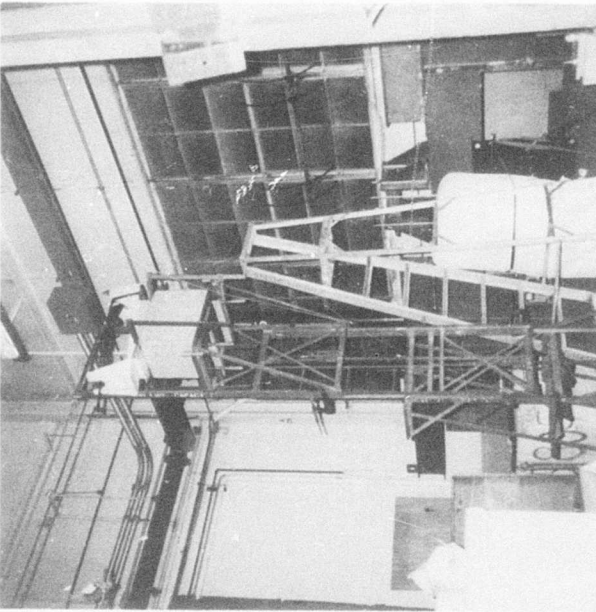


Figure 159. Structural Armor Fuselage, Ballistic Test Setup Showing Weapon and Chronograph.

Figure 161. View of Fuselage Inside Surface Behind Impact Zones of Rounds 1 and 2.

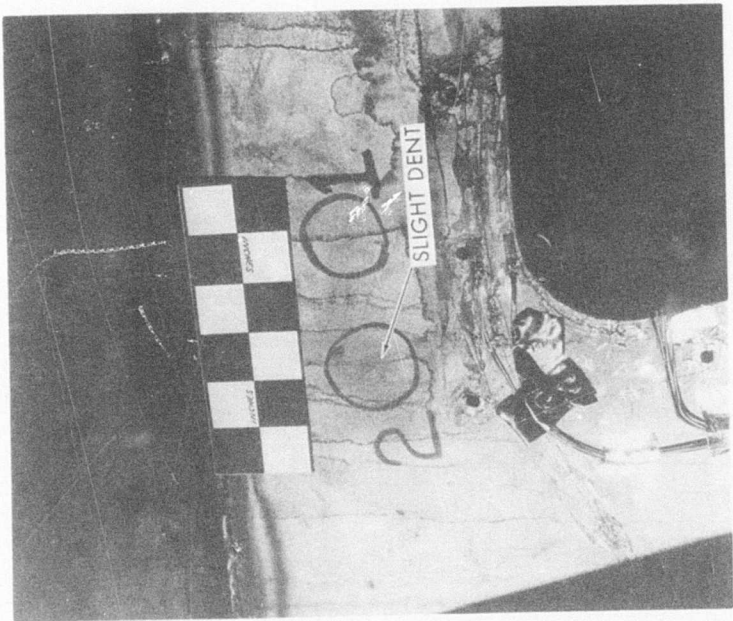


Figure 160. Ballistic Impact Zones, Rounds 1 and 2, Armor-Piercing Projectiles.



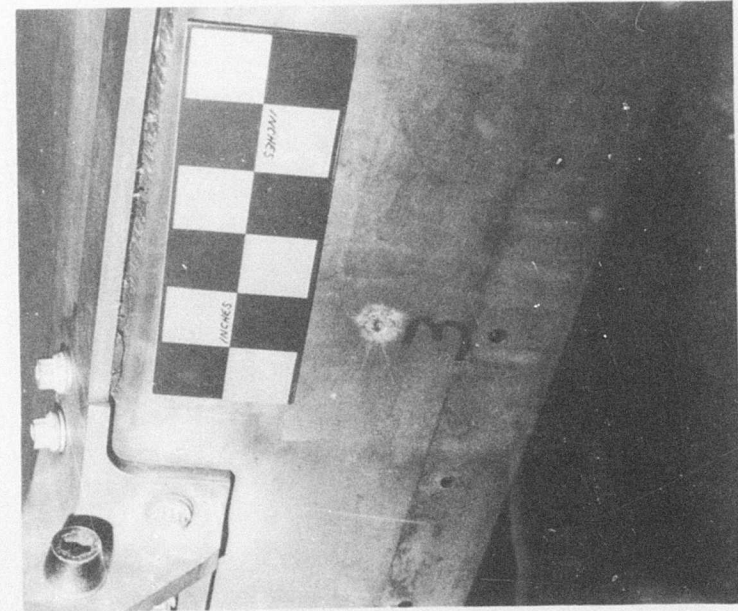


Figure 162. Ballistic Impact Zone,
Round 3, Armor-Piercing
Projectile.

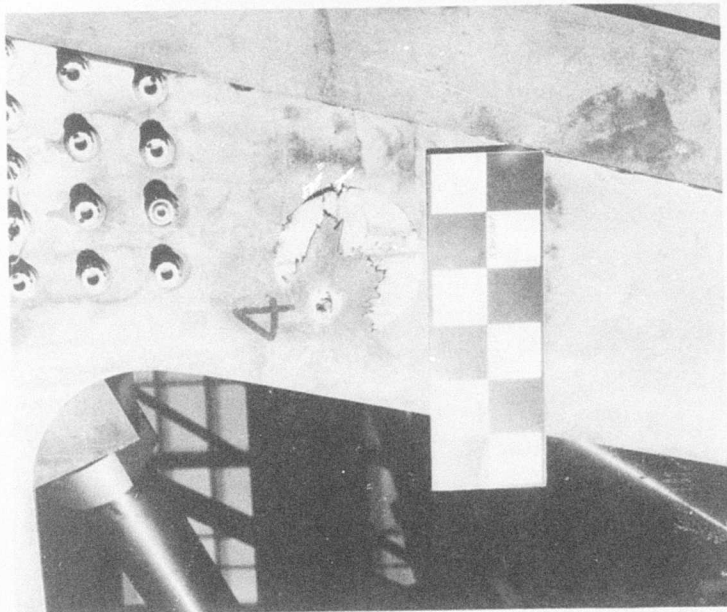


Figure 163. Ballistic Impact Zone,
Round 4, Armor-Piercing
Projectile.

Surfaces Behind Impact Zones

of Rounds 4 and 5.

Figure 165.

View of Fuselage Inside

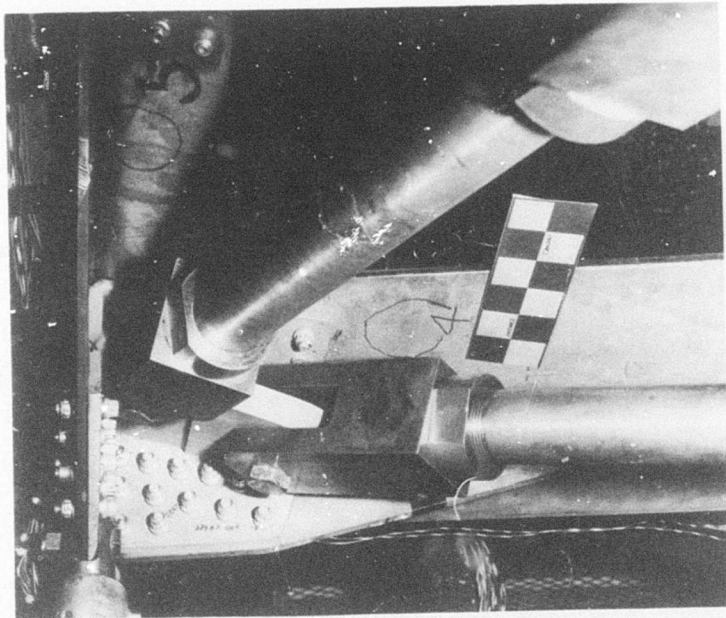


Figure 164. Ballistic Impact Zone,
Round 5, Armor-Piercing
Projectile.

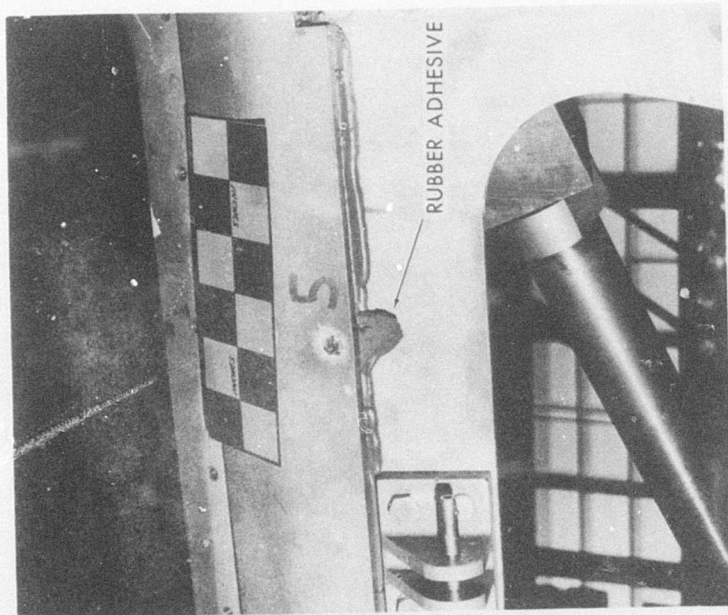


Figure 167. Ballistic Impact Zone,
Round 7, Armor-Piercing
Projectile.

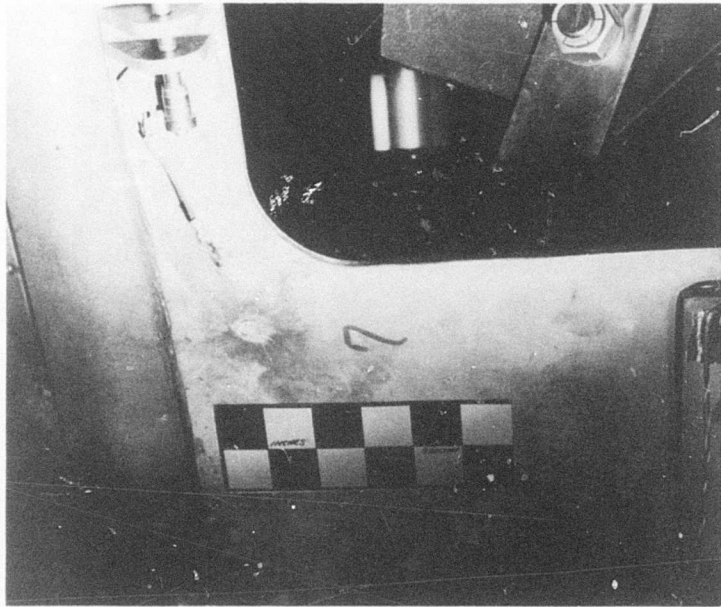


Figure 166. Ballistic Impact Zone,
Round 6, Armor-Piercing
Projectile.

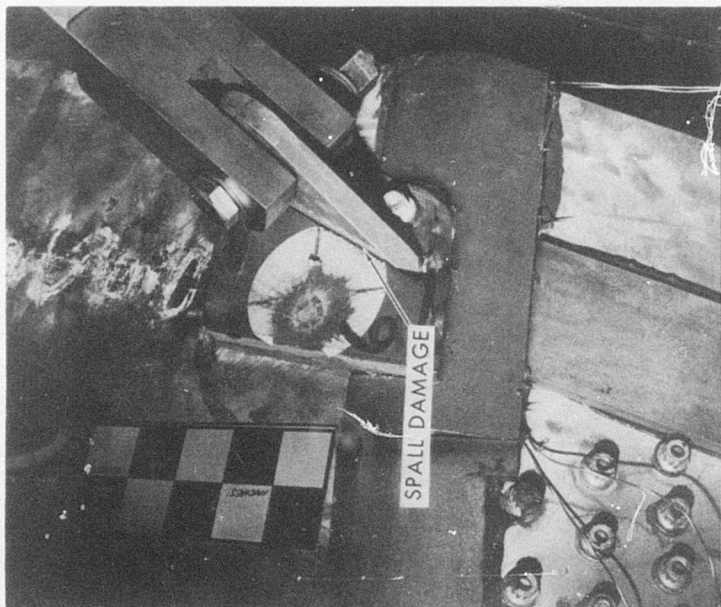


Figure 169. Ballistic Impact Zone,
Round 9, Ball Projectile.

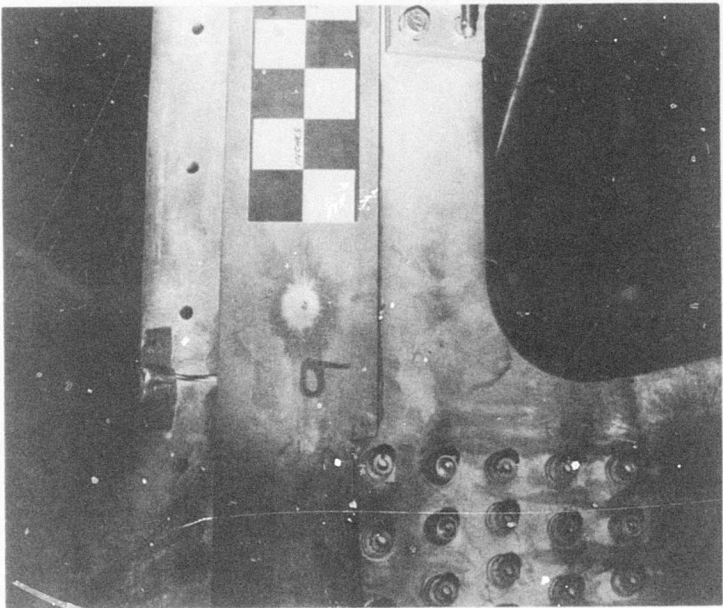
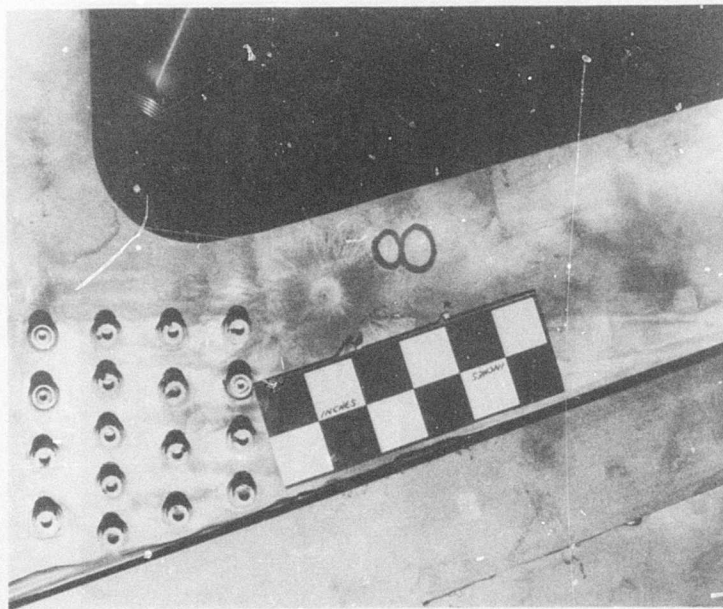


Figure 168. Ballistic Impact Zone,
Round 8, Ball Projectile.



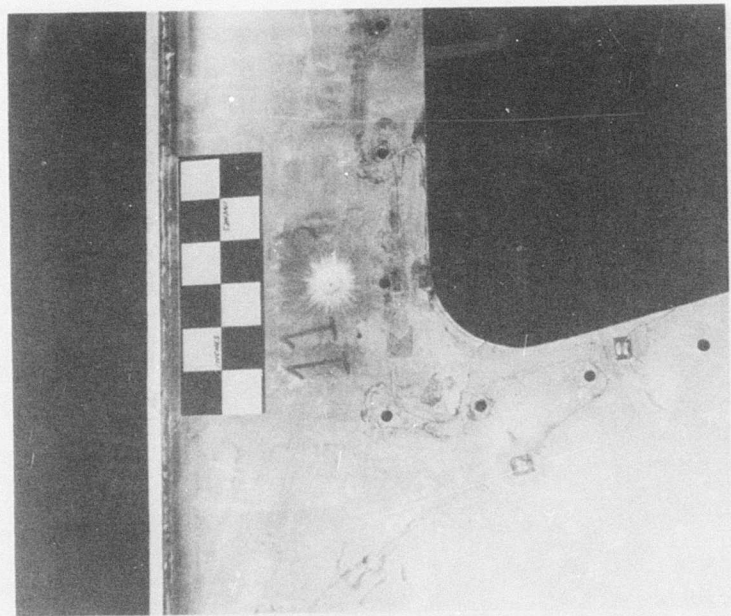


Figure 171. Ballistic Impact Zone,
Round 11, Ball Projectile.

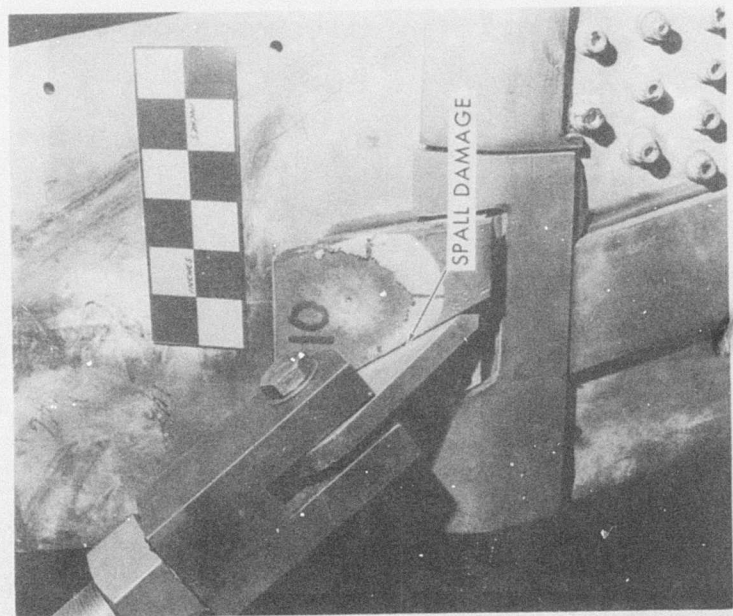


Figure 170. Ballistic Impact Zone,
Round 10, Ball Projectile.

Figure 172. Ballistic Impact Zone,
Round 12, Ball Projectile.

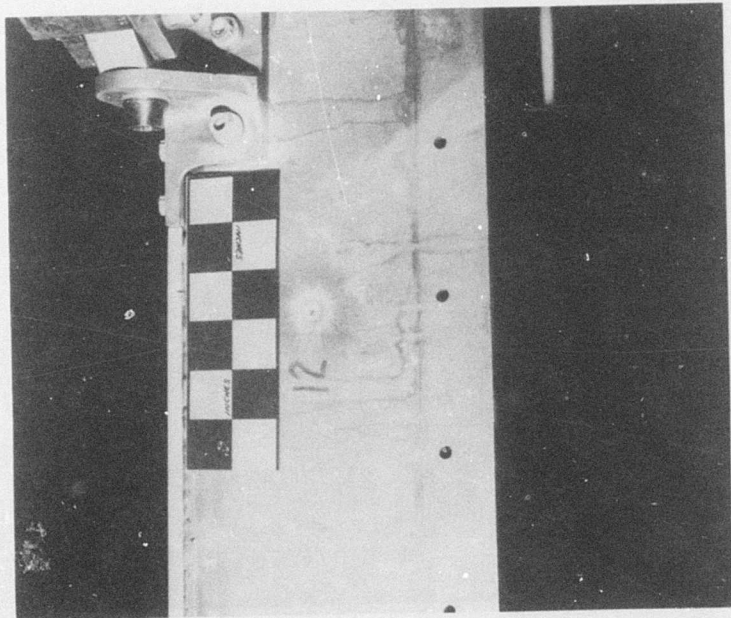
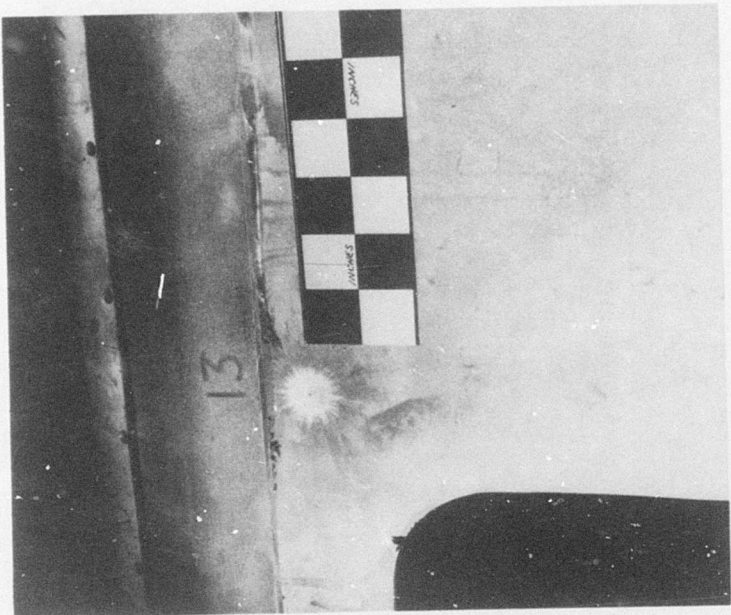


Figure 173. Ballistic Impact Zone,
Round 13, Ball Projectile.



Residual Strength Test

A residual strength test to 150% of symmetrical pullout design limit loading was performed on completion of the 600-hour fatigue test. The specimen was loaded twice to 112% of design limit load and once to 150% of symmetrical pullout design limit load. Measured strains and deflections as well as visual observations showed no indications of yielding. The measured stresses are plotted in Figure 174.

Final Damage Inspection

At the completion of all testing, a visual and dye penetrant inspection was performed at the high stressed areas. In addition, the bonded weld joint protection strip was removed from the highest stressed weld area and a dye penetrant inspection performed. The results of these inspections showed no new cracks and no measurable differences in existing material processing cracks as a result of these tests.

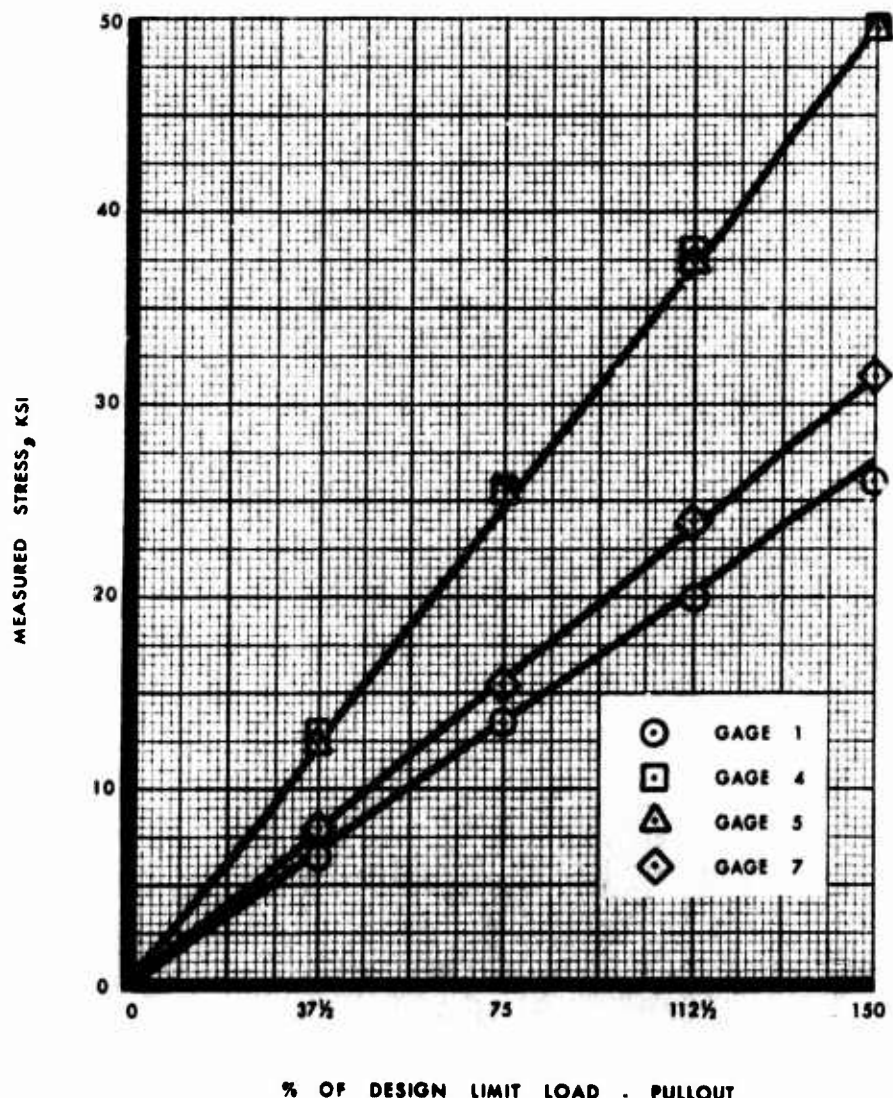


Figure 174. Residual Strength Test,
Measured Stress vs % of Design Limit
Load - Pullout.

CONCLUSIONS

1. The results of this program have demonstrated the feasibility of designing and constructing a helicopter fuselage using dual hardness steel armor as primary structure capable of achieving realistic mission requirements and sustaining realistic flight loads while providing enhanced survivability in a hostile environment involving small-arms fire.
2. A preliminary design study has established a practical aircraft configuration within the design and equipment constraints required in an actual aerial reconnaissance aircraft.
3. The fuselage design - largely defined by ballistic survivability criteria - is considerably in excess of static required strength. Design limit loads result in equivalent vibratory stresses only marginally over the material endurance limit. High frequency, low amplitude stresses produced by harmonic rotor loads and motions are nondamaging, and low frequency, high amplitude loads which occur during maneuvers, takeoffs and landings result in negligible fatigue damage in 3600 hours of service.
4. The fuselage, as demonstrated in actual testing, is structurally adequate for an equivalent of 3600 service hours.
5. The fuselage is capable of surviving the designated ballistic threat from both AP and ball type caliber .30 projectiles.
6. No loss of structural integrity was experienced by the fuselage as a result of static, fatigue and ballistic testing despite the presence of numerous material processing and residual stress cracks.
7. The present specifications for dual-hardness steel material are not adequate to assure an aircraft quality material from the supplier.
8. There are processing variables with forming and welding that resulted in cracks. This cracked structure although satisfactory for this program would not be acceptable on an aircraft, and solutions to these problems are being sought.

RECOMMENDATIONS

During the performance of this project, as well as previous contracts (DAAG46-69-C-0159 and DAAG46-71-C-0042), several areas of structural armor research and development have been identified which should be pursued. Among these areas for future study are:

1. Effect of Temperature on V_o - Initial test results have demonstrated a significant decrease in ballistic capability at 250°F , from that at ambient temperature. It is not known, however, if this decrease occurs gradually over the entire range of temperature, or rapidly above some critical temperature. The choice of a method in dealing with this ballistic reduction (additional armor, cooling or insulation) is dependent upon its behavior. This task would examine the ballistic capability at various temperatures between ambient and 250°F to determine either a linear relationship of V_o versus T , or a critical temperature (T_c), in order that a method may be selected and optimized.
2. Determination of Joint Protection Strip Thickness - The thickness of the bonded joint protection strips, in the initial testing, was selected as equal to that of the base material. Tests results have shown this thickness to be significantly more than is required for protection equivalent to that of the base material. The reduction in thickness would allow a considerable decrease in fuselage weight.
3. Effect of Hard/Soft Ratio on Armor Properties - Dual hardness steel is a composite material and its properties depend in various ways on those of its components and on the amount of each in the composite. The tests conducted to date have given some indication as to which component properties determine certain composite properties, but they have not provided the effects of changes in the components or their relative thicknesses. This task is designed to investigate the ballistic, static and fatigue properties of the composite; to determine the critical factors for each property; and to determine the effect of variation in relative thickness on each. This would allow a model to be constructed by which the composite may be tailored to fit certain requirements for ballistic, static and fatigue properties in various applications.
4. Additional Fatigue Characterization - All fatigue testing conducted to date has been at a constant ratio of σ_{\min} to σ_{\max} . This has allowed construction of a straight line Goodman diagram for axial tension-tension loading which is felt to be very conservative. To improve analytical capabilities for various structural configurations and loading conditions, more data are required. This task would involve testing under various steady load conditions to generate data for tension-compression loading, as well as for bending fatigue with the maximum stress on both hard and soft sides. This would allow the construction of a more accurate Goodman diagram under a wider range of conditions.
5. Effect of Environmental Exposure on V_o

6. Environmental Fracture Toughness
7. Environmental Effects on Fatigue - These three tasks are grouped for convenience since they all address themselves to the same basic consideration - the effect on the properties of armor, when exposed to long-term extreme conditions. Various environments such as chlorides and nitrates are known to be detrimental to steel, predominantly due to their corrosive effects. Obviously, long-term exposure would be expected to reduce ballistic and strength properties; however, the extent of this reduction remains to be determined. In addition, the protective finish to be used should be evaluated to determine the degree of protection afforded. Lastly, since ballistic impact would be expected to damage the protective finish to some degree, the protection afforded by a partial finish should be investigated to allow the determination of inspection requirements and maintenance intervals.
8. Fracture Toughness at Temperature Extremes - A preliminary program has been conducted on a few specimens which indicates little effect on KIC at -65°F and $+250^{\circ}\text{F}$, compared to ambient temperature. This task is designed to increase the confidence in these results and to expand the range of test data. At the same time, it will provide a clearer indication of the effect of temperature and improve the analysis of cracked life under various conditions.
9. Effect of Projectile Velocity on Residual Strength - For a number of materials, the velocity of an impacting projectile exerts a significant effect on residual strength, predominantly due to the degree of damage inflicted. For other materials, the effect is less marked. It has not been determined clearly in which class dual hardness steel should be placed. Preliminary results indicate that a defeated round at a velocity slightly below V_o may have a more detrimental effect than a higher velocity penetrating round. In earlier test programs, the assumption was made that only a penetrating round would reduce mechanical properties. This task would evaluate this assumption by examining the residual strength properties of armor impacted by projectiles over a range of velocities centered around V_o . If necessary, the effect of these lower velocity rounds could be included in future structural analyses.
10. Effect of Higher Caliber Projectiles - Although the ballistic capability of dual hardness steel against caliber .30 ball and AP projectiles has been made of its capability against caliber .50 rounds at various obliquities. In addition, there is no available data on the residual strength after such higher caliber impacts. This task is designed to generate such data by evaluating both the ballistic limit and residual strength for the material with caliber .50 ball and AP projectiles at various velocities and obliquities.
11. Effect of Projectile Impact on Existing Cracks - The ability of dual hardness steel to sustain multiple hits while under stresses of up to 30 ksi has been demonstrated. However, cracks from a single impact may grow with time due to fatigue crack propagation. The effect of this

crack growth on multiple hit capability has not been studied. This task will examine the crack length at which rapid fracture occurs under various conditions of stress and ballistic impact. The information generated will be used in future analysis and to determine the crack lengths at which repair or replacement is necessary.

12. Investigation of Defeat Mechanism Change - Ballistic test results to date have indicated that a slope change or an actual reduction of ballistic protection with increasing armor thickness occurs for some heats of dual hardness steel. The reasons for this are not well understood, but mechanisms have been suggested involving factors such as a change in projectile defeat from shattering to blunting, stress wave interactions or dimensional effects. This task is designed to investigate the mechanism of this phenomenon in an attempt to increase the capability of the material in this thickness range.
13. Manufacturing Techniques Investigation - Although earlier investigations have demonstrated the feasibility of working with dual-hardness steel, in many cases, the optimum parameters and equipment have not been determined. Also, in the design of the AARS, new concepts have been suggested to improve the economics of fuselage construction. This task is designed to study some of these processes and their effects on ballistic properties. Among these are:
 - a) Forming, drilling and processing before hardening
 - b) Forming entire fuselage sides by standard and non-standard techniques, such as explosive forming
 - c) Automated joining processes
14. Residual Stress Investigation - Because of the difficulties experienced in manufacturing armor for the center section test article, especially the presence of cracks in some panels, it appears obvious that significant residual stresses are present in some cases. These residual stresses will affect both static and fatigue strength, in addition to ballistic resistance, and should be included if correlation with the structural analysis is to be valid. This task involves the measurement of residual stresses present in the material and the inclusion of these stresses in a revised analysis of the test article.
15. Laser Welding - While an acceptable method of joining armor by fusion welding has been demonstrated, the potential exists in laser welding to perform the same operation with a reduced heat-affected zone. It is considered possible that laser welding could reduce the current heat-affected zone width to perhaps 0.25 inch or less. This would allow significant reduction of protective cover weight, if indeed it is needed at all. This task would first further investigate the feasibility of laser welding dual-hardness steel in the present thickness range and the quality and appearance of the weld and heat-affected zone and would also involve determination of optimum parameters. If this approach is successful, further studies of the ballistic, static and fatigue properties of laser-welded armor would be conducted.

LITERATURE CITED

1. Burr, Carleton W. et al., AERIAL ARMORED FUSELAGE ENGINEERING AND MANUFACTURING REPORT, PART I, Sikorsky Aircraft, USAMMRC Technical Report 70-2/1, U.S. Army Materials and Mechanics Research Center, Watertown, Massachusetts, February 1970.
2. Paglino, Vincent M., and Beno, Edward A., FULL-SCALE WIND TUNNEL INVESTIGATION OF THE ADVANCING BLADE CONCEPT ROTOR SYSTEM, Sikorsky Aircraft, USAAMRDL Technical Report 71-25, U.S. Army Air Mobility Research and Development Laboratory, Fort Eustis, Virginia, August 1971.
3. Horner, S. F., FLUID DYNAMIC DRAG, published by the author, 1958.
Huak, E. D. (editor), USAF STABILITY AND CONTROL DATCOM, McDonnell Douglas Corporation, October 1961.
4. CRASH SURVIVAL DESIGN GUIDE, Dynamic Science (The AvSER Facility), USAAMRDL Technical Report 71-22, U.S. Army Air Mobility Research and Development Laboratory, Fort Eustis, Virginia, October 1971.
5. STRUCTURAL DESIGN REQUIREMENTS (HELICOPTERS) Military Specification MIL-S-8698 (ASG), Amendment 1, dated 28 February 1958.
6. GROUND LOADS, Department of Defense, Munitions Board Aircraft Committee Bulletin ANC-2, October 1952.
7. STRUCTURAL DESIGN REQUIREMENTS (HELICOPTERS), Aeronautical Requirement AR-56, Naval Air Systems Command, Department of the Navy, 17 February 1970.
8. Carri, R., and McLaud, E. C., REPEATED LOADS AND FATIGUE CRITERIA, Sikorsky Engineering Report SER-65167, August 1963.
9. Degnan, W. G., FATIGUE PROPERTIES AND ANALYSIS, Sikorsky Engineering Report SER-50586, April 1969.
10. Forman, R. G., Kearney, V. E., and Engle, R. M., NUMERICAL ANALYSIS OF CRACK PROPAGATION IN CYCLIC-LOADED STRUCTURES, Journal of Basic Engineering Transactions of ASME, Vol. 89, 1967, pp. 459-464.
11. Schneider, G. J., and Sainsbury-Carter, J. B., FAIL SAFE STRUCTURAL DESIGN, Sikorsky Engineering Report SER-50722, September 1971.
12. Wilhem, D. P., FRACTURE MECHANICS GUIDELINES FOR AIRCRAFT STRUCTURAL APPLICATIONS, Northrop Corporation, USAFFDL Technical Report 69-111, U.S. Air Force Flight Dynamics Laboratory, Wright-Patterson Air Force Base, Ohio, February 1970.
14. Schneider, G. J., COMPUTER PROGRAMS FOR TREATMENT OF CRACK PROPAGATION DATA, Sikorsky Engineering Report SER-50735, May 1972.

15. Murphy, T. M., AERIAL ARMORED FUELAGE MATERIALS EVALUATION, Sikorsky Aircraft, USAMMRC Technical Report 71-11, U.S. Army Materials and Mechanics Research Center, Watertown, Massachusetts, August 1971 (Classified Confidential).
16. CRACK PROPAGATION DATA REDUCTION AND FORMAN EQUATION FIT, Sikorsky Computer Program Y-124.
17. TENTATIVE METHOD OF TEST FOR PLANE-STRAIN FRACTURE TOUGHNESS OF METALLIC MATERIALS, American Society for Testing and Materials Method E 399-70T, 1971 Annual Book of ASTM Standards, Part 31.
18. Brown, W. F., Jr. and Srawley, J. E., PLANE STRAIN CRACK TOUGHNESS TESTING OF HIGH STRENGTH METALLIC MATERIALS, American Society for Testing and Materials Special Technical Publication STP-410, 1966, p. 13.
19. Cullity, B. D., ELEMENTS OF X-RAY DIFFRACTION, Reading, Massachusetts, Addison-Wesley, 1959.
20. Koistinen, P. P., and Marburger, R. E., A SIMPLIFIED PROCEDURE FOR CALCULATING PEAK POSITION IN X-RAY RESIDUAL STRESS MEASUREMENTS ON HARDENED STEEL, Transactions of the American Society for Metals, Vol. 51, 1959, pp. 537-555.
21. Manganello, S. J., and Abbot, K. H., METALLURGICAL FACTORS AFFECTING THE BALLISTIC BEHAVIOR OF STEEL TARGETS, Journal of Materials, JMSA, Vol. 7, No. 2, June 1972, pp. 231-239.

DISTRIBUTION

Director of Defense Research & Engineering	1
Assistant Secretary of the Army-(R&D)	1
Assistant Chief of Staff for Force Development, DA	1
Deputy Chief of Staff for Logistics, DA	1
United States Army, Pacific	1
Chief of Research & Development, DA	1
Army Materiel Command	4
Army Aviation Systems Command	2
Hq, Army Air Mobility Research & Development Laboratory	2
Systems Research Integration Office, AMRDL	1
Ames Directorate, Army Air Mobility R&D Laboratory	1
Eustis Directorate, Army Air Mobility R&D Laboratory	18
Langley Directorate, Army Air Mobility R&D Laboratory	2
Lewis Directorate, Army Air Mobility R&D Laboratory	2
Army Aviation Systems Test Activity	2
Army R&D Group (Europe)	2
Army Scientific & Technical Information Team (Europe)	1
Army Advanced Materiel Concepts Agency	1
Army Aeromedical Research Laboratory	1
Army Coating & Chemical Laboratory	1
Army Human Engineering Laboratories	1
Army Natick Laboratories	2
Army Ballistic Research Laboratories	1
Army Research Office	1
Army Mobility Equipment R&D Center	1
Army Materials & Mechanics Research Center	6
Army Plastics Technical Evaluation Center	1
Army Test & Evaluation Command	1
Army Materiel Systems Analysis Agency	1
Army Electronics Command	2
Army Electronic Warfare Laboratory	2
Army Missile Command	2
USACDC Experimentation Command	1
USACDC Aviation Agency	3
Army Medical R&D Command	1
Army Tank-Automotive Command	2
Picatinny Arsenal	1
Edgewood Arsenal	1
Army Command & General Staff College	1
Army Aviation Test Board	2
Army Arctic Test Center	1
Army Aviation Human Research Unit	1
Army Agency for Aviation Safety	1
Army Field Office, AFSC	1
Hq, USAF	1
Air Force Flight Test Center	1
Air Force Armament Development & Test Center	1

Air Force Aero Propulsion Laboratory	1
Air Force Materials Laboratory	4
Air Force Flight Dynamics Laboratory	3
Aeronautical Systems Division, AFSC	2
Naval Air Systems Command	13
Chief of Naval Research	3
Naval Research Laboratory	1
Naval Air Rework Facility	1
Naval Air Test Center, Patuxent River	1
Naval Air Development Center	4
Naval Air Propulsion Test Center	1
Naval Weapons Laboratory	1
Naval Ship Research & Development Center	3
Commandant of the Marine Corps	1
Marine Corps Development & Education Command	2
Marine Corps Liaison Officer, Army Transportation School	1
U.S. Coast Guard	1
Ames Research Center, NASA	2
Langley Research Center, NASA	2
Lewis Research Center, NASA	1
Manned Spacecraft Center, NASA	1
Scientific & Technical Information Facility, NASA	2
Department of Transportation Library	1
Eastern Region Library, FAA	1
Federal Aviation Administration, Washington	2
Civil Aeromedical Institute, FAA	1
Bureau of Aviation Safety, National Transportation Safety Board	1
Government Printing Office	1
Defense Documentation Center	2

Unclassified
Security Classification

DOCUMENT CONTROL DATA - R & D

(Security classification of title, body of abstract and indexing annotation must be entered when the overall report is classified.)

1. ORIGINATING ACTIVITY (Corporate author) Sikorsky Aircraft Division of United Aircraft Corporation Stratford, Connecticut		2a. REPORT SECURITY CLASSIFICATION Unclassified
2b. GROUP		
3. REPORT TITLE ARMORED STRUCTURAL HELICOPTER FUSELAGE STUDY		
4. DESCRIPTIVE NOTES (Type of report and inclusive dates) Final Report		
5. AUTHOR(S) (First name, middle initial, last name) Robert T. Welge Walter E. Huebner		
6. REPORT DATE November 1973	7a. TOTAL NO. OF PAGES 294	7b. NO. OF REFS 21
8a. CONTRACT OR GRANT NO. DAAJ02-72-C-0018	8b. ORIGINATOR'S REPORT NUMBER(S) USAAMRDL Technical Report 73-78A	
8c. PROJECT NO. 1F163211D157	8d. OTHER REPORT NO(S) (Any other numbers that may be assigned this report) SER-50834	
10. DISTRIBUTION STATEMENT Distribution limited to U.S. Government agencies only; test and evaluation; November 1973. Other requests for this document must be referred to the Eustis Directorate, U.S. Army Air Mobility Research and Development Laboratory, Fort Eustis, VA 23604.		
11. SUPPLEMENTARY NOTES Appendix containing ballistic test results under separate cover, classified confidential.	12. SPONSORING MILITARY ACTIVITY Eustis Directorate U.S. Army Air Mobility R&D Laboratory Fort Eustis, Virginia	
13. ABSTRACT <p>This program was initiated to evaluate the feasibility of using dual hardness steel armor as primary structure for a helicopter fuselage in order to enhance survivability in a hostile environment involving small-arms fire.</p> <p>This report is the result of the work conducted under a two-phase program. The Phase I effort involved the preliminary design of an aerial armored reconnaissance system (AARS) aircraft for the aerial scout mission, with a defined threat as provided by the U.S. Army. An extensive materials study was also conducted to determine the characteristics of the armor under severe environmental conditions. The armor thickness required to defeat the defined threat was established by ballistic testing, which was followed by static and fatigue testing on damaged and undamaged armor specimens. Fatigue crack initiation and propagation were also measured, and residual life after ballistic damage was identified. Ballistic tests were conducted at high and low temperatures to determine the effects of temperature on the ballistic capability of the armor.</p> <p>During Phase II, a special test facility was constructed, and a full-scale center section of the helicopter was fabricated and tested under loads determined in Phase I. Ballistic tests were also conducted on the center section test specimen while subjected to simulated flight loads. A second center section was also fabricated for subsequent testing by the U.S. Army.</p> <p>Design, analysis and test results indicate that dual hardness steel armor provides a structural material which is suitable for both primary structure and ballistic protection for an integrally armored helicopter fuselage.</p>		

DD FORM 1 NOV 68 1473 REPLACES DD FORM 1473, 1 JAN 64, WHICH IS
OBsolete FOR ARMY USE.

Unclassified

Security Classification

Unclassified
Security Classification

14. KEY WORDS	LINK A		LINK B		LINK C	
	ROLE	WT	ROLE	WT	ROLE	WT
Aerial Armaments Reconnaissance System Structural Armor Aircraft Design Dual Hardness Steel Fatigue and Static Testing, Small Scale Fatigue and Static Testing, Full Scale Structural Analysis NASTRAN Advancing Blade Concept (ABC) Rotor Crashworthiness Analysis						

Unclassified
Security Classification

12037-73